frontiers | Research Topics

New challenges and future perspectives in brain imaging methods, 2nd edition

Edited by
Nico Sollmann, Dahua Yu and Kai-Hsiang Chuang

Published in
Frontiers in Neuroscience
Frontiers in Neuroimaging

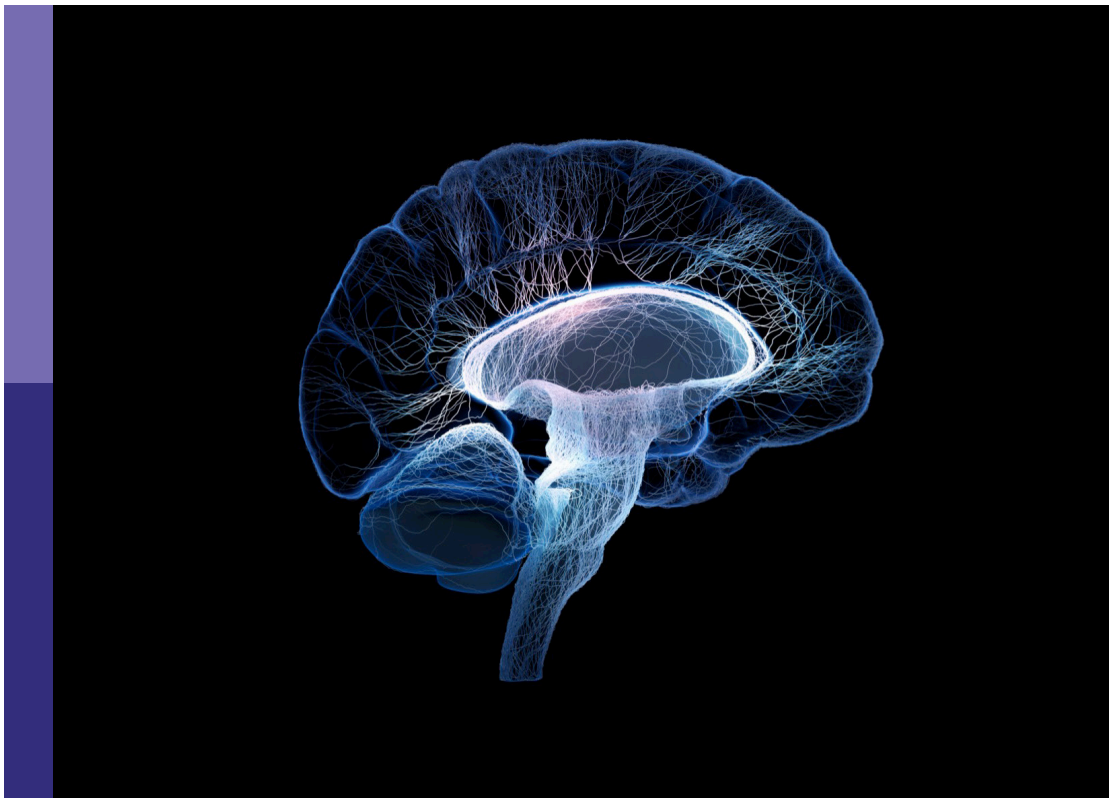

ISSN 1664-8714
ISBN 978-2-8325-5560-6
DOI 10.3389/978-2-8325-5560-6

About Frontiers

Frontiers is more than just an open access publisher of scholarly articles: it is a pioneering approach to the world of academia, radically improving the way scholarly research is managed. The grand vision of Frontiers is a world where all people have an equal opportunity to seek, share and generate knowledge. Frontiers provides immediate and permanent online open access to all its publications, but this alone is not enough to realize our grand goals.

Frontiers journal series

The Frontiers journal series is a multi-tier and interdisciplinary set of open-access, online journals, promising a paradigm shift from the current review, selection and dissemination processes in academic publishing. All Frontiers journals are driven by researchers for researchers; therefore, they constitute a service to the scholarly community. At the same time, the *Frontiers journal series* operates on a revolutionary invention, the tiered publishing system, initially addressing specific communities of scholars, and gradually climbing up to broader public understanding, thus serving the interests of the lay society, too.

Dedication to quality

Each Frontiers article is a landmark of the highest quality, thanks to genuinely collaborative interactions between authors and review editors, who include some of the world's best academicians. Research must be certified by peers before entering a stream of knowledge that may eventually reach the public - and shape society; therefore, Frontiers only applies the most rigorous and unbiased reviews. Frontiers revolutionizes research publishing by freely delivering the most outstanding research, evaluated with no bias from both the academic and social point of view. By applying the most advanced information technologies, Frontiers is catapulting scholarly publishing into a new generation.

What are Frontiers Research Topics?

Frontiers Research Topics are very popular trademarks of the *Frontiers journals series*: they are collections of at least ten articles, all centered on a particular subject. With their unique mix of varied contributions from Original Research to Review Articles, Frontiers Research Topics unify the most influential researchers, the latest key findings and historical advances in a hot research area.

Find out more on how to host your own Frontiers Research Topic or contribute to one as an author by contacting the Frontiers editorial office: frontiersin.org/about/contact

New challenges and future perspectives in brain imaging methods, 2nd edition

Topic editors

Nico Sollmann — University of California, San Francisco, United States

Dahua Yu — Inner Mongolia University of Science and Technology, China

Kai-Hsiang Chuang — The University of Queensland, Australia

Citation

Sollmann, N., Yu, D., Chuang, K.-H., eds. (2024). *New challenges and future perspectives in brain imaging methods, 2nd edition*. Lausanne: Frontiers Media SA. doi: 10.3389/978-2-8325-5560-6

Publisher's note: This is a 2nd edition due to an article retraction.

Table of contents

frontiers | Frontiers in Neuroscience

TYPE Editorial
PUBLISHED 01 November 2023
DOI 10.3389/fnins.2023.1265054

OPEN ACCESS

EDITED AND REVIEWED BY
Vince D. Calhoun,
Georgia State University, United States

*CORRESPONDENCE
Nico Sollmann
✉ nico.sollmann@tum.de

RECEIVED 21 July 2023
ACCEPTED 09 October 2023
PUBLISHED 01 November 2023

CITATION
Yu D, Chuang K-H and Sollmann N (2023) Editorial: New challenges and future perspectives in brain imaging methods. *Front. Neurosci.* 17:1265054. doi: 10.3389/fnins.2023.1265054

Editorial: New challenges and future perspectives in brain imaging methods

Dahua Yu[1], Kai-Hsiang Chuang[2] and Nico Sollmann[3,4,5]*

[1]Inner Mongolia Key Laboratory of Pattern Recognition and Intelligent Image Processing, School of Information Engineering, Inner Mongolia University of Science and Technology, Baotou, China, [2]Queensland Brain Institute, The University of Queensland, Brisbane, QLD, Australia, [3]Department of Diagnostic and Interventional Radiology, University Hospital Ulm, Ulm, Germany, [4]Department of Diagnostic and Interventional Neuroradiology, School of Medicine, Klinikum rechts der Isar, Technical University of Munich, Munich, Germany, [5]TUM-Neuroimaging Center, Klinikum rechts der Isar, Technical University of Munich, Munich, Germany

KEYWORDS

brain imaging methods, multi-modal imaging, magnetic resonance imaging, functional near-infrared spectroscopy (fNIRS), resting-state

Editorial on the Research Topic
New challenges and future perspectives in brain imaging methods

Brain imaging has seen considerable advances over the recent years. Both developments and validation of advanced image acquisition techniques as well as post-processing and analyses pipelines have contributed to contemporary imaging, including parallel imaging, (semi-)automated segmentation, generation of synthetic images, and application of machine learning and radiomics. Multi-modal approaches using structural, metabolic, and functional imaging methods are emerging to build a framework for a better understanding of anatomical features and physiological processes of the brain. This Research Topic entitled "*New challenges and future perspectives in brain imaging methods*" included 12 articles (nine original research articles, one review article, one case report, and one brief research report) covering a broad spectrum of developments and applications in the field of advanced neuroimaging.

The majority of research articles published in this Research Topic covered advances in magnetic resonance imaging (MRI) (Tafuri et al.; Lan et al.; Alberti et al.; Tomasi and Volkow; Dai et al.; He et al.; Berson et al.; Ebersberger et al.; Charyasz et al.). In a multi-center study, Tafuri et al. evaluated harmonization of radiomics features to limit site-dependent effects, given that radiomics features commonly demonstrate considerable variability related to variations between sites and imaging protocols. To overcome this issue that is limiting the reproducibility and generalizability of radiomics, T1-weighted (T1w) sequences from different sites and derived from healthy subjects and patients with Parkinson's disease (PD) were analyzed, and the authors found that data from healthy subjects may be corrected with a ComBat-based harmonization approach (Tafuri et al.). Further, an area under the curve (AUC) of 0.77 (harmonized radiomics features) vs. an AUC of 0.71 (raw radiomics measures) was revealed to distinguish patients with PD from healthy subjects, emphasizing the considerable impact of site-related effects that need to be addressed by harmonization approaches also in future multi-centric studies (Tafuri et al.). A study by Lan et al. aimed to investigate the role of extracellular fluid in the context of cerebral small vessel disease (CSVD), considering a multi-sequence MRI protocol that has been composed of T1w and T2-weighted (T2w) imaging including fluid-attenuated inversion recovery (FLAIR)

sequences, as well as diffusion tensor imaging (DTI) and susceptibility-weighted imaging (SWI). White matter (WM) hyperintensities were identified on T2w images (using Fazekas scoring), cerebral microbleeds were assessed on SWI, perivascular spaces (using 4-point scoring) were screened on T2w images, and lacunar infarction was detected on T2w and T1w images, in order to generate a CSVD MR marker score (Lan et al.). Furthermore, mean free water (FW) and fractional anisotropy (FA) were calculated based on DTI data for each patient's WM mask (Lan et al.). The authors found that mean FW of WM was significantly associated with some of the CSVD MR markers, and age, hypertension, diabetes mellitus, and FW were significantly associated with the derived CSVD MR marker score, while FW of WM matter was significantly inversely associated with FA (Lan et al.). Hence, an MRI-derived scoring system may be helpful to systematically assess CSVD burden, and extracellular fluid of WM may relate to CSVD severity and decline in WM integrity (Lan et al.). The DTI technique with extraction of FA has also been used by Alberti et al. to investigate varicella zoster-related brachial plexopathy in a case report of a 72-year-old woman, who presented with unilateral segmental paresis of the upper limb and painful dermatomal vesicular eruption. The authors observed a decrease in FA and an increase in mean, axial, and radial diffusivity for C6 and C7 roots of the affected compared to the unaffected side, indicative of microstructural fiber damage, which could be quantified by the presented approach and then considered during initial assessment and follow-up investigations in patients with plexopathy (Alberti et al.).

Using functional MRI (fMRI), Tomasi and Volkow evaluated the impact of head motion during image acquisition on functional connectivity (FC) by applying connectome-based predictive modeling to fMRI data with low frame-to-frame motion. Leave-one-out was used for internal cross-validation of head motion prediction in half of the dataset, and two-fold cross-validation was used in the other half (defined as the independent sample) (Tomasi and Volkow). Both parametric testing and connectome-based predictive modeling permutations for null hypothesis testing demonstrated strong linear associations between observed and predicted head motion (Tomasi and Volkow). Of note, prediction accuracy for head motion was higher for task-based fMRI as compared to rest-fMRI (whereas, however, prediction accuracy was lower for individuals with low motion than for those with moderate motion), and denoising attenuated the predictability of head motion, while stricter framewise displacement thresholds for motion censoring did not alter the accuracy of the predictions obtained with lenient censoring (Tomasi and Volkow). In a study by Dai et al., resting-state fMRI was used to define reproducible resting-state networks (RSNs) in healthy rats, followed by investigations of FC changes within and between RSNs following a chronic restraint stress model, given that no consensus has been made available for reproducible RSNs in rodents. In the anesthetized animals, default mode network-like, spatial attention-limbic, corpus striatum, and autonomic network patterns were identified (Dai et al.). The chronic restraint stress model decreased the anti-correlation between default mode network-like and autonomic networks and the correlation between amygdala and the nucleus accumbens and ventral pallidum within the corpus striatum network, while high individual variability in FC prior and subsequent to the stress model within RSNs became evident (Dai et al.). This high variability in FC may imply that rats may demonstrate different neural phenotypes, which should be classified further in the future to improve the sensitivity and translational impact of rodent models (Dai et al.). Furthermore, one study applied perfusion imaging by means of dynamic susceptibility contrast (DSC)-MRI in patients who had suffered ischemic stroke within the internal carotid artery territory, had related neurological deficits for at least one week after the insult, and did not receive intravenous thrombolysis or mechanical thrombectomy (He et al.). The patients underwent perfusion MRI at four time points (few weeks to 7 months after ischemic stroke), together with assessments of the National Institutes of Health Stroke Scale (NIHSS) and the modified Rankin Scale (mRS) (He et al.). Following the analysis of perfusion MRI with a whole-lesion approach and voxel-based parametric response mapping at each time point, voxels with decreased time-to-maximum values, and voxels with decreased or increased relative cerebral blood volume values derived from assessments about 3 months after ischemic stroke were superior to the mean values of the corresponding maps when predicting long-term clinical outcome at 7-months follow-up investigations (He et al.). Further, correlations were identified between the clinical prognosis and DSC-MRI parameters, thus potentially emphasizing the superiority of parametric response mapping over the whole-lesion approach for predicting long-term clinical outcome, which could be accompanied by information on heterogeneity of stroke lesions that can be derived from parametric response mapping (He et al.).

Regarding MRI with non-standard field strength, studies on both low- and high-field imaging have been published in the Research Topic (Berson et al.; Ebersberger et al.; Charyasz et al.). Specifically, Berson et al. used a point-of-care 1-Tesla MRI system to image intracranial pathologies within neonatal intensive care units (average gestational age at scan time: 38.5 $\pm$ 2.3 weeks) by acquiring T1w, T2w, and diffusion-weighted sequences. Transcranial ultrasound, 3-Tesla MRI, or both were available for comparison among the majority of the examined subjects, with the most common indications for 1-Tesla MRI being term-corrected age scans for extremely preterm neonates, intra-ventricular hemorrhage follow-up examinations, and suspected hypoxic injury (Berson et al.). The 1-Tesla MRI scan enabled identification of ischemic lesions in two infants with suspected hypoxic injury, confirmed by follow-up 3-Tesla MRI, while two lesions were identified on 3-Tesla MRI that were missed on 1-Tesla MRI (punctate parenchymal injury vs. microhemorrhage and small intra-ventricular hemorrhage) (Berson et al.). On the other hand, 1-Tesla MRI enabled the detection of parenchymal microhemorrhages that were not captured by ultrasound, emphasizing the potential of a point-of-care 1-Tesla MRI system on a neonatal intensive care unit (Berson et al.). Using a 7-Tesla MRI system in a proof-of-concept study, Ebersberger et al. investigated a 55-year-old male patient with early subacute stroke by dynamic oxygen-17 imaging in the context of a three-phase inhalation experiment, thus enabling direct and non-invasive assessment of cerebral oxygen metabolism. However, the analysis of relative oxygen-17 water

signal for the stroke region compared to the healthy contralateral side revealed no significant difference; nevertheless, the technical feasibility of oxygen-17 imaging has been demonstrated in this study, which could in the future help to distinguish between viable and non-viable tissue in neurovascular diseases (Ebersberger et al.). Furthermore, in a study by Charyasz et al., a 9.4-Tesla MRI system was used for dedicated functional mapping of sensorimotor activation in the human thalamus within the scope of a task-based fMRI experiment with assessment of subject-specific sensorimotor blood oxygenation level dependent (BOLD) responses from a combined passive sensory (tactile finger) and active motor (finger tapping) paradigm. Both applied tasks related to an increase in the BOLD signal response in the lateral nuclei and pulvinar nuclei group, with the finger tapping paradigm resulting in a stronger BOLD response compared to the tactile finger paradigm and also engaging the intralaminar nuclei group (Charyasz et al.). This study with high-field imaging may give detailed insight into functions of individual thalamic nuclei regarding processing of input signals from the sensorimotor domain (Charyasz et al.).

Besides MRI, studies on other techniques such as electrocorticography (ECoG), contrast-enhanced electrical impedance tomography (C-EIT), and functional near-infrared spectroscopy (fNIRS) have been considered in the Research Topic (Kentar et al.; Zhang et al.; Ye et al.). In this regard, ECoG was used by Kentar et al. to study spatial and temporal signal changes following ischemia due to clipping of the middle cerebral artery (for 8–12 min) in a pig model. During the experiments, five-contact ECoG stripes were placed bilaterally over the fronto-parietal cortices, thus corresponding to the irrigation territory of the middle as well as anterior cerebral artery, with ECoG recordings obtained before and after the occlusion (Kentar et al.). The electrodes close to the occlusion showed instant decay in all frequency bands and spreading depolarization onset during the first 5 h, whereas electrodes far from the occlusion showed immediate loss of fast frequencies and progressive decline of slow frequencies with an increased spreading depolarization incidence between 6 and 14 h (Kentar et al.). After 8 h, the electrode capturing the anterior cerebral artery territory showed secondary reductions of all frequency bands except gamma and high spreading depolarization incidence within 12 to 17 h (Kentar et al.). Furthermore, all electrodes showed a decline in all frequency bands during spreading depolarization, while after spreading depolarization passage the frequency band recovery was impaired only in electrodes for the middle cerebral artery; thus, ECoG may allow to capture and characterize infarct progression and secondary brain injury (Kentar et al.). In a pilot study using a rabbit model, Zhang et al. aimed to assess the feasibility of monitoring perfusion with the C-EIT technique. The animals were allocated to a group without and with unilateral internal carotid artery occlusion due to clipping (for 30 min), following injection of glucose as an electrical impedance-enhanced contrast agent through the right internal carotid artery (Zhang et al.). In the non-occlusion group, impedance values of the left cerebral hemisphere did not change significantly, whereas the impedance value of the right cerebral hemisphere gradually increased (Zhang et al.). In the occlusion group, the impedance values of both cerebral hemispheres increased gradually and then began to decrease after reaching the peak value, with significant differences in the remodeling impedance values between the left and right hemispheres in both groups, respectively, while also a significant difference for the left hemispheres between groups was revealed (Zhang et al.). Hence, C-EIT may determine brain perfusion, offering broad application perspectives from disease progression monitoring or collateral circulation judgment to detections of malignancy-related lesions (Zhang et al.). Finally, a review article by Ye et al. set the focus on recent hotspots and trends in fNIRS research, highlighting that major topics of interest included activation, prefrontal cortex, working memory, cortex, and fMRI, while particularly research on gait function has received much attention. According to the review, fNIRS seems to play an increasingly important role as a non-invasive brain functional imaging technique for the detection of function-related activity (Ye et al.).

To conclude, this Research Topic covered a large spectrum of advanced imaging technology, with a focus of the published articles on applications of MRI. Both human and animal studies have been considered, contributing to an improved understanding of brain (patho)physiology, image acquisition and processing strategies, and disease characteristics. However, also techniques that are not widely available or are emerging have been covered, which could provide either unique or complementary information when related to MRI investigations. Finally, more research is necessary regarding tailoring existing procedures to clinical needs for methods that have already been made available for the *in-vivo* study of the human brain, or to accelerate the transition of findings from animal studies to potential human applications.

Author contributions

DY: Writing—original draft. K-HC: Writing—review and editing. NS: Writing—review and editing.

Acknowledgments

The editors would like to thank the authors, reviewers, and Frontiers team for their help during the emergence of this Research Topic. DY acknowledges support from the National Natural Science Foundation of China (Grant no. 82260359).

Conflict of interest

The authors declare that the research was conducted in the absence of any commercial or financial relationships that could be construed as a potential conflict of interest.

The authors declare that they were an editorial board member of Frontiers at the time of submission. This had no impact on the peer review process and the final decision.

Publisher's note

frontiers | Frontiers in Neuroscience

TYPE Original Research
PUBLISHED 10 October 2022
DOI 10.3389/fnins.2022.1012287

OPEN ACCESS

EDITED BY
Dahua Yu,
Inner Mongolia University of Science and Technology, China

REVIEWED BY
Lydia Yahia Cherif,
Institut du cerveau et de la moelle, INSERM, France
Johann Faouzi,
INSERM U1127 Institut du Cerveau et de la Moelle Épinière (ICM), France

*CORRESPONDENCE
Benedetta Tafuri
benedetta.tafuri@uniba.it
Giancarlo Logroscino
giancarlo.logroscino@uniba.it

†These authors share last authorship

SPECIALTY SECTION
This article was submitted to Brain Imaging Methods, a section of the journal Frontiers in Neuroscience

RECEIVED 05 August 2022
ACCEPTED 20 September 2022
PUBLISHED 10 October 2022

CITATION
Tafuri B, Lombardi A, Nigro S, Urso D, Monaco A, Pantaleo E, Diacono D, De Blasi R, Bellotti R, Tangaro S and Logroscino G (2022) The impact of harmonization on radiomic features in Parkinson's disease and healthy controls: A multicenter study. *Front. Neurosci.* 16:1012287. doi: 10.3389/fnins.2022.1012287

The impact of harmonization on radiomic features in Parkinson's disease and healthy controls: A multicenter study

Benedetta Tafuri[1,2]*, Angela Lombardi[3,4], Salvatore Nigro[1,5], Daniele Urso[1,6], Alfonso Monaco[3], Ester Pantaleo[3,4], Domenico Diacono[3], Roberto De Blasi[1,7], Roberto Bellotti[3,4], Sabina Tangaro[3,8†] and Giancarlo Logroscino[1,2*†]

[1]Dipartimento di Ricerca Clinica in Neurologia, Centro per le Malattie Neurodegenerative e l'Invecchiamento Cerebrale, Pia Fondazione Cardinale G. Panico, Università degli Studi di Bari Aldo Moro, Lecce, Italy, [2]Dipartimento di Scienze Mediche di Base, Neuroscienze e Organi di Senso, Università degli Studi di Bari Aldo Moro, Bari, Italy, [3]Istituto Nazionale di Fisica Nucleare (INFN), Sezione di Bari, Bari, Italy, [4]Dipartimento Interateneo di Fisica M. Merlin, Università degli Studi di Bari Aldo Moro, Bari, Italy, [5]Istituto di Nanotecnologia, Consiglio Nazionale delle Ricerche (CNR-NANOTEC), Lecce, Italy, [6]Department of Neurosciences, King's College London, Institute of Psychiatry, Psychology and Neuroscience, London, United Kingdom, [7]Dipartimento di Radiologia, Pia Fondazione Cardinale G. Panico, Lecce, Italy, [8]Dipartimento di Scienze del Suolo, Della Pianta e degli Alimenti, Università degli Studi di Bari Aldo Moro, Bari, Italy

Radiomics is a challenging development area in imaging field that is greatly capturing interest of radiologists and neuroscientists. However, radiomics features show a strong non-biological variability determined by different facilities and imaging protocols, limiting the reproducibility and generalizability of analysis frameworks. Our study aimed to investigate the usefulness of harmonization to reduce site-effects on radiomics features over specific brain regions. We selected T1-weighted magnetic resonance imaging (MRI) by using the MRI dataset *Parkinson's Progression Markers Initiative* (PPMI) from different sites with healthy controls (HC) and Parkinson's disease (PD) patients. First, the investigation of radiomics measure discrepancies were assessed on healthy brain regions-of-interest (ROIs) *via* a classification pipeline based on LASSO feature selection and support vector machine (SVM) model. Then, a ComBat-based harmonization approach was applied to correct site-effects. Finally, a validation step on PD subjects evaluated diagnostic accuracy before and after harmonization of radiomics data. Results on healthy subjects demonstrated a dependence from site-effects that could be corrected with ComBat harmonization. LASSO regressor after harmonization was unable to select any feature to distinguish controls by site. Moreover, harmonized radiomics features achieved an area under the receiving operating characteristic curve (AUC) of 0.77 (compared to AUC of 0.71 for raw radiomics measures) in distinguish Parkinson's patients from

HC. We found a not-negligible site-effect studying radiomics of HC pre- and post-harmonization of features. Our validation study on PD patients demonstrated a significant influence of non-biological noise source in diagnostic performances. Finally, harmonization of multicenter radiomic data represent a necessary step to make analysis pipelines reliable and replicable for multisite neuroimaging studies.

KEYWORDS

radiomics analysis, ComBat, multi-site harmonization, structural MRI, Parkinson's disease

Introduction

Radiomics is a challenging development area in imaging field that is greatly capturing interest of radiologists and neuroscientists (Kumar et al., 2012; Gillies et al., 2016; Salvatore et al., 2019; Guiot et al., 2022). Allowing quantitative radiographic phenotyping over several types of magnetic resonance imaging (MRI) acquisition, radiomic analysis has been proposed as a primary task to improve knowledge about diagnosis, prognosis and predictions of pharmaceutical response in oncology and neurodegenerative diseases (Mayerhoefer et al., 2020). Moreover, thanks to its capability to extract engineered measures from specific regions of interest (ROIs), radiomics has shown to be a useful approach for characterizing and classifying patients with pathological conditions (Gillies et al., 2016; Feng and Ding, 2020). Indeed, many oncological applications have demonstrated the radiomics ability to capture intra-tumoral heterogeneity in a non-invasive way. Concerning neurodegenerative diseases, instead, recent studies on Alzheimer's (AD) and Parkinson's diseases (PD) have highlighted the potentiality of radiomics to detect abnormalities beyond standard morphological imaging markers. In particular, radiomics approach had achieved interesting results in distinguishing patients with PD from controls (Cao et al., 2020; Liu et al., 2020) and from atypical parkinsonian syndromes (Tupe-Waghmare et al., 2021). Moreover, associations between radiomics measures and clinical variables have been described in both cross-sectional and longitudinal studies (Feng et al., 2018; Salmanpour et al., 2022).

Despite the outstanding results, radiomics features have showed a strong dependence from different research facilities or different acquisition protocols, limiting the reproducibility and generalizability of the proposed frameworks especially for application on multi-site dataset (Nieuwenhuis et al., 2017). Recent studies have addressed this issue using an intensity normalization step before the feature extraction (Nyul et al., 2000; Shinohara et al., 2014; Reinhold et al., 2018; Dewey et al., 2019). However, the elimination of non-biological variability caused by site-effects represents a not-trivial problem that makes sometimes the normalization approach ineffective for application on multi-scanner datasets (Eshaghzadeh Torbati et al., 2021; Li et al., 2021). Therefore, latest applications in the field of oncology have proposed an additional step of feature harmonization based on ComBat method (Crombé et al., 2020; Da-Ano et al., 2020; Li et al., 2021; Mali et al., 2021), originally implemented as batch-effect correction method for microarray expression data (Johnson et al., 2007). This approach has been also applied to classical morphometric properties such as cortical thickness, cortical surface area and subcortical volumes in brain MRI removing scan effect and increasing the power and statistical significance of the results (Fortin et al., 2018; Pomponio et al., 2020; Radua et al., 2020; Eshaghzadeh Torbati et al., 2021).

In the current study, we investigated the effectiveness of normalization and harmonization approaches to reduce site-effects on radiomics features from healthy brain ROIs. At first, we extracted radiomics features on T1-weighted MRI images of healthy subjects collected from different acquisition sites in the context of the *Parkinson's Progression Markers Initiative* (PPMI), sponsored by the *Michael J. Fox Foundation*, evaluating the sensitivity to site-related effects. In a second step, normalization and harmonization models defined on healthy subjects were applied on patients with PD to evaluate the classification performance pre- and post- site-effect correction.

Materials and methods

Participants

Data used in the preparation of this study were obtained from the PPMI database.[1] For up-to-date information on the study, visit ppmi-info.org. The T1-weighted MR images selected for this study were acquired using a 1.5–3 Tesla scanner

1 www.ppmi-info.org/access-data-specimens/download-data

from different manufactures (Philips, GE, Siemens). Acquisition protocols from each site are reported in **Supplementary Table 1**.

Magnetic resonance imaging pre-processing

Structural MR images were segmented using the *recon-all* script included in Freesurfer v6.0.[2] After removal of non-brain tissue and bias of each structural brain image, we used the non-uniform intensity corrected image (*nu.mgz*) in the Freesurfer space to compute radiomics features. An additional step of intensity normalization was performed using the *Z-Score* method by centering each pre-processed T1w volume at the mean with standard deviation. To identify and characterize the site effect on radiomic features, we extracted the ROIs using the Desikan–Killiany atlas cortical parcelation from the individual subcortical segmentation image (*aparc* + *aseg.mgz*) (Desikan et al., 2006). Then, we thresholded each brain parcelation using FSL (Smith et al., 2004) tools to extract the binary masks for the next radiomics analysis.

Radiomics features extraction and harmonization

Data used for our analysis was collected from three ROIs, namely Caudate, Putamen and Thalamus, for both hemispheres, as a set of subcortical brain regions pertinent to PD (Shimohama et al., 2003; Halliday, 2009). For each ROI, we defined a set of 88 radiomic features, including 18 first-order features to describe voxel intensity distribution within image mask, and 70 second-level textural measures to highlight spatial distribution of voxels through four different matrices: 24 features from Gray Level Co-occurrence Matrices (GLCM), 16 from Gray Level Run Length Matrices (GLRLM), 14 measures from Gray Level Dependence Matrices (GLDM) and 16 features from Gray Level Size Zone Matrices (GLSZM) (detailed information about extracted features are reported in **Supplementary Table 2**; Zwanenburg et al., 2020). The extraction procedure was implemented using Pyradiomics, an open-source Python package (Van Griethuysen et al., 2017).

The multicenter harmonization was performed using ComBat algorithm (Johnson et al., 2007) for location (mean) and scale (variance) adjustments of data due to the site differences between subjects. Particularly, this approach assume that the batch effects can be modeled out by standardizing means and variances across batches. We applied the generalized additive model (GAM) of ComBat, also called NeuroHarmonize, that considered sex and non-linear age effects as covariates in the input data (Pomponio et al., 2020). More in details, this method combines the ComBat harmonization pipeline (Fortin et al., 2017, 2018), with the GAM (Hastie and Tibshirani, 1986). The former aims to remove unwanted sources of variability due to site differences, while preserving the variability due to other biological significant covariates; the latter introduces a penalized non-linear term to better take into account the age effects and capture also non-linearities in age-related differences in radiomic feature. In contrast to a general linear model approach that includes site as a fixed effect covariate, the GAM of ComBat considers only age and sex as covariates to control for during harmonization. This approach assumes that for a given site, the effects across features derive from a common distribution, and thus borrows information across features to shrink estimates toward a common mean. In addition to removing additive site effects, ComBat also corrects multiplicative site effects by removing heteroscedasticity of model errors across site. In our framework, NeuroHarmonize was implemented using Empirical Bayes framework, which is useful for harmonizing multiple features, such as brain regional measures. The estimation of the site hyperparameters (γ as an additive batch effect affecting the measurement, δ as a multiplicative batch effect) of the prior distribution for site-effect correction was conducted considering only healthy controls (HC). Of note, to ensure unbiased results, the harmonization parameters was calculated over control subjects in the training set of each cross-validation fold and then applied on the remaining subjects in train and test folds to correct the site-effect. The Python implementation of harmonization framework was found at https://github.com/rpomponio/neuroHarmonize (Pomponio et al., 2020).

Radiomics modeling

To characterize site effects on radiomics features, a "site vs. site" classification model was built in Leave-One-Out cross validation (LOOCV) considering only HC. To this end, classification performances were first evaluated using raw data. Next, we evaluated the impact of image normalization and ComBat harmonization on the classification performances. For each classification model, at each inner loop of LOOCV, we firstly reduced the burden of high dimensionality of radiomics set of features using least absolute shrinkage and selection operator (LASSO) (Tibshirani, 1996; Friedman et al., 2010). Therefore, the optimal penalty parameter of LASSO was defined *via* minimization of "Binomial Deviance" and features with non-zero regression coefficients were retained. Then, for classification purpose, we trained a radial basis Support Vector Machines (SVM) model (Cortes and Vapnik, 1995; Chang and Lin, 2011) for each binary site-classifier on previously selected radiomics features.

2 https://surfer.nmr.mgh.harvard.edu/

As second step of our framework, we implemented the same pipeline for PD detection. This procedure was implemented in a ten-times repeated 10-fold cross validation setting. At each of 100 bootstraps, nine folds was used to define a LASSO regression model to select optimal radiomics features. The selected features were saved in a vector to further analysis (Lombardi et al., 2020). These features were also used to train a radial basis SVM. At each iteration, we tested the predictive power of the model by using the excluded fold. The whole pipeline is illustrated in Figure 1.

Statistical analysis

Demographic and clinical information of the dataset were provided with descriptive statistics (mean ± SD). Group differences in age, sex, MoCA (Montreal Cognitive Assessment), UPDRS-III (Unified Parkinson's Disease Rating Scale) scales and H&Y (Hoehn and Yahr) stage were investigated through Chi-square test, one-way analysis of variance (ANOVA) and Kruskal–Wallis ANOVA followed by *post-hoc* comparisons. For all analyses, the corrected significance threshold was set at $p < 0.05$ after Bonferroni's correction for multiple comparisons. Statistical analysis was performed by using R software (Version 3.6.3: R Foundation for Statistical Computing, Vienna, Austria).

The Area Under the receiving operating characteristic Curves (AUCs) were used as evaluation metric for our "site vs. site" models. Classification performances for HC vs. PD models were evaluated by accuracy, sensitivity and specificity, mediated over the 100 bootstraps of classification. Finally, the diagnostic capabilities of the radiomics signatures were evaluated with Receiver Operating Characteristic (ROC) curve analysis.

To assess the stability of radiomics features selected by LASSO regression over HC vs. PD model, we used a frequency-based criterion. For each round of the bootstraps, we stored as relevant features only those corresponding to non-zero weights assigned by LASSO. Subsequently, we selected as most stable radiomics features those that occurred in at least 95° percentile of the frequency vector.

Results

Demographic and clinical data

We selected MR images from seven sites of the PPMI database according with the number of enrolled HC. Table 1 reports all demographic and clinical details for each clinical site included in our study. No statistical difference was found between HC from clinical sites in age, sex, H&Y score and MoCA scales.

For each site, we also selected a set of age- and sex-matched PD. Data is reported in Table 2. As expected, we found significant differences in H&Y score, UPDRS-III and MoCA scales (p-values < 0.001) between HC and PD patients.

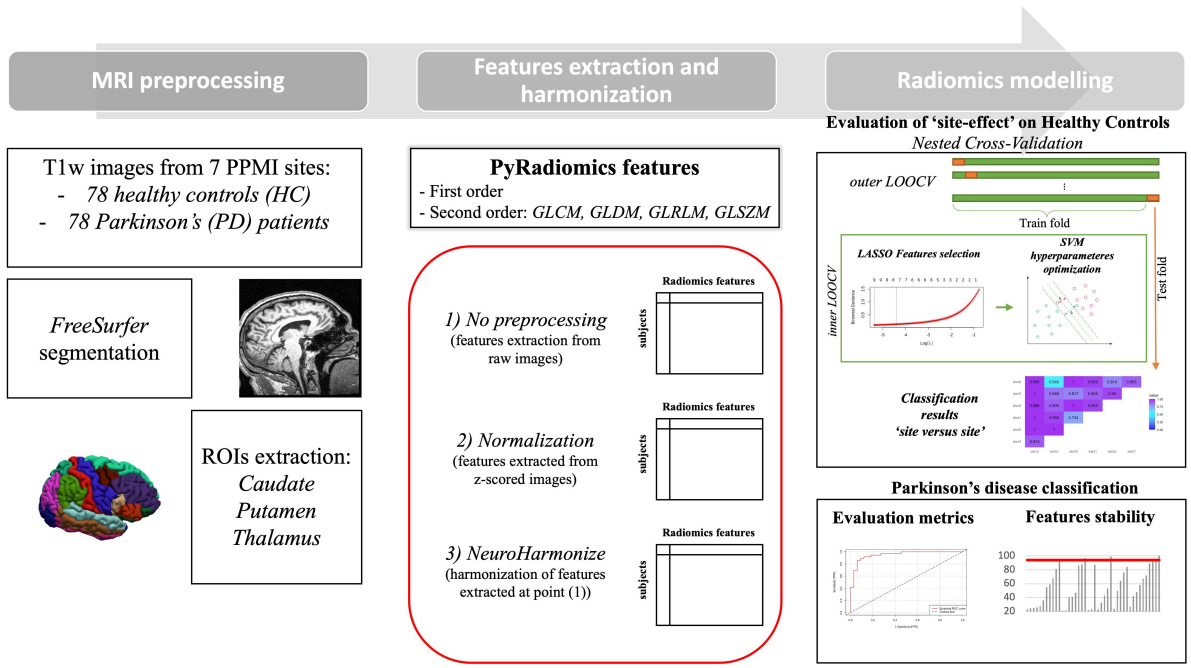

FIGURE 1
Processing pipeline.

TABLE 1 Demographic and clinical details of healthy controls for each site.

	Site 12	Site 19	Site 20	Site 21	Site 22	Site 27	Site 52	*P*-value
n	10	12	12	11	11	10	11	
Age [mean (SD)]	58.56 (13.68)	52.73 (13.81)	58.08 (10.37)	60.47 (8.75)	63.16 (11.86)	58.98 (7.63)	64.25 (6.55)	–
Female (%)	5 (50.0)	4 (33.3)	6 (50.0)	4 (36.4)	2 (18.2)	2 (20.0)	7 (63.6)	–
Hoehn and Yahr stage = 0 (%)	10 (100.0)	12 (100.0)	12 (100.0)	11 (100.0)	11 (100.0)	10 (100.0)	11 (100.0)	–
MoCA [mean (SD)]	28.30 (0.82)	28.92 (1.16)	28.25 (0.97)	27.82 (0.87)	28.55 (1.13)	28.60 (1.17)	27.82 (0.98)	–

Characterization and correction of the "Site Effects" on healthy controls

As first step, we studied the variability of radiomics features from healthy ROIs in different acquisition sites. Figure 2 presents, respectively, bivariate scatter plots of the first two principal components (*dim*) from a principal component analysis (PCA) (Figure 2A) and a histogram-based representation on one textural feature (i.e., GLCM-Correlation) (Figure 2B) for no pre-processed/normalized/harmonized approaches. As expected, a large proportion of the variation by site was corrected by harmonization of data. In Figure 3, we also report AUCs results from each binary comparison across HC from different sites. Classification performance of raw radiomics features (Figure 3, left panel) showed optimal discriminative power for all comparisons, except for *Site 19* vs. *Site 52*. Similar results were obtained using radiomics features calculated from normalized MRI (Figure 3, right panel). To evaluate pairwise differences between the models, we also performed a Wilcoxon signed rank test obtaining a *p*-value of 0.035.

After harmonization of radiomics features, LASSO regressions were unable to select any features for prediction of the outcomes. Indeed, LOOCV plots for each pairwise site comparison resulted in a penalty factor that shrinked all regression coefficients to zero (see Supplementary Figure 1).

TABLE 2 Demographic and clinical details of patients with Parkinson's disease and healthy controls.

	PD	HC	*P*-value
N	78	78	
Age [mean (SD)]	58.85 (9.68)	59.37 (10.93)	–
Female (%)	28 (36.4)	30 (39.0)	–
Hoehn and Yahr stage (%)			–
0	0 (0.0)	77 (100.0)	
1	41 (53.2)	0 (0.0)	
2	36 (46.8)	0 (0.0)	
UPDRS-III [mean (SD)]	20.01 (9.06)	1.10 (1.95)	<0.001
MoCA [mean (SD)]	27.16 (2.42)	28.32 (1.06)	<0.001

Parkinson's disease classification

As second step of our analysis, we evaluated goodness of classification of PD from HC in our three different radiomics approaches, namely without any pre-processing prior to radiomics features calculation, with normalization of image before radiomics computations and with harmonization from site-effect of radiomics features. We report results of each model in Table 3. Figure 4 also shows the corresponding ROCs for trained SVM. Respect to raw and normalized radiomics implementations, harmonization of features determined an increased classification power of the radiomics model.

As shown in Figure 5, we found five features over 95th percentile as most stable, with a predominance of radiomics measures in the right thalamus, involving energy features as measure of the magnitude of voxel values in an image, and "Gray Level Non-Uniformity Normalized" measure, quantifying the variability of gray-level intensity values in the image. Moreover, we found features in putamen, bilaterally, as most frequent predictors.

Discussion

This study demonstrated the sensitivity of radiomic features to site-effects in multicenter neuroimaging study. We firstly investigated the problem of data variability due to non-biological effects on healthy brain regions. Then, implementing a ComBat-based harmonization procedure of radiomics features, we modelized site-related noise source reducing differences across healthy subjects. Lastly, as validation task, we evaluated the effectiveness of our harmonization approach for classification of PD patients.

The small sample size made necessary some methodological choices. First of all, it was mandatory to use a feature selection method to avoid a course of dimensionality problem due to the imbalance between the number of radiomic features and the sample size (Koutroumbas and Theodoridis, 2008; Zollanvari et al., 2020). On the other hand, a feature selection method such as LASSO was preferred over other feature reduction

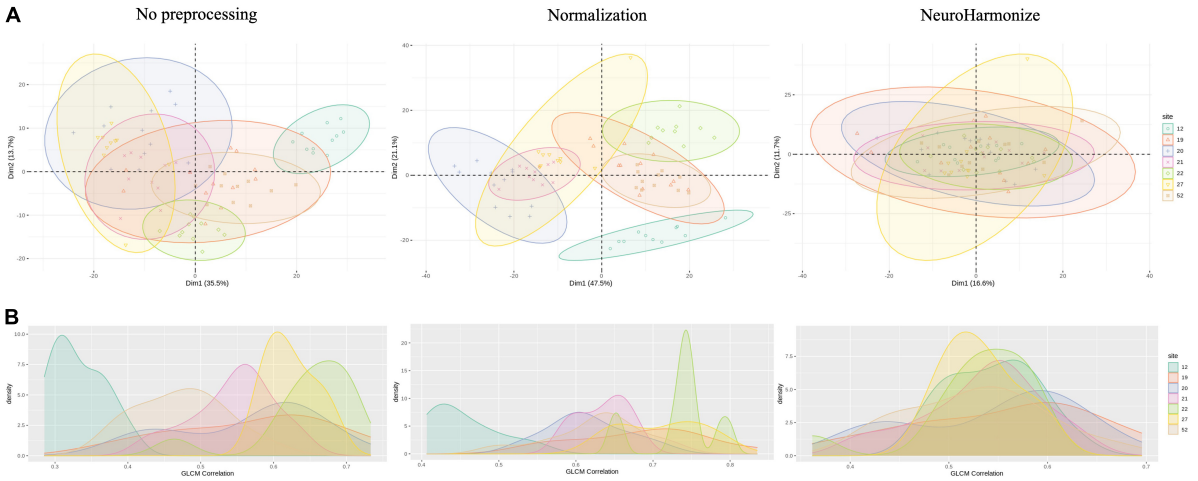

FIGURE 2
(A) Plots of the first 2 principal components (*dim*) from principal component analysis (PCA), colored by site; **(B)** histograms of example radiomic feature for raw, normalized, and harmonized processing.

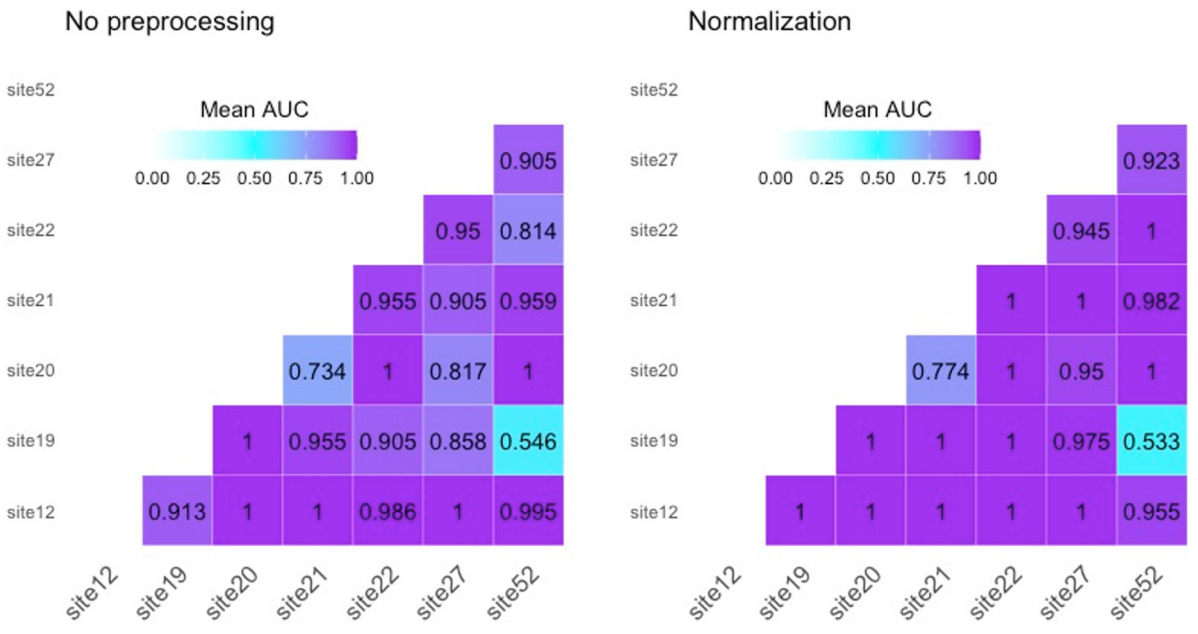

FIGURE 3
Area under the receiving operating characteristic curves (AUCs) for "site vs. site" classification on healthy controls. **Left panel** reports performances for not pre-processed radiomics features; **right panel** reports results using radiomics features from normalized MRI.

TABLE 3 **Performances of PD classification model from different pre-processed radiomics features.**

	Accuracy (mean + st .dev)	Sensitivity (mean + st. dev)	Specificity (mean + st.dev)	AUC (mean + st.dev)
No pre-processing	0.700 + 0.120	0.730 + 0.140	0.669 + 0.182	0.709 + 0.247
Normalization	0.713 + 0.078	0.811 + 0.115	0.662 + 0.134	0.715 + 0.212
NeuroHarmonize	0.710 + 0.122	0.754 + 0.173	0.685 + 0.161	0.766 + 0.110

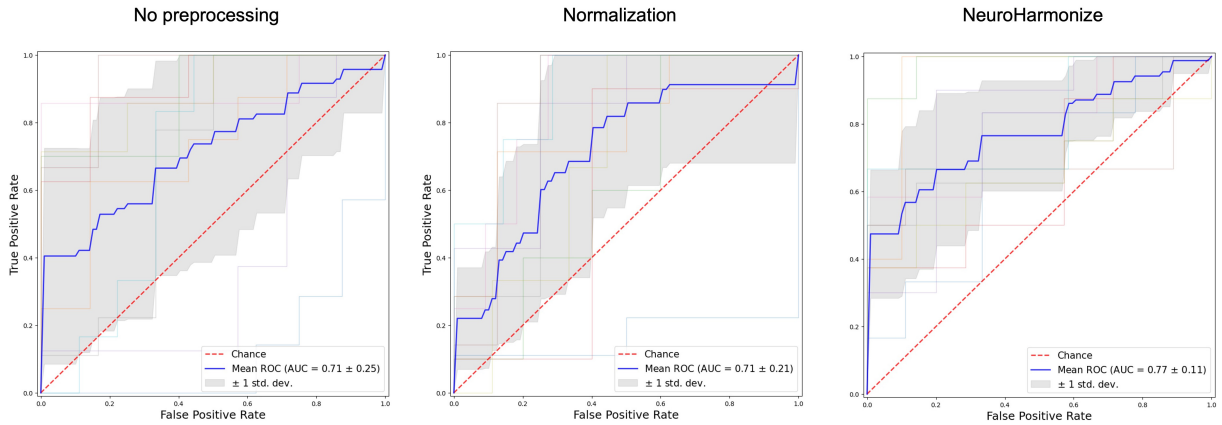

FIGURE 4
Receiver operating characteristic (ROC) curves for three different radiomics features processing.

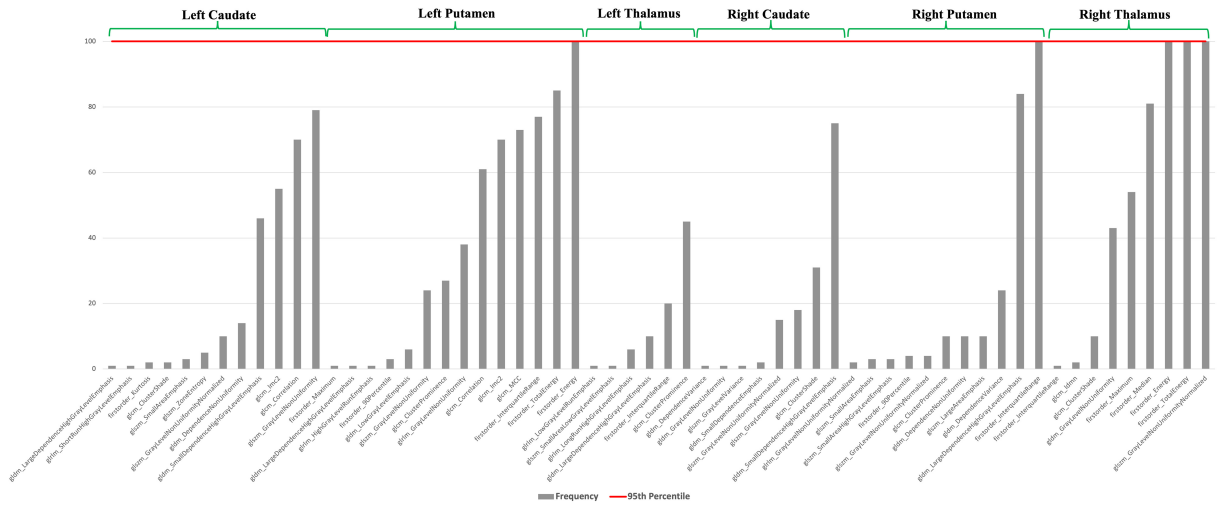

FIGURE 5
Frequency of radiomics features for PD vs. HC classification. Red line defines 95th percentile beyond which we choose the most stable measures.

methods (PCA, LDA, etc.) in order to achieve a more explainable model (Lombardi et al., 2021). Indeed, the cross-validated optimization of penalty factor for LASSO feature selection allowed to define the most important predictors over the radiomics features, also guaranteeing the interpretability of the model in the clinical/radiological field (Lombardi et al., 2022). Overall, the implementation of a leave-one-out cross-validation procedure for site-vs.-site classification (compared to k-fold cross-validation as a bias-variance tradeoff) was used to guarantee approximately unbiased results over our small sample size. Concerning site-effects on radiomic features, PCA and histogram-based representation of radiomics measures highlighted the need of correcting for site effects before performing further analyses. Indeed, this allowed to distinguish HC from each site with high accuracy. Similar results were observed for normalized images. By contrast, after application of NeuroHarmonize algorithm, no subset of features could be identified to differentiate HCs each other. On note, only comparison between subjects of *Site 19* and *Site 52* reported an AUC close to random choice without using the harmonization approach, probably due to common scanner and protocol parameters used in MRI acquisition.

These findings demonstrated an effective dependency of radiomics features from scanner and acquisition protocol that could not be eliminated with normalization of image intensity but only using a ComBat-based algorithm. Our results were in line with previous findings in radiomics, over both oncology and neuroimaging, that have demonstrated a better standardization

capabilities of ComBat-based models compared with different intensity normalization techniques, such as normalization (Z-Score), WhiteStripe and Ravel (Nyul et al., 2000; Shinohara et al., 2014; Reinhold et al., 2018; Dewey et al., 2019; Eshaghzadeh Torbati et al., 2021; Li et al., 2021).

As further result, harmonization pipeline applied to PD patients allowed to improve prediction performance with respect to raw data, suggesting that site noise factor might affect classification performance in multicenter study using radiomic features. Moreover, classification performance obtained in the current study using thalamus, caudate and putamen overcame results reported in previous radiomics studies using similar region-based approach for PD classification (Liu et al., 2020; Tupe-Waghmare et al., 2021). Specifically, Tupe-Waghmare et al. (2021) achieved 0.72 of AUC highlighting the T1 radiomics of substantia nigra as most predictive features. On the other hand, Liu et al. (2020) studied radiomics of putamen and caudate separately on T2w MRI with a 0.77 of AUC of caudate model. Our study further confirmed the impact of right thalamus, besides the involvement of more classical neostriatal regions (*caudate* + *putamen*) (Sikiö et al., 2015), in PD pathophysiology, highlighting at the same time its usefulness as diagnostic marker for PD.

Our work has some limitations. Firstly, the limited sample size for each site could produce unstable LASSO regression results, as well as a possible overfitting in SVM training, that we have tried to overcome with a bootstrapped 10-fold CV. Overall, cohorts of subjects from other international neuroimaging studies can be added to solve these issues guarantying greater generalizability of the results. Second, we applied only one type of normalization and harmonization techniques limiting other possible comparisons and further optimizations of performances. Future works can consider more complex intensity normalization methods, such as RAVEL or WhiteStripe, and recently developed alternative versions of ComBat with improved flexibility (M-ComBat) and robustness (B-ComBat) (Da-Ano et al., 2020).

The harmonization of MRI data represents a crucial problem in several medical imaging applications due to non-biological effects determined by different acquisition sites, scanners and multiparametric sequences. Our study aimed to assess the variability of radiomics features extracted on T1w MR images collected in a multicentric context. We found a not-negligible site-effect comparing radiomics features of HC pre- and post-harmonization pipeline. Moreover, our study demonstrated a significant influence of scan noise in distinguishing controls from PD patients. Overall, harmonization of radiomic features represents a necessary requirement for reliable and replicable analysis frameworks in multicenter study.

Data availability statement

Publicly available datasets were analyzed in this study. This data can be found here: https://www.ppmi-info.org/access-data-specimens/download-data.

Ethics statement

The PPMI study was approved by the local Institutional Review Boards of all participating sites (https://www.ppmi-info.org/about-ppmi/ppmi-clinical-sites/) and written informed consent for imaging data and clinical questionnaires was obtained from each participant at the time of enrollment

Author contributions

BT: conceptualization, formal analysis, methodology, software, visualization, and roles/writing – original draft. AL: conceptualization, methodology, validation, supervision, and writing – review and editing. SN: methodology, project administration, supervision, validation, and writing – review and editing. DU: data curation, resources, and writing – review and editing. AM, EP, and DD: data curation and writing – review and editing. RD: validation, visualization, and writing – review and editing. RB: project administration and writing – review and editing. ST: conceptualization, project administration, supervision, and writing – review and editing. GL: funding acquisition, conceptualization, project administration, supervision, and writing – review and editing. All authors contributed to the article and approved the submitted version.

Funding

This project was supported in part by the Michael J. Fox Foundation, including use of data available from the PPMI—a public-private partnership—funded by the Michael J. Fox Foundation for Parkinson's Research and funding partners (listed at https://www.ppmi-info.org/about-ppmi/who-we-are/study-sponsors) and supported with the founding of Regione Puglia and CNR for Tecnopolo per la Medicina di Precisione. D.G.R. n. 2117 of 21.11.2018 (B84I18000540002).

Conflict of interest

The authors declare that the research was conducted in the absence of any commercial or financial relationships that could be construed as a potential conflict of interest.

Publisher's note

All claims expressed in this article are solely those of the authors and do not necessarily represent those of their affiliated organizations, or those of the publisher, the editors and the reviewers. Any product that may be evaluated in this article, or claim that may be made by its manufacturer, is not guaranteed or endorsed by the publisher.

Supplementary material

The Supplementary Material for this article can be found online at: https://www.frontiersin.org/articles/10.3389/fnins.2022.1012287/full#supplementary-material

References

Cao, X., Wang, X., Xue, C., Zhang, S., Huang, Q., and Liu, W. (2020). A radiomics approach to predicting Parkinson's disease by incorporating whole-brain functional activity and gray matter structure. *Front. Neurosci.* 14:751. doi: 10.3389/fnins.2020.00751

Chang, C., and Lin, C. (2011). LIBSVM: A library for support vector machines. *ACM Trans. Intell. Syst. Technol.* 2:27.

Cortes, C., and Vapnik, V. (1995). Support-vector networks. *Mach. Learn.* 20, 273–297. doi: 10.1007/BF00994018

Crombé, A., Kind, M., Fadli, D., Le Loarer, F., Italiano, A., Buy, X., et al. (2020). Intensity harmonization techniques influence radiomics features and radiomics-based predictions in sarcoma patients. *Sci. Rep.* 10:15496. doi: 10.1038/s41598-020-72535-0

Da-Ano, R., Masson, I., Lucia, F., Doré, M., Robin, P., Alfieri, J., et al. (2020). Performance comparison of modified ComBat for harmonization of radiomic features for multicenter studies. *Sci. Rep.* 10:10248. doi: 10.1038/s41598-020-66110-w

Desikan, R. S., Ségonne, F., Fischl, B., Quinn, B. T., Dickerson, B. C., Blacker, D., et al. (2006). An automated labeling system for subdividing the human cerebral cortex on MRI scans into gyral based regions of interest. *Neuroimage* 31, 968–980. doi: 10.1016/j.neuroimage.2006.01.021

Dewey, B. E., Zhao, C., Reinhold, J. C., Carass, A., Fitzgerald, K. C., Sotirchos, E. S., et al. (2019). DeepHarmony: A deep learning approach to contrast harmonization across scanner changes. *Magn. Reson. Imaging* 64, 160–170. doi: 10.1016/j.mri.2019.05.041

Eshaghzadeh Torbati, M., Minhas, D. S., Ahmad, G., O'Connor, E. E., Muschelli, J., Laymon, C. M., et al. (2021). A multi-scanner neuroimaging data harmonization using RAVEL and ComBat. *Neuroimage* 245:118703. doi: 10.1016/j.neuroimage.2021.118703

Feng, F., Wang, P., Zhao, K., Zhou, B., Yao, H., Meng, Q., et al. (2018). Radiomic features of hippocampal subregions in Alzheimer's disease and amnestic mild cognitive impairment. *Front. Aging Neurosci.* 10:290. doi: 10.3389/fnagi.2018.00290

Feng, Q., and Ding, Z. (2020). MRI radiomics classification and prediction in Alzheimer's disease and mild cognitive impairment: A review. *Curr. Alzheimer Res.* 17, 297–309. doi: 10.2174/1567205017666200303105016

Fortin, J.-P., Cullen, N., Sheline, Y. I., Taylor, W. D., Aselcioglu, I., Cook, P. A., et al. (2018). Harmonization of cortical thickness measurements across scanners and sites. *Neuroimage* 167, 104–120. doi: 10.1016/j.neuroimage.2017.11.024

Fortin, J.-P., Parker, D., Tunç, B., Watanabe, T., Elliott, M. A., Ruparel, K., et al. (2017). Harmonization of multi-site diffusion tensor imaging data. *Neuroimage* 161, 149–170. doi: 10.1016/j.neuroimage.2017.08.047

Friedman, J., Hastie, T., and Tibshirani, R. (2010). Regularization paths for generalized linear models via coordinate descent. *J. Stat. Softw.* 33, 1–22.

Gillies, R. J., Kinahan, P. E., and Hricak, H. (2016). Radiomics: Images are more than pictures. *Radiology* 278, 563–577. doi: 10.1148/radiol.2015151169

Guiot, J., Vaidyanathan, A., Deprez, L., Zerka, F., Danthine, D., Frix, A.-N., et al. (2022). A review in radiomics: Making personalized medicine a reality via routine imaging. *Med. Res. Rev.* 42, 426–440. doi: 10.1002/med.21846

Halliday, G. M. (2009). Thalamic changes in parkinson's disease. *Parkinsonism Relat. Disord.* 15,(Suppl. 3), S152–S155. doi: 10.1016/S1353-8020(09)70804-1

Hastie, T., and Tibshirani, R. (1986). Generalized additive models. *Stat. Sci.* 1, 297–310. doi: 10.1214/ss/1177013604

Johnson, W. E., Li, C., and Rabinovic, A. (2007). Adjusting batch effects in microarray expression data using empirical Bayes methods. *Biostat. Oxf. Engl.* 8, 118–127. doi: 10.1093/biostatistics/kxj037

Koutroumbas, K., and Theodoridis, S. (2008). *Pattern recognition*. Cambridge, MA: Academic Press.

Kumar, V., Gu, Y., Basu, S., Berglund, A., Eschrich, S. A., Schabath, M. B., et al. (2012). Radiomics: The process and the challenges. *Magn. Reson. Imaging* 30, 1234–1248. doi: 10.1016/j.mri.2012.06.010

Li, Y., Ammari, S., Balleyguier, C., Lassau, N., and Chouzenoux, E. (2021). Impact of preprocessing and harmonization methods on the removal of scanner effects in brain MRI radiomic features. *Cancers* 13:3000. doi: 10.3390/cancers13123000

Liu, P., Wang, H., Zheng, S., Zhang, F., and Zhang, X. (2020). Parkinson's disease diagnosis using neostriatum radiomic features based on T2-weighted magnetic resonance imaging. *Front. Neurol.* 11:248. doi: 10.3389/fneur.2020.00248

Lombardi, A., Amoroso, N., Bellantuono, L., Bove, S., Comes, M. C., Fanizzi, A., et al. (2022). Accurate evaluation of feature contributions for sentinel lymph node status classification in breast cancer. *Appl. Sci.* 12:7227. doi: 10.3390/app12147227

Lombardi, A., Amoroso, N., Diacono, D., Monaco, A., Tangaro, S., and Bellotti, R. (2020). Extensive evaluation of morphological statistical harmonization for brain age prediction. *Brain Sci.* 10:364. doi: 10.3390/brainsci10060364

Lombardi, A., Diacono, D., Amoroso, N., Monaco, A., Tavares, J. M., Bellotti, R., et al. (2021). Explainable deep learning for personalized age prediction with brain morphology. *Front. Neurosci.* 15:674055. doi: 10.3389/fnins.2021.674055

Mali, S. A., Ibrahim, A., Woodruff, H. C., Andrearczyk, V., Müller, H., Primakov, S., et al. (2021). Making radiomics more reproducible across scanner and imaging protocol variations: A review of harmonization methods. *J. Pers. Med.* 11:842. doi: 10.3390/jpm11090842

Mayerhoefer, M. E., Materka, A., Langs, G., Häggström, I., Szczypiński, P., Gibbs, P., et al. (2020). Introduction to radiomics. *J. Nucl. Med.* 61, 488–495. doi: 10.2967/jnumed.118.222893

Nieuwenhuis, M., Schnack, H. G., van Haren, N. E., Lappin, J., Morgan, C., Reinders, A. A., et al. (2017). Multi-center MRI prediction models: Predicting sex and illness course in first episode psychosis patients. *Neuroimage* 145, 246–253. doi: 10.1016/j.neuroimage.2016.07.027

Nyul, L. G., Udupa, J. K., and Zhang, X. (2000). New variants of a method of MRI scale standardization. *IEEE Trans. Med. Imaging* 19, 143–150. doi: 10.1109/42.836373

Pomponio, R., Erus, G., Habes, M., Doshi, J., Srinivasan, D., Mamourian, E., et al. (2020). Harmonization of large MRI datasets for the analysis of brain imaging patterns throughout the lifespan. *Neuroimage* 208:116450. doi: 10.1016/j.neuroimage.2019.116450

Radua, J., Vieta, E., Shinohara, R., Kochunov, P., Quidé, Y., Green, M. J., et al. (2020). Increased power by harmonizing structural MRI site differences with the

ComBat batch adjustment method in ENIGMA. *Neuroimage* 218:116956. doi: 10.1016/j.neuroimage.2020.116956

Reinhold, J. C., Dewey, B. E., Carass, A., and Prince, J. L. (2018). *Evaluating the impact of intensity normalization on MR image synthesis*. Available online at: http://arxiv.org/abs/1812.04652 (accessed February 28, 2022).

Salmanpour, M. R., Shamsaei, M., Hajianfar, G., Soltanian-Zadeh, H., and Rahmim, A. (2022). Longitudinal clustering analysis and prediction of Parkinson's disease progression using radiomics and hybrid machine learning. *Quant. Imaging Med. Surg.* 12, 906–919. doi: 10.21037/qims-21-425

Salvatore, C., Castiglioni, I., and Cerasa, A. (2019). Radiomics approach in the neurodegenerative brain. *Aging Clin. Exp. Res.* 33, 1709–1711. doi: 10.1007/s40520-019-01299-z

Shimohama, S., Sawada, H., Kitamura, Y., and Taniguchi, T. (2003). Disease model: Parkinson's disease. *Trends Mol. Med.* 9, 360–365. doi: 10.1016/s1471-4914(03)00117-5

Shinohara, R. T., Sweeney, E. M., Goldsmith, J., Shiee, N., Mateen, F. J., Calabresi, P. A., et al. (2014). Statistical normalization techniques for magnetic resonance imaging. *Neuroimage Clin.* 6, 9–19. doi: 10.1016/j.nicl.2014.08.008

Sikiö, M., Holli-Helenius, K. K., Harrison, L. C. V., Ryymin, P., Ruottinen, H., Saunamäki, T., et al. (2015). MR image texture in Parkinson's disease: A longitudinal study. *Acta Radiol. Stockh. Swed.* 1987, 97–104. doi: 10.1177/0284185113519775

Smith, S. M., Jenkinson, M., Woolrich, M. W., Beckmann, C. F., Behrens, T. E. J., Johansen-Berg, H., et al. (2004). Advances in functional and structural MR image analysis and implementation as FSL. *Neuroimage* 23(Suppl. 1), S208–S219. doi: 10.1016/j.neuroimage.2004.07.051

Tibshirani, R. (1996). Regression shrinkage and selection via the lasso. *J. R. Stat. Soc. Ser. B Methodol.* 58, 267–288.

Tupe-Waghmare, P., Rajan, A., Prasad, S., Saini, J., Pal, P. K., and Ingalhalikar, M. (2021). Radiomics on routine T1-weighted MRI can delineate Parkinson's disease from multiple system atrophy and progressive supranuclear palsy. *Eur. Radiol.* 31, 8218–8227. doi: 10.1007/s00330-021-07979-7

Van Griethuysen, J. J. M., Fedorov, A., Parmar, C., Hosny, A., Aucoin, N., Narayan, V., et al. (2017). Computational radiomics system to decode the radiographic phenotype. *Cancer Res.* 77, e104–e107. doi: 10.1158/0008-5472.CAN-17-0339

Zollanvari, A., James, A. P., and Sameni, R. (2020). A theoretical analysis of the peaking phenomenon in classification. *J. Classif.* 37, 421–434. doi: 10.1007/s00357-019-09327-3

Zwanenburg, A., Leger, S., Vallières, M., and Löck, S. (2020). Image biomarker standardisation initiative. *Radiology* 295, 328–338. doi: 10.1148/radiol.2020191145

frontiers | Frontiers in Neuroscience

TYPE Original Research
PUBLISHED 20 October 2022
DOI 10.3389/fnins.2022.1042824

OPEN ACCESS

EDITED BY
Nico Sollmann,
University of California, San Francisco, United States

REVIEWED BY
Hui Fang,
First Affiliated Hospital of Zhengzhou University, China
Yan Wang,
Washington University in St. Louis, United States

*CORRESPONDENCE
Zhihua Xu
xuzhihua001@yeah.net

†These authors have contributed equally to this work

SPECIALTY SECTION
This article was submitted to Brain Imaging Methods, a section of the journal Frontiers in Neuroscience

RECEIVED 13 September 2022
ACCEPTED 04 October 2022
PUBLISHED 20 October 2022

CITATION
Lan H, Lei X, Xu Z, Chen S, Gong W and Cai Y (2022) New insights in addressing cerebral small vessel disease: Associated with extracellular fluid in white matter.
Front. Neurosci. 16:1042824.
doi: 10.3389/fnins.2022.1042824

New insights in addressing cerebral small vessel disease: Associated with extracellular fluid in white matter

Haiyuan Lan[1†], Xinjun Lei[1†], Zhihua Xu[2*], Songkuan Chen[2], Wanfeng Gong[2] and Yunqi Cai[1]

[1]Department of Radiology, Lishui Hospital of Traditional Chinese Medicine affiliated Zhejiang Chinese Medical University, Lishui, China, [2]Department of Radiology, Tongde Hospital of Zhejiang Province, Hangzhou, China

Objective: To explore the role of extracellular fluid, assessed by diffusion tensor imaging (DTI) metrics of free water (FW), in the white matter of patients with cerebral small vessel disease (CSVD).

Materials and methods: The baseline clinical and imaging data of 129 patients with CSVD were collected and reviewed. CSVD MR markers, including periventricular white matter hyperintensity (PWMH), deep white matter hyperintensity (DWMH), cerebral microbleed (CMB), enlarged perivascular space (PVS), and lacunar infarction (LI), were identified, and CSVD burden was calculated. According to total CSVD MR marker score, cases were classified as mild, moderate, or severe. The mean FW and fractional anisotropy (FA) values were calculated using DTI images.

Results: The mean white matter FW was associated with the CSVD MR markers, including PWMH, DWMH, LI and PVS ($P < 0.05$). Moreover, age, hypertension, diabetes mellitus, and FW value were associated with total CSVD MR marker score ($P < 0.05$). Ordinal logistic regression analysis revealed that FW and age were independently associated with CSVD burden ($P < 0.05$). Finally, FW in white matter was associated with FA ($r = -0.334$, $P < 0.001$).

Conclusion: Extracellular fluid changes, assessed by DTI metrics of FW in white matter, were associated with CSVD markers and burden. An increased extracellular fluid volume in the white matter was associated with lower FA.

KEYWORDS

cerebral small vessel disease, diffusion tensor imaging, extracellular fluid, white matter, free water, age

Introduction

Cerebral small vessel disease (CSVD) is an aging-related disease that affects the small vessels of the brain. It is a leading cause of stroke, cognitive decline, and dementia (Chen et al., 2019). However, the underlying pathophysiology of CSVD remains unclear.

In recent years, alteration of extracellular fluid in white matter, assessed by diffusion tensor imaging (DTI) metrics of free water (FW), has been indicated as a novel imaging marker for Alzheimer's disease (AD) (Ji et al., 2017; Dumont et al., 2019). Like AD, CSVD is associated with certain changes, such as lower cerebral flood (Lu et al., 2022), increased permeability of blood brain barrier (Thrippleton et al., 2019), and neuroinflammation (Evans et al., 2021). All these factors may lead to increased extracellular fluid volume. Moreover, some studies have indicated that deep medullary vein disruption and venous hypertension are associated with the presence and burden of CSVD (Xu et al., 2020; Ao et al., 2021). Venous hypertension and draining obstruction may lead to interstitial edema and increased extracellular fluid volume. Therefore, we hypothesized that extracellular fluid content is associated with the presence and severity of CSVD.

Furthermore, DTI can identify microstructural changes of white matter *in vivo*. CSVD-associated cognitive decline may be due to demyelination of white matter tracts, destroying the nerve network and ultimately leading to impaired transmission of information within the brain. Microenvironmental changes often cause microstructural changes. In this study, we aimed to explore the relationship between microenvironmental changes in extracellular fluid in white matter and CSVD markers, burden, and microstructural changes in patients with CSVD using multimodal magnetic resonance imaging (MRI).

Materials and methods

Patients

The protocol for this study was approved by the Institutional Review Board of our hospital. Each patient or patient proxy provided written informed consent prior to participation in this study. The clinical and imaging data of patients with CSVD gathered from January 2022 to July 2022 were reviewed. The inclusion criteria were as follows: (a) age $>$ 40 years; (b) MR imaging meeting the Standards for Reporting Vascular changes on Neuroimaging (STRIVE) for CSVD (Wardlaw et al., 2013); and (c) presence of at least one vascular risk factor, such as current smoking, diabetes mellitus, hypertension, and hyperlipidemia. The exclusion criteria were as follows: (a) diagnosis of other demyelinating diseases, such as metabolic, hereditary, and inflammatory diseases; (b) severe stenosis or occlusion of an internal carotid artery or large intracranial artery; (c) presence of other brain abnormalities, such as cerebral infarction except lacunar infarction, trauma, tumor, and vascular malformation; and (d) heart, lung, and kidney insufficiency.

Clinical information

The baseline information of the enrolled patients, including sex, age, and vascular risk factors of hypertension, current smoking, diabetes mellitus, and hyperlipidemia, were collected.

Magnetic resonance imaging protocol

All patients underwent multimodal MRI, including 3D T1WI, T2WI, T2 Flair, and DTI sequences, on a 1.5 Tesla scanner (MAGNETOM Aera, Syngo Platform VD13A, Siemens Healthcare, Erlangen, Germany) equipped with an eight-channel phased-array head coil. The parameters of the DTI were as follows: repetition time = 3,600 ms, echo time = 95 ms, slice thickness = 3 mm, field of view = 23 cm $\times$ 23 cm, matrix = 128 $\times$ 128, diffusion directions = 30, b value = 0, 1,000, and 2,000 s/mm^2.

Imaging analysis

Cerebral small vessel disease MR markers

All images were reviewed separately by two neuroradiologists. Disagreements were resolved by consensus. Using the STRIVE guidelines, we identified white matter hyperintensities (WMH), cerebral microbleed (CMB), perivascular space (PVS), and lacunar infarction (LI). WMH was defined as abnormal hyperintensity of periventricular white matter or deep white matter on T2 FLAIR images. The extent of WMH was assessed and scored using the Fazekas scoring system, and high-grade (H) WMH was defined by a Fazekas score of $\geq$ 2 in the periventricular white matter (PWMH) and/or $\geq$ 2 in the deep white matter (DWMH). CMBs were defined as homogeneous hypointensities with an average diameter of 3–5 mm on SWI after excluding calcification, vascular cross section, and abnormal iron deposits. PVS enlargement was defined by the presence of small dot-like or linear fluid signals and small blood vessels on MR images. To evaluate the extent of PVS, a scoring system was used according to the number of PVSs at the level of the maximum number of PVSs in the unilateral vasal ganglia: 0, none-PVS; 1, $<$ 10; 2, $<$ 20; 3, 20–40; 4, $>$ 40. High-grade (H) PVS indicated that the number of enlarged PVSs was $>$ 10. LI was defined as round or ovoid lesions measuring 3–15 mm in diameter, which manifested as hyperintense lesions on T2WI and as hypointense lesions on T1WI.

Cerebral small vessel disease burden

Cerebral small vessel disease (CSVD) burden was calculated based on the total CSVD MR score, an ordinal scale ranging from 0 to 4, depending on the absence or presence (0 or 1) of each of the four CSVD features (HWMH, CMB, HPVS, and LI). Based on the total CSVD MR score, patients were divided into three groups: mild (total CSVD MR score = 0 or 1), moderate (total CSVD MR score = 2), and severe (total CSVD MR score = 3 or 4). For example, a patient with CMB, HWMH, HPVS, and LI and a total CSVD MR score of 4 was classified into the severe group.

Extracellular fluid of white matter and fractional anisotropy

First, the DTI images underwent preprocessing steps, including denoising, Gibbs artifact removal, EPI distortion correction, and eddy current correction using MRtrix3.[1] Thereafter, extracellular fluid was analyzed with the free water elimination two-compartmental model (Hoy et al., 2014), a way to correct partial volume effects of the cerebral spinal fluid and measure the volume of extracellular fluid [free water (FW)] and tissue compartment [fractional anisotropy (FA)] removed the signal of FW, for preprocessed DTI images using the DIPY software.[2] FW and FA maps were generated. The 3D T1WI images were co-registered as b = 0 (b0) images. Finally, mean white matter FW and FA were calculated with each patient's white matter mask, including CSVD lesions, segmented by FSL fast[3] using co-registered 3D T1WI images. The values of FW and FA ranged from 0 to 1. The value of FW reflected the volume of the extracellular fluid. An FW value closer to 1 indicated a markedly increased extracellular fluid volume.

Statistical analysis

Categorical variables are reported as frequencies and percentages; normally distributed continuous data are reported as means and standard deviations (SD); and non-parametric data are reported as medians and interquartile ranges (IQRs). Associations between FW and CSVD markers were analyzed using Spearman correlation coefficient, and then multivariate linear regression analysis to determine who contribute to FW. associations between FW and total CSVD MR score (mild, moderate, and severe group), age, sex, and vascular risk factors were analyzed using Kruskal-Wallis test or one-way ANOVA test. The relationship between FW and FA was analyzed using the Pearson correlation coefficient. Ordinal regression analysis was performed to identify independent factors associated with total CSVD MR score (mild, moderate, and severe group). A P-value < 0.05 was considered statistically significant. All data analyses were performed using the Statistical Package for Social Sciences for Windows, Version 20 (IBM Corp., Armonk, NY, USA). **Figures 1–3** were made using "ggplot2" in R 4.2. To avoid overlapping data points and affect the observation, we also used the "jitter" function when making **Figures 1**, **2**.

Results

The study enrolled 129 patients, including 60 men. Their mean age was 60 ± 11 years. The number of patients with HWMH, CMB, HPVS, and LI, were 47 (36.43%), 29 (22.48%), 19 (14.72%), and 49 (37.98%) patients, respectively. The median (IQR) total CSVD MR score was 1 (0, 2).

Extracellular fluid in white matter and cerebral small vessel disease MR markers

White matter FW values were associated with the CSVD MR markers, including PWMH, DWMH, CMB, PVS, and LI ($P < 0.05$, see **Figures 1A–E**). White matter FW values were higher in patients with HWMH than in patients without HWMH. Similarly, patients with CMB, HPVS, and LI had higher FW values. After multivariate linear regression analysis, PVS, DWMH, PWMH, and number of LI were independently associated with FW ($P < 0.05$, see **Table 1**); number of CMB was not independently correlated with FW ($P > 0.05$).

Extracellular fluid in white matter and cerebral small vessel disease burden

The clinical and imaging characteristics and comparisons among study participants according to CSVD burden are shown in **Table 2**. The number of patients with mild, moderate and severe CSVD were 86 (66.67%), 19 (14.73%), and 24 (18.60%) patients, respectively. The mean FW of mild group (0.24 ± 0.01) significantly differed from moderate (0.25 ± 0.01) and sever (0.26 ± 0.01) group ($P < 0.05$, see **Figure 2**).

Age, hypertension, diabetes mellitus, and FW had associations with CSVD burden ($P < 0.05$). After ordinal logistic regression analysis, FW and age were independently associated with CSVD burden ($P < 0.05$) (**Table 3**).

1 https://www.mrtrix.org/
2 https://dipy.org/
3 https://fsl.fmrib.ox.ac.uk/fsl/fslwiki/FAST

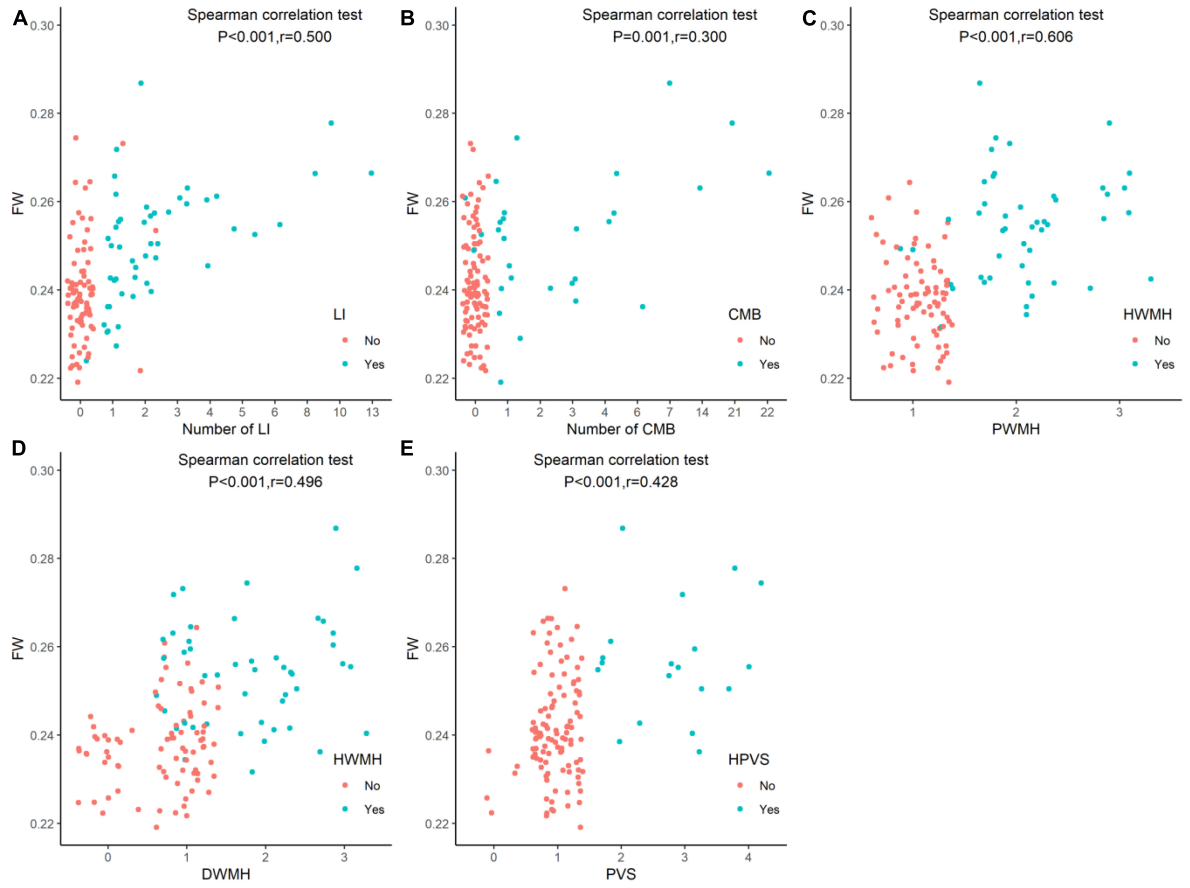

FIGURE 1
Comparison of extracellular fluid volume of white matter among study participants according to cerebral small vessel disease markers. White matter FW values were associated with the CSVD MR markers of LI **(A)**, CMB **(B)**, PWMH **(C)**, DWMH **(D)**, and PVS **(E)** ($P < 0.05$). FW, free water; LI, lacunar infarction; CMB, cerebral microbleed; DWMH, deep white matter hyperintensity; PWMH, periventricular white matter hyperintensity; HWMH, high-grade white matter hyperintensity; HPVS, high-grade perivascular space.

Extracellular fluid of white matter and fractional anisotropy

Using Pearson correlation coefficient, the extracellular fluid in white matter was associated with FA ($r = -0.334$, $P < 0.001$). A higher volume of extracellular fluid of white matter often had a lower FA (see **Figure 3**).

Discussion

CSVD is an aging-related disease. Consistent with findings from other studies, our findings showed that CSVD burden was associated with age. Additionally, changes in extracellular fluid volume, assessed using DTI metrics of white matter FW, was associated with CSVD MR markers (PWMH, DWMH, PVS and LI) and CSVD burden. Moreover, an increased extracellular fluid volume in the white matter was associated with lower FA. Therefore, extracellular fluid volume in the white matter was considered to play an important role in CSVD severity, and increased extracellular fluid was associated with loss of white matter integrity.

Based on the definitions of the CSVD MR markers, the mean white matter FW value can be understood to be higher in patients with higher Fazekas score of PWMH or DWMH. Similarly, patients with higher score of PVS and a greater number of LI had higher mean white matter FW values. Enlarged PVS and LI were filled with fluid, which typically manifested as hyperintense lesions on T2WI and hypointense lesions on T1WI. Although the petrophysical mechanism of WMH remains unclear, a hyperintensity on T2 Flair image, WMH, often indicated an increased water volume, according to the principle of MRI. This finding corroborates similar findings from previous studies (Rau et al., 2021). However, all CSVD MR markers were only lesions in white matter. Several studies (Zhong and Lou, 2016; Khan et al., 2021; Mayer et al., 2022) have shown that microenvironmental and microstructural changes were present in white matter without lesions. Therefore, the

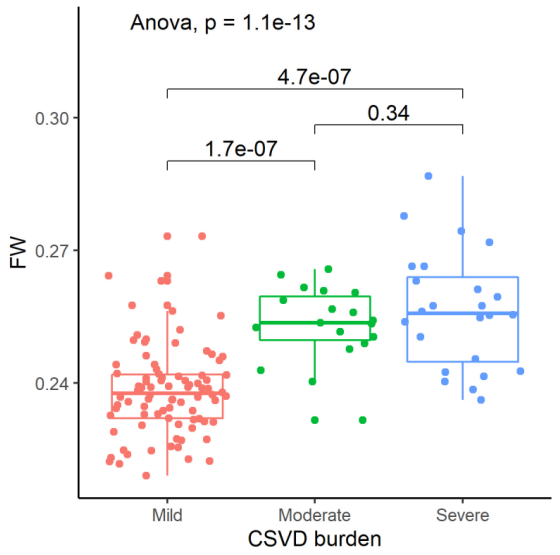

FIGURE 2
Comparison of extracellular fluid volume of white matter among participants according to cerebral small vessel disease burden. FW, free water.

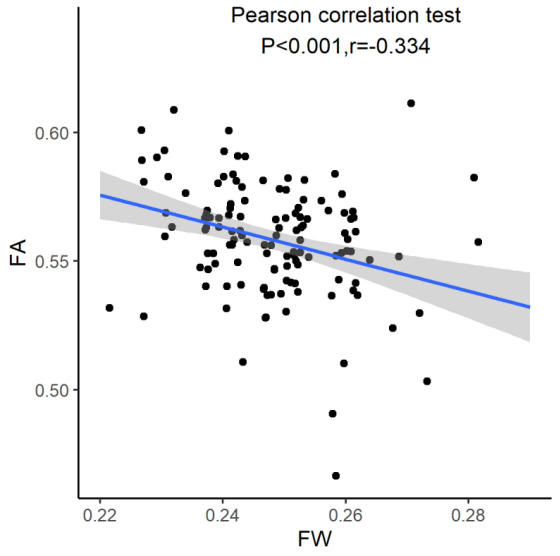

FIGURE 3
Relationship between extracellular fluid of white matter and fraction anisotropy. FW, free water; FA, fractional anisotropy.

global white matter was selected as the region of interest in this study because global white matter extracellular fluid and integrity could reflect pathological changes in CSVD.

CSVD is a clinical syndrome that affects small vessels. It has different clinical presentations and radiomic features (Dey et al., 2019; Wang et al., 2021), which may be due to differences in its pathogenesis and severity. In patients with CSVD, cerebral blood flow is often low (Zhang et al., 2022) and brain tissues

TABLE 1 Multivariate linear regression analysis for free water in white matter in patients with cerebral small vessel disease.

	β (95% CI)	*P*-value
DWMH	0.158 (0.002, 0.332)	0.046
PWMH	0.341 (0.157, 0.525)	<0.001
Number of LI	0.297 (0.109, 0.486)	0.002
Number of CMB	−0.102 (−0.294, 0.089)	0.292
PVS	0.154 (0.001, 0.309)	0.045

DWMH, deep white matter hyperintensity; PWMH, periventricular white matter hyperintensity; LI, lacunar infarction; CMB, cerebral microbleed; PVS, perivascular space.

are often ischemic, resulting in increased extracellular fluid volume. With respect to the venous system, multiple studies (Chen et al., 2020; Xu et al., 2020; Ao et al., 2021) have shown that deep medullary vein disruption, lumen stenosis, and venous hypertension may lead to interstitial edema and promote CSVD. Moreover, Zhang et al. (2021) indicated that the glymphatic system may play an important role in CSVD. When the glymphatic system was weakened or dysfunctional, cerebrospinal fluid-interstitial fluid exchange and drainage were obstructed and interstitial fluid volume increased. On the other hand, due to blood-brain barrier leakage and glymphatic system dysfunction, brain metabolite (including toxins and αβ proteins) accumulation cannot be effectively cleared in a timely manner, leading to neuroinflammatory reactions and further increase in interstitial fluid volume of the brain tissues (Thrippleton et al., 2019; Zhang et al., 2021). The different pathological mechanisms underlying the development of CSVD result in increased extracellular fluid volume. Therefore, change in cerebral extracellular fluid volume is probably a comprehensive response to CSVD.

Moreover, the increased extracellular fluid volume in the white matter was associated with lower FA. Previously, several studies (Liu et al., 2019, 2020; Kerkhofs et al., 2021) found that microstructural changes were associated with cognitive impairment in patients with CSVD. Therefore, we sought to understand the association between the risk factors and microstructural changes. According to our study, the increased extracellular fluid volume could cause an accumulation of harmful substances, such as plasma proteins, which are toxic to surrounding white matter microstructures, including myelin and axons. Increased extracellular fluid volume possibly occurs first, followed by demyelination and axonal damage within the white matter. Therefore, microstructural changes may be mediated by accumulation of extracellular fluid in patients with CSVD. To corroborate these findings, further studies are needed.

This study had some limitations. First, the sample size was relatively small and did not include patients with CSVD and associated cognitive decline or dementia. Second, participants were not followed up to study the relationship between CSVD

TABLE 2 Clinical and imaging features and comparison among participants according to burden of cerebral small vessel disease.

	Burden of cerebral small vessel disease			*P*-value
	Mild (n = 86)	Moderate (n = 19)	Severe (n = 24)	
Male	36 (41.9%)	10 (52.6%)	14 (58.3%)	0.304
Age, years	55.69 ± 10.34	67.95 ± 9.93	68.79 ± 8.65	<0.001
Hypertension, yes	37 (43.0)	16 (84.2)	17 (70.8)	0.001
Diabetes mellitus, yes	12 (14.0)	7 (36.8)	3 (12.5)	0.045
Current smoking, yes	20 (23.3)	3 (15.8)	6 (25.0)	0.739
Hyperlipidemia, yes	22 (25.6)	4 (21.1)	6 (25.0)	0.918
FW	0.24 ± 0.01	0.25 ± 0.01	0.26 ± 0.01	<0.001
FA	0.45 ± 0.02	0.44 ± 0.02	0.43 ± 0.02	0.001

FW, free water; FA, fractional anisotropy.

TABLE 3 Multivariate analysis for burden of cerebral small vessel disease.

	β	*P*-value
Age, years	0.861	0.002
Hypertension, yes	−0.526	0.284
Diabetes mellitus, yes	0.151	0.782
FW	1.152	<0.001

FW, free water.

progression and changes in extracellular fluid volume and FA in the white matter. Although FW in global white matter may provide more potential pathological changes to reflect CSVD burden, FW and FA in normal appearing white matter may be more informative to explore CSVD progression. Further multi-center studies with large sample sizes are needed to address these limitations.

Conclusion

Changes in cerebral extracellular fluid volume, assessed using DTI metrics of white matter FW, may be a comprehensive response to CSVD. Additionally, an increased extracellular fluid volume was associated with lower FA.

Data availability statement

The original contributions presented in this study are included in the article/supplementary material, further inquiries can be directed to the corresponding author.

Ethics statement

The studies involving human participants were reviewed and approved by Tongde Hospital of Zhejiang Province. The patients/participants provided their written informed consent to participate in this study.

Author contributions

HL, XL, and ZX conceived the project idea and wrote the manuscript. ZX provided the critical suggestions for the design of the experiments. HL, XL, WG, SC, and YC collected the imaging and clinical data. HL, XL, ZX, and SC provided the imaging analysis. XL and ZX supervised the project. All authors contributed to the article and approved the submitted version.

Funding

This study was supported by grant 2022KY707 from the Medical and Health Science and Technology Program of Zhejiang Provincial Health Commission of China.

Conflict of interest

The authors declare that the research was conducted in the absence of any commercial or financial relationships that could be construed as a potential conflict of interest.

Publisher's note

References

Ao, D.-H., Zhang, D.-D., Zhai, F.-F., Zhang, J.-T., Han, F., Li, M.-L., et al. (2021). Brain deep medullary veins on 3-T MRI in a population-based cohort. *J. Cereb. Blood Flow Metab.* 41, 561–568. doi: 10.1177/0271678X20918467

Chen, X., Wang, J., Shan, Y., Cai, W., Liu, S., Hu, M., et al. (2019). Cerebral small vessel disease: Neuroimaging markers and clinical implication. *J. Neurol.* 266, 2347–2362. doi: 10.1007/s00415-018-9077-3

Chen, X., Wei, L., Wang, J., Shan, Y., Cai, W., Men, X., et al. (2020). Decreased visible deep medullary veins is a novel imaging marker for cerebral small vessel disease. *Neurol. Sci.* 41, 1497–1506. doi: 10.1007/s10072-019-04203-9

Dey, A. K., Stamenova, V., Bacopulos, A., Jeyakumar, N., Turner, G. R., Black, S. E., et al. (2019). Cognitive heterogeneity among community-dwelling older adults with cerebral small vessel disease. *Neurobiol. Aging* 77, 183–193. doi: 10.1016/j.neurobiolaging.2018.12.011

Dumont, M., Roy, M., Jodoin, P.-M., Morency, F. C., Houde, J.-C., Xie, Z., et al. (2019). Free water in white matter differentiates MCI and AD from control subjects. *Front. Aging Neurosci.* 11:270. doi: 10.3389/fnagi.2019.00270

Evans, L. E., Taylor, J. L., Smith, C. J., Pritchard, H. A. T., Greenstein, A. S., and Allan, S. M. (2021). Cardiovascular comorbidities, inflammation, and cerebral small vessel disease. *Cardiovasc. Res.* 117, 2575–2588. doi: 10.1093/cvr/cvab284

Hoy, A. R., Koay, C. G., Kecskemeti, S. R., and Alexander, A. L. (2014). Optimization of a free water elimination two-compartment model for diffusion tensor imaging. *Neuroimage* 103, 323–333. doi: 10.1016/j.neuroimage.2014.09.053

Ji, F., Pasternak, O., Liu, S., Loke, Y. M., Choo, B. L., Hilal, S., et al. (2017). Distinct white matter microstructural abnormalities and extracellular water increases relate to cognitive impairment in Alzheimer's disease with and without cerebrovascular disease. *Alzheimers Res. Ther.* 9:63. doi: 10.1186/s13195-017-0292-4

Kerkhofs, D., Wong, S. M., Zhang, E., Staals, J., Jansen, J. F. A., van Oostenbrugge, R. J., et al. (2021). Baseline blood-brain barrier leakage and longitudinal microstructural tissue damage in the periphery of white matter hyperintensities. *Neurology* 96, e2192–e2200. doi: 10.1212/WNL.0000000000011783

Khan, W., Khlif, M. S., Mito, R., Dhollander, T., and Brodtmann, A. (2021). Investigating the microstructural properties of normal-appearing white matter (NAWM) preceding conversion to white matter hyperintensities (WMHs) in stroke survivors. *Neuroimage* 232:117839. doi: 10.1016/j.neuroimage.2021.117839

Liu, C., Zou, L., Tang, X., Zhu, W., Zhang, G., Qin, Y., et al. (2020). Changes of white matter integrity and structural network connectivity in nondemented cerebral small-vessel disease. *J. Magn. Reson. Imaging* 51, 1162–1169. doi: 10.1002/jmri.26906

Liu, D., Li, K., Ma, X., Li, Y., Bu, Q., Pan, Z., et al. (2019). Correlations between the microstructural changes of the medial temporal cortex and mild cognitive impairment in patients with cerebral small vascular disease (cSVD): A diffusion kurtosis imaging study. *Front. Neurol.* 10:1378. doi: 10.3389/fneur.2019.01378

Lu, W., Yu, C., Wang, L., Wang, F., and Qiu, J. (2022). Perfusion heterogeneity of cerebral small vessel disease revealed via arterial spin labeling MRI and machine learning. *Neuroimage Clin.* 36:103165. doi: 10.1016/j.nicl.2022.103165

Mayer, C., Nägele, F. L., Petersen, M., Frey, B. M., Hanning, U., Pasternak, O., et al. (2022). Free-water diffusion MRI detects structural alterations surrounding white matter hyperintensities in the early stage of cerebral small vessel disease. *J. Cereb. Blood Flow Metab.* 42, 1707–1718. doi: 10.1177/0271678X221093579

Rau, A., Reisert, M., Kellner, E., Hosp, J. A., Urbach, H., and Demerath, T. (2021). Increased interstitial fluid in periventricular and deep white matter hyperintensities in patients with suspected idiopathic normal pressure hydrocephalus. *Sci. Rep.* 11:19552. doi: 10.1038/s41598-021-98054-0

Thrippleton, M. J., Backes, W. H., Sourbron, S., Ingrisch, M., van Osch, M. J. P., Dichgans, M., et al. (2019). Quantifying blood-brain barrier leakage in small vessel disease: Review and consensus recommendations. *Alzheimers Dement.* 15, 840–858. doi: 10.1016/j.jalz.2019.01.013

Wang, T., Jin, A., Fu, Y., Zhang, Z., Li, S., Wang, D., et al. (2021). Heterogeneity of white matter hyperintensities in cognitively impaired patients with cerebral small vessel disease. *Front. Immunol.* 12:803504. doi: 10.3389/fimmu.2021.803504

Wardlaw, J. M., Smith, E. E., Biessels, G. J., Cordonnier, C., Fazekas, F., Frayne, R., et al. (2013). Neuroimaging standards for research into small vessel disease and its contribution to ageing and neurodegeneration. *Lancet Neurol.* 12, 822–838. doi: 10.1016/S1474-4422(13)70124-8

Xu, Z., Li, F., Wang, B., Xing, D., Pei, Y., Yang, B., et al. (2020). New insights in addressing cerebral small vessel disease: Association with the deep medullary veins. *Front. Aging Neurosci.* 12:597799. doi: 10.3389/fnagi.2020.597799

Zhang, R., Huang, P., Wang, S., Jiaerken, Y., Hong, H., Zhang, Y., et al. (2022). Decreased cerebral blood flow and delayed arterial transit are independently associated with white matter hyperintensity. *Front. Aging Neurosci.* 14:762745. doi: 10.3389/fnagi.2022.762745

Zhang, W., Zhou, Y., Wang, J., Gong, X., Chen, Z., Zhang, X., et al. (2021). Glymphatic clearance function in patients with cerebral small vessel disease. *Neuroimage* 238:118257. doi: 10.1016/j.neuroimage.2021.118257

Zhong, G., and Lou, M. (2016). Multimodal imaging findings in normal-appearing white matter of leucoaraiosis: A review. *Stroke Vasc. Neurol.* 1, 59–63. doi: 10.1136/svn-2016-000021

frontiers | Frontiers in Neuroscience

TYPE Original Research
PUBLISHED 24 November 2022
DOI 10.3389/fnins.2022.1027948

OPEN ACCESS

EDITED BY
Nico Sollmann,
University of California, San Francisco, United States

REVIEWED BY
Fajun Wang,
Saint Louis University, United States
Yang Tiansong,
Heilongjiang University of Chinese Medicine, China

*CORRESPONDENCE
Liang Wang
drwangliang@126.com
Canhua Xu
canhuaxu@fmmu.edu.cn

†These authors have contributed equally to this work

SPECIALTY SECTION
This article was submitted to Brain Imaging Methods, a section of the journal Frontiers in Neuroscience

RECEIVED 25 August 2022
ACCEPTED 04 November 2022
PUBLISHED 24 November 2022

CITATION
Zhang Y, Ye J, Jiao Y, Zhang W, Zhang T, Tian X, Shi X, Fu F, Wang L and Xu C (2022) A pilot study of contrast-enhanced electrical impedance tomography for real-time imaging of cerebral perfusion. *Front. Neurosci.* 16:1027948. doi: 10.3389/fnins.2022.1027948

A pilot study of contrast-enhanced electrical impedance tomography for real-time imaging of cerebral perfusion

Yuyan Zhang[1,2,3†], Jian'an Ye[2,3†], Yang Jiao[4†], Weirui Zhang[2,3], Tao Zhang[2,3], Xiang Tian[2,3], Xuetao Shi[2,3], Feng Fu[2,3], Liang Wang[4*] and Canhua Xu[2,3*]

[1]College of Life Sciences, Northwest University, Xi'an, China, [2]Department of Biomedical Engineering, Fourth Military Medical University, Xi'an, China, [3]Shaanxi Provincial Key Laboratory of Bioelectromagnetic Detection and Intelligent Perception, Xi'an, China, [4]Department of Neurosurgery, Tangdu Hospital of Fourth Military Medical University, Xi'an, China

Background: Real-time detection of cerebral blood perfusion can prevent adverse reactions, such as cerebral infarction and neuronal apoptosis. Our previous clinical trial have shown that the infusion of therapeutic fluid can significantly change the impedance distribution in the brain. However, whether this alteration implicates the cerebral blood perfusion remains unclear. To explore the feasibility of monitoring cerebral blood perfusion, the present pilot study established a novel cerebral contrast-enhanced electrical impedance tomography (C-EIT) technique.

Materials and methods: Rabbits were randomly divided into two groups: the internal carotid artery non-occlusion (ICAN) and internal carotid artery occlusion (ICAO) groups. Both of groups were injected with glucose, an electrical impedance-enhanced contrast agent, through the right internal carotid artery under EIT monitoring. The C-EIT reconstruction images of the rabbits brain were analyzed according to the collected raw data. The paired and independent *t*-tests were used to analyze the remodeled impedance values of the left and right cerebral hemispheres within and between studied groups, respectively. Moreover, pathological examinations of brain were performed immediately after C-EIT monitoring.

Results: According to the reconstructed images, the impedance value of the left cerebral hemisphere in the ICAN group did not change significantly, whereas the impedance value of the right cerebral hemisphere gradually increased, reaching a peak at approximately 10 s followed by gradually decreased. In the ICAO group, the impedance values of both cerebral hemispheres increased gradually and then began to decrease after reaching the peak value. According to the paired *t*-test, there was a significant difference ($P < 0.001$) in the remodeling impedance values between the left and right hemispheres in the ICAN group, and there was also a significant

difference ($P < 0.001$) in the ICAO group. According to the independent t-test, there was a significant difference ($P < 0.001$) of the left hemispheres between the ICAN and ICAO groups.

Conclusion: The cerebral C-EIT proposed in this pilot study can reflect cerebral blood perfusion. This method has potential in various applications in the brain in the future, including disease progression monitoring, collateral circulation judgment, tumor-specific detection, and brain function research.

KEYWORDS

electrical impedance tomography, cerebral perfusion, angiography, imaging, rabbits

Introduction

Cerebral perfusion plays a particularly important role as it reflects the blood supply provided by cerebral blood vessels (Leng et al., 2016). Good cerebral perfusion is conducive to maintaining the normal function of the brain, and stenosis or occlusion of blood vessels supplying the brain will lead to insufficient cerebral perfusion (Clayton et al., 2008; Ginsberg, 2018). When cerebral ischemia is severe and compensatory blood flow is insufficient, a series of reactions that are especially injurious to neurons are triggered (Pivonkova et al., 2010; Ofengeim et al., 2011). Furthermore, studies have shown that neurons die in ischemic conditions in approximately half the time as non-neural cells, indicating ischemia and subsequent hypoxia are extremely damaging to neural tissue (Song and Yu, 2014; Roh and Kim, 2016). Therefore, it is particularly important to monitor cerebral blood perfusion in real time during surgery and other procedures to prevent adverse events, such as neuronal apoptosis or brain tissue infarction.

Cerebral perfusion imaging evaluates regional microvascular hemodynamics in the living brain, allowing for *in-vivo* measurement of a variety of hemodynamic parameters. Clinical perfusion imaging techniques typically rely on X-ray computed tomography (CT) or magnetic resonance imaging (MRI), which is called CT perfusion (CTP) and MR perfusion (MRP), respectively (Copen et al., 2016). CTP and MRP have been used as a routine examination and clinical standard of care for stroke (Vagal et al., 2019). In addition, PET scan, regarded as the "gold standard" for the blood perfusion imaging, can provide information of cerebral blood flow due to its capability of evaluating the uptake of nutrients in the blood flow (Heurling et al., 2017). However, these technologies all have their own shortcomings, such as bulky equipment, high price, scarce resources, difficulty in usage in local or rural hospitals. Therefore, there is an urgent need for a novel, lightweight, convenient, and low-cost cerebral blood perfusion imaging technology that can be used as a powerful assistant to the existing imaging technology.

Electrical impedance tomography (EIT) is a portable, economical, safe, and constant real-time imaging technology, which applies a safe excitation current to the human body through contact electrodes, and the resulting changes in impedance distribution allow reconstructed image analysis using algorithms (Holder, 2005; Adler and Boyle, 2017; Pan et al., 2020). Due to its advantages, such as small time interval for data collection, sensitivity to changes in electrical conductivity of different tissues, and that it requires no use of radiation, EIT has been widely applied in many fields, for instance, lung respiratory function imaging (Aguiar Santos et al., 2018; Tomicic and Cornejo, 2019), prostate cancer detection function imaging (Tan and Rossa, 2021), and abdominal organ function imaging (Shuai et al., 2009).

In recent years, EIT has become a research hotspot in the field of functional brain imaging. Sana et al. characterized and imaged certain impedance distribution changes during seizures in neocortex and hippocampus using the rat model. The results suggest that EIT can be used as an ancillary imaging method for conventional electroencephalogram to improve the localization of epileptogenic regions in patients with refractory epilepsy who undergo surgery to control seizures (Hannan et al., 2021). Using an intraoperative EIT system to monitor the brain impedance of patients, Li et al. (2018) found that brain impedance was negatively correlated with cerebral blood perfusion, and the slow rise in brain resistivity might reflect changes in brain tissue caused by ischemia. The results showed that changes in regional cerebral impedance could be detected by EIT, and these changes were larger with lower blood perfusion, suggesting that EIT is expected to reflect quantitative information about cerebral blood perfusion in certain regions (Li et al., 2018). However, the accuracy of traditional electrical impedance functional imaging is insufficient to reflect the impedance changes caused by heartbeats. Based on previous clinical experiments by our research group, the infusion of a therapeutic liquid can significantly change the impedance distribution of the brain. Therefore, we propose a new method of brain contrast-enhanced electrical impedance tomography

(C-EIT), which fully utilizes the advantages of differential subtraction imaging to reflect cerebral blood perfusion.

In the study, we established a rabbit model of unilateral internal carotid artery occlusion (ICAO) and normal cerebral blood perfusion and further explored the one-dimensional impedance and reconstructed images of the left and right hemispheres after electrical impedance contrast perfusion to reflect cerebral blood perfusion. This study aimed to establish an animal model of internal carotid artery occlusion in rabbits to explore the feasibility of brain electrical impedance-enhanced contrast perfusion imaging to reflect cerebral blood perfusion.

Materials and methods

Animal preparation

All animals in this study were purchased from the Experimental Animal Center of Fourth Military Medical University. The experimental protocols and procedures were approved by the Animal Ethics Committee of the Fourth Military Medical University (Shaanxi, P. R. China) and complied with the "Guide for the Care and Use of Laboratory Animals" published by the National Institutes of Health (National Academy Press, Washington, DC, revised 1996). Twenty New Zealand white rabbits (male and female) weighing 2.5–3.0 kg were randomly divided into two groups: the internal carotid artery non-occlusion (ICAN) group (n = 10) and the ICAO group (n = 10). In the ICAO group, unilateral internal carotid artery clipping was controlled for 30 min to ensure adequate changes in cerebral perfusion.

Before the experiment, an electric heating plate was used to maintain the animal's body temperature to prevent death due to the loss of temperature caused by deep anesthesia. The animals were anesthetized with isoflurane gas (3% for induction and 2% for maintenance). The skin of the cranium was cut longitudinally with a sterile scalpel, the periosteum was removed, coronal and sagittal sutures were positioned, and a 4.0 × 2.5 cm area was exposed. Four sterile copper electrodes 0.12 cm in length were implanted 1.2 cm from the sagittal suture and 1.0 cm from the coronal suture. The remaining 12 copper electrodes were symmetrically and evenly spaced, and 16 copper electrodes formed an elliptical ring (**Figure 1**). None of the copper electrodes penetrated the intracranial dura mater in the skull. This operation ensured that the copper electrode was separated from the surrounding periosteum and skin to prevent the impedance value from being affected by skin contact.

The internal carotid artery was isolated after the electrodes were successfully implanted into the skull. The animal was supine and fixed to the dissection table; the skin and subcutaneous fascia of the middle of the neck were cut and the muscle was bluntly separated near the trachea. The bilateral common carotid arteries were exposed sequentially, and the dissection was continued upward to the position of the mastoid bone to expose the bifurcation of the internal carotid artery and the external carotid artery.

Contrast-enhanced electrical impedance tomography monitoring

In this study, the in-house FMMU-EIT-5 system was used to collect the injection and metabolism signals of the internal carotid artery contrast agent. The frequency range of the system was 1–190 Hz, and the output current range was 10–1250 μ Ap-p (Cao et al., 2020). Studies have shown that a small interference of 0.35% volume (cross-sectional area of 1.99%) and 17% resistivity can be detected in human brain models (Shi et al., 2018). A special electrode wire wrapped with insulating material was connected to the copper electrode through the end hook to transmit the excitation current. A 500 μ Ap-p current stimulus was administered between two polar pairs of electrodes, and the voltage difference was measured on the remaining adjacent electrode pairs at a rate of one frame/sec (Xu et al., 2007).

After the cranial electrodes were successfully placed and connected to the FMMU-EIT-5 system, electrical impedance-enhanced contrast perfusion imaging was performed (**Figure 2**). The contrast medium uses 5% glucose injection, which is a common clinical isotonic agent, and its electrical conductivity (0.02 S/m) was measured by a four-electrode box and the Solartron 1260 + 1294 impedance analyzer (Schlumberger Company, Hampshire, UK) (Liu et al., 2019). This value is about 30 times different from the blood conductivity (0.67 S/m). For the ICAN group, after the right external carotid artery was ligated, a 26G needle was used to puncture near the branch of the right common carotid artery, and glucose was injected, while the left internal carotid artery was left intact (**Figure 3A**). The contrast agent glucose perfusion dose was 1.0 ml/kg, and the perfusion rate was 0.25 ml/s. For the ICAO group, the left common carotid artery was ligated using a surgical silk suture. The right external carotid artery was ligated near the branch of the right common carotid artery. A 26G puncture needle was then used to puncture the right common carotid artery at a distance of 0.5 cm from the branch, and glucose was injected (**Figure 3B**).

The data acquisition of brain electrical impedance was divided into two parts: (1) After the electrical impedance system was connected to the animal through the electrode line, a blank measurement was performed for 10 min to determine whether the electrode connection was good by observing the size of the one-dimensional impedance value and the sinusoidal waveform of the original data (Xu et al., 2010). (2) After confirming that the electrodes were in good contact and that the connection was stable, carotid perfusion was performed and the start and end

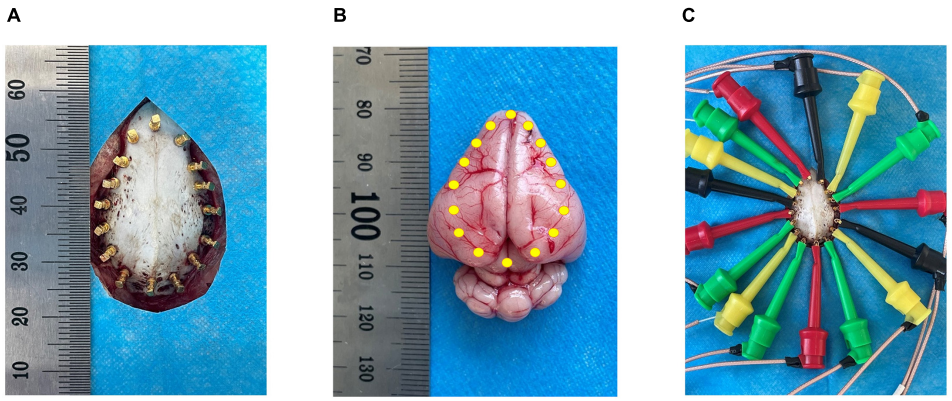

FIGURE 1
Schematic diagram of electrode positions. **(A)** Shows the 16 copper electrode positions on the skull; **(B)** Shows the relative position of the copper electrodes in the brain parenchyma; **(C)** Shows the electrode wire with a hook-shaped tool at the end connected to the copper electrode.

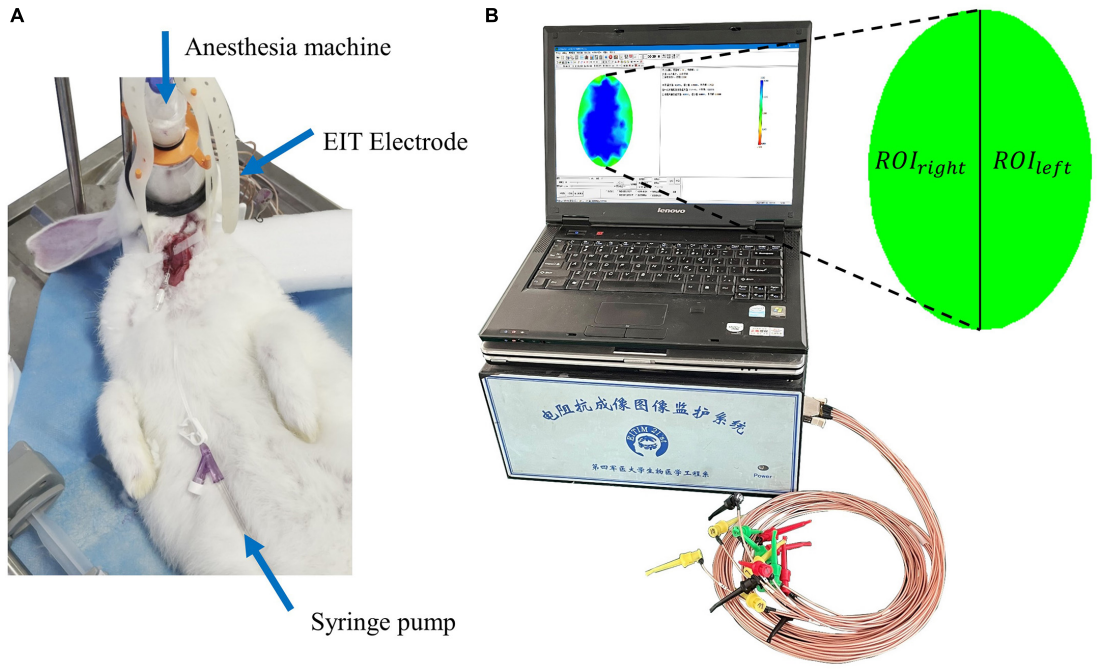

FIGURE 2
(A) The electrical impedance tomography (EIT) imaging experiment. **(B)** The FMMU-EIT5 monitoring system, where ROI_{left} refers to the region of interest in the left hemisphere, and ROI_{right} refers to the region of interest in the right hemisphere.

frames of angiography perfusion were recorded to observe the changes in brain impedance.

Data analysis

To further analyze and explore the ability of electrical impedance-enhanced angiographic perfusion to detect intracranial impedance of the normal or occluded unilateral internal carotid artery, we performed a statistical analysis of the reconstructed impedance values from the collected raw voltages. When an animal was given an excitation current with a fixed amplitude, the system collected the original voltage. The data collected by the software were exported, and the forward problem was calculated using an elliptical finite element model that conforms to the actual electrode distribution position, and then the inverse problem was calculated with a damped least squares algorithm and a reconstructed image was obtained., as

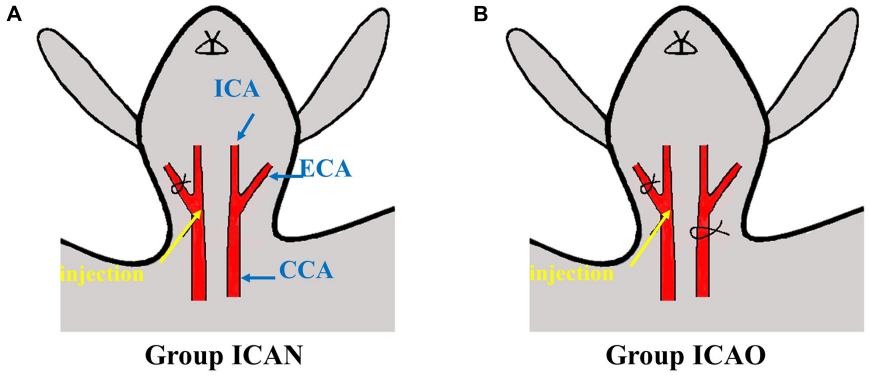

FIGURE 3
Schematic diagram of injection. **(A)** Indicates injection to the ICA with a normal CCA. **(B)** Represents injection to the ICA with occlusion of the CCA. (CCA, common carotid artery; ECA, external carotid artery; ICA, internal carotid artery).

in Equation 1 (Xu C. et al., 2011).

$$\triangle\rho = (J^T J + \lambda R)^{-1} J^T \triangle V \quad (1)$$

where $\triangle\rho$ is the change in resistivity distribution at two different time points, J is the Jacobian matrix, λ is the regularization parameter (set to five here), R is the regularization matrix, and $\triangle V$ is the boundary voltage variation vector.

According to anatomical and physiological knowledge, the left and right brains of animals are two relatively independent regions and the unilateral middle cerebral artery is mainly supplied by the ipsilateral internal carotid artery. Therefore, for C-EIT reconstructed images, the left hemisphere is defined as an independent ROI_{left} and the right hemisphere as an independent ROI_{right}. From the contrast agent perfusion monitoring process, we selected a time point every 2 s for a total of eight times (T0 = 0 s, T1 = 2 s, T2 = 4 s, T3 = 6 s, T4 = 8 s, T5 = 10 s, T6 = 12 s, T7 = 14 s) to reconstruct the image. In addition, the average resistivity variation index (ARVI) was calculated for ROI_{left} and ROI_{right} of the whole process using Equation 2 (Sadleir et al., 2008; Dai et al., 2018), expressed as $ARVI_{left}$ and $ARVI_{right}$.

$$ARVI = \left(\sum_{i=1}^{N} \triangle\rho_i\right)/N \quad (2)$$

where $\triangle\rho_i$ is the reconstructed impedance change for each surface element in the finite element network and N is the number of surface elements in the finite element network. A paired-sample t-test was used on the impedance change peaks of ROI_{left} and ROI_{right} in the two groups. In addition, a paired t-test was performed to statistically analyze the remodeled impedance values of the left and right cerebral hemispheres in the two groups, and an independent t-test was performed to analyze the remodeled impedance values of the left and right cerebral hemispheres between the two groups. Statistical significance was considered $P < 0.05$. The above analyses were from SPSS24 software (IBM Corporation, Armonk, NY, USA).

Pathological validation

The animals were euthanized in accordance with experimental animal ethics after surgery, and the brains were cut into four coronal slices of 2 mm each. The slices were soaked in 2% 2,3,5-triphenyltetrazolium chloride (TTC) staining solution in a emperature box at 30–37° for 15–30 min. After dyeing, the slices were washed with a phosphate buffer solution and immediately observed and photographed.

In addition, we performed hematoxylin-eosin staining (HE) on the brain tissue of two rabbits in the ICAN and ICAO groups to further microscopically examine the neuronal micromorphology and structure of the left middle cerebral artery. The abdominal aorta was occluded, the left ventricle was impaled, and phosphate buffered saline (150 ml) was continuously perfused, followed by 4% paraformaldehyde (250 ml). The brains were harvested, fixed in 4% paraformaldehyde for 72 h, and wrapped in paraffin. Coronal sections (4 μ m) were prepared, and the morphology of the neurons was observed under a microscope after staining.

Results

Pathological results

Figure 4 indicates the TTC results for the ICAN and ICAO groups. Figure 4A indicates the normal brain tissue in the ICAN group (red). Figure 4B shows the brain tissue of the ICAO group, which is also red, indicating that there is no cerebral infarction area. The results of HE staining of the hippocampus of the two groups are shown in Figure 5, with light microscopy at 40 × magnification. After the operation, the rabbit brain tissue in the ICAN group was evenly stained, as shown in Figure 5A, and the ICAO group was also uniformly stained,

resembling that of the ICAN group, as shown in Figure 5B. The nuclei and cytoplasm of the left and right cerebral hemispheres were clear in the ICAN group, as shown in Figure 5C. The boundary between the nucleus and cytoplasm of the left cerebral hemisphere in the ICAO group was clear, and most of the cells had intact structures without pyknosis and rupture, as shown in Figure 5D, which was similar to the normal brain tissue in the ICAN group.

Contrast-enhanced electrical impedance tomography reconstructed image results

The C-EIT monitoring data of five rabbits in the ICAN and ICAO groups were randomly selected and the reconstructed images are shown in Figure 6. Figure 6A shows the C-EIT reconstruction images of the ICAN group at each 2 s time point (T1–T8). With the injection of the contrast agent, a blue electrical impedance-enhancing area appeared in ROI_{right}, and the electrical impedance-enhancing area continued to expand and gradually fill. Figure 6B shows C-EIT reconstruction images of the clamped (ICAO) group at T1–T8. With the injection of the contrast medium, blue areas of electrical impedance enhancement appeared in both ROI_{left} and ROI_{right}. These results indicated that the ICAO group successfully changed the original cerebral blood perfusion pathway. Because of the occlusion of the left common carotid artery, the blood supply to the left side of the rabbit brain was insufficient, and the right side of the rabbit brain provided a compensatory blood supply to the left side of the rabbit brain through the blood supply artery. Among them, the area of electrical impedance enhancement of R8 and R9 at T8 = 14 s was smaller than that at T7 = 12 s, considering that which may be caused by the absorption and dilution of the contrast agent with systemic blood circulation.

Electrical impedance analysis results

To quantitatively analyze $ARVI_{left}$ and $ARVI_{right}$ of ROI_{left} and ROI_{right} of rabbits after contrast agent perfusion, the experimental data were calculated by intercepting 15 frames from the beginning of the contrast agent injection. Figure 7A shows that the $ARVI_{right}$ of the ROI_{right} in the ICAN group increased with the perfusion process and gradually decreased to a plateau after reaching the peak at 10 frames, and it remained at the baseline level despite fluctuations of the ROI_{left}. There was a small increase in $ARVI_{left}$ of ROI_{left}. Considering the small size of the rabbit brain, the measurement data could not be accurately controlled. In the future, animal models with larger brain volumes, such as piglets, should be explored. Figure 7B shows that the ARVI of both ROI_{left} and ROI_{right} in the ICAO group increased with the perfusion process, and gradually decreased to a plateau after reaching the peak at 10 frames, and the $ARVI_{right}$ of ROI_{right} was higher than $ARVI_{left}$ of ROI_{left}. This is due to the fact that blood in the left hemisphere is compensated by the right hemisphere through the circle of Willis, so the contrast medium perfusion in the left hemisphere is lower than that in the right hemisphere.

Figure 8A shows the results of the electrical impedance changes in the ROI_{left} and ROI_{right} in the two groups, and the electrical impedance changes in the ICAN group were statistically significant (ICAN-Left: 0.0188 ± 0.0104; ICAN-Right: 0.0885 ± 0.0116; $P < 0.001$). The electrical impedance changes of ROI_{left} and ROI_{right} in the ICAO group were also statistically significant (ICAO-Left: 0.0637 ± 0.0112; ICAO-Right: 0.0899 ± 0.0069; $P < 0.001$). This is because the left

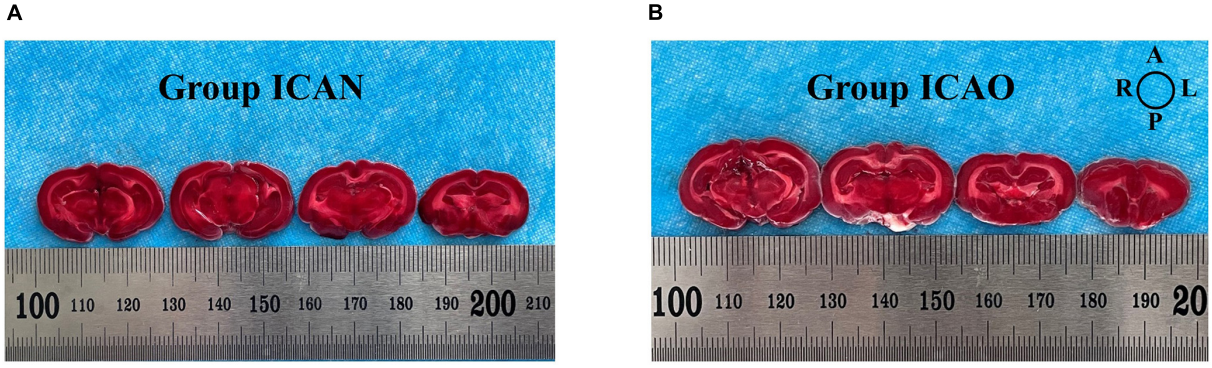

FIGURE 4
2,3,5-triphenyltetrazolium chloride (TTC)-stained samples from the two groups. **(A)** Indicates the brain tissue in the ICAN group. **(B)** Indicates the brain tissue in the ICAO group. Each slice is 2 mm thick and the slices are arranged from the pineal gland to the olfactory bulb along the sagittal suture. The image orientation is shown in the top-right diagram, where A, L, P, and R represent the anterior, left, posterior, and right parts of the brain, respectively.

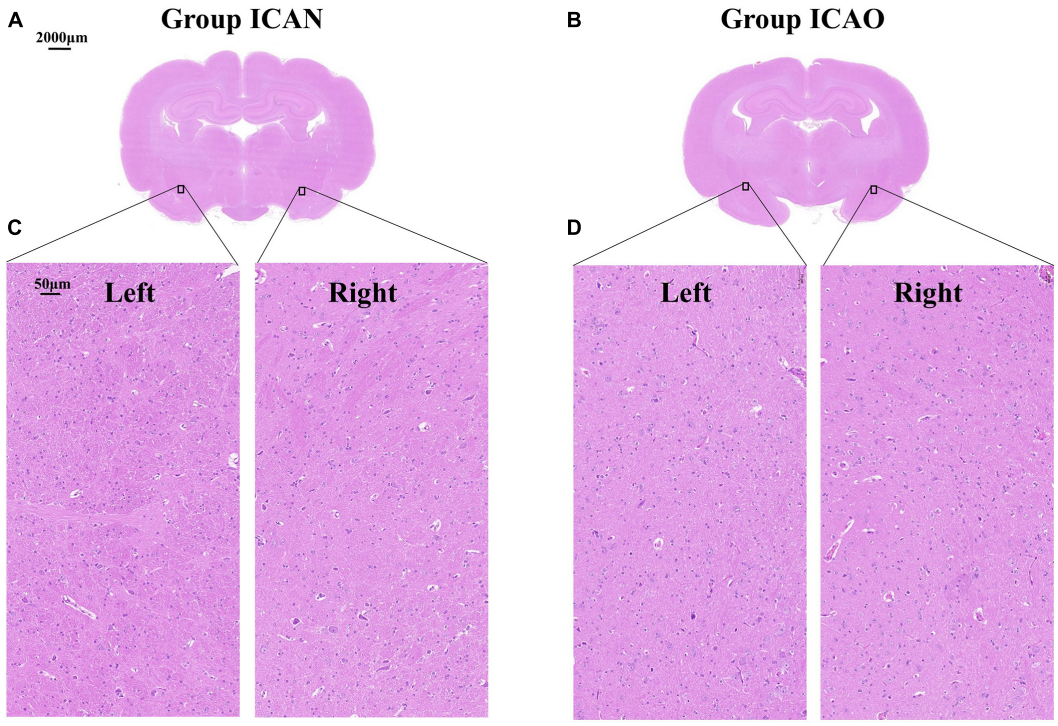

FIGURE 5
Microstructure of rabbit whole brain tissue under a light microscope at 40 × magnification. **(A,B)** Represent the coronal microstructure of the rabbit brain in the two groups. **(C)** Represents the normal tissue of the left and right cerebral hemispheres of the internal carotid artery non-occlusion (ICAN) group, and **(D)** Represents the brain tissues of the left and right cerebral hemispheres of the internal carotid artery occlusion (ICAO) group, which were the same as the normal brain tissues of the ICAN group.

cerebral hemisphere was supplied with blood from the right cerebral hemisphere after the left common carotid artery was occluded in the ICAO group. Owing to the limited blood supply, the electrical impedance of the right cerebral hemisphere was higher than that of the left cerebral hemisphere. Figure 8B shows the results of the electrical impedance changes in the ipsilateral cerebral hemisphere for the two groups. The electrical impedance changes in ROI_{left} of the ICAN group and ROI_{left} of the ICAO group were statistically significant (ICAN-Left: 0.0188 ± 0.0104; ICAO-Left: 0.0637 ± 0.0112; $P < 0.001$), and there was no statistically significant difference in the electrical impedance changes in the ROI_{right} between the ICAN and ICAO groups (ICAN-Right: 0.0885 ± 0.0116; ICAO-Right: 0.0899 ± 0.0069; $P > 0.05$).

The 30 s reconstructed impedance value detected before D5W infusion was used as EIT control (ICAN-Left: 0.0084 ± 0.0025; ICAN-Right: 0.0082 ± 0.0028; ICAO-Left: 0.0096 ± 0.0020; ICAO-Right: 0.0084 ± 0.0038). Compared to the EIT without the contrast agent, injection of 5% glucoses significantly changed the electrical impedance: the $ARVI_{right}$ of the ROI_{right} ($P < 0.001$) and the $ARVI_{left}$ of ROI_{left} ($P < 0.05$) in the ICAN group; the $ARVI_{right}$ of the ROI_{right} ($P < 0.001$) and the $ARVI_{left}$ of ROI_{left} ($P < 0.001$) in the ICAO group.

Discussion

In the study, the feasibility of C-EIT in reflecting cerebral blood perfusion was investigated by monitoring a rabbit model of internal carotid artery embolism. In this experiment, the unilateral internal carotid artery occlusion model was successfully established in ten rabbits, the ICAO group, while the other 10 rabbits with normal internal carotid arteries (ICA) group were monitored by electrical impedance tomography after the model was successfully established. A glucose contrast agent with high blood conductivity was injected into the body through the other internal carotid artery, the collected one-dimensional impedance data were analyzed, and the reconstructed image was reconstructed by the algorithm. The results showed that the impedance value of the left cerebral hemisphere in the ICAN group remained unchanged, while the impedance value of the right hemisphere gradually increased, reached the peak value, and then decreased. According to statistical analysis, there was a statistically significant ($P < 0.001$) difference between the impedance values of the left and right hemispheres. This reflects the cerebral blood flow perfusion in the right cerebral hemisphere. In the ICAO group, the impedance values of both cerebral hemispheres were gradually enhanced, and then began to decrease after reaching the

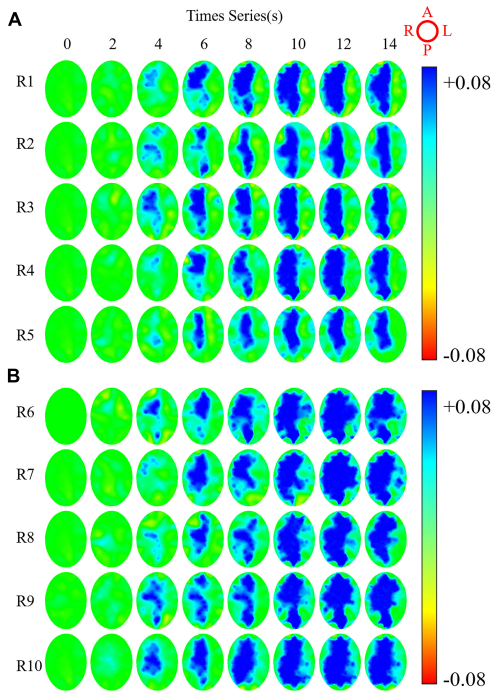

FIGURE 6
Reconstructed images of rabbits whole brain at eight time points under contrast-enhanced electrical impedance tomography (C-EIT). **(A)** Indicates five rabbits (R1–R5) in the internal carotid artery non-occlusion (ICAN) group. **(B)** Represents five rabbits (R6–R10) in the internal carotid artery occlusion (ICAO) group. The image orientation is shown in the upper right image, A, L, P, R represent the anterior, left, posterior, and right parts of the brain, respectively. The color bar represents the range of possible colors, from increasing electrical resistivity value (blue) to normal baseline intensity (green) and decreasing electrical resistivity value (red).

peak value. According to the statistical analysis, there was a significant difference ($P < 0.001$) between the left brain remodeling impedance and that of the right brain. This reflects the compensatory cerebral blood perfusion after diverting some of the original blood supply through the cerebral collateral circulation. Therefore, the C-EIT method proposed in this study is feasible and reflects the state of blood perfusion.

This pilot study was only a qualitative study that explored the feasibility of contrast-enhanced perfusion imaging using cerebral electrical impedance tomography. There has been no comparative study with other existing imaging methods, and it is uncertain whether the cerebral blood perfusion results obtained by C-EIT are accurate. In future research, our research group will not only increase the number of experimental cases but also carry out quantitative research and design other existing means to carry out simultaneous measurements to further verify the effectiveness of this method.

One of the important causes of cerebral ischemia is the occlusion of the ICA, which is a common site of vascular disease (Chen et al., 2021; Hoving et al., 2021). Therefore, a rabbit internal carotid artery occlusion model was selected to replicate clinical internal carotid artery occlusion. When the internal carotid artery, the main blood supply vessel of the cerebral artery, is narrowed or even occluded, collateral circulation of the brain is triggered to ensure an adequate blood supply to the brain tissue, and the blood supply pathway of the cerebral hemisphere on the infarcted side changes (Cuccione et al., 2016). Therefore, internal carotid occlusion can be used as an animal model to analyze cerebral blood perfusion. Sun et al. (2007) established a rat model of subarachnoid hemorrhage to study the effect of *G. biloba* extract on cerebral blood perfusion. Chen et al. (2021) studied the effects of exogenous endothelial progenitor cells on cerebral blood perfusion and microvessels in the injured areas of a rat traumatic brain injury model (Xiao et al., 2013). In the future, our group will explore more cerebral blood perfusion models to better reflect the actual state of cerebral blood perfusion.

Because glucose injection has the advantages of non-conductivity, high contrast with blood conductivity, and a strong reconstructed image signal, glucose injection was selected as the electrical impedance enhancement contrast agent in this study. On the premise of obtaining the patient's informed consent and not interfering with the normal clinical treatment process, Dai et al. in our research group conducted a clinical dural hematoma drainage test using 5% glucose injection and used EIT to monitor the inflow and discharge process of the glucose solution (Dai et al., 2013). The experimental results indicated that the impedance of the injection area increased significantly with the injection of the glucose solution, indicating that EIT is highly sensitive to intracranial glucose infusion. Therefore, in this study, 5% glucose injection was selected as the contrast agent for brain electrical impedance-enhanced contrast perfusion imaging. In a follow-up study, our team will explore more types of contrast agents, such as normal saline, to achieve better imaging results.

In previous EIT studies, our research group has explored the placement methods of electrodes in various experimental animals and clinical trials. In clinic, the method is non-invasive, in which the patch electrode is directly attached to the scalp (Xu S. et al., 2011; Dai et al., 2013; Li et al., 2018). For large experimental animals, such as piglets, the electrodes were placed on the piglet's head, and then the hooked copper electrodes were fixed on the piglet's skull (Dai et al., 2010); For small experimental animals, such as rabbits, electrode placement involves cutting the skin of the cranial dome, followed by exposing the skull and implanting sterile copper electrodes into the skull (Yang et al., 2014, 2017; Dai et al., 2018). Reasons for implantable electrodes in rabbits are as follow: firstly, the skin bleeding may interfere the electrode data collection, resulting in inaccurate measurements of impedance. Secondly, the anatomical size of rabbits' head is too small to have enough space to fix the sixteen patch electrodes, which could cause unstable measurements and affect the signal quality. Finally,

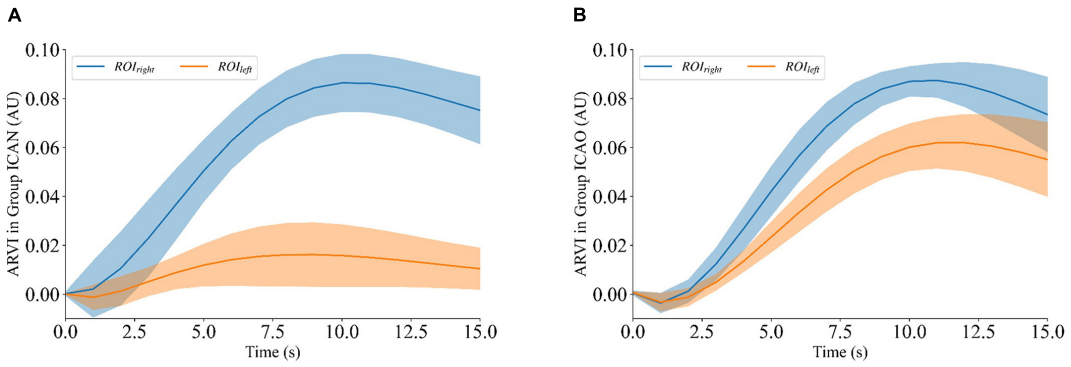

FIGURE 7
ARVI$_{left}$ and ARVI$_{right}$ of ROI$_{left}$ and ROI$_{right}$ during contrast-enhanced electrical impedance tomography (C-EIT) monitoring. **(A)** Indicates that the ARVI$_{right}$ of ROI$_{right}$ in the internal carotid artery non-occlusion (ICAN) group was significantly increased after the injection of the contrast agent, and the ARVI$_{left}$ of the ROI$_{left}$ did not change significantly. **(B)** Indicates that the average resistivity variation index (ARVI) of both ROI$_{left}$ and ROI$_{right}$ in the internal carotid artery occlusion (ICAO) group was significantly increased after injection of the contrast agent.

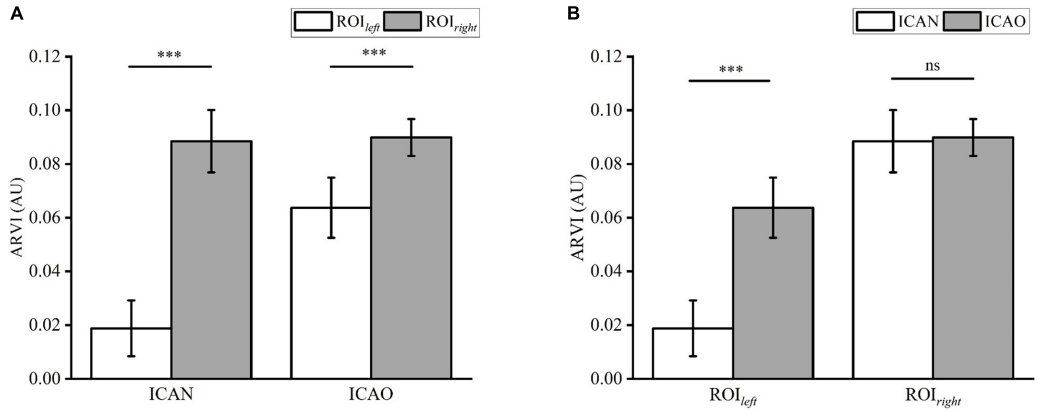

FIGURE 8
(A) Shows the statistical analysis of the reconstructed impedance values of ROI$_{left}$ and ROI$_{right}$ in the two groups using a paired *t*-test. **(B)** Analysis of the reconstructed impedance values between ROI$_{left}$ and ROI$_{right}$ of the two groups using an independent *t*-test. (***means $p < 0.001$).

an invasive implantable electrode inside the rabbits' head can secure the position of the electrode, which can avoid the impact of skin contact on the impedance value. In the future research, we will change the animal model to explore a safer and more reliable electrode placement method for better application.

In this study, arteriography was used as the contrast medium injection method, considering its advantages of stronger enhanced signals and fewer circulatory factors. According to the implementation approach of the existing contrast agent, optional contrast agent injection methods include the internal carotid artery, common carotid artery, cubital vein, and femoral vein. Regardless of whether a vein or artery is selected for contrast medium perfusion, the existing contrast medium can eventually reach the brain through the blood circulation to achieve contrast-enhanced imaging. However, considering that the arteriography perfusion method has the disadvantages of large trauma and inconvenient operation, and we adopted the method of puncturing the internal carotid artery. Hence, this may change the original blood perfusion condition. Therefore, in follow-up research, we will gradually carry out venography exploration experiments with less trauma and a simple operation in combination with different types of contrast agents.

In conclusion, the new cerebral contrast-enhanced electrical impedance tomography method proposed in this study can reflect cerebral blood perfusion through the reconstructed image of the contrast agent, which provides a platform for exploratory research for the detection of cerebral blood perfusion-related diseases. Furthermore, because this method can reflect the distribution of the contrast agent in real time, C-EIT is expected to be used in thrombolytic effect detection, vascular stenosis judgment, collateral circulation evaluation,

tumor localization detection, brain function research, and other important applications. Especially in the detection of tumor localization, research on contrast agents that can specifically bind to tumor targets can be further explored. In addition, many other electromagnetic imaging techniques can be adapted to incorporate the principle of differential imaging. In the future, magnetic and magneto-acoustic contrast agents can also be studied, and other electromagnetic and magneto-acoustic imaging technologies can be used for enhanced contrast imaging.

Data availability statement

The raw data supporting the conclusions of this article will be made available by the authors, without undue reservation.

Ethics statement

This animal study was reviewed and approved by Experimental Animal Center of Fourth Military Medical University.

Author contributions

YZ, JY, TZ, WZ, and CX helped design, collect, and analyze data. All authors contributed to this research and subsequent manuscript from conception to final preparation of the article and approved the submitted version.

Funding

This work was supported by the Technology Field Foundation on Basic Strengthen Project under Grant (2019-JCJQ-JJ-096), the National Key R&D Program of China (2021YFC1200104), and the National Natural Science Foundation of China under Grant (31771073).

Conflict of interest

The authors declare that the research was conducted in the absence of any commercial or financial relationships that could be construed as a potential conflict of interest.

Publisher's note

All claims expressed in this article are solely those of the authors and do not necessarily represent those of their affiliated organizations, or those of the publisher, the editors and the reviewers. Any product that may be evaluated in this article, or claim that may be made by its manufacturer, is not guaranteed or endorsed by the publisher.

References

Adler, A., and Boyle, A. (2017). Electrical impedance tomography: Tissue properties to image measures. *IEEE Trans. Biomed. Eng.* 64, 2494–2504.

Aguiar Santos, S., Czaplik, M., Orschulik, J., Hochhausen, N., and Leonhardt, S. (2018). Lung pathologies analyzed with multi-frequency electrical impedance tomography: Pilot animal study. *Respir. Physiol. Neurobiol.* 254, 1–9. doi: 10.1016/j.resp.2018.03.016

Cao, L., Li, H., Fu, D., Liu, X., Ma, H., Xu, C., et al. (2020). Real-time imaging of infarction deterioration after ischemic stroke in rats using electrical impedance tomography. *Physiol. Meas.* 41:015004. doi: 10.1088/1361-6579/ab69ba

Chen, T. Y., Chang, W. L., Chen, P. Y., Hsiao, C. L., and Lin, S. K. (2021). Acute and chronic bilateral internal carotid artery occlusion. *Acta Neurol. Taiwan.* 30, 128–140.

Clayton, J. A., Chalothorn, D., and Faber, J. E. (2008). Vascular endothelial growth factor-a specifies formation of native collaterals and regulates collateral growth in Ischemia. *Circ. Res.* 103, 1027–1036. doi: 10.1161/CIRCRESAHA.108.181115

Copen, W. A., Lev, M. H., and Rapalino, O. (2016). "Brain perfusion: Computed tomography and magnetic resonance techniques," in *Handbook of clinical neurology*, Vol. 135, eds C. Joseph, R. Masdeu, and G. Gilberto (Amsterdam: Elsevier), 117.

Cuccione, E., Padovano, G., Versace, A., Ferrarese, C., and Beretta, S. (2016). Cerebral collateral circulation in experimental ischemic stroke. *Exp. Transl. Stroke Med.* 8:2.

Dai, M., Li, B., Hu, S., Xu, C., Yang, B., Li, J., et al. (2013). In vivo imaging of twist drill drainage for subdural hematoma: A clinical feasibility study on electrical impedance tomography for measuring intracranial bleeding in humans. *PLoS One* 8:e55020. doi: 10.1371/journal.pone.0055020

Dai, M., Liu, X., Li, H., Xu, C., Yang, B., Wang, H., et al. (2018). EIT imaging of intracranial hemorrhage in rabbit models is influenced by the intactness of cranium. *Biomed Res. Int.* 2018:1321862. doi: 10.1155/2018/1321862

Dai, M., Wang, L., Xu, C., Li, L., Gao, G., and Dong, X. (2010). Real-time imaging of subarachnoid hemorrhage in piglets with electrical impedance tomography. *Physiol. Meas.* 31, 1229–1239. doi: 10.1088/0967-3334/31/9/012

Ginsberg, M. D. (2018). The cerebral collateral circulation: Relevance to pathophysiology and treatment of stroke. *Neuropharmacology* 134 (Pt. B), 280–292.

Hannan, S., Aristovich, K., Faulkner, M., Avery, J., Walker, M. C., and Holder, D. S. (2021). Imaging slow brain activity during neocortical and hippocampal epileptiform events with electrical impedance tomography. *Physiol. Meas.* 42:014001. doi: 10.1088/1361-6579/abd67a

Heurling, K., Leuzy, A., Jonasson, M., Frick, A., Zimmer, E., Nordberg, A., et al. (2017). Quantitative positron emission tomography in brain research. *Brain Res.* 1670, 220–234.

Holder, D. (2005). *Electrical impedance tomography : Methods, history and applications*. London: Institute of Physics.

Hoving, J. W., Kappelhof, M., Schembri, M., Emmer, B. J., Berkhemer, O. A., Groot, A. E. D., et al. (2021). Thrombectomy for acute ischemic stroke patients with isolated distal internal carotid artery occlusion: A retrospective

observational study. *Neuroradiology* 63, 777–786. doi: 10.1007/s00234-020-02550-5

Leng, X., Lan, L., Liu, L., Leung, T. W., and Wong, K. S. (2016). Good collateral circulation predicts favorable outcomes in intravenous thrombolysis: A systematic review and meta-analysis. *Eur. J. Neurol.* 23, 1738–1749. doi: 10.1111/ene.13111

Li, Y., Zhang, D., Liu, B., Jin, Z., Duan, W., Dong, X., et al. (2018). Noninvasive cerebral imaging and monitoring using electrical impedance tomography during total aortic arch replacement. *J. Cardiothorac. Vasc. Anesth.* 32, 2469–2476.

Liu, X., Li, H., Ma, H., Xu, C., Yang, B., Dai, M., et al. (2019). An iterative damped least-squares algorithm for simultaneously monitoring the development of hemorrhagic and secondary ischemic lesions in brain injuries. *Med. Biol. Eng. Comput.* 57, 1917–1931. doi: 10.1007/s11517-019-02003-z

Ofengeim, D., Miyawaki, T., and Zukin, R. (2011). *Molecular and cellular mechanisms of ischemia-induced neuronal death*. Amsterdam: Elsevier Inc, 75–106.

Pan, W., Zhuang, W., Chong, Y., Qin, M., Li, Y., Xiao, J., et al. (2020). Noninvasive real-time detection of cerebral blood perfusion in hemorrhagic shock rabbits based on whole-brain magnetic induction phase shift: An experimental study. *Physiol. Meas.* 41:095004. doi: 10.1088/1361-6579/abad12

Pivonkova, H., Benesova, J., Butenko, O., Chvatal, A., and Anderova, M. (2010). Impact of global cerebral ischemia on K+ channel expression and membrane properties of glial cells in the rat *Hippocampus*. *Neurochem. Int.* 57, 783–794. doi: 10.1016/j.neuint.2010.08.016

Roh, E., and Kim, M. (2016). Brain regulation of energy metabolism. *Endocrinol. Metab.* 31, 519–524.

Sadleir, R. J., Zhang, S. U., Tucker, A. S., and Oh, S. (2008). Imaging and quantification of anomaly volume using an eight-electrode 'hemiarray' EIT reconstruction method. *Physiol. Meas.* 29, 913–927. doi: 10.1088/0967-3334/29/8/005

Shi, X., Li, W., You, F., Huo, X., Xu, C., Ji, Z., et al. (2018). High-Precision electrical impedance tomography data acquisition system for brain imaging. *IEEE Sens. J.* 18, 5974–5984. doi: 10.1109/IEMBS.2008.4649375

Shuai, W., You, F., Zhang, H., Zhang, W., Fu, F., Shi, X., et al. (2009). Application of Electrical impedance tomography for continuous monitoring of retroperitoneal bleeding after blunt trauma. *Ann. Biomed. Eng.* 37, 2373–2379. doi: 10.1007/s10439-009-9778-y

Song, M., and Yu, S. P. (2014). Ionic regulation of cell volume changes and cell death after Ischemic stroke. *Transl. Stroke Res.* 5, 17–27. doi: 10.1007/s12975-013-0314-x

Sun, B., Yuan, H., Yang, M., Xia, Z., Zhang, S., and Wang, L. (2007). Effects of extract of *Ginkgo biloba* on intracranial pressure, cerebral perfusion pressure, and cerebral blood flow in a rat model of subarachnoid haemorrhage. *Int. J. Neurosci.* 117, 655–665. doi: 10.1080/00207450600773871

Tan, H., and Rossa, C. (2021). Electrical impedance tomography for robot-aided internal radiation therapy. *Front. Bioeng. Biotechnol.* 9:698038. doi: 10.3389/fbioe.2021.698038

Tomicic, V., and Cornejo, R. (2019). Lung monitoring with electrical impedance tomography: Technical considerations and clinical applications. *J. Thorac. Dis.* 11, 3122–3135. doi: 10.21037/jtd.2019.06.27

Vagal, A., Wintermark, M., Nael, K., Bivard, A., Parsons, M., Grossman, A., et al. (2019). Automated CT perfusion imaging for acute ischemic stroke: Pearls and pitfalls for real-world use. *Neurology* 93, 888–898. doi: 10.1212/WNL.0000000000008481

Xiao, C., Yin, J., Wu, X., Li, R., Fang, J., Chen, R., et al. (2013). Effects of magnetically labeled exogenous endothelial progenitor cells on cerebral blood perfusion and microvasculature alterations after traumatic brain injury in rat model. *Acta Radiol.* 54, 313–323. doi: 10.1258/ar.2012.120605

Xu, C., Dai, M., You, F., Shi, X., Fu, F., Liu, R., et al. (2011). An optimized strategy for real-time hemorrhage monitoring with electrical impedance tomography. *Physiol. Meas.* 32, 585–598.

Xu, C., Dong, X., Fu, F., Shuai, W., Liu, X., and Zhang, C. (2007). "A novel image monitoring software system of electrical impedance tomography for internal hemorrhage," in *Proceedings of the world congress on medical physics and biomedical engineering 2006. IFMBE*, (Berlin: Springer), 3882–3885.

Xu, C., Wang, L., Shi, X., You, F., Fu, F., Liu, R., et al. (2010). Real-time imaging and detection of intracranial haemorrhage by electrical impedance tomography in a piglet model. *J. Int. Med. Res.* 38, 1596–1604. doi: 10.1177/147323001003800504

Xu, S., Dai, M., Xu, C., Chen, C., Tang, M., Shi, X., et al. (2011). Performance evaluation of five types of Ag/AgCl bio-electrodes for cerebral electrical impedance tomography. *Ann. Biomed. Eng.* 39, 2059–2067. doi: 10.1007/s10439-011-0302-9

Yang, B., Shi, X., Dai, M., Xu, C., You, F., Fu, F., et al. (2014). Real-time imaging of cerebral infarction in rabbits using electrical impedance tomography. *J. Int. Med. Res.* 42, 173–183. doi: 10.1177/0300060513499100

Yang, L., Liu, W., Chen, R., Zhang, G., Li, W., Fu, F., et al. (2017). In Vivo bioimpedance spectroscopy characterization of healthy, hemorrhagic and ischemic rabbit brain within 10 Hz–1 MHz. *Sensors* 17:791. doi: 10.3390/s17040791

frontiers | Frontiers in Neuroscience

TYPE Original Research
PUBLISHED 05 December 2022
DOI 10.3389/fnins.2022.1025967

OPEN ACCESS

EDITED BY
Nico Sollmann,
University of California, San Francisco, United States

REVIEWED BY
Jialing Liu,
University of California, San Francisco, United States
David Chung,
Massachusetts General Hospital and Harvard Medical School, United States

*CORRESPONDENCE
Edgar Santos
edgar.santos@uni-heidelberg.de

SPECIALTY SECTION
This article was submitted to Brain Imaging Methods, a section of the journal Frontiers in Neuroscience

RECEIVED 16 September 2022
ACCEPTED 18 November 2022
PUBLISHED 05 December 2022

CITATION
Kentar M, Díaz-Peregrino R, Trenado C, Sánchez-Porras R, San-Juan D, Ramírez-Cuapio FL, Holzwarth N, Maier-Hein L, Woitzik J and Santos E (2022) Spatial and temporal frequency band changes during infarct induction, infarct progression, and spreading depolarizations in the gyrencephalic brain.
Front. Neurosci. 16:1025967.
doi: 10.3389/fnins.2022.1025967

Spatial and temporal frequency band changes during infarct induction, infarct progression, and spreading depolarizations in the gyrencephalic brain

Modar Kentar[1], Roberto Díaz-Peregrino[1], Carlos Trenado[2], Renán Sánchez-Porras[3], Daniel San-Juan[4], F. Leonardo Ramírez-Cuapio[1], Niklas Holzwarth[5], Lena Maier-Hein[5], Johannes Woitzik[3] and Edgar Santos[1,3]*

[1]Department of Neurosurgery, University Hospital Heidelberg, Ruprecht-Karls-University Heidelberg, Heidelberg, Germany, [2]Institute of Clinical Neuroscience and Medical Psychology, Medical Faculty, Heinrich Heine University, Düsseldorf, Germany, [3]Department of Neurosurgery, Evangelisches Krankenhaus, Carl-von-Ossietzky University, Oldenburg, Germany, [4]Epilepsy Clinic, National Institute of Neurology and Neurosurgery, Manuel Velasco Suárez, Mexico City, Mexico, [5]Division of Intelligent Medical Systems, German Cancer Research Center, Heidelberg, Germany

Aim: To describe the spatial and temporal electrocorticographic (ECoG) changes after middle cerebral artery occlusion (MCAo), including those caused by spreading depolarization (SD) in the pig brain.

Methods: The left middle cerebral arteries (MCAs) were clipped in six pigs. The clipping procedure lasted between 8 and 12 min, achieving a permanent occlusion (MCAo). Five-contact ECoG stripes were placed bilaterally over the frontoparietal cortices corresponding to the irrigation territory of the MCA and anterior cerebral artery (ACA). ECoG recordings were performed around 24 h: 1 h before and 23 h after the MCAo, and SDs were quantified. Five-minute ECoG signal segments were sampled before, 5 min, and 4, 8, and 12 h after cerebral artery occlusion and before, during, and after the negative direct current shift of the SDs. The power spectrum of the signals was decomposed into delta, theta, alpha, beta, and gamma bands. Descriptive statistics, Wilcoxon matched-pairs signed-rank tests, and Friedman tests were performed.

Results: Electrodes close to the MCAo showed instant decay in all frequency bands and SD onset during the first 5 h. Electrodes far from the MCAo exhibited immediate loss of fast frequencies and progressive decline of slow frequencies with an increased SD incidence between 6 and 14 h. After 8 h, the ACA electrode reported a secondary reduction of all frequency bands except gamma and high SD incidence within 12–17 h. During the SD, all electrodes showed a decline in all frequency bands. After SD passage, frequency band recovery was impaired only in MCA electrodes.

Conclusion: ECoG can identify infarct progression and secondary brain injury. Severe disturbances in all the frequency bands are generated in the cortices where the SDs are passing by.

KEYWORDS

spreading depolarization, stroke progression, ECoG recording, power spectrum of signal decomposition, frequency bands

Introduction

Spreading depolarization (SD) is recognized as a negative direct current (DC) shift in the brain frequency range of <0.05 Hz, which propagates sequentially at adjacent recording sites. It is induced by severe neurological disorders, such as stroke, aneurysmal subarachnoid hemorrhage, intracerebral hemorrhage, traumatic brain injury, or epilepsy. SD produces a decrease in amplitudes of spontaneous activity, also known as spreading depression, in electrically active brain tissue (Hartings et al., 2011; Dreier et al., 2017). SDs have heterogeneous propagation patterns (Santos et al., 2017), making it difficult to detect SD using electroencephalography (EEG). The SDs contribute to the worsening of the penumbra and the infarct progression after an ischemic stroke (Ayata and Lauritzen, 2015). However, the specific anatomical and temporal frequency band disturbances produced by SDs are not well known.

During artery occlusion in the brain, there is a decrease in the spectral power of the frequency bands referred to as the non-spreading depression of activity (**Figure 1**; Dreier et al., 2017). How it occurs and behaves over time in humans is difficult to document because of the lack of electrocorticography (ECoG) monitoring during acute ischemic stroke. Moreover, dynamic pathophysiological changes in several brain areas after the spreading depression of spontaneous electrical activity should be investigated.

Similarly, scientists have studied infarct progression after stroke in humans using EEG and magnetoencephalography. The most consistent findings were the reduction of fast frequency bands and the predominance of delta and theta frequencies, which predict an unfavorable prognosis (Cillessen et al., 1994; Tecchio et al., 2005, 2007; Burghaus et al., 2007; Diedler et al., 2009; Moeller et al., 2011).

Due to the great complexity and variation in brain ischemia-induced pathophysiology, a consensus regarding the modifications of frequency bands after stroke is difficult to reach, except that brain activity appears to correlate with cerebral blood flow, oxygen, and glucose levels (Rabiller et al., 2015). Power declines in alpha, beta, and gamma frequencies are observed when the cerebral oxygen metabolism is critically reduced (Nagata et al., 1989). In addition, delta and theta rhythms seem to be reliable parameters correlating with cerebral blood flow and metabolic changes during focal ischemia in the cortex (Rabiller et al., 2015). Additionally, a lesion in the white matter induces irregular delta activity in the cortex overlying the infarct (Gloor et al., 1977; Rabiller et al., 2015).

The study of frequency band dynamics will help identify the presumed penumbra and infarct progression over time. Analysis of the initially unaffected areas facilitated the identification of the gradual changes produced by ischemia. Furthermore, the brain frequency bands will elucidate how harmful the SDs are and how they cause secondary damage to the penumbra and healthy structures.

Therefore, the primary aims of this study were to characterize the temporal and spatial changes in frequency bands 5 min and 4, 8, and 12 h after middle cerebral artery occlusion (MCAo) and during SD development.

Materials and methods

Experimental set-up

The Institutional Animal Care and Use Committee in Karlsruhe, Baden-Württemberg, Germany authorized the experimental protocol (Protocol No. G-13/15, G-148-15, G-69/16). The experiments were conducted in compliance with the University of Heidelberg Animal Ethics Policy of the Interfacultary Biomedical Faculty (IBF 347). The Animal Research: Reporting *In Vivo* Experiments (ARRIVE) guidelines were followed.

Ten female Landrace pigs (3–4 months old and 28–32 kg) were kept under general anesthesia using midazolam (2–10 mg/mL), propofol (1 mL/20 mg), and isoflurane (1–1.5%). Four animals were used to establish models and settings. Six animals were used for this study. The sample rate of all ECoG recordings was ≥200 Hz. Two subdural five-contact, platinum wall strip electrodes were used (Ad-tech, Racine, Wisconsin, USA). A ground electrode was placed in the zygomatic bone. The recording was performed using a Powerlab 16/SP analog-to-digital converter (ADInstruments, Sydney, Australia), which has 16 independent single-ended analog inputs with the signal referenced to the ground. The alternating current (AC) recorder had a 0.1-Hz filter. A notch filter (50 Hz) was applied to eliminate line disturbances. Registration and analysis of ECoG were performed using LabChart v7 (ADInstruments). After

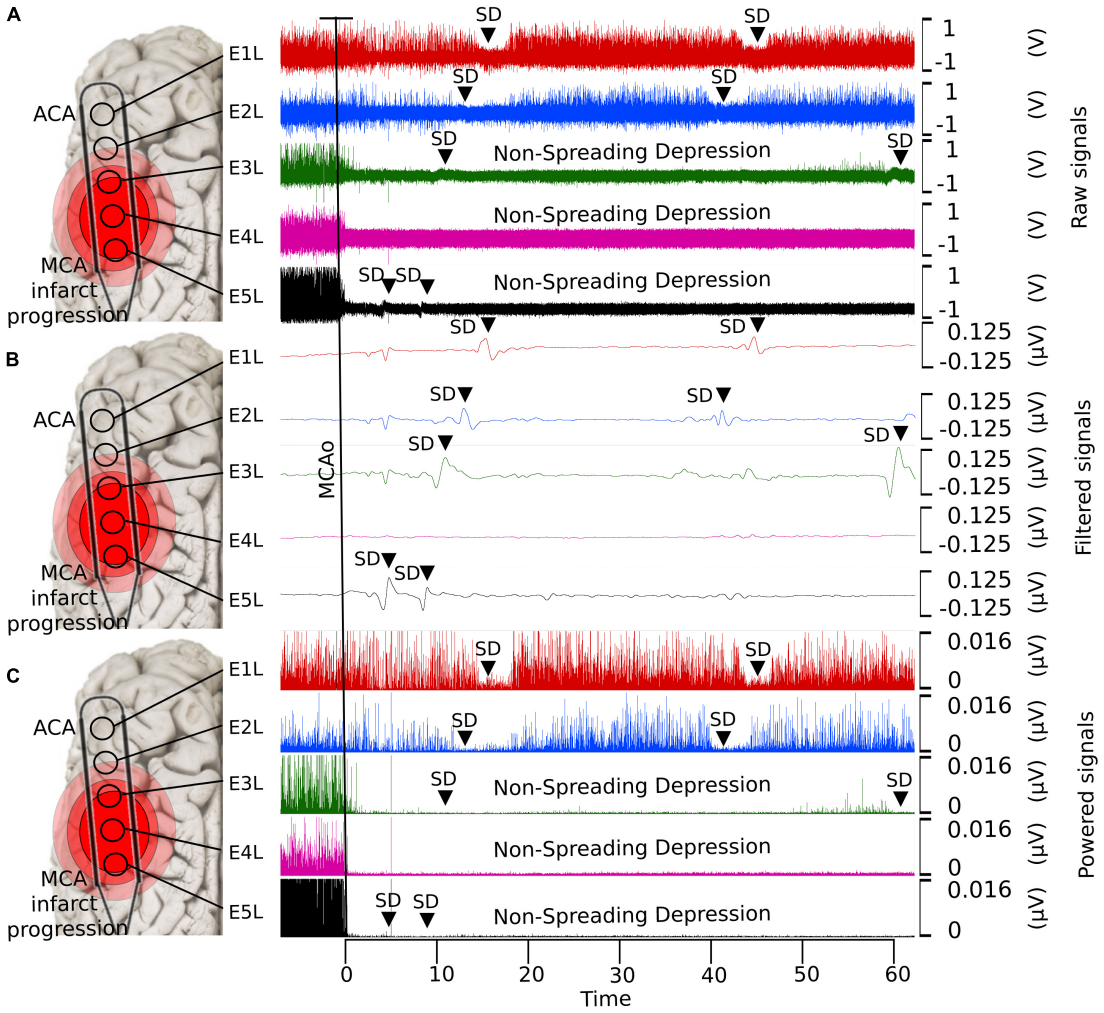

FIGURE 1
Detection of SDs using ECoG with different filters. **(A)** Raw data, **(B)** low-pass filtered, and **(C)** powered signal. With the low-pass filter, it is possible to observe the shape of the near-DC shift typic of the SDs. The non-spreading depression occurring after the MCAo is highlighted in the last two electrodes (E4L-E5L) at the raw and powered signal filters, which correspond to the site close to the MCAo. SD, spreading depolarization; ECoG, electrocorticography; DC, direct current; MCAo, middle cerebral artery occlusion.

the experiment, animals were euthanized with intravenous potassium chloride under general anesthesia.

Study design

A transorbital approach was used to present the left middle cerebral arteries (MCAs), as described previously (Schöll et al., 2017; Kentar et al., 2020). Up to four MCAs were found and occluded with aneurysm clips. For ECoG recording, extensive craniectomy and dura mater excision were performed over the temporal line of the swine to expose parts of the frontal and parietal lobes of both hemispheres. Five-contact ECoG strips were placed bilaterally on the cortex surface, corresponding to the MCA and anterior cerebral artery (ACA) territories. The distance between electrodes was 10 mm. ECoG signals from 10 electrodes were obtained: five electrodes (E1R–E5R) from the healthy right hemisphere and five electrodes from the insulted left hemisphere (E1L–E5L). E1 was located rostrally in the frontal hemisphere corresponding to the ACA territory, whereas E5 was caudal and coincided with the MCA territory. The location of the electrodes was verified by identifying the non-spreading depression of electrical activity in the caudal electrodes E4L and E5L (**Figure 1**). The durations of the ECoG recordings were planned to be 24 h; 1 h before MCAo, and 23 h after MCAo.

Frequency analysis

To study infarct progression, 5-min ECoG signal segments were obtained 5 min before MCAo, as well as 5 min and 4, 8,

and 12 after MCAo (Figure 2A). SD is presented as a negative near DC-shift (NDCS) and as a decrease in power in the ECoG bands in adjacent electrodes using an AC recorder (Dreier et al., 2017). For SD examination, 5-min signal segments before and after the NDCS of the SDs were analyzed. Moreover, the NDCS of the SDs were studied, presenting a mean duration of 51.3 s ($\sigma = \pm 14.1$ s). For reliable SD evaluation, the SDs included in the analysis had signal segments of 5 min before and after the NDCS free of artifacts and other SDs. The ECoG recording segments before, during, and after the NDCS were referred to as "preSD," "SD," and "postSD" (Figure 2B).

For signal decomposition, the discrete 512-point Fourier transform (Hanning window) was computed for each data segment and, subsequently, the power spectrum (Al-Fahoum and Al-Fraihat, 2014; Delimayanti et al., 2020). For each segment, we estimated the mean power spectrum corresponding to each frequency band: delta (0.1–4 Hz), theta (4–7 Hz), alpha (8–12 Hz), beta (13–31 Hz), and gamma (32–45 Hz). The power calculation was performed using customized MATLAB programs (MathWorks, Natick, MA) (Figure 2C). To determine infarct progression, the spectral power of the frequency bands was calculated every 4 h starting from the MCAo, with four timepoints plus the baseline obtained 5 min before the MCAo. For each pig (n = 6), the power spectrum of each frequency band was calculated for each timepoint to obtain a dataset of six elements for each timepoint. Similarly, the SDs were collected and analyzed in periods of 3 h per electrode, with eight time lapses in total. The power spectrum of each frequency band was computed for each SD phase (preSD, SD, and postSD), resulting in a dataset of eight elements for each phase. To observe the results in the right hemisphere, please see Supplementary Figure 1.

Statistical analysis

SPSS v25 (IBM, Armonk, NY) was used for statistical analysis and plots were created using GraphPad Prism 8.0.1 (GraphPad Software, San Diego, CA). Data were subjected to Shapiro–Wilk analysis to determine their distribution. The data had a non-normal distribution. Therefore, non-parametric tests were conducted, as follows:

(A) Spectral power of the frequency bands after MCAo: The Wilcoxon matched-pairs signed-rank test was applied to determine the variations over time between the spectral powers of the frequency bands. For comparison, the frequency bands gathered before MCAo were used as a reference to compare the power alterations of the frequency bands 5 min immediately after artery occlusion (0 h) and at 4, 8, and 12 h.

(B) Spectral power of the frequency bands during and after SDs: The five frequency bands within 5 min of the preSD period were used as the baseline to evaluate the power changes at SD and postSD, respectively. For the comparison between preSD and SD and between preSD and postSD, the Wilcoxon matched-pairs signed-rank test was executed.

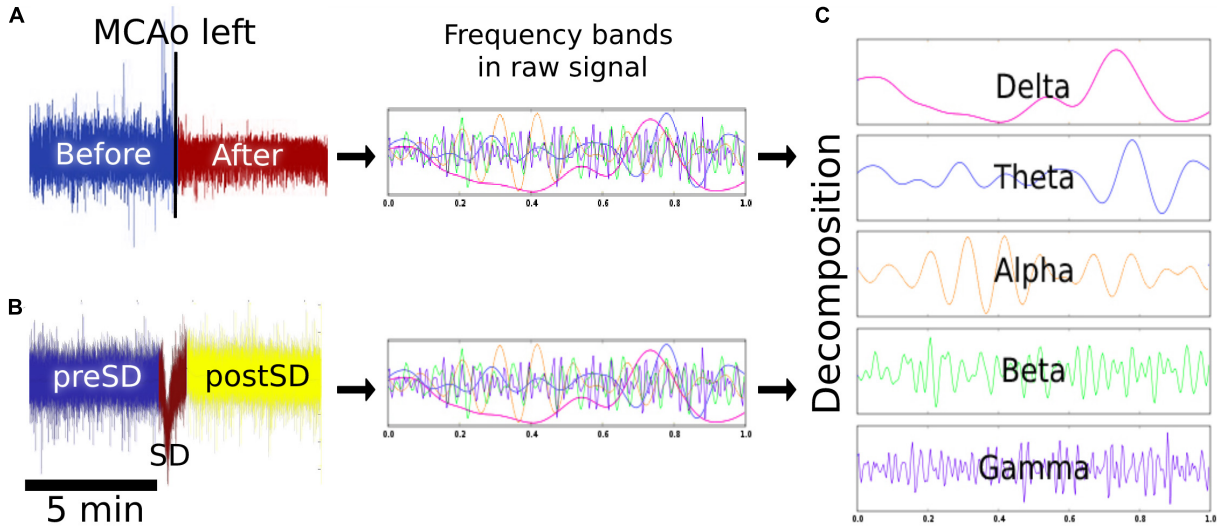

FIGURE 2
Signal analysis. **(A)** Effects of MCAo on the brain electrical activity. Five-minute epochs were obtained before, 5 min, and 4, 8, and 12 h after the left MCAo to analyze the modifications in the spectral power of each frequency band over time. **(B)** Effects of SD on the brain electrical activity. The SD signal was studied 5 min before (preSD), during (SD), and 5 min after the near DC-shift (postSD) to observe the alterations caused by the development and passage of the SDs. **(C)** Signal decomposition: the signal segments were decomposed to delta, theta, alpha, beta, and gamma bands. MCAo, middle cerebral artery occlusion; SD, spreading depolarization; DC, direct current.

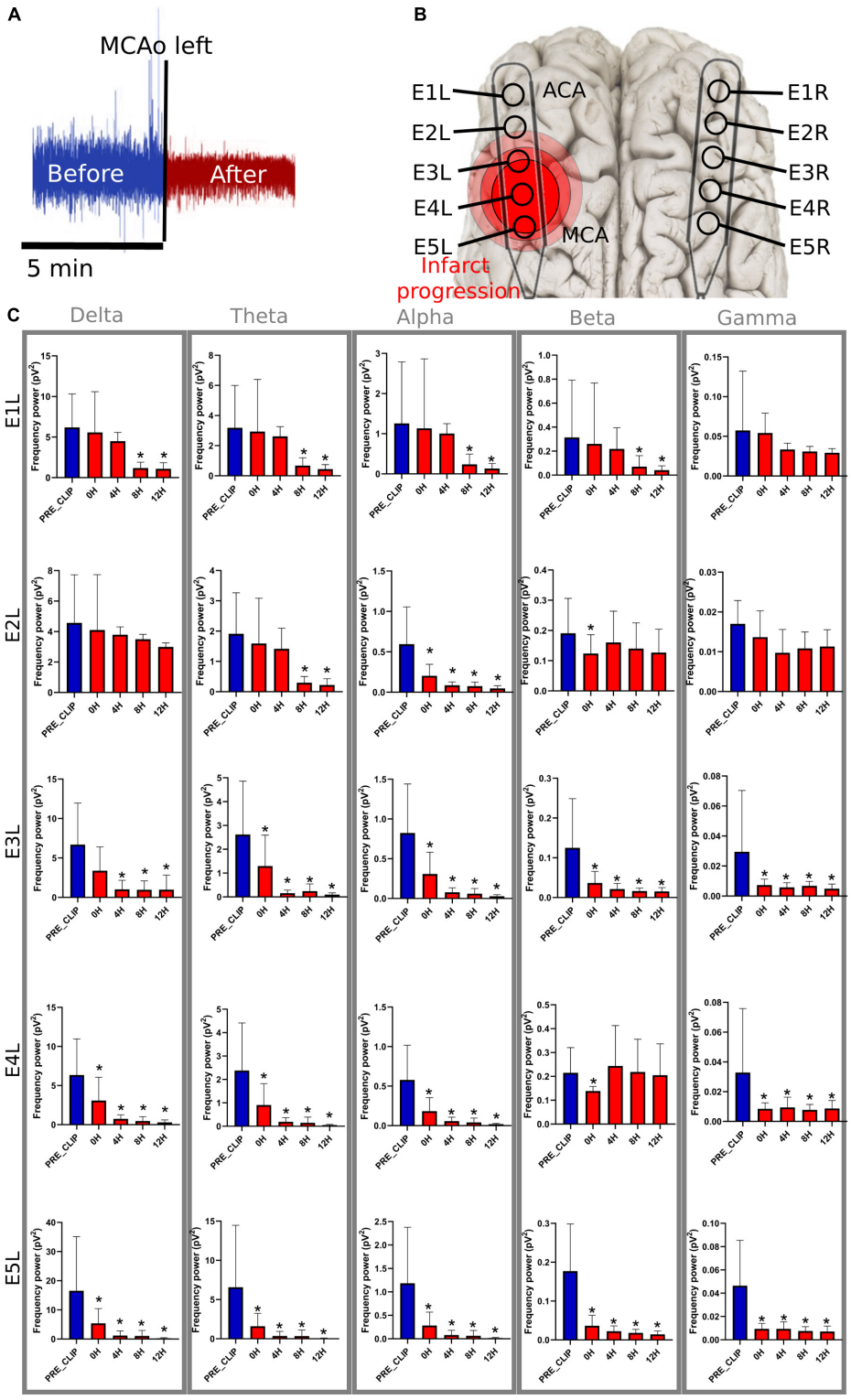

FIGURE 3
Frequency bands in the left electrodes after MCAo. **(A)** The 5-min signal segment before MCAo was used as the baseline to compare the changes in the spectral power at 0 h (5 min immediately after), 4, 8, and 12 h after MCAo. For each timepoint, 5 min of the ECoG recording were used for the analysis. **(B)** The electrodes were placed parallel over the primary frontoparietal cortex. Electrodes E1L-E5L acquired information from the left ischemic hemisphere. It is speculated that E5 was set over the cerebral cortex near the MCAo, and E1 over the ACA territory. **(C)** The significant drop in the spectral power of the frequency bands is represented as * (≤0.05). MCAo, middle cerebral artery occlusion; ECoG, electrocorticography; ACA, anterior cerebral artery; pV2, squared picovolts.

Results

Four experiments lasted 24 h, one 18 h, and one 13 h; the latter experiments were shorter due to technical problems during the ECoG recording. After MCAo, the following findings were elucidated: (1) the electrode over the frontal cortex supplied by the ACA (E1L) did not undergo changes in the frequency bands during the first 8 h, while electrodes over the parietal cortex close to the MCAo (E5L and E4L) showed a decrease in spectral power in all frequency bands immediately after MCAo, which was sustained for the rest of the recording (**Figure 3**); (2) specific anatomical and temporal patterns of power reduction were observed at different frequencies according to the location of the electrodes (**Figure 3**); (3) the peak of the highest incidence of SDs differed depending on the anatomic location of the electrodes (**Figure 4**); (4) during the SD period, all frequency bands were suppressed in both the ACA (E1L) and MCA (E2L and E3L) (**Figure 5**); (5) E2L and E3L showed impaired recovery in postSD in all the frequency bands when the penumbra was suspected, whereas the E1L preserved recovery of all frequency bands in the same period, which might be classified as an unaffected zone (**Figure 5**); and (6) the right healthy hemisphere showed no significant ECoG changes over the whole experiment (**Supplementary Figure 1**).

Spectral power of the frequency bands after middle cerebral artery occlusion

Spectral power analysis was performed for only 12 h to maximize the reliability of the results because two animals did not complete the 24 h for technical problems (mainly artifacts that altered the ECoG signal).

E1L, corresponding to the ACA territory, did not show any modifications in the spectral power of the frequency bands during the first 8 h of blood restriction. However, 8 h later, the power of the delta, theta, alpha, and beta frequencies diminished significantly, maintaining intact gamma power over time, showing a pattern of delayed damage.

E2L suffered soon after MCAo, with an alpha power drop and a temporary reduction in beta power. The theta power frequency decreased after 8 h. Delta and gamma frequencies were preserved in the electrode during the experiment. E3L, the power of all brain frequencies except delta, decreased immediately after the MCAo. Second, the delta band suffered a delayed drop after 8 h of blood flow constraints.

E4L reported a spectral power decline in all frequency bands; nevertheless, the beta band recovered 4 h later. E5L registered an initial decrease in all frequencies without recovery over time (**Supplementary Table 2** and **Figure 3**).

Incidence of spreading depolarizations after middle cerebral artery occlusion

In the left ischemic hemisphere, the SDs showed a peak incidence at the electrodes over the cortex supplied by the MCA and ACA. E1L, located over the ACA territory, recorded 99 SDs, with the highest incidence between 12 and 17 h after MCAo. Similarly, E2L displayed the highest SD incidence, recording 163 SDs and exhibiting a peak between 12 and14 h. E3L detected 120 SDs and showed a crest at 6–8 h. E4L recorded 12 SDs, registering an incidence peak at 3–8 h, whereas E5L showed 26 SDs with a peak at 3–5 h, and later signs of brain electrical depression (**Figure 4**).

Spectral power of the frequency bands during and after the spreading depolarization

To facilitate the decomposition and analysis of the SDs, only SDs with signal segments of 5 min before and after the DC shift,

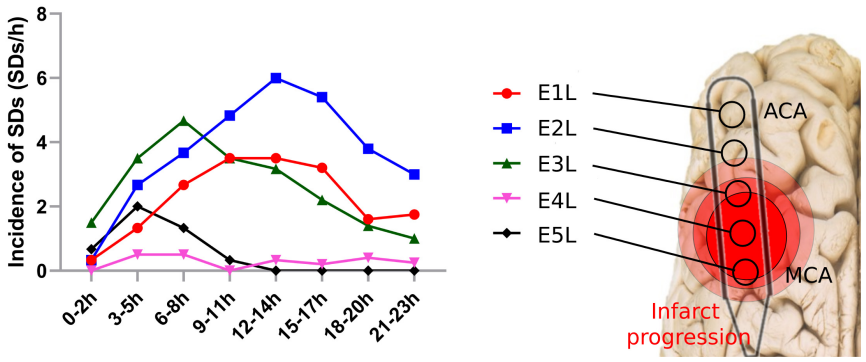

FIGURE 4
Spreading depolarization incidence after MCAo in each electrode. SDs were quantified in each electrode of the affected hemisphere after the MCAo. SD, spreading depolarization; MCAo, middle cerebral artery occlusion.

without electrographic artifacts and other SDs, were studied. There were 35, 43, and 48 SDs included in the E1L, E2L, and E3L groups, respectively. No SDs from E4L and E5L were included because of the low or null brain activity found early in the ECoG recording after MCAo (**Figure 1**).

The SD and postSD periods were compared to the preSD segment. E1L, E2L, and E3L showed a significant spectral power drop in all frequency bands during SD. Furthermore, the spectral power of all the frequency bands remained reduced in postSD only in E2L and E3L. No differences were found in the frequency bands at postSD in E1L (**Supplementary Table 3** and **Figure 5**). Thus, the brain cortex underlying E1L recovered its spectral power to basal levels shown in the preSD, but the gray matter at both E2L and E3L withheld the damage caused by SD passage.

Discussion

ECoG recordings were helpful in detecting and characterizing modifications in frequency bands caused by MCAo and SDs during the onset and evolution of cerebral infarction in gyrencephalic brains. We could discern which zones were affected by ischemia and SDs, which frequency bands were disrupted, by how much, and how they evolved over time. Thus, ECoG might be implemented as a bedside device to guide treatment approaches, such as decompressive craniectomy or neuroprotective measurements, to counter the deleterious effects of brain ischemia and avoid secondary injury.

Variations in the spectral power of frequency bands are difficult to document in patients with acute ischemic stroke because they occur seconds to minutes after occlusion, where non-invasive and invasive EEG recordings are usually not available and are not routinely used for diagnosis or treatment. Experiments in pigs overcome limitations in small laboratory animals such as rodents, as pigs allow for more space to set the electrodes, more precision in locating the anatomic sources, and their brains are more similar to the human brain (gyrencephalic), thus allowing the use of the same measurement instruments as in humans.

In contrast, the main limitations of EEG are related to the tissue barrier of the scalp, which prevents the detection of low-energy brain activity, such as frequencies higher than 100 Hz and those lower than 0.1 Hz (Rabiller et al., 2015) and low spatial resolution when detecting cerebral ischemia (Faught, 1993). In these experiments, it was possible to monitor the exact moment of infarction and its evolution across the brain cortex, recognizing the pathophysiological phases that influence the outcome of patients.

The anesthetic effect on brain activity in humans and pigs should be considered during the evaluation of the frequency bands in cerebral ischemic scenarios. The anesthetic agents had a dynamic effect on cerebral activity during the different phases of induction, maintenance, and emergence. The anesthetic drugs have specific anatomic regions of action and the frontoparietal cortex is one of their targets, the same place the electrodes were set. It was expected that the anesthetic agents such as midazolam, propofol, and isoflurane induce an unconscious state by modulating the brain activity of swine when attenuating the fast frequencies and increasing the slower ones (Akeson et al., 1993; Mäkiranta et al., 2002; Bojak et al., 2015; Mirra et al., 2022). Furthermore, isoflurane is capable to suppress SD development. Thus, the SD accounts might be decreased in all the experiments (Takagaki et al., 2014; Klass et al., 2018).

It was observed that the electrodes in the right hemisphere reported a lowering in the spectral power in all the frequency bands compared to the left electrodes but accentuated in beta and gamma bands (**Supplementary Figure 1** and **Supplementary Table 1**). Nonetheless, the baseline power spectrum of the frequency bands at the right hemisphere remained stable over time, even when the left side suffered an ischemic insult.

Three conditions might influence the basal spectral power of the frequency bands since the beginning of the experiment: (I) The anatomical differences among the hemispheres; (II) The asymmetric activity of the brain activity; (III) The heterogeneous effect of the anesthesia in the cortex.

Anatomical variations are found in the frontoparietal cortices, being the right side more extensive than the left one. As a result, the location of the electrodes is not completely symmetric between hemispheres, and the gathered signals and frequency bands might slightly vary (Toga and Thompson, 2003; Goldberg et al., 2013). Additionally, the physiological interhemispheric asymmetry in brain activity is exemplified in the left hemisphere, which exhibits a high dominance of fast frequencies in the resting state than the right one (Mahjoory et al., 2020; Mason et al., 2022). Regarding anesthesia, it has a heterogeneous and dynamic effect across the brain cortex, provoking deep alterations in the cerebral metabolic rate, the brain blood oxygenation, and the cerebral blood flow in some specific brain areas. In our experiments, the right hemisphere may be the most affected by the anesthetic agents (Ciobanu et al., 2012; Hudetz, 2012; Bojak et al., 2015; Halder et al., 2021).

Spectral power of the frequency bands after clipping the middle cerebral artery

Immediately after artery clipping, a spectral power weakening of the frequency bands at various scales was observed in some electrodes. This change is defined as a non-spreading depression of electrical activity according to nomenclature standards (Dreier et al., 2017), which we previously reported (Sánchez-Porras et al., 2022). When cerebral blood flow reaches 12 mL/100 g/min or less, infarction becomes evident because of the progressive loss of transmembrane potential gradients of neurons (Rabiller et al., 2015). In E4L and E5L over the parietal

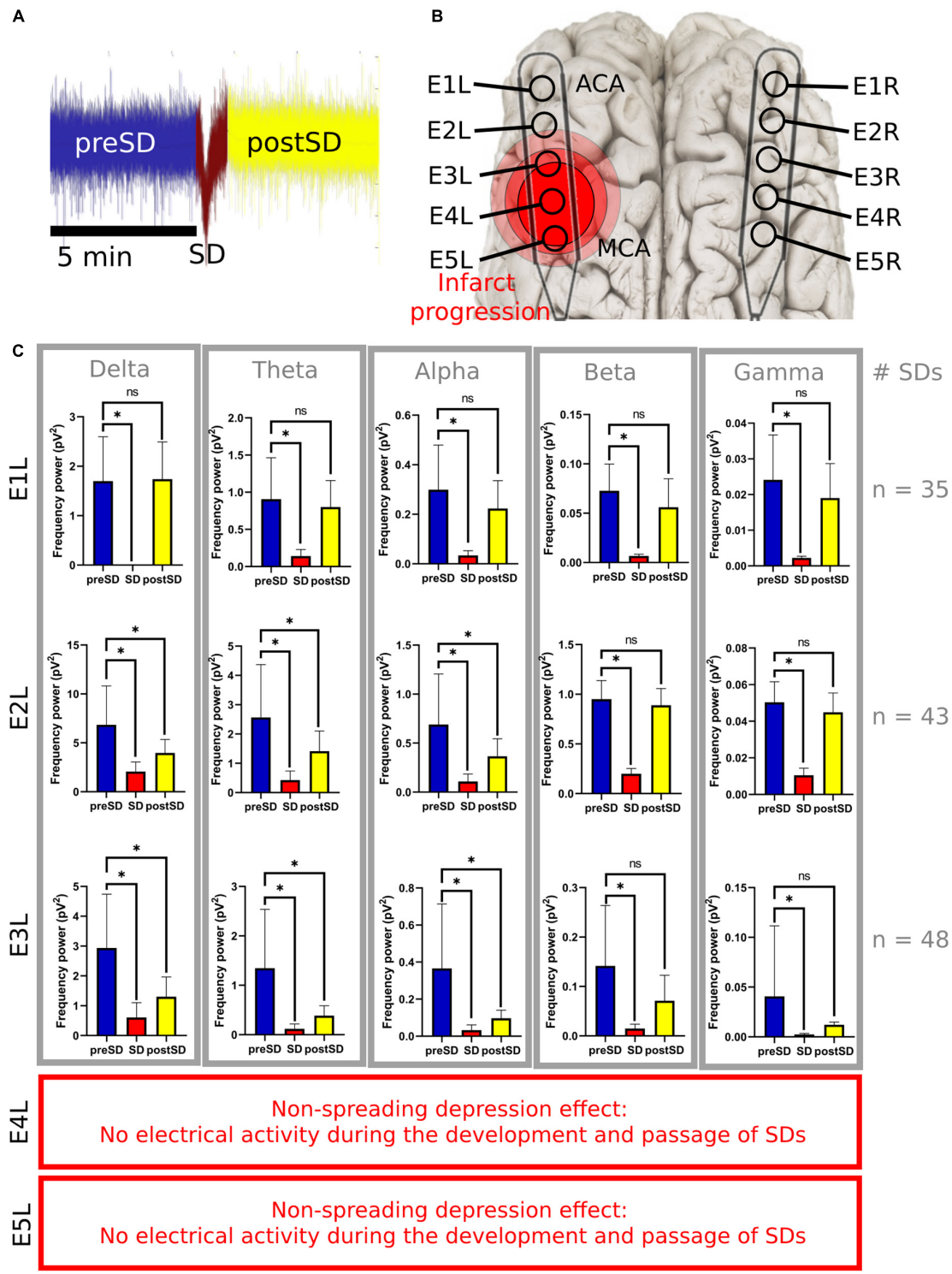

FIGURE 5
Frequency bands in the left electrodes during and after SDs. **(A)** The 5-min signal segment before the SD (preSD) was used as the baseline to compare the variations in the spectral power during (SD) and after the SD (postSD) segments. Five minutes of the ECoG recording were used to analyze postSD. Meanwhile, the mean recording time of the near DC-shift of the SD was 51.3 s ($\sigma = \pm 14.1$s). **(B)** E1L was in the ACA territory and E5L was closer to the MCA territory. **(C)** Statistical analysis of SD segments: preSD was used as the baseline to compare the variations in the spectral power at SD and postSD segments, respectively. *Statistically significant difference among SD segments ($p \leq 0.05$). E4L and E5L recorded isoelectric SDs with few or null electrical activities not relevant for the spectral power analysis of the frequency bands. SD, spreading depolarization; ECoG, electrocorticography; DC, direct current; ACA, anterior cerebral artery; MCA, middle cerebral artery; pV^2, squared picovolts.

cortex, the cerebral blood flow values surpassed this infarct threshold, showing a non-spreading depression of spontaneous brain activity in all frequency bands that lasted the whole experiment (**Figure 1**).

If cerebral blood flow is below the ischemic threshold but maintained above the infarction threshold, the effect on metabolism or cell survival is still reversible, with visible electrical activity in the delta frequency, as seen in E2L and E3L in the first 4 h after stroke. Delta band is well-recognized as prognostic markers in stroke patients (Schaul et al., 1986) and are predictive of a malignant course (Burghaus et al., 2007). Even at later stages (from 4 to 10 days), it has a negative prognostic prediction (Assenza et al., 2013). Speculative cerebral blood flow at E2L–E3L may reach levels of 20–30 mL/100 g/min, where the abnormal release of glutamate occurs (Sharbrough et al., 1973; Hossmann, 1994; Guyot et al., 2001; Gallinat et al., 2006; Rabiller et al., 2015).

Additionally, the maintenance of fast frequencies, mainly the gamma band, was present in the electrodes distant to the MCAo (E1L and E2L) and absent in those located close to vessel clipping (E4L and E5L), indicating that the presence of this frequency band might a biomarker of the integrity of the neural network. It is not clear whether beta recovery occurred in E2L and E4L. Nonetheless, we expected to find a steady decay of the beta band mainly close to the MCAo at the E4L as a resemblance to neural circuitry dysfunction found in the adjacent electrodes E1L, E3L, and E5L and other studies (Cillessen et al., 1994; Tecchio et al., 2005, 2007; Burghaus et al., 2007; Diedler et al., 2009; Moeller et al., 2011; Hertle et al., 2016). The heterogeneous infarct evolution might have an influence on the preservation of the beta band at E2L and E4L.

After the characterization of the frequency bands in each electrode, it can be inferred that E1L represents the initial normal cortex with secondary injury, E2L and E3L represent the transitional cortex or penumbra, and E4L and E5L represent the ischemic core (**Figure 3**). Further imaging and neurophysiological studies are needed to corroborate these neurophysiological findings.

Incidence of spreading depolarization

It is important to note that infarct progression is related to SD incidence. The infarct core zone was recorded by E4L and E5L, having fewer SDs, displaying the early appearance of SDs after MCAo but a premature cessation of SD development. The arrest of SD development indicates a lack of excitability in the neural network due to irreversible neuronal damage. For E1L, E2L, and E3L, the incidence of SDs was higher, with a steep peak in SD incidence at the late stages of the ECoG recording. Normal and salvageable tissue, which was recorded by E1L–E3L, would be the target for onset due to their preserved neural network and excitability. As a result, it is possible to differentiate between normal and damaged tissues based on their SD incidence. The benefit of recognizing these zones is the implementation of approaches to block SD development and test new strategies for neuroprotection.

One advantage of the swine model is that the periodicity of SD is more regular and the inter-event intervals are more prolonged in comparison to the lyssencephalic brain models, allowing a profound study of the SDs underpinning mechanisms.

Spectral power of the frequency bands during and after spreading depolarization

All frequency bands suffered significant depression during SD passage in the analyzed electrodes (E1L, E2L, and E3L). A similar phenomenon was observed in electrodes located in the tissue with the most restrictive blood supply after MCAo (E4L and E5L), confirming the ischemic effect of SD in the penumbra and normal cortical zones (Sharbrough et al., 1973; Strong et al., 2006; Dreier et al., 2009; Ayata and Lauritzen, 2015; Østergaard et al., 2015). Thus, SDs reach sites far from their origin, causing distant ischemic effects (Santos et al., 2016). Using laser speckle analysis, it has been documented that SDs can move to the ACA territory, producing secondary cerebral blood flow arrest in a matter of minutes (Kentar et al., 2020; Sánchez-Porras et al., 2022).

However, we identified three differences between E1L and both E2L and E3L. First, E1L was not affected by MCAo in the early stages of the ECoG recording. Second, E1L registered fewer SDs than E2 or E3L in the whole experiment (**Figure 4**). Finally, there was a full recovery of the spectral power of all frequency bands at E1L, while all the frequency bands remained depressed at E2 and E3L during postSD (**Figure 5**). These three statements support the SD characterization according to the anatomical regions, confirming the location of the recorded zones: E2L and E3L were located in the penumbra and E1L in normal tissue. The disrupted recovery of all frequency bands in the E2L and E3L would result in prolonged depression of electrical activity. SDs might not be compensated by tissue because of neuronal death and net malfunction in these areas caused by infarction progression and SDs. These findings coincide with the results presented in the DISCHARGE-1 study, which showed that the total SD-induced depression duration of a recording better predicts delayed infarction than other variables (Dreier et al., 2022). In our work, the high SD and prolonged depression time of the frequency bands forecast the delayed evolution of the infarction.

SDs were also detected in E4L and E5L as isoelectric SDs (**Figure 1**), where low or no electrical activity was present. Thus, spectral power analysis would not provide any additional information to the two electrodes. As expected, clusters of

agglomerated SDs were detected in the electrodes. A re-entrance phenomenon would probably help explain the high incidence of SDs in early ECoG recordings (Santos et al., 2014). Once the energy in this region is exhausted, few or no SDs appear in the ischemic core. Subsequently, a higher incidence occurred in the penumbra (E2L and E3L), reaching normal tissue in E1L.

Effect of middle cerebral artery occlusion and spreading depolarizations in further cortical zones

During the study, no modifications in the spectral power of the frequency bands were observed in the right hemisphere, either during MCAo or during SD development or passage. Nevertheless, it is impossible to discard the possibility that some of the changes seen close to the ACA territory could be observed in other brain areas.

In previous studies, researchers reported alterations in frequency bands on the contralateral side. Interestingly, the distant cortices displayed the same brain signal pattern observed in the primary cortical injury: the suppression of fast frequencies and the maintenance and magnification of slower ones (Tecchio et al., 2005, 2007; Assenza et al., 2013).

Study limitations

Our speculations about the core-penumbra map should be corroborated by studying the modifications in the cerebral blood flow and oxygen metabolism timewise with direct methods, such as single-photon emission computed tomography (SPECT), positron emission tomography (PET), magnetic resonance with contrast agents, and indirect technics like transcranial Doppler ultrasound imaging, phase-contrast MRI, and near-infrared spectroscopy (NIRS). The cytoarchitectonic changes must be assessed by histological analysis to determine the final infarct volume and verify the disposition of the core, penumbra, and healthy tissue. Finally, it is relevant to record remote brain areas to identify any distant injury caused by MCAo and SDs.

Data availability statement

The datasets presented in this study can be found in online repositories. The names of the repository/repositories and accession number(s) can be found below: Diaz Peregrino, Roberto (2022), "SD_Frequency_Power", Mendeley Data, V1, doi: 10.17632/gy8t7vwmtz.1 Diaz Peregrino, Roberto (2022), "Infarction_Progression_Frequency_Power", Mendeley Data, V1, doi: 10.17632/rz3xyynvnc.1 Diaz Peregrino, Roberto (2022), "SD_Accounts", Mendeley Data, V1, doi: 10.17632/x5k49h5x6m.1.

Ethics statement

The animal study was reviewed and approved by the Institutional Animal Care and Use Committee in Karlsruhe, Baden-Württemberg, Germany.

Author contributions

MK performed the experiments and wrote the manuscript. RD-P assisted in the experiments, performed the analysis, and wrote the manuscript. CT performed the analyses and wrote the manuscript. RS-P performed the experiments and corrected the manuscript. DS-J, FR-C, NH, LM-H, and JW corrected the manuscript and provided the scientific support. ES designed the project, performed the experiments, and wrote the manuscript. All authors contributed to the article and approved the submitted version.

Funding

This project was funded by the Deutsche Forschungsgemeinschaft (DFG, German Research Foundation; no. 462569370). RD-P was supported by a scholarship granted by the Consejo Mexiquense de Ciencia y Tecnología del Estado de México (COMECYT, Council of Science and Technology from the Estate of Mexico; reference: 2021BPS2-E0405). FR-C was supported by the Consejo Nacional de Ciencia y Tecnología of Mexico (CONACyT, National Council of Science and Technology; Reference: 2019-000021-01 ETF-00514).

Conflict of interest

The authors declare that the research was conducted in the absence of any commercial or financial relationships that could be construed as a potential conflict of interest.

Publisher's note

Supplementary material

The Supplementary Material for this article can be found online at: https://www.frontiersin.org/articles/10.3389/fnins.2022.1025967/full#supplementary-material

References

Akeson, J., Björkman, S., Messeter, K., and Rośen, I. (1993). Low-dose midazolam antagonizes cerebral metabolic stimulation by ketamine in the pig. *Acta Anaesthesiol. Scand.* 37, 525–531. doi: 10.1111/j.1399-6576.1993.tb03759.x

Al-Fahoum, A. S., and Al-Fraihat, A. A. (2014). Methods of EEG signal features extraction using linear analysis in frequency and time-frequency domains. *ISRN Neurosci.* 2014:730218.

Assenza, G., Zappasodi, F., Pasqualetti, P., Vernieri, F., and Tecchio, F. (2013). A contralesional EEG power increase mediated by interhemispheric disconnection provides negative prognosis in acute stroke. *Restor. Neurol. Neurosci.* 31, 177–188. doi: 10.3233/RNN-120244

Ayata, C., and Lauritzen, M. (2015). Spreading depression, spreading depolarizations, and the cerebral vasculature. *Physiol. Rev.* 95, 953–993.

Bojak, I., Stoyanov, Z. V., and Liley, D. T. J. (2015). Emergence of spatially heterogeneous burst suppression in a neural field model of electrocortical activity. *Front. Syst. Neurosci.* 9:18. doi: 10.3389/fnsys.2015.00018

Burghaus, L., Hilker, R., Dohmen, C., Bosche, B., Winhuisen, L., Galldiks, N., et al. (2007). Early electroencephalography in acute ischemic stroke: Prediction of a malignant course? *Clin. Neurol. Neurosurg.* 109, 45–49.

Cillessen, J. P., van Huffelen, A. C., Kappelle, L. J., Algra, A., and van Gijn, J. (1994). Electroencephalography improves the prediction of functional outcome in the acute stage of cerebral ischemia. *Stroke* 25, 1968–1972. doi: 10.1161/01.str.25.10.1968

Ciobanu, L., Reynaud, O., Uhrig, L., Jarraya, B., and Le Bihan, D. (2012). Effects of anesthetic agents on brain blood oxygenation level revealed with ultra-high field MRI. *PLoS One* 7:e32645. doi: 10.1371/journal.pone.0032645

Delimayanti, M. K., Purnama, B., Nguyen, N. G., Faisal, M. R., Mahmudah, K. R., Indriani, F., et al. (2020). Classification of brainwaves for sleep stages by high-dimensional FFT features from EEG signals. *Appl. Sci.* 10:1797.

Diedler, J., Sykora, M., Bast, T., Poli, S., Veltkamp, R., Mellado, P., et al. (2009). Quantitative EEG correlates of low cerebral perfusion in severe stroke. *Neurocrit. Care* 11, 210–216. doi: 10.1007/s12028-009-9236-6

Dreier, J. P., Fabricius, M., Ayata, C., Sakowitz, O. W., Shuttleworth, C. W., Dohmen, C., et al. (2017). Recording, analysis, and interpretation of spreading depolarizations in neurointensive care: Review and recommendations of the COSBID research group. *J. Cereb. Blood Flow Metab.* 37, 1595–1625. doi: 10.1177/0271678X16654496

Dreier, J. P., Major, S., Manning, A., Woitzik, J., Drenckhahn, C., Steinbrink, J., et al. (2009). Cortical spreading ischaemia is a novel process involved in ischaemic damage in patients with aneurysmal subarachnoid haemorrhage. *Brain* 132, 1866–1881. doi: 10.1093/brain/awp102

Dreier, J. P., Winkler, M., Major, S., Horst, V., Lublinsky, S., Kola, V., et al. (2022). Spreading depolarizations in ischaemia after subarachnoid haemorrhage, a diagnostic phase III study. *Brain* 145, 1264–1284. doi: 10.1093/brain/awab457

Faught, E. (1993). Current role of electroencephalography in cerebral ischemia. *Stroke* 24, 609–613.

Gallinat, J., Kunz, D., Senkowski, D., Kienast, T., Seifert, F., Schubert, F., et al. (2006). Hippocampal glutamate concentration predicts cerebral theta oscillations during cognitive processing. *Psychopharmacology* 187, 103–111.

Gloor, P., Ball, G., and Schaul, N. (1977). Brain lesions that produce delta waves in the EEG. *Neurology* 27, 326–333.

Goldberg, E., Roediger, D., Kucukboyaci, N. E., Carlson, C., Devinsky, O., Kuzniecky, R., et al. (2013). Hemispheric asymmetries of cortical volume in the human brain. *Cortex* 49, 200–210.

Guyot, L. L., Diaz, F. G., O'Regan, M. H., McLeod, S., Park, H., and Phillis, J. W. (2001). Real-time measurement of glutamate release from the ischemic penumbra of the rat cerebral cortex using a focal middle cerebral artery occlusion model. *Neurosci. Lett.* 299, 37–40. doi: 10.1016/s0304-3940(01)01510-5

Halder, S., Juel, B. E., Nilsena, A. S., Raghavand, L. V., and Storma, J. F. (2021). Changes in measures of consciousness during anaesthesia of one hemisphere Wada test). *Neuroimage* 226:117566. doi: 10.1016/j.neuroimage.2020.117566

Hartings, J. A., Bullock, M. R., Okonkwo, D. O., Murray, L. S., Murray, G. D., Fabricius, M., et al. (2011). Spreading depolarisations and outcome after traumatic brain injury: A prospective observational study. *Lancet Neurol.* 10, 1058–1064.

Hertle, D. N., Heer, M., Santos, E., Schöll, M., Kowoll, C. M., Dohmen, C., et al. (2016). Changes in electrocorticographic beta frequency components precede spreading depolarization in patients with acute brain injury. *Clin. Neurophysiol.* 127, 2661–2667. doi: 10.1016/j.clinph.2016.04.026

Hossmann, K. A. (1994). Viability thresholds and the penumbra of focal ischemia. *Ann. Neurol.* 36, 557–565.

Hudetz, A. G. (2012). General anesthesia and human brain connectivity. *Brain Connect.* 2, 291–302.

Kentar, M., Mann, M., Sahm, F., Olivares-Rivera, A., Sanchez-Porras, R., Zerelles, R., et al. (2020). Detection of spreading depolarizations in a middle cerebral artery occlusion model in swine. *Acta Neurochir.* 162, 581–592. doi: 10.1007/s00701-019-04132-8

Klass, A., Sánchez-Porras, R., and Santos, E. (2018). Systematic review of the pharmacological agents that have been tested against spreading depolarizations. *J. Cereb. Blood Flow Metab.* 38, 1149–1179. doi: 10.1177/0271678X18771440

Mahjoory, K., Schoffelen, J. M., Keitel, A., and Gross, J. (2020). The frequency gradient of human resting-state brain oscillations follows cortical hierarchies. *Elife* 9:e53715. doi: 10.7554/eLife.53715

Mäkiranta, M. J., Jauhiainen, J. P., Oikarinen, J. T., Suominen, K., Tervonen, O., Alahuhta, S., et al. (2002). Functional magnetic resonance imaging of swine brain during change in thiopental anesthesia into EEG burst-suppression level–a preliminary study. *MAGMA* 15, 27–35. doi: 10.1007/BF02693841

Mason, L. M., Barry, R. J., and Clarke, A. R. (2022). Age-related changes in the EEG in an eyes-open condition: I. Normal development *Int. J. Psychophysiol.* 172, 40–45. doi: 10.1016/j.ijpsycho.2021.11.005

Mirra, A., Spadavecchia, C., and Levionnois, O. (2022). Correlation of Sedline-generated variables and clinical signs with anaesthetic depth in experimental pigs receiving propofol. *PLoS One* 17:e0275484. doi: 10.1371/journal.pone.0275484

Moeller, J. J., Tu, B., and Bazil, C. W. (2011). Quantitative and qualitative analysis of ambulatory electroencephalography during mild traumatic brain injury. *Arch. Neurol.* 68, 1595–1598. doi: 10.1001/archneurol.2011.1080

Nagata, K., Tagawa, K., Hiroi, S., Shishido, F., and Uemura, K. (1989). Electroencephalographic correlates of blood flow and oxygen metabolism provided by positron emission tomography in patients with cerebral infarction. *Electroencephalogr. Clin. Neurophysiol.* 72, 16–30. doi: 10.1016/0013-4694(89)90027-8

Østergaard, L., Dreier, J. P., Hadjikhani, N., Jespersen, S. N., Dirnagl, U., and Dalkara, T. (2015). Neurovascular coupling during cortical spreading depolarization and -depression. *Stroke* 46, 1392–1401. doi: 10.1177/0271678X15617954

Rabiller, G., He, J.-W., Nishijima, Y., Wong, A., and Liu, J. (2015). Perturbation of brain oscillations after ischemic stroke: A potential biomarker for post-stroke function and therapy. *Int. J. Mol. Sci.* 16, 25605–25640. doi: 10.3390/ijms161025605

Sánchez-Porras, R., Kentar, M., Zerelles, R., Geyer, M., Trenado, C., Hartings, J. A., et al. (2022). Eighteen-hour inhibitory effect of s-ketamine on potassium- and ischemia-induced spreading depolarizations in the gyrencephalic swine brain. *Neuropharmacology* 216:109176. doi: 10.1016/j.neuropharm.2022.109176

Santos, E., León, F., Silos, H., Sanchez-Porras, R., Shuttleworth, C. W., Unterberg, A., et al. (2016). Incidence, hemodynamic, and electrical characteristics of spreading depolarization in a swine model are affected by local but not by intravenous application of magnesium. *J. Cereb. Blood Flow Metab.* 36, 2051–2057. doi: 10.1177/0271678X16671317

Santos, E., Sánchez-Porras, R., Sakowitz, O. W., Dreier, J. P., and Dahlem, M. A. (2017). Heterogeneous propagation of spreading depolarizations in the lissencephalic and gyrencephalic brain. *J. Cereb. Blood Flow Metab.* 37, 2639–2643.

Santos, E., Schöll, M., Sánchez-Porras, R., Dahlem, M. A., Silos, H., Unterberg, A., et al. (2014). Radial, spiral and reverberating waves of spreading depolarization occur in the gyrencephalic brain. *Neuroimage* 99, 244–255. doi: 10.1016/j.neuroimage.2014.05.021

Schaul, N., Green, L., Peyster, R., and Gotman, J. (1986). Structural determinants of electroencephalographic findings in acute hemispheric lesions. *Ann. Neurol.* 20, 703–711. doi: 10.1002/ana.410200609

Schöll, M. J., Santos, E., Sanchez-Porras, R., Kentar, M., Gramer, M., Silos, H., et al. (2017). Large field-of-view movement-compensated intrinsic optical signal imaging for the characterization of the haemodynamic response to spreading depolarizations in large gyrencephalic brains. *J. Cereb. Blood Flow Metab.* 37, 1706–1719. doi: 10.1177/0271678X16668988

Sharbrough, F. W., Messick, J. M. Jr., and Sundt, T. M. Jr. (1973). Correlation of continuous electroencephalograms with cerebral blood flow measurements during carotid endarterectomy. *Stroke* 4, 674–683.

Strong, A. J., Anderson, P. J., Watts, H. R., Virley, D. J., Lloyd, A., Irving, E. A., et al. (2006). Peri-infarct depolarizations lead to loss of perfusion in ischaemic gyrencephalic cerebral cortex. *Brain* 130, 995–1008. doi: 10.1093/brain/awl392

Takagaki, M., Feuerstein, D., Kumagai, T., Gramer, M., Yoshimine, T., and Graf, R. (2014). Isoflurane suppresses cortical spreading depolarizations compared to propofol – Implications for sedation of neurocritical care patients. *Exp. Neurol.* 252, 12–17. doi: 10.1016/j.expneurol.2013.11.003

Tecchio, F., Pasqualetti, P., Zappasodi, F., Tombini, M., Lupoi, D., Vernieri, F., et al. (2007). Outcome prediction in acute monohemispheric stroke *via* magnetoencephalography. *J. Neurol.* 254, 296–305. doi: 10.1007/s00415-006-0355-0

Tecchio, F., Zappasodi, F., Pasqualetti, P., Tombini, M., Salustri, C., Oliviero, A., et al. (2005). Rhythmic brain activity at rest from rolandic areas in acute mono-hemispheric stroke: A magnetoencephalographic study. *Neuroimage* 28, 72–83. doi: 10.1016/j.neuroimage.2005.05.051

Toga, A. W., and Thompson, P. M. (2003). Mapping brain asymmetry. *Nat. Rev. Neurosci.* 4, 37–48. doi: 10.1038/nrn1009

frontiers | Frontiers in Neuroimaging

TYPE Case Report
PUBLISHED 04 January 2023
DOI 10.3389/fnimg.2022.1034241

OPEN ACCESS

EDITED BY
Nico Sollmann,
University of California, San Francisco, United States

REVIEWED BY
Xiangchuang Kong,
Huazhong University of Science and Technology, China
Dahua Yu,
Inner Mongolia University of Science and Technology, China

*CORRESPONDENCE
Lucia Monti
lucia.monti@unisi.it

SPECIALTY SECTION
This article was submitted to Brain Imaging Methods, a section of the journal Frontiers in Neuroimaging

RECEIVED 01 September 2022
ACCEPTED 07 November 2022
PUBLISHED 04 January 2023

CITATION
Alberti M, Ginanneschi F, Rossi A and Monti L (2023) Case report: A quantitative and qualitative diffusion tensor imaging (DTI) study in varicella zoster-related brachial plexopathy. *Front. Neuroimaging* 1:1034241. doi: 10.3389/fnimg.2022.1034241

Case report: A quantitative and qualitative diffusion tensor imaging (DTI) study in varicella zoster-related brachial plexopathy

Manfredi Alberti[1,2], Federica Ginanneschi[1,2], Alessandro Rossi[1,2] and Lucia Monti[3]*

[1]Neurology Unit, Department of Neurology and Human Movement Sciences, University Hospital of Siena, Siena, Italy, [2]Department of Medical, Surgical and Neurological Science, University of Siena, Siena, Italy, [3]Diagnostic and Functional Neuroimaging Unit, Department of Neurology and Human Movement Sciences, University Hospital of Siena, Siena, Italy

Diffusion tensor imaging (DTI) is considered feasible for the nerve plexuses' imaging and quantitative evaluation but its value in the clinical practice is still virtually unexplored. We present the DTI profile of a case of acute varicella-zoster virus (VZV)-related brachial plexopathy. A 72-year-old woman presented with left upper-limb segmental paresis involving the spinal metamers C6–C7, preceded by a painful dermatomal vesicular eruption in C5-T1 dermatomes. Clinical and electrophysiological findings and magnetic resonance imaging indicated a plexus involvement. DTI analysis showed decreased fractional anisotropy (FA) and an increase of all the other diffusivity indexes, i.e., mean, axial, and radial diffusivity. The mechanisms underlying DTI parameter differences between healthy and pathologic brachial plexus sides could be related to microstructural fiber damage. Water diffusion is affected within the nerve roots by increasing the diffusion distance, leading to increased diffusion perpendicular to the largest eigenvalue and therefore to decreased FA values The role of DTI in clinical practice has not been defined yet. Additional quantitative and qualitative DTI information could improve the assessment and follow-up of brachial plexopathy.

KEYWORDS

diffusion tensor imaging (DTI), varicella-zoster virus (VZV), brachial plexus, electromyography, fractional anisotropy (FA)

Introduction

Although diffusion tensor imaging (DTI) has been widely applied to the study of the brain microstructure, its usefulness for peripheral nervous system pathology is a more recent acquisition (Hodel et al., 2011, 2022; Chhabra et al., 2013; Wade et al., 2020a,b). DTI is based on the principle that water molecules tend to diffuse more freely along the direction of axonal fascicles rather than across them. Such directional dependence of diffusivity is termed anisotropy.

DTI metrics, including fractional anisotropy (FA) and estimates of diffusivity, are sensitive to the microstructure of peripheral nerves and may provide a quantitative evaluation. In addition, DTI may offer qualitative features displayed as 3D tractography (Tagliafico et al., 2011; Chhabra et al., 2013; Gasparotti et al., 2013; Wade et al., 2020a, 2021; Fajar et al., 2022). The parameters derived from DTI are an expression of water diffusion characteristics through biological barriers and are referred to as FA, mean diffusivity (MD), axial diffusivity (AD), and radial diffusivity (RD) (Lope-Piedrafita, 2018; Fajar et al., 2022; Ranzenberger and Snyder, 2022). FA measures the degree of anisotropy of water molecules. FA depends upon the diffusion of the water molecules along a single axis (i.e., bidirectional diffusion along the length of the nerve).

AD refers to the magnitude of diffusion parallel to fiber tracts; it depends on the first eigenvalue (l1) and thus describes diffusion along the principal movement direction (Fajar et al., 2022; Ranzenberger and Snyder, 2022). AD is influenced by axonal count, caliber, and direction continuity, whereas it is not influenced by myelin integrity. Axial diffusivity is a quantification of the axonal integrity, and lower AD may reflect axonal injury, reduced axonal caliber, or less coherent axonal orientation (Ranzenberger and Snyder, 2022).

RD refers to the magnitude of diffusion perpendicular to fiber tracts and may be sensitive to myelin damage. Higher RD may reflect myelin loss or glial cell damage, reduced axonal integrity, and/or packing density. RD is the apparent water diffusion coefficient in the direction perpendicular to the axonal fibers. An increase in RD is correlated with an increased perpendicular diffusion of water molecules. This is not only correlated to tract demyelination but also to decreased axonal count and nerve degeneration due to the fact that damage to physical barriers favors an isotropic movement of the extracellular fluids (Ranzenberger and Snyder, 2022).

MD describes the average motion of water molecules, obtained from the average of the three eigenvectors (l1, l2, l3). In pathological conditions, MD should increase due to the damage of biological barriers such as myelin and cell membranes. MD is a sensitive marker of reduced white matter microstructural integrity due to either axonal or myelin damage occurring in neurological conditions such as developmental and degenerative disorders.

In the last decade, anatomical studies (Wade et al., 2020a) showed that DTI has been dedicated to pathological conditions such as traumatic, neoplastic, or inflammatory events. It has been shown that DTI may demonstrate normal tracts, tract displacement, deformation, infiltration, disruption, and disorganization of fibers due to lesions localized within or along the brachial plexus (Heckel et al., 2015; Vavasour et al., 2019; Wade et al., 2020b).

The brachial plexus has a very complex geometry which requires a 3D tractography to be analyzed. Furthermore, to differentiate brachial plexus pathologies, a 3D tractography with different angular and anisotropy thresholds for each cervical root needs to be studied (Wade et al., 2020b, 2021).

We describe the DTI profile of a case of acute varicella-zoster virus (VZV)-related brachial plexopathy.

Case description

We report the case of a 72-year-old woman who presented with pain along the whole left upper limb. Two days later, a typical group of herpetiform vesicles on an erythematous base appeared at the level of C6 and C7 dermatomes. Within the first week, a segmental paresis of the left arm with hyperalgesia, allodynia, edema, and both color and skin-temperature changes in the left hand developed. The paresis involved the muscles innervated by C6 and C7 roots. In these muscles, there was no increase in the duration or amplitude of motor unit potentials. The lack of reinnervation of the motor units suggests that the brachial plexopathy (namely, the neurogenic muscle damage) was unequivocally recent. Anti-VZV IgM and IgG antibodies were found in the serum.

Electromyography (EMG) revealed positive sharp waves/fibrillation potentials with markedly reduced motor unit recruitment in the left extensor muscles of the wrist and the fingers, the brachioradialis, the triceps brachii, and the flexor carpi radialis. Acute denervation was absent in the muscles corresponding to the spinal metamers C5 and T1.

Based on clinical and laboratory data, a diagnosis of monoparesis of the left arm due to VZV-related brachial plexopathy was made.

Diagnostic assessment

Imaging acquisition

The diffusion images were acquired on a Siemens Aera 1.5T MRI scanner using a 2D echo-planar imaging (EPI) diffusion sequence of [ep2d_diff_tensor_64_gap0], an echo time of (TE) = 81 ms, and a repetition time of (TR) = 7,100 ms. A DTI diffusion protocol was used, and a total of 64 diffusion sampling directions were acquired. The b-value was 1,000 s/mm^2. The in-plane resolution was 2.45 mm and the slice thickness was 2.5 mm. The restricted diffusion was quantified using restricted diffusion imaging (Yeh et al., 2017). Diffusion data were reconstructed using generalized q-sampling imaging (Yeh et al., 2010) with a diffusion sampling length ratio of 1.25. The tensor metrics were calculated using DWI with a b-value lower than 1,750 s/mm^2. A deterministic fiber tracking algorithm (Yeh et al., 2013) was used. The STIR sequence was acquired in the coronal plane (TR = 3,530 ms; TE = 56 ms; inversion time [IT] = 170 ms; flip angle = 150 degrees; slice thickness = 3 mm). MR examination was performed without intravenous administration

of a contrast medium in view of the lack of sufficient information on the kidney function of the patient.

Data sampling

An intraindividual study was performed, and the comparison was made between the healthy (right) and the pathological (left) side. The healthy side was considered as the reference standard for morphological and quantitative comparative study. The right and left sides were studied and measured with the same methodology using ROI size, symmetric (left, right) ROI position, FA range, and angular thresholds. Several FA, AD, RD, and MD measures were obtained for each ROI positioned on the nerve roots, as described in the following paragraphs.

DTI quantitative and qualitative analyses

Quantitative and qualitative analyses were performed by using DSI studio (https://dsi-studio.labsolver.org/) on both sides (left and right) of the pathological levels, C6 and C7 roots.

To improve the diagnostic accuracy of the FA, MD, AD, and RD values, multiple measures were acquired on each involved root. Qualitative and quantitative analyses were performed using 4 different steps: (a) placing bilateral and symmetrical ROI in the proximal, medium, and distal tracts of nerve roots visualized on axial and coronal STIR images; (b) setting FA threshold values for tractogram reconstruction; c) 3D-DTI tractograms of C6 and C7 roots were obtained with different threshold values, and d) collecting the acquired diffusion parameters. Anisotropy thresholds, angular thresholds, and the minimum lengths of selected fibers were measured by considering the following values and criteria: 0.077, 0.088, 0.099, and 0.11 as anisotropy thresholds; 50, 60, and 70° as angular thresholds; and fiber tracts with lengths shorter than 15, 25, 35, and 40 mm. FA, MD, RD, and AD values were obtained along 36 different 3D-tractograms.

Statistical analysis

The results of scaled variables are represented by the mean ± SE or SD and compared using independent samples. After verifying that the datasets fit a "not normal" distribution (Agostino-Pearson's test), DTI differences between the healthy and pathological sides were evaluated by the non-parametric Mann-Whitney's *U*-test (MWUt). Significance was set at the 5% level. The dataset was calculated on the basis of tract length series (minimum length discard criteria of 35 mm) for each anisotropy and angular threshold, respectively, 0.077, 0.088, 0.099, and 0.11 and 50, 60, and 70°. Therefore, with three series based on tract length, anisotropy, and angular thresholds, 36 measures were obtained on each nerve root for a total of 144 measurements.

Results

We report on the quantitative analysis performed on both sides (left and right) of the pathological levels (C6 and C7 roots)

Comparing the DTI values (FA, MD, AD, RD) of the C6 and C7 roots between the left and right brachial plexus, significant differences were demonstrated for FA (p-value < 0.0001, MWUt $= 792$), RD (p-value < 0.0001, MWUt $= 1{,}286$), AD (p-value < 0.0033, MWUt $= 1{,}861$), and MD (MWUt $= 1{,}563$ $p < 0.0001$) (Figure 1). Because RD and AD showed no normal distribution, a non-parametric two-tailed test was used.

Comparing the DTI values between the right and left sides for each nerve root, significant differences were demonstrated for the C6 root FA (p-value < 0.0001), C7 root FA (p-value < 0.0001), C6 root MD (p-value $= 0.0161$), C7 root MD (p-value < 0.0001), C6 root AD (p-value $= 0.0423$), C7 root AD (p-value < 0.0001), C6 root RD (p-value $= 0.0161$), and C7 root RD (p-value < 0.0001).

No statistically significant difference was demonstrated when assessing AD values between C6 and C7 roots of the same side. By contrast, C6 and C7 roots showed significant differences for the other DTI parameters such as FA, MD, and RD (p-value < 0.0001).

Qualitative results are the 3D-DTI tractograms of the C6 and C7 roots. The C6 and C7 roots are shown with a different color score corresponding to different FA values obtaining parametric images in Figure 2. A complete background suppression was obtained.

Discussion

In the current study, we presented the DTI characterization of a case of VZV-related brachial plexopathy, complicated by segmental paresis involving spinal metamers C6–C7.

In recent times, DTI has gained attention due to its unmatched ability to generate maps of neural pathways (qualitative approach) and provide objective proxy measures of nerve integrity (quantitative approach) (Righini et al., 2005; Wade et al., 2020a). DTI can differentiate healthy from acute and chronic neuropathy, but the complex geometry of the brachial plexus may be assessed only by considering anatomical notions such as fiber orientation within each emerging nerve, as well as data acquisition and pre- and post-processing approaches (Herweh et al., 2007; Hodel et al., 2011, 2022; Crim and Ingalls, 2017; Wade et al., 2020b; van Rosmalen et al., 2021). Indeed, the principal eigenvector of the tensor might not represent the actual fiber orientation(s) and therefore it might generate both qualitative and quantitative errors anywhere along the fiber path (Chung et al., 2013; van Rosmalen et al., 2021).

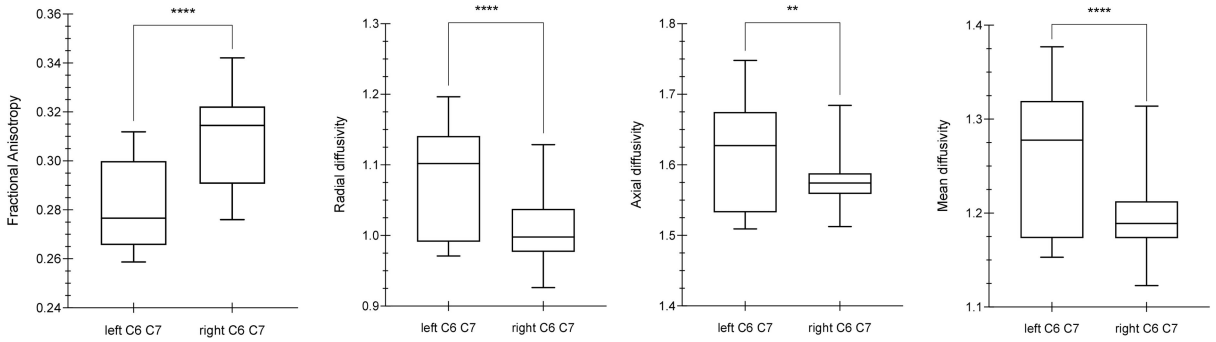

FIGURE 1
Differences between diffusion parameters in the left and right C6–C7 roots. By using the Mann Whitney U-test (MWUt), significant statistical differences were demonstrated in FA (p-value < 0.0001, MWUt = 792), RD (p-value < 0.0001, MWUt = 1,286), AD (p-value < 0.0033, MWUt = 1,861), and MD (p < 0.0001, MWUt = 1,563). The p-value lower for AD than RD suggests a minor axonal damage in comparison with dysmyelination process. **, ****indicate *p*-values significant.

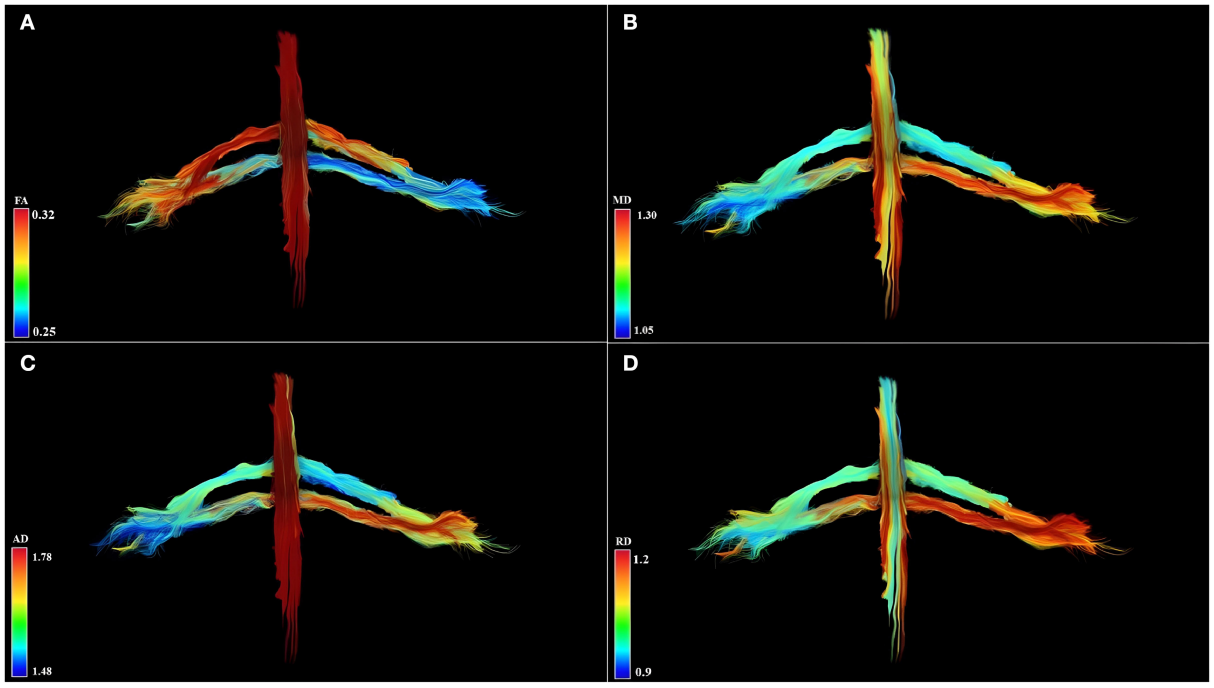

FIGURE 2
Diffusion tensor imaging tractography of the cervical cord and C6 and C7 brachial roots in three-dimensional view and parametric color maps **(A–D)**. **(A)** The color of the tract is determined by the local FA, where red denotes a high FA (0.32), scaled to yellow, green, and blue denote low FA (for rater 0.25). **(B)** The color of the tract is determined by the local MD, where red denotes a high MD (1.30), scaled to yellow, green, and blue denote low MD (for rater 1.05). **(C)** The color of the tract is determined by the local AD, where red denotes a high AD (1.78), scaled to yellow, green, and blue denote low AD (for rater 1.48). **(D)** The color of the tract is determined by the local RD, where red denotes a high RD (1.2), scaled to yellow, green, and blue denote low RD (for rater 0.9). Geometric distribution of water diffusion parameters suggests myelin damage of left C7 root, demonstrated by reduction of FA, increase of MD, AD, and RD. Left C6 root shows reduced FA values and increased MD, AD, and RD values in distal root section, suggesting a partial compromission of the nervous tissues.

Quantitative approach

For both central and peripheral nervous system conditions, demyelination and/or axonal injury may determine an FA decrease. For example, in chronic inflammatory demyelinating polyradiculoneuropathy and in brachial plexus injuries (Wade et al., 2020b, 2021; Su et al., 2021), the bundles of plexus nerve fibers and their branches showed lower FA. In the

present case report about acute VZV-related plexopathy, a significant decrease in the FA of the brachial plexus trunks with a concomitant increase of MD, AD, and RD was demonstrated (Herweh et al., 2007; Xie et al., 2010; Meng et al., 2021; Su et al., 2021). FA decrease may be explained through knowledge of the pathophysiology of the VZV infection. In brachial VZV plexitis, virus particles infect sensory and sympathetic ganglion neurons, and considering the relationship between the ranges of impaired motor functions and the distribution of skin lesions related to this herpes virus, it is a predominant opinion that the development of segmental paresis is caused by the direct or indirect spread of VZV from the dorsal root ganglion to the spinal anterior horn cells, the anterior root, and the spinal nerves, which consequently induce motor nerve damage and functional changes (Meng et al., 2021).

Previous reports showed that patients with VZV infections have extensive lymphocytic and plasma cell infiltration in both the nerves and the ganglia (Guldberg-Moller et al., 1959; Esiri and Tomlinson, 1972). This cellular invasion is presumably prevalent in motor roots and the dorsal root ganglion, where the blood-nerve barrier is anatomically less efficient and circulating cellular and humoral immune components have easy access to these structures (Hodel et al., 2011). As a result, during the acute phase of the infection, a significant increase in edema and initial cellularity infiltration among the nerve fibers would determine an obstacle to the molecular motion, causing an anisotropy decrease (Kimura-Ohba et al., 2016). In line with this hypothesis, we observed a reduction of FA and an increase in all the other indexes of molecular displacement by diffusion. In particular, the reduced FA and the increased MD, RD, and AD values suggest the presence of fiber demyelination and axonal damage, caused by extensive axonal swelling, and an altered nerve-blood barrier due to a marked inflammatory process (Xie et al., 2010; Kimura-Ohba et al., 2016; Wade et al., 2020b, 2021; van Rosmalen et al., 2021).

The quantitative analysis performed by evaluating different FA thresholds, nerve tract lengths, and degrees of fiber direction supported the corresponding microstructural damage.

Indeed, all obtained DTI values were significantly different between healthy and pathological sides and this was consistent with clinical and electrophysiological findings. In particular, the left C7 dermatome was clinically more involved than the left C6 and these findings corresponded to DTI values, independent of post-processing thresholds. When the left C6 root (pathological side) was compared with the right C6 root (healthy side), statistical significance for the AD values was lower (p^*) than that for the MD, RD, and FA values (p^{****}) (Song et al., 2002; Wade et al., 2020b, 2021; van Rosmalen et al., 2021). AD may be related to axonal integrity. Detailed analysis of directional diffusivities (i.e., RD vs. AD) may suggest the presence of specific and prevalent pathological patterns such as demyelination and/or axonal damage. It is possible to assume that there is a smaller axonal involvement in the left C6 root than in the other pathologic root (i.e., left C7). Our findings indicate that DTI analysis has the potential to represent a pathological process in that timeframe and to detect what type of damage is prevalent.

The methodological choice to analyze different FA and degree thresholds and a selected length of fiber is crucial to reduce the errors in the quantitative approach.

In addition, our DTI analysis seems to discriminate anisotropy changes between the C6 and C7 roots on the healthy side. Indeed, FA, MD, and RD showed a significant difference when the values of the C6 and C7 roots on the right side were compared. FA, MD, and RD values of the right C7 root were higher than the right C6 root, and this could be explained by a different myelination process, although there are not exhaustive literature data in support of this hypothesis. Some authors reported that "the roots of the brachial plexus have a variable axon density, specifically 6,750 per mm^2 in C5, 8,448 per mm^2 in C6, 8,665 per mm^2 in C7, 5,708 per mm^2 in C8, and ~10,000 per mm^2 in T1"

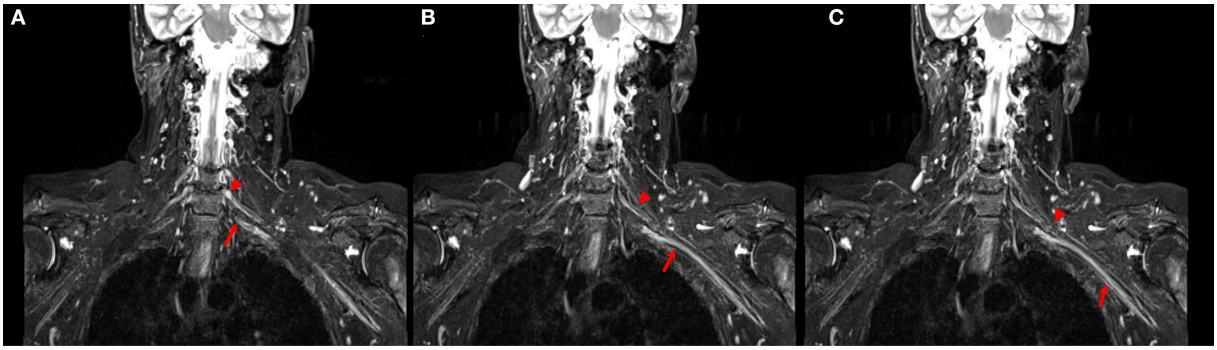

FIGURE 3
(A–C) Coronal STIR images of the brachial plexus. Different size and signal intensity are shown between the right and the left side of C6 (arrow head) and C7 (arrow) roots in proximal **(A, B)** and distal **(C)** tracts.

(Won et al., 2012; Gesslbauer et al., 2017; Wade et al., 2020a, 2021; van Rosmalen et al., 2021) and these data can explain the absence of a statistical significance of the AD values between the right C6 root and the C7 root. The difference (8,448 per mm^2 in C6 vs. 8,665 per mm^2 in C7) is not so high as that for the other roots of the brachial plexus.

Some studies (Wade et al., 2020a, 2021) demonstrated that there are physiological differences in DTI parameters between the right and left plexus in healthy subjects, when all brachial plexus roots in all subjects, are considered. By contrast, in the single subject, no differences were demonstrated between C6 and C7 roots on both sides.

Qualitative approach

There is a need for a 3D structure generating technique to display the anatomical characteristics of the brachial plexus. Indeed, the brachial plexus cannot be adequately represented on 2D images and standard structural MRI acquisitions are spoiled by other anatomical structures such as vascular trunks. DTI demonstrates the true geometry of the roots through 3D tractography of the brachial plexus without vascular signal contamination. The 3D-DTI tractography is the result of a multistep process, is a time-consuming procedure, and could be invalidated by the choice of type of acquisition, pre- and post-processing, due to the complexity and variants of the brachial plexus anatomy (Aung et al., 2013; Chung et al., 2013; Yeh et al., 2013; Kimura-Ohba et al., 2016; Wade et al., 2020b). Moreover, the fiber pathway reconstruction may be impaired by crossing, diverging/converging, twisting, or kinked fibers and this is a common DTI limitation for both brain and brachial plexus structural reconstruction. However, with the optimization and standardization of DTI acquisition, pre- and post-processing experts can obtain 3D modeling of the brachial plexus complex course and represent the true geometry of the roots (Figure 2).

DTI has been mostly used in experimental settings, with few indications for clinical practice. Our study may contribute to identifying brachial plexopathy through DTI.

Evaluation of brachial plexus abnormalities represents a diagnostic challenge due to anatomical complexity and due to the overlapping presentation of different pathologies. Peripheral nerves and adjacent structures, for example, vessels or muscles, display similar MRI signal characteristics on STIR images (Figure 3), and differentiationbetween them may be difficult (Crim and Ingalls, 2017). Using DTI, the no-anisotropic background structures are suppressed, further improving the detection of subtle nerve abnormalities. An added value of DTI is its improved detection of morphological abnormalities of the brachial plexus (3D reconstruction) and procurement of quantitative additional information regarding the microstructure of nerve fibers, thus being a potential alternative to the use of gadolinium.

It is important to acknowledge the limitations of DTI. Motion artifacts and geometrical distortions, long acquisition time and complex post-processing procedures, the robustness of the algorithms used, and complexity of brachial plexus anatomy limit the use of DTI in clinical practice. On the other hand, DTI can be used to quantify nerve microstructural integrity, non-invasively reconstruct nerve fibers *in vivo*, and can offer valuable complementary information without vascular signal intensity artifacts and is the only advanced technology to show a 3D view of the brachial plexus. In particular, in our study, the main limitation was the complex and time-consuming post-processing procedures, while the main advantage was the quantification of the nerve damage (C6 vs. C7 roots) and its correlation with the clinical and EMG findings.

Data availability statement

The raw data supporting the conclusions of this article will be made available by the authors, without undue reservation.

Ethics statement

Ethical review and approval was not required for the study on human participants in accordance with the local legislation and institutional requirements. The patients/participants provided their written informed consent to participate in this study. Written informed consent was obtained from the individual(s) for the publication of any potentially identifiable images or data included in this article.

Author contributions

LM FG, MA, and AR conceived the research, prepared the figures, drafted the manuscript, and edited and revised the manuscript. MA preprocessed the data. MA and LM analyzed the data. All authors contributed to the article and approved the submitted version.

Conflict of interest

The authors declare that the research was conducted in the absence of any commercial or financial relationships that could be construed as a potential conflict of interest.

Publisher's note

All claims expressed in this article are solely those of the authors and do not necessarily represent those of their affiliated

organizations, or those of the publisher, the editors and the reviewers. Any product that may be evaluated in this article, or claim that may be made by its manufacturer, is not guaranteed or endorsed by the publisher.

References

Aung, W. Y., Mar, S., and Benzinger, T. L. (2013). Diffusion tensor MRI as a biomarker in axonal and myelin damage. *Imag. Med.* 5, 427–40. doi: 10.2217/iim.13.49

Chhabra, A., Thakkar, R. S., Andreisek, G., Chalian, M., Belzberg, A. J., Blakeley, J., et al. (2013). Anatomic MR imaging and functional diffusion tensor imaging of peripheral nerve tumors and tumorlike conditions. *AJNR Am. J. Neuroradiol.* 34, 802–7. doi: 10.3174/ajnr.A3316

Chung, A. W., Thomas, D. L., Ordidge, R. J., and Clark, C. A. (2013). Diffusion tensor parameters and principal eigenvector coherence: relation to b-value intervals and field strength. *Magn. Reson. Imag.* 31, 742–7. doi: 10.1016/j.mri.2012.11.014

Crim, J., and Ingalls, K. (2017). Accuracy of MR neurography in the diagnosis of brachial plexopathy. *Eur. J. Radiol.* 95, 24–7. doi: 10.1016/j.ejrad.2017.07.012

Esiri, M. M., and Tomlinson, A. H. (1972). Herpes Zoster. Demonstration of virus in trigeminal nerve and ganglion by immunofluorescence and electron microscopy. *J. Neurol. Sci.* 15, 35–48. doi: 10.1016/0022-510X(72)90120-7

Fajar, A., Sarno, R., Fatichah, C., and Fahmi, A. (2022). Reconstructing and resizing 3D images from DICOM files. *J. King Saud Univ. Comput. Inform. Sci.* 34, 3517–26. doi: 10.1016/j.jksuci.2020.12.004

Gasparotti, R., Lodoli, G., Meoded, A., Carletti, F., Garozzo, D., Ferraresi, S., et al. (2013). Feasibility of diffusion tensor tractography of brachial plexus injuries at 1.5 T. *Invest. Radiol.* 48, 104–12. doi: 10.1097/RLI.0b013e3182775267

Gesslbauer, B., Hruby, L. A., Roche, A. D., Farina, D., Blumer, R., Aszmann, O. C., et al. (2017). Axonal components of nerves innervating the human arm. *Ann. Neurol.* 82, 396–408. doi: 10.1002/ana.25018

Guldberg-Moller, J., Olsen, S., and Kettel, K. (1959). Histopathology of the facial nerve in herpes zoster oticus. *AMA Arch. Otolaryngol.* 69, 266–75. doi: 10.1001/archotol.1959.00730030274003

Heckel, A., Weiler, M., Xia, A., Ruetters, M., Pham, M., Bendszus, M., et al. (2015). Peripheral nerve diffusion tensor imaging: assessment of axon and myelin sheath integrity. *PLoS ONE.* 10, e0130833. doi: 10.1371/journal.pone.0130833

Herweh, C., Jayachandra, M. R., Hartmann, M., Gass, A., Sellner, J., Heiland, S., et al. (2007). Quantitative diffusion tensor imaging in herpes simplex virus encephalitis. *J. Neurovirol.* 13, 426–32. doi: 10.1080/13550280701456498

Hodel, J., Dupuis, J., Rahmouni, A., Lefaucheur, J. P., Decq, P., Creange, A., et al. (2011). Leukemic infiltrative plexopathy: diagnosis and follow-up with diffusion tensor imaging. *AJNR Am. J. Neuroradiol.* 32, E35–6. doi: 10.3174/ajnr.A2347

Hodel, J., Lefaucheur, J. P., Toledano, S., Badat, N., Rondenet, C., Zuber, M., et al. (2022). Diffusion tensor imaging MR neurography in patients with acute or chronic plexopathy. *J. Neuroradiol.* 49, 2–8. doi: 10.1016/j.neurad.2021.06.002

Kimura-Ohba, S., Yang, Y., Thompson, J., Kimura, T., Salayandia, V. M., Cosse, M., et al. (2016). Transient increase of fractional anisotropy in reversible vasogenic edema. *J. Cereb. Blood Flow Metab.* 36, 1731–43. doi: 10.1177/0271678X16630556

Lope-Piedrafita, S. (2018). Diffusion Tensor Imaging (DTI). *Methods Mol. Biol.* 1718, 103–16. doi: 10.1007/978-1-4939-7531-0_7

Meng, Y., Zhuang, L., Jiang, W., Zheng, B., and Yu, B. (2021). Segmental zoster paresis: a literature review. *Pain Phys.* 24, 253–61. doi: 10.36076/ppj.2021/24/253

Ranzenberger, L. R., and Snyder, T. (2022). *Diffusion Tensor Imaging.* Treasure Island, FL: StatPearls.

Righini, A., Ramenghi, L., Zirpoli, S., Mosca, F., and Triulzi, F. (2005). Brain apparent diffusion coefficient decrease during correction of severe hypernatremic dehydration. *AJNR Am. J. Neuroradiol.* 26, 1690–4.

Song, S. K., Sun, S. W., Ramsbottom, M. J., Chang, C., Russell, J., Cross, A. H., et al. (2002). Dysmyelination revealed through MRI as increased radial (but unchanged axial) diffusion of water. *Neuroimage.* 17, 1429–36. doi: 10.1006/nimg.2002.1267

Su, X., Kong, X., Alwalid, O., Wang, J., Zhang, H., Lu, Z., et al. (2021). Multisequence quantitative magnetic resonance neurography of brachial and lumbosacral plexus in chronic inflammatory demyelinating polyneuropathy. *Front. Neurosci.* 15, 649071. doi: 10.3389/fnins.2021.649071

Tagliafico, A., Calabrese, M., Puntoni, M., Pace, D., Baio, G., Neumaier, C. E., et al. (2011). Brachial plexus MR imaging: accuracy and reproducibility of DTI-derived measurements and fibre tractography at 3.0-T. *Eur. Radiol.* 21, 1764–71. doi: 10.1007/s00330-011-2100-z

van Rosmalen, M. H. J., Goedee, H. S., Derks, R., Asselman, F. L., Verhamme, C., de Luca, A., et al. (2021). Quantitative magnetic resonance imaging of the brachial plexus shows specific changes in nerve architecture in chronic inflammatory demyelinating polyneuropathy, multifocal motor neuropathy and motor neuron disease. *Eur. J. Neurol.* 28, 2716–26. doi: 10.1111/ene.14896

Vavasour, I. M., Meyers, S. M., Madler, B., Harris, T., Fu, E., Li, D. K. B., et al. (2019). Multicenter measurements of T1 relaxation and diffusion tensor imaging: intra and intersite reproducibility. *J. Neuroimag.* 29, 42–51. doi: 10.1111/jon.12559

Wade, R. G., Bligh, E. R., Nar, K., Stone, R. S., Roberts, D. J., Teh, I., et al. (2020a). The geometry of the roots of the brachial plexus. *J. Anat.* 237, 999–1005. doi: 10.1111/joa.13270

Wade, R. G., Tanner, S. F., Teh, I., Ridgway, J. P., Shelley, D., Chaka, B., et al. (2020b). Diffusion tensor imaging for diagnosing root avulsions in traumatic adult brachial plexus injuries: a proof-of-concept study. *Front. Surg.* 7, 19. doi: 10.3389/fsurg.2020.00019

Wade, R. G., Teh, I., Andersson, G., Yeh, F. C., Wiberg, M., Bourke, G., et al. (2021). Fractional anisotropy thresholding for deterministic tractography of the roots of the brachial plexus. *Sci. Rep.* 11, 80. doi: 10.1038/s41598-020-79840-8

Won, S. J., Kim, B. J., Park, K. S., Kim, S. H., and Yoon, J. S. (2012). Measurement of cross-sectional area of cervical roots and brachial plexus trunks. *Muscle Nerve.* 46, 711–6. doi: 10.1002/mus.23503

Xie, M., Tobin, J. E., Budde, M. D., Chen, C. I., Trinkaus, K., Cross, A. H., et al. (2010). Rostrocaudal analysis of corpus callosum demyelination and axon damage across disease stages refines diffusion tensor imaging correlations with pathological features. *J. Neuropathol. Exp. Neurol.* 69, 704–16. doi: 10.1097/NEN.0b013e3181e3de90

Yeh, F. C., Liu, L., Hitchens, T. K., and Wu, Y. L. (2017). Mapping immune cell infiltration using restricted diffusion MRI. *Magn Reson Med.* 77, 603–12. doi: 10.1002/mrm.26143

Yeh, F. C., Verstynen, T. D., Wang, Y., Fernandez-Miranda, J. C., and Tseng, W. Y. (2013). Deterministic diffusion fiber tracking improved by quantitative anisotropy. *PLoS ONE.* 8, e80713. doi: 10.1371/journal.pone.0080713

Yeh, F. C., Wedeen, V. J., and Tseng, W. Y. (2010). Generalized q-sampling imaging. *IEEE Trans. Med. Imaging.* 29, 1626–35. doi: 10.1109/TMI.2010.2045126

frontiers | Frontiers in Neuroscience

TYPE Original Research
PUBLISHED 10 February 2023
DOI 10.3389/fnins.2023.1132173

OPEN ACCESS

EDITED BY
Nico Sollmann,
University of California, San Francisco,
United States

REVIEWED BY
Linda De Vries,
Leiden University Medical Center (LUMC),
Netherlands
Kornelia Kreiser,
Universitäts- und Rehabilitationskliniken Ulm,
Germany

*CORRESPONDENCE
Seyedmehdi Payabvash
✉ sam.payabvash@yale.edu

SPECIALTY SECTION
This article was submitted to
Brain Imaging Methods,
a section of the journal
Frontiers in Neuroscience

RECEIVED 26 December 2022
ACCEPTED 23 January 2023
PUBLISHED 10 February 2023

CITATION
Berson ER, Mozayan A, Peterec S, Taylor SN, Bamford NS, Ment LR, Rowe E, Lisse S, Ehrlich L, Silva CT, Goodman TR and Payabvash S (2023) A 1-Tesla MRI system for dedicated brain imaging in the neonatal intensive care unit.
Front. Neurosci. 17:1132173.
doi: 10.3389/fnins.2023.1132173

A 1-Tesla MRI system for dedicated brain imaging in the neonatal intensive care unit

Elisa R. Berson[1], Ali Mozayan[1], Steven Peterec[2], Sarah N. Taylor[2], Nigel S. Bamford[2,3], Laura R. Ment[2,3], Erin Rowe[1], Sean Lisse[1], Lauren Ehrlich[1], Cicero T. Silva[1], T. Rob Goodman[1] and Seyedmehdi Payabvash[1]*

[1]Department of Radiology and Biomedical Imaging, Yale School of Medicine, New Haven, CT, United States, [2]Department of Pediatrics, Yale School of Medicine, New Haven, CT, United States, [3]Department of Neurology, Yale School of Medicine, New Haven, CT, United States

Objective: To assess the feasibility of a point-of-care 1-Tesla MRI for identification of intracranial pathologies within neonatal intensive care units (NICUs).

Methods: Clinical findings and point-of-care 1-Tesla MRI imaging findings of NICU patients (1/2021 to 6/2022) were evaluated and compared with other imaging modalities when available.

Results: A total of 60 infants had point-of-care 1-Tesla MRI; one scan was incompletely terminated due to motion. The average gestational age at scan time was 38.5 ± 2.3 weeks. Transcranial ultrasound (n = 46), 3-Tesla MRI (n = 3), or both (n = 4) were available for comparison in 53 (88%) infants. The most common indications for point-of-care 1-Tesla MRI were term corrected age scan for extremely preterm neonates (born at greater than 28 weeks gestation age, 42%), intraventricular hemorrhage (IVH) follow-up (33%), and suspected hypoxic injury (18%). The point-of-care 1-Tesla scan could identify ischemic lesions in two infants with suspected hypoxic injury, confirmed by follow-up 3-Tesla MRI. Using 3-Tesla MRI, two lesions were identified that were not visualized on point-of-care 1-Tesla scan: (1) punctate parenchymal injury versus microhemorrhage; and (2) small layering IVH in an incomplete point-of-care 1-Tesla MRI with only DWI/ADC series, but detectable on the follow-up 3-Tesla ADC series. However, point-of-care 1-Tesla MRI could identify parenchymal microhemorrhages, which were not visualized on ultrasound.

Conclusion: Although limited by field strength, pulse sequences, and patient weight (4.5 kg)/head circumference (38 cm) restrictions, the Embrace® point-of-care 1-Tesla MRI can identify clinically relevant intracranial pathologies in infants within a NICU setting.

KEYWORDS

Embrace®, point-of-care MRI, neonatal intensive care unit, brain imaging, 1-Tesla, hemorrhage

1. Introduction

Transcranial ultrasound is the most commonly used modality for evaluating brain structures and intracranial pathologies within the neonatal intensive care unit (NICU) setting (Pollatou et al., 2022). Over the past two decades, MRI has been increasingly used in neonates and infants to elucidate patterns of brain development (Damaraju et al., 2014; Kline et al., 2021; Zhang et al., 2021) and to quickly and accurately diagnose suspected intraparenchymal pathologies, such as ischemia and hemorrhage (Reddy, 2022). While transcranial ultrasound can reliably identify intraventricular hemorrhage (IVH) and ventriculomegaly, brain MRI is considered more sensitive in detecting white matter (WM) disease, especially acute ischemic injury (Nowell et al., 1988; Doria et al., 2014; Simonsen et al., 2015). According to 2020 "Routine Neuroimaging of the Preterm Brain" guidance from the American Academy of Pediatrics, brain "MRI for infants born at less than 30 weeks of gestational age is not indicated as a routine procedure" (Hand et al., 2020; Inder et al., 2021). However, there is an increasing demand for readily accessible and safe brain MRI neuroimaging in this vulnerable population.

MRI in very preterm infants (VPIs), defined as being born before 32 weeks gestation, is enabled by specialized protocols that reduce noise, minimize transport burden, and utilize smaller head coils (Dalal et al., 2006; Rona et al., 2010; Flick et al., 2011; Wang et al., 2014; Ghotra et al., 2021). A novel MRI technology that received Food and Drug Administration (FDA) approval in 2017 is the 1-Tesla Embrace® for point-of-care brain MRI in the NICU (Voelker, 2017). Traditionally, MRI has been chiefly performed in term-equivalent infants stable enough for transport to the MRI suite. However, point-of-care 1-Tesla MRI enables safe imaging of a neonate's brain in the NICU without the need to transfer. This technology with a permanent magnet, 150 mT/m peak gradient, and temperature-controlled bassinet can potentially allow for earlier confirmation and prognostication of IVH, ischemic injury, and periventricular WM changes among neonates who were traditionally only suitable for transcranial ultrasound (Goeral et al., 2021).

To date, in-NICU point-of-care 1-Tesla brain MRI scanners are only available in a few centers in the United States, with limited reports on comparisons of the point-of-care 1-Tesla brain MRI with transcranial ultrasound and conventional 3-Tesla MRI (Thiim et al., 2022). In our present study, we report the results from neonatal brain MRIs performed using a point-of-care 1-Tesla MRI system during our NICU's first year of use. We compared intracranial findings on point-of-care MRI scans with conventional 3-Tesla MRI and transcranial ultrasound of neonates, whenever available.

2. Materials and methods

2.1. Patient characteristics

We retrospectively reviewed and evaluated the clinical and imaging information of all neonates who underwent a point-of-care 1-Tesla brain MRI from January 2021 through June 2022. The scanner can accommodate infants weighing up to 4.5 kg or with a head circumference of up to 38 cm. During this time, all clinically indicated non-contrast brain MRIs of neonates who fulfilled the above-mentioned physical criteria were performed in the point-of-care 1-Tesla brain MRI scanner, except for dedicated epilepsy protocol and neonates requiring contrast-enhanced MRI, who were referred for conventional 3-Tesla scanner given the imaging limitations for those indications with Embrace®. The institutional review board approved the research protocol for this study and waived the need for informed consent, given the retrospective nature of our analysis.

2.2. Brain MRI protocol

The infants were scanned within the NICU using a dedicated point-of-care 1-Tesla Embrace® MRI scanner (Aspect Imaging, Shoham, Israel). The MRI protocols on this unit are limited but include T1-weighted spin echo [slice thickness: 4 mm; repetition time (TR): 600 ms; echo time (TE): 11–12.5 ms; flip angle: 90°; field of view: 14 cm × 14 cm; and matrix: 200 × 200] in the axial and sagittal planes; T2-weighted fast spin echo (slice thickness: 4 mm; TR: 9,900–12,000 ms; TR: 130–155 ms; flip angle: 90°; field of view: 14 cm × 14 cm; and matrix 200 × 200) in axial, coronal, and sagittal planes; diffusion weighted imaging (DWI) fast spin echo (slice thickness: 4 mm; TR: 14,000–15,500 ms; TE: 127–133 ms; b = 0 and

TABLE 1 Demographic characteristics of infants who had 1-Tesla brain MRI.

Infants' characteristics	$N = 60$
Gestational age at birth (weeks, mean ± SD, range)	30.4 ± 5.4 (22–40)
≤32 weeks	41 (68%)
32–36 weeks 6 days	7 (12%)
≥37 weeks	12 (20%)
Method of delivery	
Vaginal delivery	25 (42%)
Cesarean section	35 (58%)
Birth weight (grams, mean ± SD)	1,575 ± 1,040
Apgar score [median, interquartile range]	
1 min	5 [3–7]
5 min	8 [6–9]
10 min (only recorded for 22 patients)	7.5 [7–9]
Cord pH (only measured in 25 patients)	7.26 ± 0.14
Required respiratory support	35 (58%)
Seizures	4 (7%)
Initial blood glucose at birth (mg/dl)	72.8 ± 36.3
Initial hematocrit at birth	40.6 ± 9.7
Gestational age at time of 1-Tesla scan (weeks, mean ± SD, range)	38.5 ± 2.3 (29.9–43.6)
Days of life first 1-Tesla performed (mean ± SD)	56.3 ± 39.1
Days from 1-Tesla to nearest MRI or ultrasound (mean ± SD)	44.9 ± 33.2
Primary indication for neonatal brain MRI	
Routine pre-discharge scan in extremely preterm neonates	25 (42%)
Intraventricular hemorrhage	20 (33%)
Hypoxic injury	11 (18%)
Other	4 (7%)

1,000 s/mm^2; flip angle: 90°; field of view: 11 cm × 14 cm; and matrix 92 × 43) in the axial plane; and a 3D T1 gradient echo (slice thickness: 1 mm; TR: 20 ms; TE: 3.4 ms; flip angle: 15°; field of view: 14 cm × 14 cm; and matrix 140 × 140) acquired in the sagittal plane and reconstructed in axial and coronal planes. Additional apparent diffusion coefficient (ADC) and exponential DWI maps were generated from DWI acquisition. The total scan time for this protocol is approximately 45 min.

2.3. Comparison transcranial ultrasound and 3-T brain MRI

Most infants undergoing point-of-care 1-Tesla brain MRI also underwent additional imaging in the form of transcranial ultrasound or conventional 3-Tesla brain MRI. The transcranial ultrasounds were performed using 5–12 MHz phased array transducer (Phillips, USA) *via* anterior fontanel (coronal, sagittal planes) and mastoid (coronal plane) windows. The 3-Tesla brain MRIs were performed on a Skyra scanner (Siemens, Germany) in the radiology department.

2.4. Assessment of study findings and concordance

In addition to the official clinical report, all scans were re-reviewed by a neuroradiologist with over six years of experience in pediatric neuroimaging. To facilitate the presentation of findings, we summarized the exam indication into four main categories: evaluation of potential ischemic injury, intraventricular/intraparenchymal hemorrhage, term age scan in extremely preterm infants (<28 weeks gestational age), and other indications. The findings from each scan were corroborated with the official clinical report. Concordance was determined in comparison with the 3-Tesla brain MRI or transcranial ultrasound performed at the closest interval to the target point-of-care 1-Tesla MRI scan.

2.5. Statistics

The data are expressed as mean ± SD, frequency (percentage), median (interquartile), or ratios, wherever appropriate.

3. Results

3.1. Patient demographics

A total of 60 neonates were scanned using the point-of-care 1-Tesla MRI scanner. One MRI was prematurely terminated due to motion but was still included in our evaluation. Neonate demographics and clinical information are summarized in Table 1. Of these, 3 (5%) had 3-Tesla MRI, 46 (76%) had transcranial ultrasound, and 4 (7%) had both ultrasound and 3-Tesla MRI in addition to 1-Tesla scan. However, 7 (12%) patients had no other brain imaging available for comparison with the 1-Tesla scan.

3.2. Suspected ischemic injury

A total of 11 (18%) infants underwent point-of-care 1-Tesla MRI for suspected ischemic injury; of whom, two had evidence of ischemic injury, one had evidence of IVH, and one had a subdural hematoma. Below is a summary of imaging findings from two of these seven patients. Two additional patients are listed in Table 2 under the subcategory of "Suspected ischemic injury." In the remaining

TABLE 2 Descriptors of infants who underwent 1-Tesla brain MRI imaging.

Age after birth of 1-Tesla MRI	Indication for 1-Tesla MRI imaging	1-Tesla MRI figures	1-Tesla MRI findings	Other imaging figures	Other imaging findings
Suspected ischemic injury					
7 days	Decreased fetal movement and profound anemia (hemoglobin 3.6 g/dl)	Figures 7A, B	Possible punctate focus of microhemorrhage in the right caudothalamic groove	Figure 7C	Transcranial ultrasound performed on the first day after birth confirmed the possible microhemorrhage
11 days	Fever, neonatal sepsis, and oxygen desaturations due to decreased respiratory drive	Figures 8A–F	No evidence of ischemic changes but demonstrated a 0.7 cm subdural hematoma	N/A	N/A
Other indications					
9 days	Evaluation for brainstem abnormality given decreased vocal cord mobility on laryngoscopic exam and obstructive apnea	N/A	No structural or signal abnormality in the brain	N/A	N/A
5 days	Evaluation after subgaleal hematoma was found on transcranial ultrasound	N/A	Redemonstrated subgaleal hematoma with no intracranial abnormalities	N/A	3-Tesla MRI redemonstrated subgaleal hematoma with no intracranial abnormalities
3 days	Prenatal diagnosis of ventriculomegaly and Trisomy 21		Mild dilation of the lateral ventricles to 11 mm at the level of the atrium		Transcranial ultrasounds performed before and after the MRI confirmed the ventricular dilation

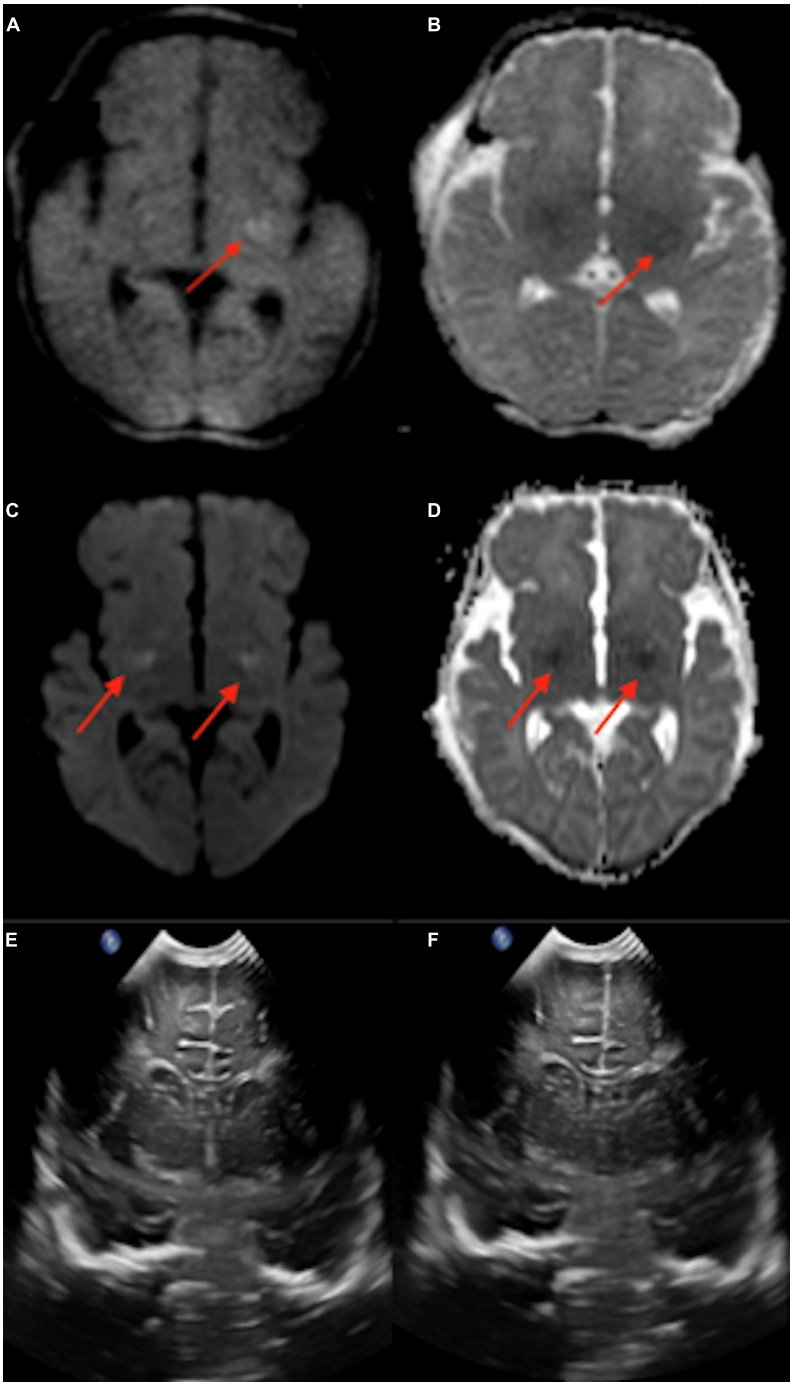

FIGURE 1
In a 4-day-old term neonate with challenging home birth, followed by transfer to hospital, resuscitation, and therapeutic hypothermia, the point-of-care 1-Tesla DWI **(A)** and ADC **(B)** showed reduced diffusion in the left basal ganglia. The next day (5 days old) follow-up 3-Tesla DWI **(C)** and ADC **(D)** showed ischemic changes and reduced diffusion in bilateral basal ganglia. Transcranial ultrasound was normal on the first day after birth **(E,F)**.

three subjects, the point-of-care 1-Tesla MRI scans were normal and concordant with findings of other imaging modalities (transcranial ultrasound in two and follow-up 3-Tesla MRIs in one).

A 4-day-old infant, 40 weeks 5 days postmenstrual age (PMA), was born *via* home birth with subsequent difficulty breathing and probable seizure. The infant was resuscitated and treated with therapeutic hypothermia. The point-of-care 1-Tesla MRI showed reduced diffusion in the left basal ganglia (Figures 1A, B). The next day follow-up 3-Tesla MRI (5 days old) showed ischemic changes and reduced diffusion in bilateral basal ganglia (Figures 1C, D). Notably, the transcranial ultrasound on the first day after birth was normal (Figures 1E, F).

A 5-day-old infant (34 weeks and 2 days PMA) born to a COVID-positive mother with poorly controlled diabetes had delivery complicated by shoulder dystocia requiring respiratory support and chest compressions. The point-of-care 1-Tesla MRI showed a 4 mm focus of ischemic injury adjacent to the right caudate body (Figures 2A–K), which was confirmed on the follow-up 3-Tesla

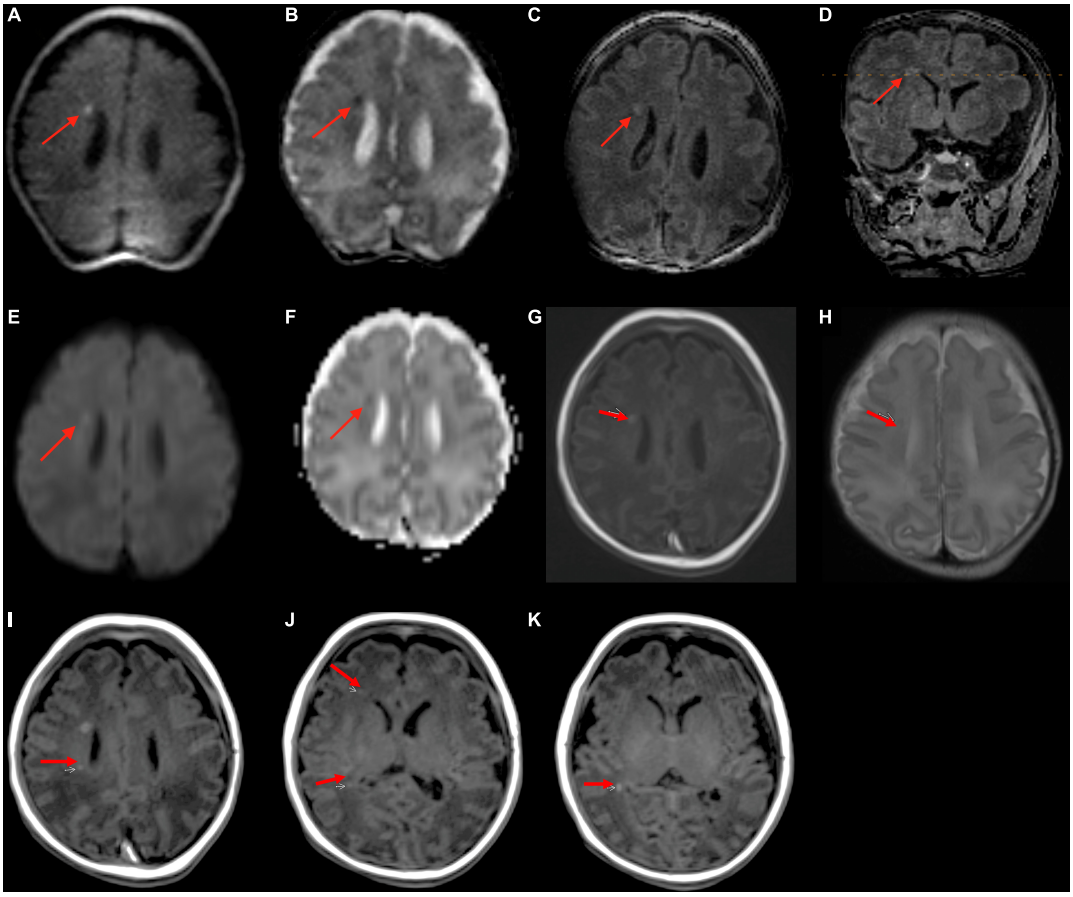

FIGURE 2
In a 5-day-old infant with a history of delivery complicated by shoulder dystocia requiring respiratory support and chest compressions, the point-of-care 1-Tesla DWI **(A)** and ADC **(B)** showed a punctate focus of reduced diffusion with associated T1 hyperintensity **(C,D)**. Two days later, follow-up 3-Tesla MRI showed diffusion restriction **(E,F)**, T1 hyperintensity **(G)**, and T2 hypointensity **(H)** of the same lesion. There were four additional punctate foci of parenchymal injury with intrinsic T1 hyperintensity on 3-Tesla MRI **(I–K)**, which could not be visualized on preceding day 1-Tesla scan. No transcranial ultrasound was obtained.

MRI on the seventh day after birth. Notably, four additional foci of punctate T1 hyperintensity were noted on the follow-up 3-Tesla MRI without corresponding signal abnormality on the initial point-of-care 1-Tesla scan (Figures 2I–K). The infant had no transcranial ultrasound for comparison.

3.3. Intraventricular/intraparenchymal hemorrhage

A total of twenty infants were scanned at term age equivalent (36–40 weeks gestational age) or before discharge for follow-up of their IVH. In 17 out of 20 infants, IVH was found on point-of-care 1-Tesla MRI scan, corroborating the findings of the most recent preceding transcranial ultrasound. Images from four of these patients appear in Figures 3A–L. IVH findings were also confirmed in one infant on the follow-up 3-Tesla MRI (Figures 3J–L). In three infants with history of grade 1 or 2 IVH, there was no evidence of IVH on the point-of-care 1-Tesla MRI. This was concordant with the most recent preceding transcranial ultrasound for each patient performed prior to the MRI, all of which reported complete interval resolution of IVH. One infant who was born at 37 weeks and 3 days, with delivery complicated by shoulder dystocia and brachial plexus injury, hypoglycemia, and seizures shortly after birth, was found to have a left temporal lobe intraparenchymal hemorrhage on transcranial ultrasound performed at 1 day old (Figures 4A, B). Follow-up conventional 3-Tesla MRI performed on day four of life as part of an epilepsy protocol (Figures 4C, D), and a point-of-care 1-Tesla MRI (when 35 days old) delineated the extent of parenchymal hemorrhage (Figures 4E, F).

3.4. Routine pre-discharge scan in preterm infants

A total of 22 infants with preterm birth had pre-discharge point-of-care 1-Tesla scans to exclude potential parenchymal injury. The postmenstrual gestational age at birth for this sub-cohort ranged from 22 weeks and 1 day to 34 weeks and 3 days. In a 63-day-old infant (36 weeks and 4 days PMA), the point-of-care 1-Tesla MRI scanner showed a punctate focus of microbleed in the deep WM next to the left frontal horn (Figures 5A, B), which was not identified on a preceding transcranial ultrasound performed 5 weeks earlier (Figure 5C). In a 4-month-old neonate (43 weeks and 4 days PMA), with no transcranial ultrasound, the pre-discharge point-of-care 1-Tesla MRI was terminated after obtaining DWI series

10.3389/fnins.2023.1132173

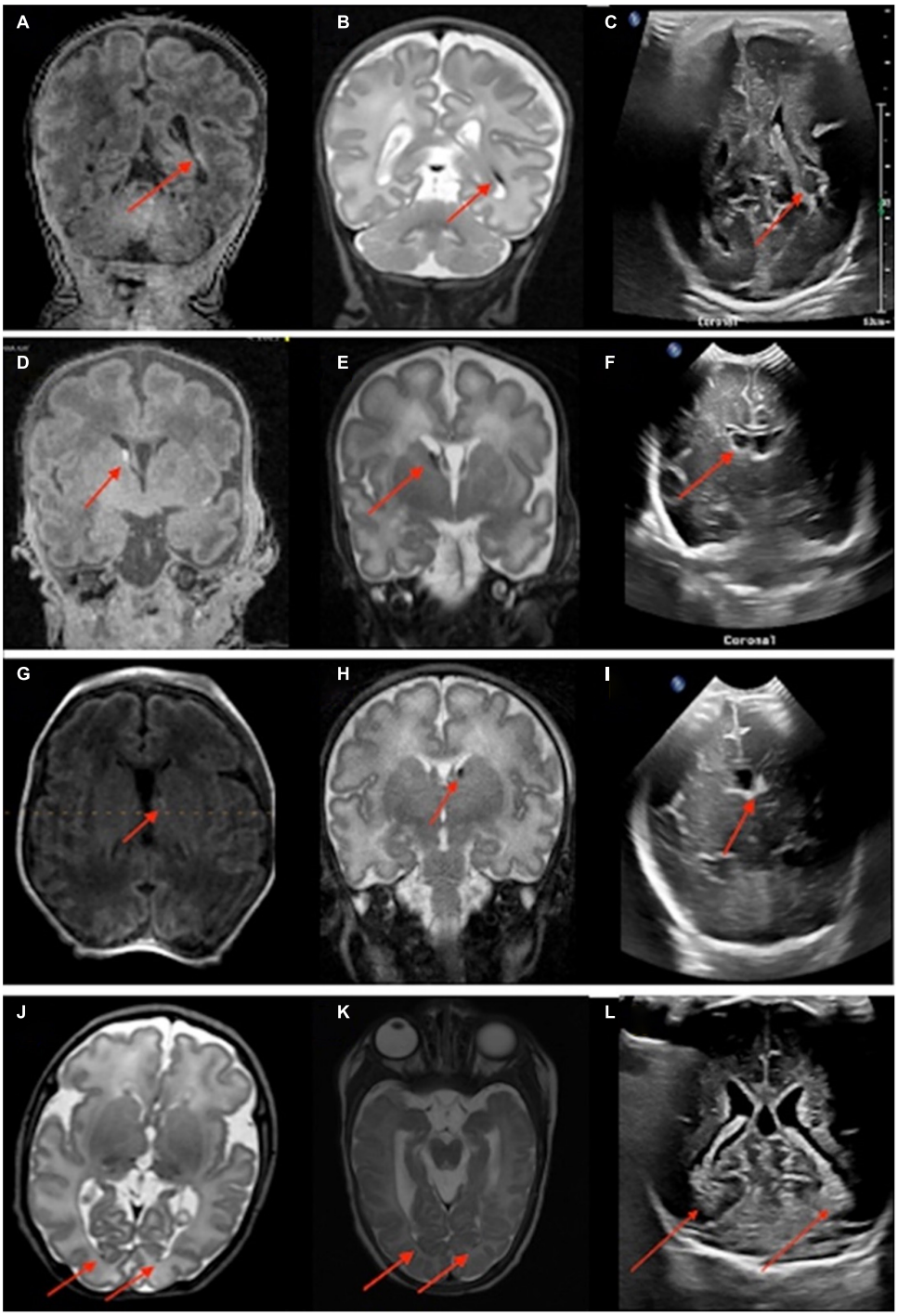

FIGURE 3
Neonates scanned on point-of-care 1-Tesla MRI for intraventricular hemorrhage (IVH) follow-up. An 80-day-old infant with T1 hyperintense **(A)** and T2 hypointense **(B)** grade II left germinal matrix hemorrhage on point-of-care 1-Tesla MRI performed 70 days after transcranial ultrasound **(C)**. A 52-day-old infant with T1 hyperintense **(D)** and T2 hypointense **(E)** right-sided grade I germinal matrix hemorrhage on point-of-care 1-Tesla MRI performed 34 days after transcranial ultrasound **(F)**. A 28-day-old infant with T1 hyperintense **(G)** and T2 hypointense **(H)** left-sided grade I germinal matrix hemorrhage on point-of-care 1-Tesla MRI performed 15 days after transcranial ultrasound **(I)**. An 85-day-old infant with layering T2 hypointense IVH **(J)** on point-of-care 1-Tesla MRI, which was also visualized on follow-up 3-Tesla MRI 38 days later **(K)** and was sequela of grade 2 IVH seen on transcranial ultrasound performed 74 days earlier **(L)**.

due to infant movement (Figure 6A). However, a follow-up 3-Tesla MRI under sedation performed 5 days later showed layering IVH (Figure 6B), which was conspicuous on ADC series. This was not visualized on the ADC map from the point-of-care 1-Tesla MRI. In the remaining twenty infants, the point-of-care 1-Tesla brain MRI showed no structural or signal abnormality, concordant with transcranial ultrasound findings performed in 17 of these infants. In three infants, point-of-care 1-Tesla MRI was the only modality of brain imaging performed during the NICU admission at our institution.

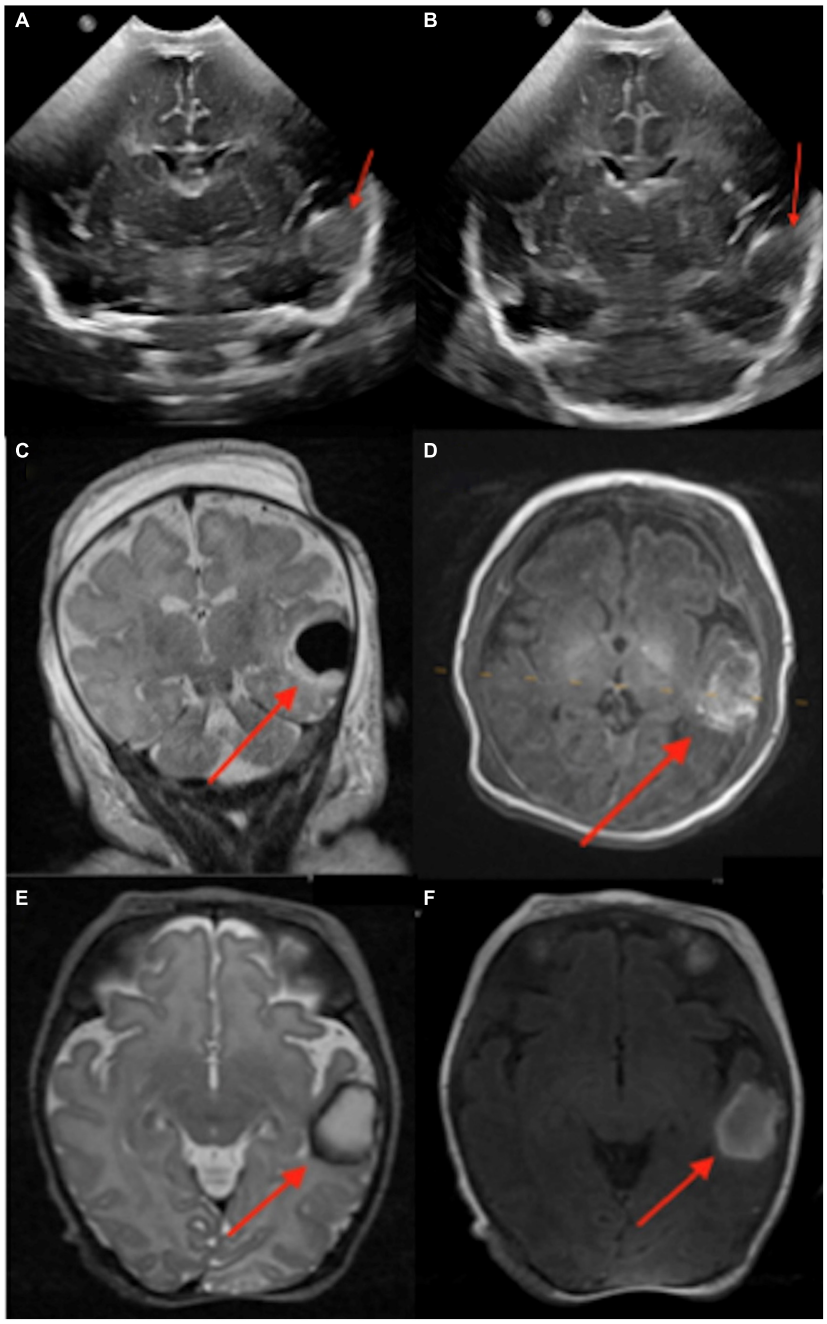

FIGURE 4
An infant born at 37 weeks and 3 days, with delivery complicated by shoulder dystocia and brachial plexus injury, was found to have hypoglycemia and seizures after birth. A left temporal lobe intraparenchymal hemorrhage was found in transcranial ultrasound (1 day old, **A,B**). This was further delineated on conventional 3-Tesla MRI (4 days old, **C,D**) and followed on point-of-care 1-Tesla MRI (35 days old, **E,F**).

3.5. Other indications

There were several other indications for the use of 1-Tesla MRI, including the assessment of brainstem abnormality, the evaluation of subgaleal hematoma, and a diagnosis of ventriculomegaly, which are detailed in Table 2 under the subheading of "Other indications." Below are detailed examples of the evaluation performed for two infants with congenital fetal abnormalities. One infant was delivered *via* late preterm C-section due to a known omphalocele and was discovered to have a patent ductus arteriosus and patent foramen ovale. After surgical correction, the patient was intubated and placed on fentanyl and dexmedetomidine (Precedex) drips for 5 days. Term-equivalent MRI was performed on the 18th day after birth using the 1T MRI. The MRI excluded post-hypoxic sequelae or intracranial hemorrhage, concordant with an earlier transcranial ultrasound on the first day after birth.

Another infant with syndactyly of the bilateral second, third, and fourth digits in all extremities and two small appendages of the midline sacrum was scanned at term with 1T MRI. There was no evidence of any intrathecal abnormality on spinal ultrasound, and Embrace® MRI performed on the third day after birth found no abnormalities.

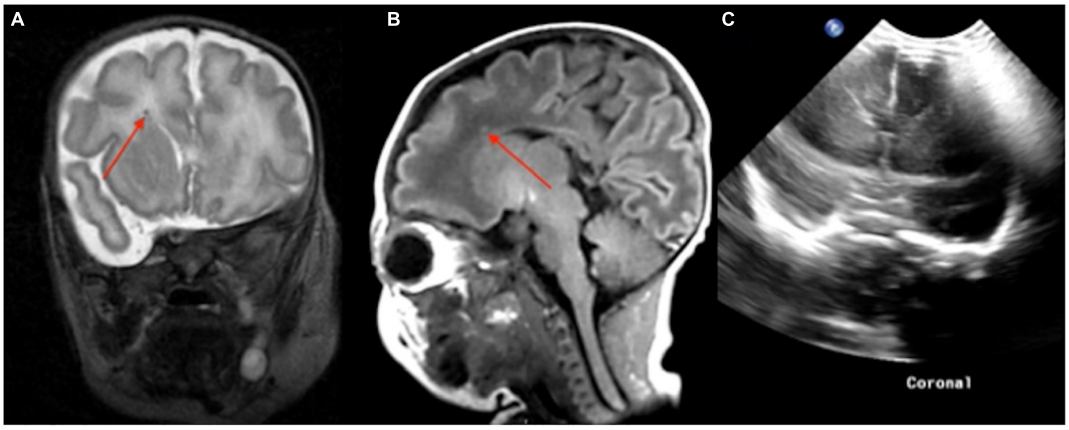

FIGURE 5
In a routine pre-discharge point-of-care 1-Tesla MRI of a preterm infant, there was a punctate focus of T1 hyperintense **(A)** and T2 hypointense **(B)** microbleed in the left anterior periventricular white matter which was not visualized on preceding transcranial ultrasound performed 5 weeks earlier **(C)**.

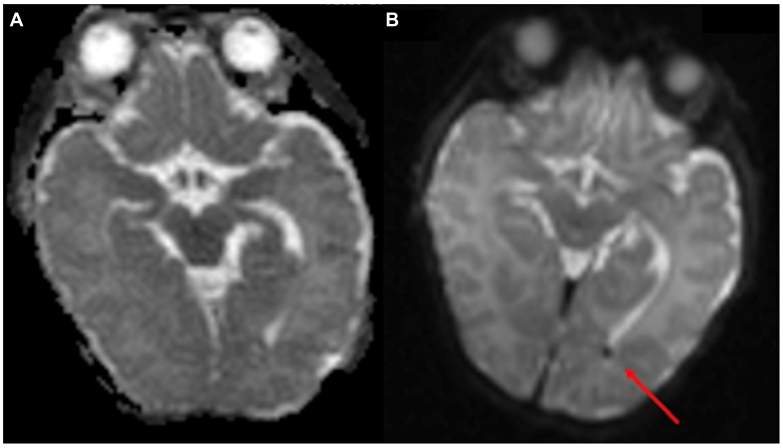

FIGURE 6
The point-of-care 1-Tesla routine pre-discharge MRI in a 4-month-old neonate was terminated after obtaining DWI/ADC due to infant movement **(A)**. Follow-up 3-Tesla MRI 5 days later showed layering IVH in occipital horns, which could be appreciated even on the ADC series **(B)**. No transcranial ultrasound was obtained.

4. Discussion

Our findings confirm the feasibility of the Embrace® point-of-care 1-Tesla scanner for imaging in the NICU setting. Using this point-of-care 1-Tesla scanner, we could identify cerebral ischemic lesions in two of seven neonates with suspected hypoxic injury, which 3-Tesla MRI confirmed. Among infants scanned by the point-of-care 1-Tesla scanner, the only potentially missed lesions were punctate foci of parenchymal injury versus microhemorrhage (Figures 2I–K) in an infant with identified ischemic injury and small layering IVH in an incomplete study that only included DWI/ADC series (Figure 6). The point-of-care 1-Tesla MRI was more sensitive than transcranial ultrasound in detecting small parenchymal hemorrhage (Figure 5). This is especially important when considering small, difficult-to-detect lesions of the deep gray matter and brainstem. Of note, the implementation of Embrace® point-of-care 1-Tesla scanner lacks a susceptivity-weighted imaging (SWI) sequence, although it is available in research protocols from outside the United States. In all infants with a history of IVH and intraparenchymal hemorrhage, point-of-care 1-Tesla MRI findings were concordant with the most recent transcranial ultrasound or follow-up MRI. Overall, the point-of-care 1-Tesla MRI could identify or exclude intracranial pathologies.

Reliable detection of ischemic injury in an infant's brain is especially valuable given transcranial ultrasound's limitations in detecting early ischemic changes in cerebral parenchyma (Guan et al., 2017; Hwang et al., 2017; Salas et al., 2018). Among infants with point-of-care 1-Tesla MRI for suspected hypoxic-ischemic injury, we could identify parenchymal lesions in two infants, which were confirmed on follow-up 3-Tesla scans. In the remaining five infants, the point-of-care 1-Tesla could potentially identify microhemorrhage (not visualized on transcranial ultrasound, Figure 7) and subdural hematoma (Figure 8), while excluding ischemic parenchymal injury. However, the point-of-care 1-Tesla scan may be limited in detecting punctate foci of parenchymal injury (Figures 2I–K). In addition, the point-of-care 1-Tesla cannot currently obtain MRI angiography or venography series.

While transcranial ultrasound provides a readily available and sensitive tool for the evaluation of IVH and hydrocephalus in the

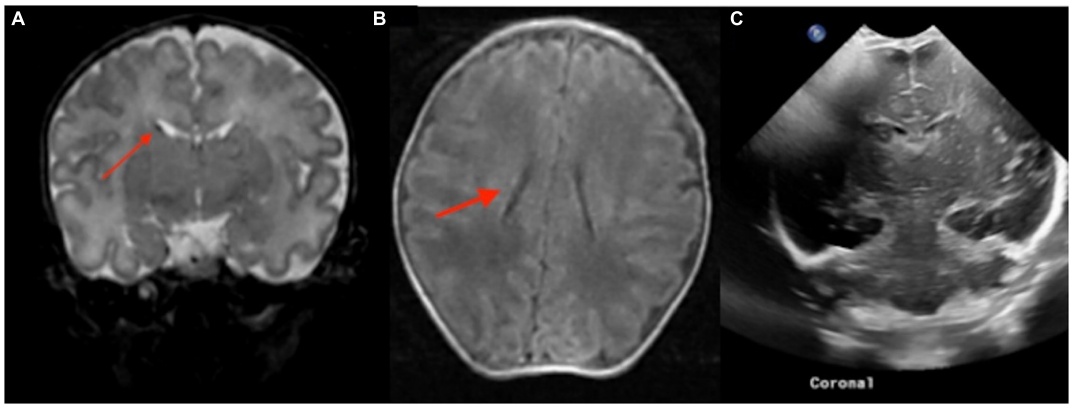

FIGURE 7
The point of care 1-Tesla MRI in a 6-day-old infant with emergency cesarean section delivery due to decreased fetal movement and variable decelerations showed a possible punctate focus of hemorrhage versus vessel in the right caudothalamic groove with T2 hypointensity **(A)** and T1 hyperintensity **(B)** but no evidence of ischemic injury. This was not seen on transcranial ultrasound on the first day after birth **(C)**.

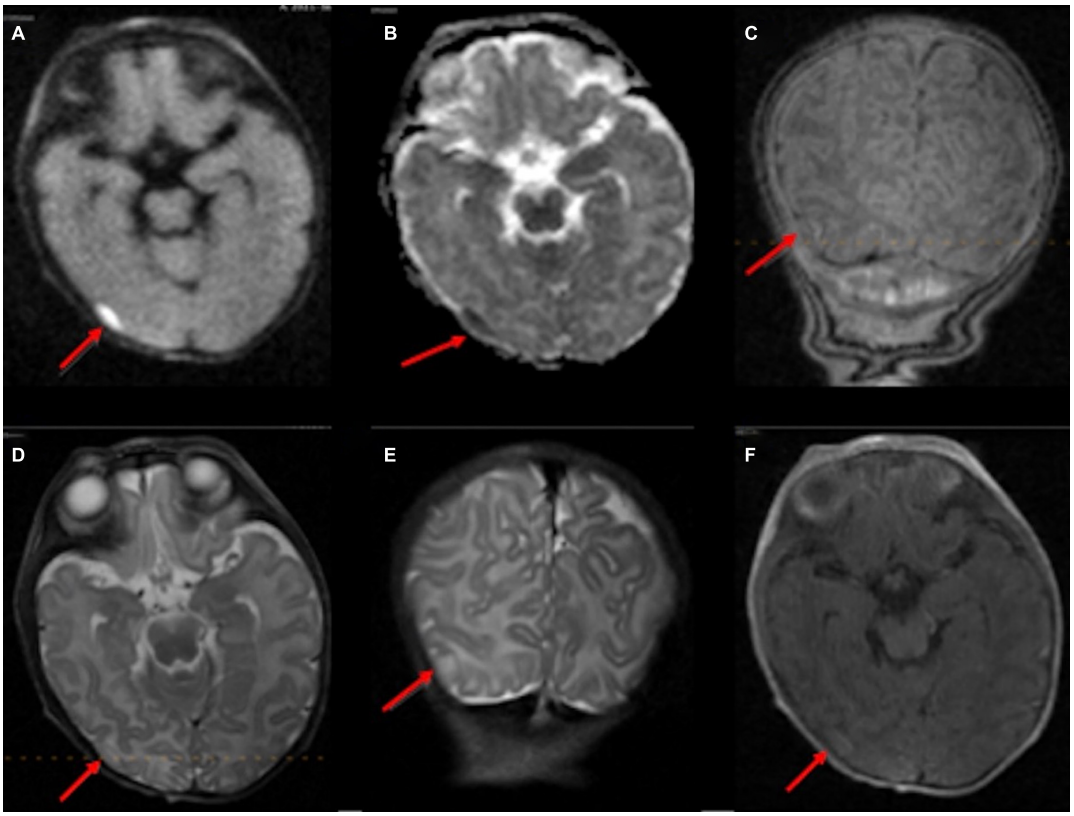

FIGURE 8
In an 11-day-old term neonate with a history of decreased respiratory drive, the 1-Tesla point-of-care MRI showed a subdural collection overlying the right temporo-occipital junction with reduced diffusion on DWI **(A)** and ADC **(B)**, which appeared isointense on T1 **(C,F)** and T2 **(D,E)**. No other brain imaging was performed.

NICU setting, MRI has the potential to increase the detection of intraparenchymal injuries, periventricular leukomalacia, and subdural hematomas (Inder et al., 1999; Williams and Hogg, 2000; Sie et al., 2005; Ahya and Suryawanshi, 2018; Arnold et al., 2023). A study by Rooks et al. (2008) found that transcranial ultrasound detected only 55% of infratentorial hematomas and no supratentorial subdural hematomas. In our series, the point-of-care 1-Tesla MRI could identify IVH in all neonates with such findings in their most recent transcranial ultrasound (Figure 3). It could also characterize subdural hematoma (Figure 8) and intraparenchymal hemorrhage (Figure 4). In two infants (Figures 5, 7), the point-of-care 1-Tesla MRI identified foci of intraparenchymal microbleeds that could not be detected on comparison transcranial ultrasounds. Of note, by adding an SWI sequence to Embrace® scanners, the sensitivity of 1-Tesla MRI for detecting intraparenchymal hemorrhage is expected to increase in the future. In addition to a role in demonstrating intraparenchymal

hemorrhage, neonatal MRI offers the opportunity to examine the effects of early anesthesia and more prolonged sedation on the brain of very young infants and to exclude associated central nervous system abnormalities in neonates presenting with axial or extra-axial deformities. Further studies with the 1-Tesla MRI can help to determine the potential clinical implications of the technology.

There is emerging evidence of clinical and research capabilities of point-of-care 1-Tesla brain MRI. Our results are in agreement with a recent report from Brigham and Women's Hospital, which showed that Embrace® 1-Tesla scanner could detect clinically relevant brain abnormalities in 207 scans of infants within the NICU setting (Thiim et al., 2022). In their series, 32 (15%) infants had a 3-Tesla MRI for comparison, and 80 (39%) had pathologies on their scans (Thiim et al., 2022), compared to our series, where 7 (12%) infants had a 3-Tesla scan comparison, and 33 (55%) had intracranial pathologies. A study from the Shaare Zedek Medical Center using the Embrace® 1-Tesla scanner found that image quality was comparable to conventional 1.5 T MRI (Nun et al., 2022). Furthermore, using the Embrace® 1-Tesla scanner, the institution demonstrated a positive association between increased T1 and T2 signal intensity in the basal ganglia and elevated serum bilirubin levels (Kasirer et al., 2021).

Aside from infants' weight and head circumference restrictions, there are technical limitations in brain imaging with the Embrace® 1-Tesla scanner. Many conventional MRI sequences are not currently available on the Embrace® 1-Tesla scanner, most notably SWI, MRI angiography, or venography. The DWI sequence is also acquired using fast-spin echo instead of echo-planar imaging, which leads to a slightly longer acquisition time. Moreover, the magnetic field inhomogeneity is associated with distortion of images at the brain periphery and limits the reliability of evaluating calvarial, orbital, facial, or neck pathologies. There are also frequent DWI hyperintensity artifacts in the posterior aspect of the brain, which can be clinically resolved by examining exponential diffusion images. Finally, although acquiring post-contrast images on the point-of-care 1-Tesla scanner is possible, infants requiring post-contrast images were referred for 3-Tesla MRI.

Our study also has methodological design limitations to consider. It is retrospective, and not all infants with point-of-care 1-Tesla scans had a comparison 3-Tesla MRI or transcranial ultrasound. In addition, the comparison scans were at least 1 day apart from the target point-of-care 1-Tesla MRI, which is suboptimal given the dynamic nature of intracranial pathologies. Additionally, several imaging series in the point-of-care 1-Tesla scan were partially degraded by motion, despite using the specialized head coil and bassinet to restrict neonate movements. Lastly, this is a very early experience with evolving technology, and standardized indications and protocols at the study institution are continuing to develop. As a result, the potential of point-of-care 1-Tesla MRI in the NICU setting to contribute to the study of early brain development in healthy preterm infants or used as an adjunct in surveying for intracranial abnormalities in infants with other musculoskeletal, cardiac, or gastrointestinal abnormalities requires further exploration.

5. Conclusion

In a year-long experience at a single institution, we scanned 50 infants with Embrace® point-of-care 1-Tesla MRI in the NICU setting and report this scanner's feasibility in detecting clinically relevant intracranial pathologies. In comparing the point-of-care 1-Tesla MRI with other imaging modalities available in 45 (90%) infants, we demonstrated the advantages of point-of-care 1-Tesla brain MRI over ultrasound in detecting small early ischemic changes and parenchymal microhemorrhage. However, compared to the 3-Tesla scanner, tiny foci of parenchymal injury or IVH may not be conspicuous on point-of-care 1-Tesla MRI. Nevertheless, implementing a dedicated point-of-care 1-Tesla scanner in the NICU setting can make brain MRI accessible to very preterm and ill newborns at earlier ages while reducing risks of transportation and sedation. Early detection of clinically relevant intracranial pathologies, especially acute ischemic changes that are challenging to identify by transcranial ultrasound, has the potential to improve clinical treatment and facilitate early prognostication in the NICU setting.

Data availability statement

The original contributions presented in this study are included in this article/supplementary material, further inquiries can be directed to the corresponding author.

Ethics statement

Ethical review and approval was not required for the study on human participants in accordance with the local legislation and institutional requirements. Written informed consent from the participants' legal guardian/next of kin was not required to participate in this study in accordance with the national legislation and the institutional requirements.

Author contributions

EB, AM, and SPa made substantial contributions to the conception of the study, collected the images and clinical information of the patients, and were responsible for the analysis and interpretation of the data. EB, AM, SPe, ST, NB, LM, ER, SL, LE, CS, TG, and SPa were responsible for manuscript preparation, editing, and review and approved the version to be published. All authors contributed to the article and approved the submitted version.

Funding

SPa received grant support from National Institutes of Health (K23NS118056), Doris Duke Charitable Foundation (2020097), and Foundation of American Society of Neuroradiology.

Conflict of interest

The authors declare that the research was conducted in the absence of any commercial or financial relationships that could be construed as a potential conflict of interest.

Publisher's note

References

Ahya, K., and Suryawanshi, P. (2018). Neonatal periventricular leukomalacia: Current perspectives. *Res. Rep. Neonatol.* 8, 1–8. doi: 10.2147/RRN.S125575

Arnold, T., Freeman, C., Litt, B., and Stein, J. (2023). Low-field MRI: Clinical promise and challenges. *J. Magn. Reson. Imaging* 57, 25–44. doi: 10.1002/jmri.28408

Dalal, P., Murray, D., Cox, T., McAllister, J., and Snider, R. (2006). Sedation and anesthesia protocols used for magnetic resonance imaging studies in infants: Provider and pharmacologic considerations. *Anesth. Analg.* 103, 863–868. doi: 10.1213/01.ane.0000237311.15294.0e

Damaraju, E., Caprihan, A., Lowe, J., Allen, E., Calhoun, V., and Phillips, J. (2014). Functional connectivity in the developing brain: A longitudinal study from 4 to 9months of age. *Neuroimage* 84, 169–180. doi: 10.1016/j.neuroimage.2013.08.038

Doria, V., Arichi, T., and David Edwards, A. (2014). Magnetic resonance imaging of the preterm infant brain. *Curr. Pediatr. Rev.* 10, 48–55.

Flick, R., Katusic, S., Colligan, R., Wilder, R., Voigt, R., Olson, M., et al. (2011). Cognitive and behavioral outcomes after early exposure to anesthesia and surgery. *Pediatrics* 128, e1053–e1061. doi: 10.1542/peds.2011-0351

Ghotra, A., Kosakowski, H., Takahashi, A., Etzel, R., May, M., Scholz, A., et al. (2021). A size-adaptive 32-channel array coil for awake infant neuroimaging at 3 Tesla MRI. *Magn. Reson. Med.* 86, 1773–1785. doi: 10.1002/mrm.28791

Goeral, K., Kasprian, G., Hüning, B., Waldhoer, T., Fuiko, R., Schmidbauer, V., et al. (2021). A novel magnetic resonance imaging-based scoring system to predict outcome in neonates born preterm with intraventricular haemorrhage. *Dev. Med. Child Neurol.* 64, 608–617. doi: 10.1111/dmcn.15116

Guan, B., Dai, C., Zhang, Y., Zhu, L., He, X., Wang, N., et al. (2017). Early diagnosis and outcome prediction of neonatal hypoxic-ischemic encephalopathy with color Doppler ultrasound. *Diagn. Interv. Imaging* 98, 469–475. doi: 10.1016/j.diii.2016.12.001

Hand, I., Shellhaas, R., and Milla, S. (2020). Routine neuroimaging of the preterm brain. *Pediatrics* 146:e2020029082.

Hwang, M., De Jong, J. R., Herman, S., Boss, R., Riggs, B., Tekes-Brady, A., et al. (2017). Novel contrast-enhanced ultrasound evaluation in neonatal hypoxic ischemic injury: Clinical application and future directions. *J. Ultrasound Med.* 36, 2379–2386. doi: 10.1002/jum.14289

Inder, T., de Vries, L., Ferriero, D., Grant, P., Ment, L., Miller, S., et al. (2021). Neuroimaging of the preterm brain: Review and recommendations. *J. Pediatr.* 237, 276–287.e4.

Inder, T., Huppi, P., Zientara, G., Maier, S., Jolesz, F., di Salvo, D., et al. (1999). Early detection of periventricular leukomalacia by diffusion-weighted magnetic resonance imaging techniques. *J. Pediatr.* 134, 631–634. doi: 10.1016/S0022-3476(99)70251-9

Kasirer, Y., Bin-Nun, A., Hammerman, C., Yosef, O., Marianayagam, N., Hammerman-Rozenberg, A., et al. (2021). Mildly elevated bilirubin levels are associated with increased magnetic resonance imaging signal intensity in the basal ganglia of preterm neonates. *Am. J. Perinatol.* doi: 10.1055/a-1649-1918 [Epub ahead of print].

Kline, J., Illapani, V., Li, H., He, L., Yuan, W., and Parikh, N. (2021). Diffuse white matter abnormality in very preterm infants at term reflects reduced brain network efficiency. *Neuroimage Clin.* 31:102739. doi: 10.1016/j.nicl.2021.102739

Nowell, M., Grossman, R., Hackney, D., Zimmerman, R., Goldberg, H., and Bilaniuk, L. T. (1988). MR imaging of white matter disease in children. *AJR Am. J. Roentgenol.* 151, 359–365.

Nun, A., Kasirer, Y., Ata, N., Rosenbaum, D., Cytter-Kuint, R., Hammerman, C., et al. (2022). Detection of global brain injury in premature neonates using novel point of care neonatal MRI scanner. *Neuropediatrics* doi: 10.1055/a-1926-2238 [Epub ahead of print].

Pollatou, A., Filippi, C., Aydin, E., Vaughn, K., Thompson, D., Korom, M., et al. (2022). An ode to fetal, infant, and toddler neuroimaging: Chronicling early clinical to research applications with MRI, and an introduction to an academic society connecting the field. *Dev. Cogn. Neurosci.* 54:101083. doi: 10.1016/j.dcn.2022.101083

Reddy, R. (2022). Magnetic resonance imaging evaluation of perinatal hypoxic ischemic encephalopathy: An institutional experience. *J. Neurosci. Rural Pract.* 13, 87–94. doi: 10.1055/s-0041-1742157

Rona, Z., Klebermass, K., Cardona, F., Czaba, C., Brugger, P., Weninger, M., et al. (2010). Comparison of neonatal MRI examinations with and without an MR-compatible incubator: Advantages in examination feasibility and clinical decision-making. *Eur. J. Paediatr. Neurol.* 14, 410–417. doi: 10.1016/j.ejpn.2010.03.005

Rooks, V., Eaton, J., Ruess, L., Petermann, G., Keck-Wherley, J., and Pedersen, R. (2008). Prevalence and evolution of intracranial hemorrhage in asymptomatic term infants. *Am. J. Neuroradiol.* 29, 1082–1089. doi: 10.3174/ajnr.A1004

Salas, J., Tekes, A., Hwang, M., Northington, F., and Huisman, T. (2018). Head ultrasound in neonatal hypoxic-ischemic injury and its mimickers for clinicians: A review of the patterns of injury and the evolution of findings over time. *Neonatology* 114, 185–197. doi: 10.1159/000487913

Sie, L., Hart, A., Van Hof, J., De Groot, L., Lems, W., Lafeber, H., et al. (2005). Predictive value of neonatal MRI with respect to late MRI findings and clinical outcome. A study in infants with periventricular densities on neonatal ultrasound. *Neuropediatrics* 36, 78–89. doi: 10.1055/s-2005-837574

Simonsen, C., Madsen, M., Schmitz, M., Mikkelsen, I., Fisher, M., and Andersen, G. (2015). Sensitivity of diffusion- and perfusion-weighted imaging for diagnosing acute ischemic stroke is 97.5%. *Stroke* 46, 98–101. doi: 10.1161/STROKEAHA.114.007107

Thiim, K., Singh, E., Mukundan, S., Grant, P., Yang, E., El-Dib, M., et al. (2022). Clinical experience with an in-NICU magnetic resonance imaging system. *J. Perinatol.* 42, 873–879. doi: 10.1038/s41372-022-01387-5

Voelker, R. (2017). MRI for Neonates. *JAMA* 318:790.

Wang, X., Xu, Z., and Miao, C. (2014). Current clinical evidence on the effect of general anesthesia on neurodevelopment in children: An updated systematic review with meta-regression. *PLoS One* 9:e85760. doi: 10.1371/journal.pone.0085760

Williams, V., and Hogg, J. (2000). Magnetic resonance imaging of chronic subdural hematoma. *Neurosurg. Clin. N. Am.* 11, 491–498.

Zhang, S., He, Z., Du, L., Zhang, Y., Yu, S., Wang, R., et al. (2021). Joint analysis of functional and structural connectomes between preterm and term infant brains via canonical correlation analysis with locality preserving projection. *Front. Neurosci.* 15:724391. doi: 10.3389/fnins.2021.724391

frontiers | Frontiers in Neuroscience

TYPE Review
PUBLISHED 02 March 2023
DOI 10.3389/fnins.2023.1097002

OPEN ACCESS

EDITED BY
Dahua Yu,
Inner Mongolia University of Science and Technology, China

REVIEWED BY
Samar Khalifa,
Independent Researcher, Kafr El-Sheikh, Egypt
Shaoyang Cui,
Shenzhen Hospital of Guangzhou University of Chinese Medicine, China

*CORRESPONDENCE
Fanrong Liang
✉ acuresearch@126.com
Ruirui Sun
✉ sunruirui@cdutcm.edu.cn

†These authors have contributed equally to this work

SPECIALTY SECTION
This article was submitted to Brain Imaging Methods, a section of the journal Frontiers in Neuroscience

RECEIVED 13 November 2022
ACCEPTED 17 February 2023
PUBLISHED 02 March 2023

CITATION
Ye X, Peng L, Sun N, He L, Yang X, Zhou Y, Xiong J, Shen Y, Sun R and Liang F (2023) Hotspots and trends in fNIRS disease research: A bibliometric analysis.
Front. Neurosci. 17:1097002.
doi: 10.3389/fnins.2023.1097002

Hotspots and trends in fNIRS disease research: A bibliometric analysis

Xiangyin Ye[1†], Li Peng[2†], Ning Sun[3†], Lian He[2], Xiuqiong Yang[2], Yuanfang Zhou[1], Jian Xiong[1], Yuquan Shen[4], Ruirui Sun[1*] and Fanrong Liang[1*]

[1]Acupuncture and Tuina School, Chengdu University of Traditional Chinese Medicine, Chengdu, China, [2]Department of Ultrasound, The First People's Hospital of Longquanyi District, Chengdu, China, [3]Rehabilitation Medicine Center and Institute of Rehabilitation Medicine, West China Hospital, Sichuan University, Chengdu, China, [4]Department of Rehabilitation Medicine, The First People's Hospital of Longquanyi District, Chengdu, China

Objective: To summarize the general information and hotspots of functional near-infrared spectroscopy (fNIRS)-based clinical disease research over the past 10 years and provide some references for future research.

Methods: The related literature published between 1 January 2011 and 31 January 2022 was retrieved from the Web of Science core database (WoS). Bibliometric visualization analysis of countries/regions, institutions, authors, journals, keywords and references were conducted by using CiteSpace 6.1.R3.

Results: A total of 467 articles were included, and the annual number of articles published over nearly a decade showed an upward trend year-by-year. These articles mainly come from 39 countries/regions and 280 institutions. The representative country and institution were the USA and the University of Tubingen. We identified 266 authors, among which Andreas J Fallgatter and Ann-Christine Ehlis were the influential authors. Neuroimage was the most co-cited journal. The major topics in fNIRS disease research included activation, prefrontal cortex, working memory, cortex, and functional magnetic resonance imaging (fMRI). In recent years, the Frontier topics were executive function, functional connectivity, performance, diagnosis, Alzheimer's disease, children, and adolescents. Based on the burst of co-cited references, gait research has received much attention.

Conclusion: This study conducted a comprehensive, objective, and visual analysis of publications, and revealed the status of relevant studies, hot topics, and trends concerning fNIRS disease research from 2011 to 2022. It is hoped that this work would help researchers to identify new perspectives on potential collaborators, important topics, and research Frontiers.

KEYWORDS

functional near-infrared spectroscopy (fNIRS), CiteSpace, diseases, Frontiers, bibliometrics

1. Introduction

Functional near-infrared spectroscopy (fNIRS) is an optical neuroimaging technique used to quantify oxy- and deoxyhemoglobin content for functional brain imaging (Irani et al., 2007). As an emerging technology, fNIRS has played an increasingly important role in functional neuroimaging over the past 10 years (Ferrari and Quaresima, 2012; Rahman et al., 2020). In addition to its non-invasiveness, radiation-free nature, wearability and portability, and insensitivity to motion artifacts, fNIRS also provides higher temporal/spatial resolution than functional magnetic resonance imaging (fMRI) and electroencephalography (EEG). These advantages make fNIRS eminently suitable for application in special cohorts such as infants (Doi and Shinohara, 2017; McDonald and Perdue, 2018), patients with motor impairments (Gramigna et al., 2017; Ranchet et al., 2020), and patients with neurological conditions (Koike et al., 2013; Kumar et al., 2017).

Functional near-infrared spectroscopy has recently developed rapidly in conjunction with advancements in near-infrared spectroscopy (NIRS) hardware, applications, and data analysis methods (Pinti et al., 2020; Eastmond et al., 2022). It has been widely used for brain function assessments under various neuropsychiatric conditions, including, but not limited to, attention-deficit/hyperactivity disorder (ADHD), affective disorders, neuropathic pain, and cognitive impairment (Ehlis et al., 2014; Kumar et al., 2017; Yeung and Chan, 2020). Meanwhile, multimodal neuroimaging studies that include fNIRS are ideally suited to examine brain function. For example, EEG-fNIRS examinations can be used to identify more features correlated with brain activation and connectivity (Muthalib et al., 2013).

With the increase in fNIRS research, several scholars have summarized the research on the application of fNIRS to a specific disease or disease system (Koike et al., 2013; Doi and Shinohara, 2017; Kumar et al., 2017; McDonald and Perdue, 2018; Pinti et al., 2020). However, the overall application of fNIRS technology in assessing the brain imaging characteristics of disease activity has not been summarized. Determination of the global research trends and hotspots of fNIRS research on clinical diseases is important to provide references for future studies.

Therefore, in this study, CiteSpace was used to conduct a thorough bibliometric analysis of research related to the use of fNIRS for clinical diseases from 2011 to 2022. The purpose of our study was to provide scholars who have recently entered the field and others who will soon follow with new perspectives on the status of relevant studies, important topics, and trends concerning fNIRS in clinical disease research from a global perspective.

2. Materials and methods

2.1. Source and retrieval

In this study, Web of Science (WoS) was selected as the data source, and the "advanced search" method was adopted. The search formula was "TS = (fNIRS or functional near-infrared spectrum or near-infrared spectrum)." Literature published from 1 January 2011 to 31 January 2022 was searched, and only English language documents were eligible for subsequent analyses.

2.2. Inclusion and exclusion criteria

We limited this analysis to studies involving patients (adult patients or children). The types of studies included clinical trials and efficacy observation studies with more than two cases. Non-medical research papers, papers with animals/healthy individuals as research objects, technical exploration papers, degree papers, and case reports, etc., were excluded.

2.3. Screening method

Two reviewers independently screened the articles by evaluating the titles and abstracts on the basis of the inclusion criteria described above. The full text of the articles was reviewed if necessary. Disagreements were discussed and resolved by the two reviewers, and further disputes were arbitrated by a third reviewer.

A total of 5,612 related studies were retrieved from the WoS core database. After screening the literature in accordance with the criteria described above, 467 studies were finally included. The specific process is shown in **Figure 1**.

2.4. Data acquisition and analytical tools

This study used CiteSpace 6.1.R3 for analysis by combining the literature metrology method, visual analysis method, and data mining algorithm. The relevant documents were manually screened and exported in the pure text format with the name "download_xx.txt." Duplicate records were removed in CiteSpace and stored in the data folder. The exported information included data regarding the author, title, keywords, abstract, source publication, document type, citation frequency, highly cited papers, research direction, and page number.

In the visual diagram, each node represents an element, and the size of the node represents the frequency of occurrence. The connection line represents the cooperation or connection between the elements. Nodes showing high betweenness centrality (> 0.1) are usually considered to be key points in the field. CiteSpace highlights nodes with high betweenness centrality using purple trims. Highly cited elements are often considered to be research hotspots in that particular field. Three special indicators–latent semantic indexing (LSI), log-likelihood test (LLR), and mutual information test (MI)–were used in the cluster analysis, and we mainly observed the outcomes of LLR, which provided the best result in terms of themes associated with a cluster. The CiteSpace parameters were as follows: time-slicing, from January 2011 to January 2022 (1 year per slice); term source, all selection; node type, choose one at a time; and pruning, pathfinder.

3. Results

3.1. Annual publication trends

A total of 467 publications were included. From 1 January 2011 to 31 January 2022, the total number of studies involving fNIRS

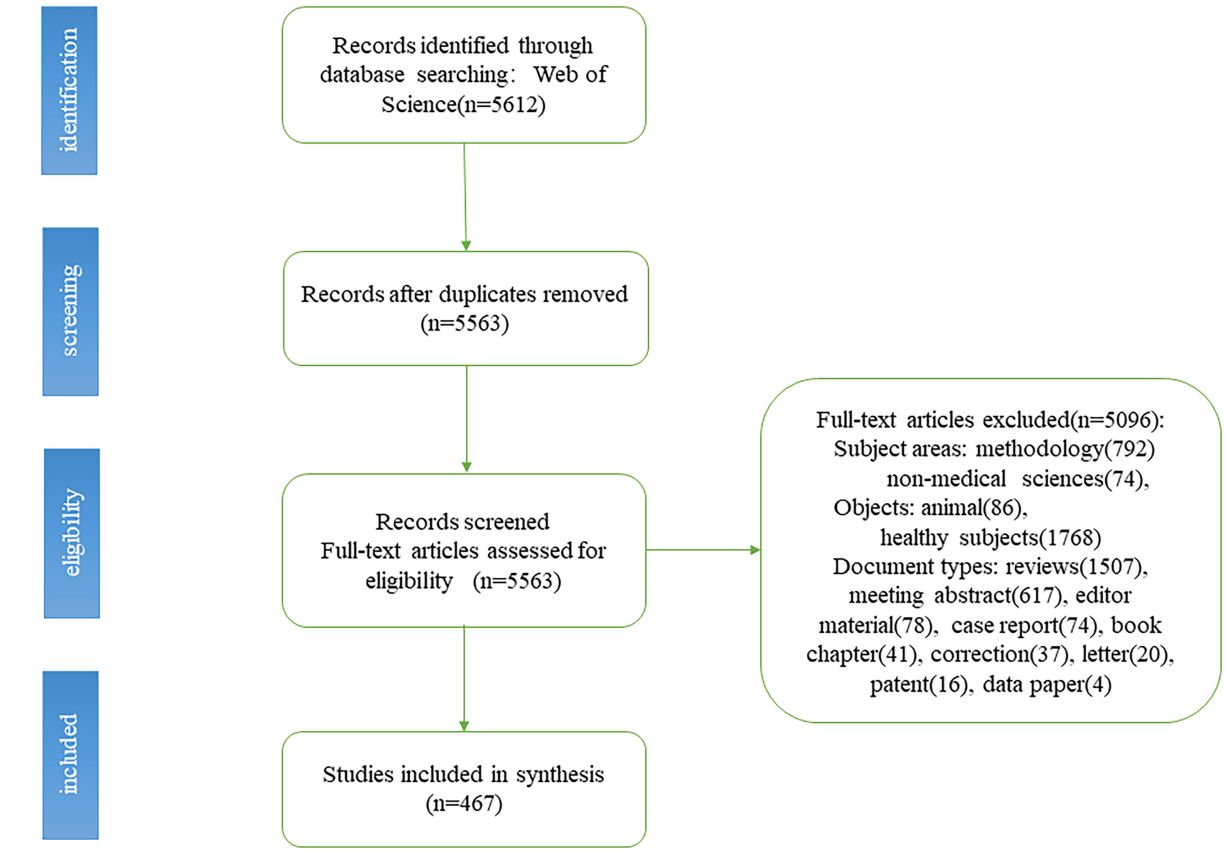

FIGURE 1
Flow chart of functional near-infrared spectroscopy (fNIRS) studies inclusion.

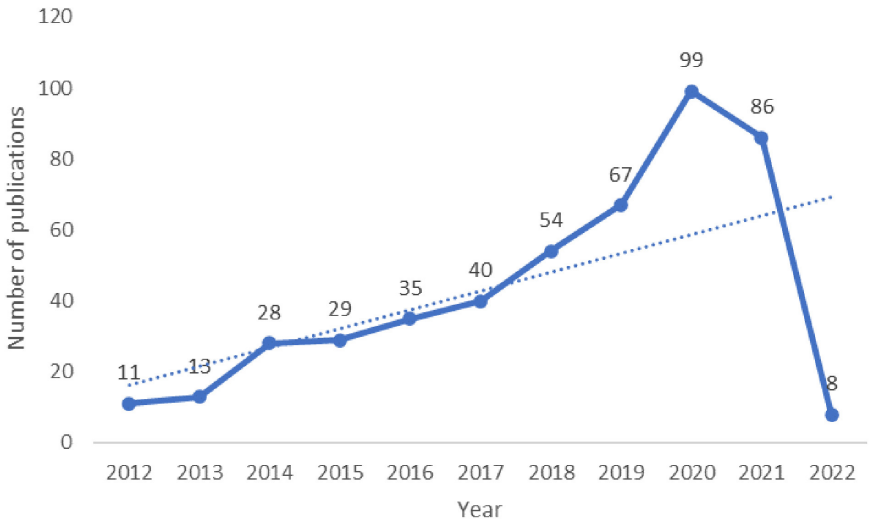

FIGURE 2
Annual publication outputs and the model fitting curve of time trend of relevant publications.

for disease research gradually increased and reached the highest value in 2019. Although the included literature from 2022 did not represent the complete year, the overall trend was still upward (Figure 2), and since 2018, the total number of articles published each year has exceeded 50.

3.2. Analysis by country/region

The maps drawn in the national visual analysis included 39 countries and 82 connection lines. The top three countries in terms of the number of articles published were the USA, China, and

Japan (Figure 3). The number of articles published by authors from these countries was 134, 83, and 70, respectively. Notably, only China (ranked 2nd) entered the top 10 as a developing country, while the remaining nations are all developed countries. Purple rings indicated countries with high centrality (≥ 0.1). The top five countries in terms of centrality were USA (0.74), Germany (0.39), China (0.34), England (0.32), and Canada (0.27). These five countries were influential in the field of fNIRS research.

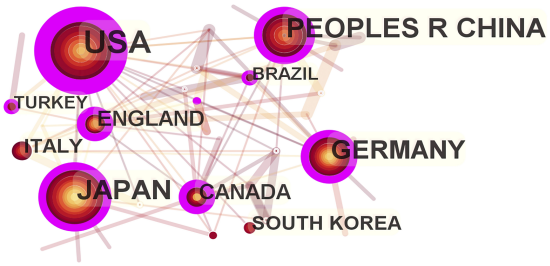

FIGURE 3
Map of active country in functional near-infrared spectroscopy (fNIRS) research on diseases.

3.3. Analysis by institution

As shown in the institutional visualization map, 280 institutions contributed to the literature on fNIRS in disease research. Among these, six institutions had contributed more than 10 studies (frequency in brackets): University of Tubingen (26), Drexel University (15), Jichi Medical University (11), Ankara University (11), Beijing Normal University (10), and Peking University (10), as shown in Figure 4. Most of the contributing institutions were universities.

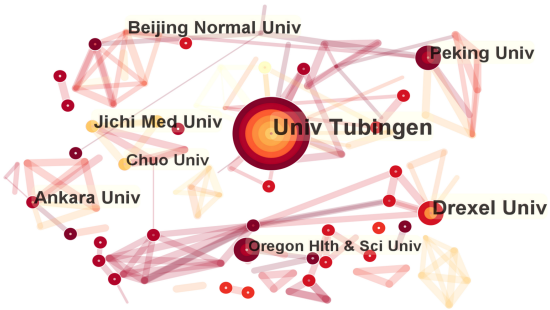

FIGURE 4
Map of active institution in functional near-infrared spectroscopy (fNIRS) research on diseases.

3.4. Analysis by authors

The number of nodes in the author visualization map was 266, and the number of connections was 854. The following eight authors had published more than 10 papers, and they represented the major researchers and teams conducting in-depth research with fNIRS from 2011 to 2022 (frequency in brackets): Andreas J Fallgatter (28) and Ann-Christine Ehlis (22) from University of Tubingen, Meltem Izzetoglu (14) from Drexel University, Yuduo Wang (11) from Beijing Information Science and Technology University, Xiaoli Li (11) from Beijing Normal University, Ippeita Dan (11) from Chuo University, Bora Baskak (10) from Ankara University, and Jun Li (10) from South China Normal University (Figure 5).

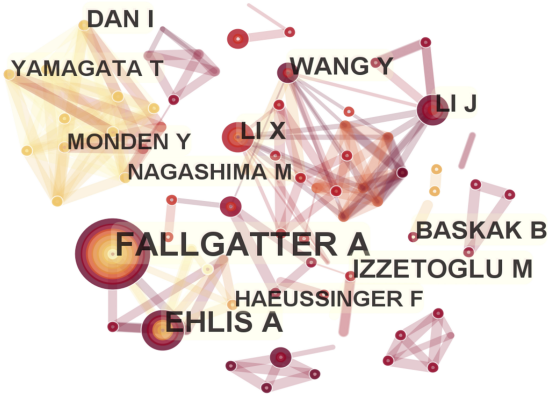

FIGURE 5
Map of active authors in functional near-infrared spectroscopy (fNIRS) research on diseases.

3.5. Analysis of the journals and cited journals

A total of 175 journals published papers on the application of fNIRS in disease, Table 1 shows the top 10 academic journals that published related papers, with the average impact factor (IF) 4.251 (median 4.37; range 3.333–4.997). The journals with more than 20 publications are Scientific Reports and Frontiers in Human Neuroscience. In this study, a map of 432 nodes and 1,868 connecting lines was formed after visual analysis of the cited journals (Figure 6). For the top 10 cited journals shown in Table 2, the average IF was 7.439 (median 6.054; range 3.054–15.255). The top five cited journals were Neuroimage, PLoS One, Human Brain Mapping, Frontiers in Human Neuroscience, and Brain. Except for PLoS One, the other four journals were brain imaging journals.

3.6. Analysis of keywords

The keyword co-occurrence map included 343 nodes and 1,209 connecting lines (Figure 7). Nine keywords occurred more than 50 times. Excluding the words related to the retrieval strategy, the top seven keywords were activation, prefrontal cortex (PFC), working memory, cortex, fMRI, performance, and brain. Keywords with high centrality were brain (0.18), cortex (0.15), abnormality (0.12), and PFC (0.1).

Fifty-four cluster labels were obtained by using LLR algorithm. The mean silhouette was 0.9578, with good homogeneity and reliable results. The top 10 clusters were #0 verbal fluency task, #1 graph theory, #2 concussion, #3 gait, #4 optical topography, #5 stimulus-specific adaptation, #6 primary motor

TABLE 1 The top 10 journals for functional near-infrared spectroscopy (fNIRS) research on diseases.

Rank	Journal	Frequency	Country	IF (2021)*	CiteScore
1	Scientific Reports	24	England	4.997	6.9
2	Frontiers in Human Neuroscience	23	Switzerland	3.473	4.6
3	Neuroimage-clinical	18	Netherlands	4.891	8.2
4	Neurophotonics	17	USA	4.212	8.3
5	Neurorehabilitation and Neural Repair	14	USA	4.895	6.1
6	PLoS One	13	USA	3.752	5.6
7	Brain Sciences	12	Switzerland	3.333	3.1
8	IEEE Transactions on Neural Systems and Rehabilitation Engineering	11	USA	4.528	8.1
9	Schizophrenia Research	9	Netherlands	4.662	8
10	Biomedical Optics Express	9	USA	3.562	6.7

*IF, impact factor; IF in category according to journal citation reports (2021).

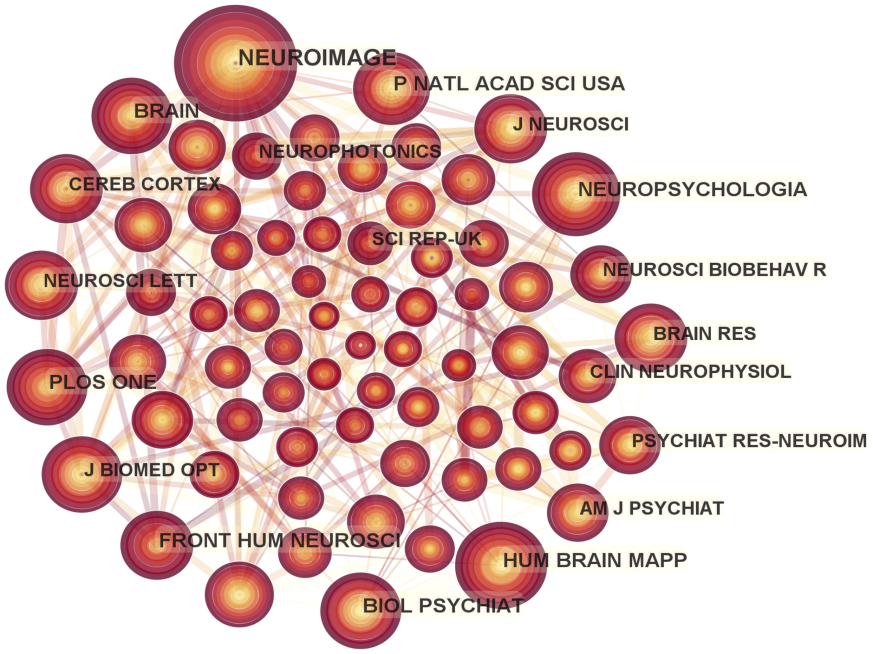

FIGURE 6
Map of cited journals in functional near-infrared spectroscopy (fNIRS) research on diseases.

cortex, #7 motor control, #8 cue reactivity, and #9 multimodal neuroimaging. The main clusters and their keywords are shown in Table 3.

The keyword burst analysis indicated 14 outbreak points, as shown in Table 4. The points with high outbreak intensity were as follows: Executive function (2017–2021), optical topography (2012–2015), and functional connectivity (2017–2021). These points represent important aspects in the field of disease research with fNIRS. Research burst is considered to be continuous. Topics such as executive function, functional connectivity, performance, diagnosis, Alzheimer's disease, children, and adolescents have the potential to continue to become research hotspots in the near future, and represent research content and topics worthy of special attention.

3.7. Analysis of references

Visual analysis of co-cited references was performed in CiteSpace, and a map with 4,072 nodes and 14,308 connections was generated. The top five co-cited references are listed in Table 5, which are five reviews that introduce the instruments and methods in near-infrared spectral imaging technology (Ehlis et al., 2014), the history of development and application fields of fNIRS (Ferrari and Quaresima, 2012), the applications of fNIRS in psychiatry (Scholkmann et al., 2014), the functional research progress of fNIRS in the last 20 years (Boas et al., 2014), and evidence-based suggestions for fNIRS walking research design and signal analysis technology (Vitorio et al., 2017).

TABLE 2 The top 10 co-cited journals for functional near-infrared spectroscopy (fNIRS) research on diseases.

Rank	Journal	Frequency	Country	IF (2021)	CiteScore
1	Neuroimage	402	USA	7.400	11.2
2	PLoS One	235	USA	3.752	5.6
3	Human Brain Mapping	210	USA	5.399	8.3
4	Frontiers in Human Neuroscience	194	Switzerland	3.473	4.6
5	Brain	172	England	15.255	19.7
6	Biological Psychiatry	150	USA	12.810	21.5
7	Neuropsychologia	150	England	3.054	5.8
8	Proceedings of the National Academy of Sciences	149	USA	12.778	18.1
9	Journal of Neuroscience	138	USA	6.709	10.2
10	Journal of Biomedical Optics	135	USA	3.758	6.6

The burst citations of references indicate numerous citations of the manuscript over a certain period of time. Table 6 shows the 11 studies with the strongest reference bursts from 2011 to 2021. The strongest reference burst was recorded for a review of the development history and application fields of fNIRS in humans published by Ferrari and Quaresima (2012). A more recent study with a reference burst was a paper published by Nieuwhof et al. (2016).

4. Discussion

As a non-invasive brain functional imaging technique, fNIRS plays an increasingly important role in the detection of function-related activity. The current study applied a visualization-based bibliometric method to analyze the profiles, research hotspots, and research trends in relation to the use of fNIRS technology in disease research. fNIRS is gradually becoming an important technique for the studying related diseases in the field of neuroimaging.

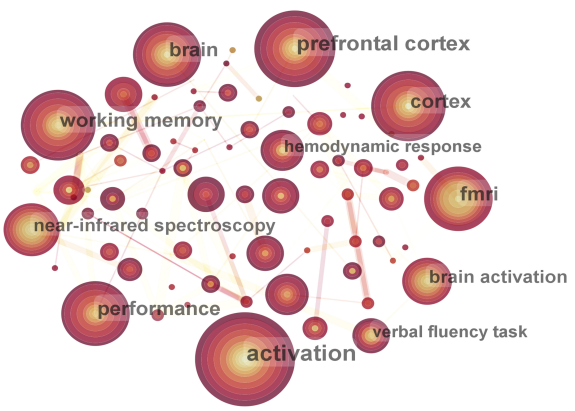

FIGURE 7
Map of active keywords in functional near-infrared spectroscopy (fNIRS) research on diseases.

4.1. General information regarding fNIRS research on diseases

In terms of the country-wise distribution of the published literature on this topic, the USA ranks first in the number and centrality of literature, indicating its leading position in this research field. The brain program implemented by the National Institutes of Health (NIH) in the USA since 2013 has provided huge financial support and driven advancements in clinical research in neuroimaging. The major institutions contributing to the research output in this topic were University of Tubingen in Germany, Drexel University in USA, and Jichi Medical University in Japan, which was consistent with the analysis results of national distribution. Among the most prolific authors, Andreas J Fallgatter and Ann-Christine Ehlis published as many as 16 manuscripts, mainly focusing on ADHD and depression (Ehlis et al., 2007; Zeller et al., 2010; Marx et al., 2014; Metzger et al., 2016a,b). However, the findings indicate that institutional and author cooperations are lacking and need to be strengthened. In addition to the emphasis on neuroimaging, the research direction of journals indicates that most of the publications involve neuroscience, psychiatry, and multidisciplinary sciences. Further collaboration should be implemented in the future to obtain more significant evidence.

4.2. Research hotspots and trends in fNIRS research on diseases

Disease research using fNIRS was more focused on the activation of brain regions of patients in the task state, with an emphasis on the PFC. The typical activation of fNIRS in observed in the cerebral cortex area, that is, the increase in oxygenated hemoglobin (HbO) and the relative decrease in deoxygenated hemoglobin (HHb) reflect the increase in local cerebral blood capacity caused by increased local arterial vascular relaxation. The PFC is closely related to cognitive functions such as working memory, stimulus selection, rule switching, and decision-making (Ott and Nieder, 2019), and its dysfunction is associated

TABLE 3 The list of main keyword clusters.

Cluster ID	Size	Silhouette	Mean (year)	Top terms (LSI)*	Top terms (LLR)*	Terms (MI)*
0	76	0.909	2015	Prefrontal cortex	Verbal fluency task	Percussion
1	74	0.906	2016	Functional near-infrared spectroscopy	Graph theory	Discrimination
2	74	0.963	2014	Activation	Concussion	Motor inhibition
3	71	0.905	2015	Prefrontal cortex	Gait	Cerebral oxygenation
4	64	0.951	2015	Optical topography	Optical topography	Inhibitory task-evoked activation
5	59	0.975	2016	Functional near-infrared spectroscopy	Stimulus-specific adaptation	Stimulus-specific adaptation
6	55	0.952	2016	Functional near-infrared spectroscopy	Primary motor cortex	Upper limb reduction
7	55	0.984	2015	Motor control	Motor control	Brain map
8	51	0.978	2016	Optical topography	Cue reactivity	Cue exposure
9	51	0.947	2017	Functional near-infrared spectroscopy	Multimodal neuroimaging	Brain computer interface

*LSI, latent semantic indexing; LLR, log-likelihood test; MI, mutual information test.

TABLE 4 Top 12 keywords with the strongest citation bursts.

Keywords	Year	Strength	Begin	End	2011–2021
Optical topography	2011	3.94	2012	2015	
Near-infrared spectroscopy	2011	3.55	2012	2013	
Blood flow	2011	3	2013	2014	
fMRI	2011	2.99	2014	2015	
Plasticity	2011	3.07	2017	2018	
Executive function	2011	5.09	2019	2021	
Functional connectivity	2011	3.92	2019	2021	
Performance	2011	3.67	2019	2021	
Diagnosis	2011	3	2019	2021	
Alzheimer's disease	2011	2.99	2019	2021	
Children	2011	2.99	2019	2021	
Adolescent	2011	2.77	2019	2021	

TABLE 5 Top five cited references related to functional near-infrared spectroscopy (fNIRS) research on diseases.

Ranking	Co-cited counts	Co-cited reference	References
1	29	Application of functional near-infrared spectroscopy in psychiatry.	Ehlis et al., 2014
2	29	A brief review on the history of human functional near-infrared spectroscopy (fNIRS) development and fields of application.	Ferrari and Quaresima, 2012
3	29	A review on continuous wave functional near-infrared spectroscopy and imaging instrumentation and methodology.	Scholkmann et al., 2014
4	26	Twenty years of functional near-infrared spectroscopy: introduction for the special issue.	Boas et al., 2014
5	18	fNIRS response during walking—artifact or cortical activity? A systematic review.	Vitorio et al., 2017

with social deficits, affective disturbances and memory loss in brain disorders including autism, schizophrenia, depression, and Alzheimer's disease (AD) (Yan and Rein, 2022). For example, Krishnamurthy et al. found that children with autism had altered PFC function, manifested by PFC hyperactivation and decreased right frontal connectivity (Krishnamurthy et al., 2020).

TABLE 6 Top 11 co-cited references with the strongest citation bursts.

References	Year	Strength	Begin	End	2011–2021
Schecklmann et al., 2008	2008	5.9	2011	2013	
Schecklmann et al., 2010	2010	3.27	2011	2013	
Negoro et al., 2010	2010	3.17	2012	2014	
Rubia et al., 2009	2009	2.54	2012	2014	
Ferrari and Quaresima, 2012	2012	9.23	2013	2017	
Cui et al., 2011	2011	4.68	2013	2016	
Holtzer et al., 2011	2011	3.27	2013	2016	
Haeussinger et al., 2011	2011	4.93	2014	2016	
Sasai et al., 2011	2011	3.45	2014	2016	
Kirilina et al., 2012	2012	2.73	2014	2017	
Nieuwhof et al., 2016	2016	2.9	2018	2021	

Xiang et al. found that the activation of the extensive PFC was significantly reduced in patients with schizophrenia and major depressive disorder (MDD), especially in certain channels of the dorsolateral PFC (DLPFC) (Xiang et al., 2021). Tang and Chan found that the functional connectivity of PFC in patients with AD generally decreased, the laterality became insignificant, and the clustering coefficient decreased significantly (Tang and Chan, 2018). Working memory is a memory system that temporarily processes and stores information and is an important basis for complex cognitive tasks (Baddeley, 1992). The PFC is thought to play a key role in encoding, updating, and maintaining internal representations of task situations in working memory (D'Ardenne et al., 2012). fNIRS can quantify the workload of PFC during experimental conditions (Herff et al., 2013), which is helpful for the neuropsychological assessment of working memory under n-back tasks (León-Domínguez et al., 2015). The "Verbal Fluency Task (VFT)," which showed the largest cluster in keyword clustering, is a neuropsychological task involving multiple cognitive domains, which can reflect the fluency of individuals in using language to transmit information (Liu et al., 2022). The combined monitoring of fNIRS and VFT provides neural evidence of executive function in patients and is widely used in the diagnosis and differential diagnosis of depression, bipolar disorder, and schizophrenia (Koike et al., 2013; Downey et al., 2019; Feng et al., 2021; Xiang et al., 2021; Gao et al., 2022). The primary motor cortex (M1) is involved in the control of advanced gait movements (McCrimmon et al., 2018). When the function of the motor cortex changes due to brain injury, stroke, Parkinson's disease and other diseases, it may lead to abnormal gait. Clinically, regulating the activity of M1 may be an effective treatment to improve the motor function of patients (Underwood and Parr-Brownlie, 2021). In addition, motor control, defined as the ability to regulate or manage the mechanisms necessary for movement (Levin and Piscitelli, 2022), is an effective rehabilitation strategy for abnormal gait after stroke and is an important theory in clinical rehabilitation at present (Beyaert et al., 2015). fMRI is the gold standard for functional imaging of the brain, but it suffers from some shortcomings in terms of temporal resolution. The sampling rate of fNIRS can reach 0.1 s, and at the same time, there is a strong correlation between the hemoglobin signal of fNIRS and the BOLD signal of fMRI (Strangman et al., 2002). Multimodal neuroimaging can complement each other and provide more information.

Keyword bursts indicate emerging trends and potentially valuable research directions to a certain extent. In this study, executive function, functional connectivity, performance, diagnosis, AD, children, and adolescent were the most recent burst keywords. The relevance of these keywords can be summarized as follows: (1) Executive function, including working memory, cognitive flexibility and inhibition, is closely related to PFC function (Jones and Graff-Radford, 2021). Executive dysfunction is extremely common in neurological diseases (Rabinovici et al., 2015). fNIRS studies of ADHD showed hypoactivity in the right PFC in multiple executive function tasks, which was essentially consistent with the results of fMRI (Gossé et al., 2022). (2) Functional connectivity refers to the information flow between brain networks to explore the interactions between different brain functional areas, which is an important area of disease research, especially for diseases considered to be related to connectivity. In this regard, narrowband resting-state functional connectivity based on fNIRS measurements can be used for prediction of autism spectrum disorder (Sun et al., 2021). (3) By tracking the progression of working memory tasks, fNIRS revealed a link between brain activity and task performance (Meidenbauer et al., 2021). During cooperative tasks, better task performance was associated with interpersonal brain synchronization (Zhou et al., 2022). Patients with schizophrenia (SZ) performed worse on the VFT than patients with MDD and healthy controls, and patients performed worse on the Tower of London task than healthy controls (Xiang et al., 2021). (4) In terms of disease diagnosis and identification, Zhu et al. studied the brain function of autistic patients during related tasks through fNIRS (Zhu et al., 2015; Li and Yu, 2016; Vo et al., 2021); Li et al. found that the HbO concentration in the region of interest changed sharply as the disease severity progressed from mild cognitive impairment to moderate/severe dementia (Li et al., 2018; Nakamura et al., 2021); Stuart et al. measured the activity of the PFC during a task by using fNIRS to distinguish patients with Parkinson's disease and healthy individuals (Stuart et al., 2019); and Chou et al. used fNIRS to measure the correlation between the activation of

specific brain regions in patients with schizophrenia and their clinical symptoms and functional results (Chou et al., 2020), facilitating clinical differentiation of schizophrenia, depression and bipolar disorder (Kumar et al., 2017). (5) fNIRS is also of great significance in the early diagnosis of AD (Perpetuini et al., 2019), since it can distinguish AD from normal aging based on functional connectivity (Tang and Chan, 2018), and can be used for AD screening with the help of refined PFC working memory-related networks (Kim et al., 2021). fNIRS revealed different patterns of activation in the frontoparietal cortex between AD and behavioral-subtype frontotemporal dementia (Metzger et al., 2016b), and showed more severe disruption of connectivity and frontal oxygenation changes in AD patients than in patients with mild cognitive impairment patients (Yeung and Chan, 2020), which can facilitate AD diagnosis and identification of disease progression. (6) Because of its high ecological efficiency, fNIRS can be used to conduct functional neuroimaging research in a participant-friendly environment (Chou et al., 2020). Moreover, fNIRS also shows a high tolerance for the influence of patients' head movements. Thus, it is particularly useful in research on infants and adolescents, and is widely used in the studies of ADHD, Parkinson's disease, epilepsy, etc.

Our analysis of the cited references shows that continuous advancements and improvements in fNIRS instruments and technical methods will provide strong conditions for expanding the field of disease research on the basis of existing experience. The recent burst reference reflects research on testing the effectiveness and development prospects of fNIRS by measuring the PFC activity in Parkinson's disease patients during dual-task walking, which was published by Nieuwhof et al. (2016).

4.3. Limitations

Although we performed a comprehensive, objective, and visual analysis of publications related to the use of fNIRS in clinical disease research and the relevant developing trends, this study still had some limitations. First, the topic search was only conducted in WoS and did not include other databases, such as China National Knowledge Infrastructure (CNKI). Second, bibliometric software cannot distinguish the abbreviation of the terms with different names, potentially causing deviations in the statistical results.

5. Conclusion

In conclusion, this study revealed the status of relevant studies, important topics, and trends related to the use of fNIRS in clinical disease research from 2011 to 2022. Over the past decade, the number of relevant articles has grown significantly. In addition, scholars can use fNIRS technology to conduct more relevant neuroscience research in children and adolescents. Notably, AD is another hot topic in this field. As a relatively new neurological imaging technique, fNIRS has developed rapidly in the field of disease diagnosis. Simultaneously, using the advantages of fNIRS, researchers can strengthen the combination of fNIRS with traditional imaging technology.

Author contributions

XYe, RS, and FL conceptualized the study. LH, XYa, YZ, and YS collected the data. XYe, LP, and NS analyzed the data and drafted the manuscript. XYe, NS, JX, RS, and FL revised the final version of the manuscript. All authors contributed to the article and approved the submitted version.

Funding

This work was supported by the Major Project of the National Natural Science Foundation of China (No. 81590951) and the National Natural Science Foundation of China for the Youth (No. 81904096).

Conflict of interest

The authors declare that the research was conducted in the absence of any commercial or financial relationships that could be construed as a potential conflict of interest.

Publisher's note

All claims expressed in this article are solely those of the authors and do not necessarily represent those of their affiliated organizations, or those of the publisher, the editors and the reviewers. Any product that may be evaluated in this article, or claim that may be made by its manufacturer, is not guaranteed or endorsed by the publisher.

References

Baddeley, A. (1992). Working memory. *Science (New York, NY)* 255, 556–559.

Beyaert, C., Vasa, R., and Frykberg, G. E. (2015). Gait post-stroke: Pathophysiology and rehabilitation strategies. *Neurophysiol. Clin. Clin. Neurophysiol.* 45, 335–355.

Boas, D. A., Elwell, C. E., Ferrari, M., and Taga, G. (2014). Twenty years of functional near-infrared spectroscopy: Introduction for the special issue. *Neuroimage* 85(Pt 1), 1–5. doi: 10.1016/j.neuroimage.2013.11.033

Chou, P. H., Huang, C. J., and Sun, C. W. (2020). The potential role of functional near-infrared spectroscopy as clinical biomarkers in schizophrenia. *Curr. Pharm. Des.* 26, 201–217. doi: 10.2174/1381612825666191014164511

Cui, Y., Liu, B., Luo, S., Zhen, X., Fan, M., Liu, T., et al. (2011). Identification of conversion from mild cognitive impairment to Alzheimer's disease using multivariate predictors. *PLoS One* 6:e21896. doi: 10.1371/journal.pone.0021896

D'Ardenne, K., Eshel, N., Luka, J., Lenartowicz, A., Nystrom, L. E., and Cohen, J. D. (2012). Role of prefrontal cortex and the midbrain dopamine system in working memory updating. *Proc. Natl. Acad. Sci. U.S.A.* 109, 19900–19909. doi: 10.1073/pnas.1116727109

Doi, H., and Shinohara, K. (2017). fNIRS studies on hemispheric asymmetry in atypical neural function in developmental disorders. *Front. Hum. Neurosci.* 11:137. doi: 10.3389/fnhum.2017.00137

Downey, D., Brigadoi, S., Trevithick, L., Elliott, R., Elwell, C., McAllister-Williams, R. H., et al. (2019). Frontal haemodynamic responses in depression and the effect of electroconvulsive therapy. *J. Psychopharmacol.* 33, 1003–1014. doi: 10.1177/0269881119858313

Eastmond, C., Subedi, A., De, S., and Intes, X. (2022). Deep learning in fNIRS: A review. *Neurophotonics* 9:041411. doi: 10.1117/1.NPh.9.4.041411

Ehlis, A. C., Herrmann, M. J., Plichta, M. M., and Fallgatter, A. J. (2007). Cortical activation during two verbal fluency tasks in schizophrenic patients and healthy controls as assessed by multi-channel near-infrared spectroscopy. *Psychiatry Res.* 156, 1–13. doi: 10.1016/j.pscychresns.2006.11.007

Ehlis, A. C., Schneider, S., Dresler, T., and Fallgatter, A. J. (2014). Application of functional near-infrared spectroscopy in psychiatry. *Neuroimage* 85(Pt 1), 478–488. doi: 10.1016/j.neuroimage.2013.03.067

Feng, K., Law, S., Ravindran, N., Chen, G. F., Ma, X. Y., Bo, X., et al. (2021). Differentiating between bipolar and unipolar depression using prefrontal activation patterns: Promising results from functional near infrared spectroscopy (fNIRS) findings. *J. Affect. Disord.* 281, 476–484. doi: 10.1016/j.jad.2020.12.048

Ferrari, M., and Quaresima, V. (2012). A brief review on the history of human functional near-infrared spectroscopy (fNIRS) development and fields of application. *Neuroimage* 63, 921–935. doi: 10.1016/j.neuroimage.2012.03.049

Gao, C., Zhou, H., Liu, J., Xiu, J., Huang, Q., Liang, Y., et al. (2022). Characteristics of frontal activity relevant to cognitive function in bipolar depression: An fNIRS study. *Biomed. Opt. Express* 13, 1551–1563. doi: 10.1364/BOE.448244

Gossé, L. K., Bell, S. W., and Hosseini, S. M. H. (2022). Functional near-infrared spectroscopy in developmental psychiatry: A review of attention deficit hyperactivity disorder. *Eur. Arch. Psychiatry Clin. Neurosci.* 272, 273–290. doi: 10.1007/s00406-021-01288-2

Gramigna, V., Pellegrino, G., Cerasa, A., Cutini, S., Vasta, R., Olivadese, G., et al. (2017). Near-infrared spectroscopy in gait disorders: Is it time to begin. *Neurorehabil. Neural. Repair* 31, 402–412. doi: 10.1177/1545968317693304

Haeussinger, F. B., Heinzel, S., Hahn, T., Schecklmann, M., Ehlis, A. C., and Fallgatter, A. J. (2011). Simulation of near-infrared light absorption considering individual head and prefrontal cortex anatomy: Implications for optical neuroimaging. *PLoS One* 6:e26377. doi: 10.1371/journal.pone.0026377

Herff, C., Heger, D., Fortmann, O., Hennrich, J., Putze, F., and Schultz, T. (2013). Mental workload during n-back task-quantified in the prefrontal cortex using fNIRS. *Front. Hum. Neurosci.* 7:935. doi: 10.3389/fnhum.2013.00935

Holtzer, R., Mahoney, J. R., Izzetoglu, M., Izzetoglu, K., Onaral, B., and Verghese, J. (2011). fNIRS study of walking and walking while talking in young and old individuals. *J. Gerontol. A Biol. Sci. Med. Sci.* 66, 879–887. doi: 10.1093/gerona/glr068

Irani, F., Platek, S. M., Bunce, S., Ruocco, A. C., and Chute, D. (2007). Functional near infrared spectroscopy (fNIRS): An emerging neuroimaging technology with important applications for the study of brain disorders. *Clin. Neuropsychol.* 21, 9–37. doi: 10.1080/13854040600910018

Jones, D. T., and Graff-Radford, J. (2021). Executive dysfunction and the prefrontal cortex. *Continuum (Minneap Minn)* 27, 1586–1601. doi: 10.1212/CON.0000000000001009

Kim, E., Yu, J. W., Kim, B., Lim, S. H., Lee, S. H., Kim, K., et al. (2021). Refined prefrontal working memory network as a neuromarker for Alzheimer's disease. *Biomed. Opt. Express* 12, 7199–7222. doi: 10.1364/BOE.438926

Kirilina, E., Jelzow, A., Heine, A., Niessing, M., Wabnitz, H., Brühl, R., et al. (2012). The physiological origin of task-evoked systemic artefacts in functional near infrared spectroscopy. *Neuroimage* 61, 70–81. doi: 10.1016/j.neuroimage.2012.02.074

Koike, S., Nishimura, Y., Takizawa, R., Yahata, N., and Kasai, K. (2013). Near-infrared spectroscopy in schizophrenia: A possible biomarker for predicting clinical outcome and treatment response. *Front. Psychiatry* 4:145. doi: 10.3389/fpsyt.2013.00145

Krishnamurthy, K., Yeung, M. K., Chan, A. S., and Han, Y. M. Y. (2020). Effortful control and prefrontal cortex functioning in children with autism spectrum disorder: An fNIRS study. *Brain Sci.* 10:880. doi: 10.3390/brainsci10110880

Kumar, V., Shivakumar, V., Chhabra, H., Bose, A., Venkatasubramanian, G., and Gangadhar, B. N. (2017). Functional near infra-red spectroscopy (fNIRS) in schizophrenia: A review. *Asian J. Psychiatr.* 27, 18–31. doi: 10.1016/j.ajp.2017.02.009

León-Domínguez, U., Martín-Rodríguez, J. F., and León-Carrión, J. (2015). Executive n-back tasks for the neuropsychological assessment of working memory. *Behav. Brain Res.* 292, 167–173. doi: 10.1016/j.bbr.2015.06.002

Levin, M. F., and Piscitelli, D. (2022). Motor control: A conceptual framework for rehabilitation. *Motor Cont.* 26, 497–517. doi: 10.1123/mc.2022-0026

Li, R., Rui, G., Chen, W., Li, S., Schulz, P. E., and Zhang, Y. (2018). Early detection of Alzheimer's disease using non-invasive near-infrared spectroscopy. *Front. Aging Neurosci.* 10:366. doi: 10.3389/fnagi.2018.00366

Li, Y., and Yu, D. (2016). Weak network efficiency in young children with Autism Spectrum Disorder: Evidence from a functional near-infrared spectroscopy study. *Brain Cogn.* 108, 47–55. doi: 10.1016/j.bandc.2016.07.006

Liu, X., Cheng, F., Hu, S., Wang, B., Hu, C., Zhu, Z., et al. (2022). Cortical activation and functional connectivity during the verbal fluency task for adolescent-onset depression: A multi-channel NIRS study. *J. Psychiatr Res.* 147, 254–261. doi: 10.1016/j.jpsychires.2022.01.040

Marx, A. M., Ehlis, A. C., Furdea, A., Holtmann, M., Banaschewski, T., Brandeis, D., et al. (2014). Near-infrared spectroscopy (NIRS) neurofeedback as a treatment for children with attention deficit hyperactivity disorder (ADHD)-a pilot study. *Front. Hum. Neurosci.* 8:1038. doi: 10.3389/fnhum.2014.01038

McCrimmon, C. M., Wang, P. T., Heydari, P., Nguyen, A., Shaw, S. J., Gong, H., et al. (2018). Electrocorticographic encoding of human gait in the leg primary motor cortex. *Cereb. Cortex (New York, NY: 1991)* 28, 2752–2762. doi: 10.1093/cercor/bhx155

McDonald, N. M., and Perdue, K. L. (2018). The infant brain in the social world: Moving toward interactive social neuroscience with functional near-infrared spectroscopy. *Neurosci. Biobehav. Rev.* 87, 38–49. doi: 10.1016/j.neubiorev.2018.01.007

Meidenbauer, K. L., Choe, K. W., Cardenas-Iniguez, C., Huppert, T. J., and Berman, M. G. (2021). Load-dependent relationships between frontal fNIRS activity and performance: A data-driven PLS approach. *Neuroimage* 230:117795. doi: 10.1016/j.neuroimage.2021.117795

Metzger, F. G., Hobert, M. A., Ehlis, A. C., Hasmann, S. E., Hahn, T., Eschweiler, G. W., et al. (2016a). Dual tasking for the differentiation between depression and mild cognitive impairment. *Front. Aging Neurosci.* 8:235. doi: 10.3389/fnagi.2016.00235

Metzger, F. G., Schopp, B., Haeussinger, F. B., Dehnen, K., Synofzik, M., Fallgatter, A. J., et al. (2016b). Brain activation in frontotemporal and Alzheimer's dementia: A functional near-infrared spectroscopy study. *Alzheimers Res. Ther.* 8:56. doi: 10.1186/s13195-016-0224-8

Muthalib, M., Anwar, A. R., Perrey, S., Dat, M., Galka, A., Wolff, S., et al. (2013). Multimodal integration of fNIRS, fMRI and EEG neuroimaging. *Clin. Neurophysiol.* 124, 2060–2062. doi: 10.1016/j.clinph.2013.03.018

Nakamura, S., Yomota, S., Ito, H., Akinaga, N., Hori, A., Chinomi, K., et al. (2021). A novel cognitive function scale using functional near-infrared spectroscopy for evaluating cognitive dysfunction. *J. Alzheimers Dis.* 81, 1579–1588. doi: 10.3233/JAD-210072

Negoro, H., Sawada, M., Iida, J., Ota, T., Tanaka, S., and Kishimoto, T. (2010). Prefrontal dysfunction in attention-deficit/hyperactivity disorder as measured by near-infrared spectroscopy. *Child Psychiatry Hum. Dev.* 41, 193–203. doi: 10.1007/s10578-009-0160-y

Nieuwhof, F., Reelick, M. F., Maidan, I., Mirelman, A., Hausdorff, J. M., Olde Rikkert, M. G., et al. (2016). Measuring prefrontal cortical activity during dual task walking in patients with Parkinson's disease: Feasibility of using a new portable fNIRS device. *Pilot Feasibility Stud.* 2:59. doi: 10.1186/s40814-016-0099-2

Ott, T., and Nieder, A. (2019). Dopamine and cognitive control in prefrontal cortex. *Trends Cogn. Sci.* 23, 213–234. doi: 10.1016/j.tics.2018.12.006

Perpetuini, D., Chiarelli, A. M., Cardone, D., Filippini, C., Bucco, R., Zito, M., et al. (2019). Complexity of frontal cortex fNIRS can support Alzheimer disease diagnosis in memory and visuo-spatial tests. *Entropy (Basel)* 21:E26. doi: 10.3390/e21010026

Pinti, P., Tachtsidis, I., Hamilton, A., Hirsch, J., Aichelburg, C., Gilbert, S., et al. (2020). The present and future use of functional near-infrared spectroscopy (fNIRS) for cognitive neuroscience. *Ann. N. Y. Acad. Sci.* 1464, 5–29. doi: 10.1111/nyas.13948

Rabinovici, G. D., Stephens, M. L., and Possin, K. L. (2015). Executive dysfunction. *Continuum (Minneap Minn)* 21, 646–659. doi: 10.1212/01.CON.0000466658.05156.54

Rahman, M. A., Siddik, A. B., Ghosh, T. K., Khanam, F., and Ahmad, M. (2020). A narrative review on clinical applications of fNIRS. *J. Digit. Imaging* 33, 1167–1184. doi: 10.1007/s10278-020-00387-1

Ranchet, M., Hoang, I., Cheminon, M., Derollepot, R., Devos, H., Perrey, S., et al. (2020). Changes in prefrontal cortical activity during walking and cognitive functions among patients with Parkinson's disease. *Front. Neurol.* 11:601686. doi: 10.3389/fneur.2020.601686

Rubia, K., Halari, R., Cubillo, A., Mohammad, A. M., Brammer, M., and Taylor, E. (2009). Methylphenidate normalises activation and functional connectivity deficits in attention and motivation networks in medication-naïve children with ADHD during a rewarded continuous performance task. *Neuropharmacology* 57, 640–652. doi: 10.1016/j.neuropharm.2009.08.013

Sasai, S., Homae, F., Watanabe, H., and Taga, G. (2011). Frequency-specific functional connectivity in the brain during resting state revealed by NIRS. *Neuroimage* 56, 252–257. doi: 10.1016/j.neuroimage.2010.12.075

Schecklmann, M., Ehlis, A. C., Plichta, M. M., Romanos, J., Heine, M., Boreatti-Hümmer, A., et al. (2008). Diminished prefrontal oxygenation with normal and above-average verbal fluency performance in adult ADHD. *J. Psychiatr. Res.* 43, 98–106. doi: 10.1016/j.jpsychires.2008.02.005

Schecklmann, M., Romanos, M., Bretscher, F., Plichta, M. M., Warnke, A., and Fallgatter, A. J. (2010). Prefrontal oxygenation during working memory in ADHD. *J. Psychiatr. Res.* 44, 621–628. doi: 10.1016/j.jpsychires.2009.11.018

Scholkmann, F., Kleiser, S., Metz, A. J., Zimmermann, R., Mata Pavia, J., Wolf, U., et al. (2014). A review on continuous wave functional near-infrared spectroscopy and imaging instrumentation and methodology. *Neuroimage* 85(Pt 1), 6–27. doi: 10.1016/j.neuroimage.2013.05.004

Strangman, G., Culver, J. P., Thompson, J. H., and Boas, D. A. (2002). A quantitative comparison of simultaneous BOLD fMRI and NIRS recordings during functional brain activation. *Neuroimage* 17, 719–731. doi: 10.1006/nimg.2002.1227

Stuart, S., Belluscio, V., Quinn, J. F., and Mancini, M. (2019). Pre-frontal cortical activity during walking and turning is reliable and differentiates across young, older adults and people with Parkinson's disease. *Front. Neurol.* 10:536. doi: 10.3389/fneur.2019.00536

Sun, W., Wu, X., Zhang, T., Lin, F., Sun, H., and Li, J. (2021). Narrowband resting-state fNIRS functional connectivity in autism spectrum disorder. *Front. Hum. Neurosci.* 15:643410. doi: 10.3389/fnhum.2021.643410

Tang, T. B., and Chan, Y. L. (2018). Functional connectivity analysis on mild Alzheimer's disease, mild cognitive impairment and normal aging using fNIRS. *Annu. Int. Conf. IEEE Eng. Med. Biol. Soc.* 2018, 17–20. doi: 10.1109/EMBC.2018.8512186

Underwood, C. F., and Parr-Brownlie, L. C. (2021). Primary motor cortex in Parkinson's disease: Functional changes and opportunities for neurostimulation. *Neurobiol. Dis.* 147:105159. doi: 10.1016/j.nbd.2020.105159

Vitorio, R., Stuart, S., Rochester, L., Alcock, L., and Pantall, A. (2017). fNIRS response during walking - Artefact or cortical activity? A systematic review. *Neurosci. Biobehav. Rev.* 83, 160–172. doi: 10.1016/j.neubiorev.2017.10.002

Vo, T. M. T., Mondal, S., Nguyen, V. T., Park, S., Choi, J., Bui, N. T., et al. (2021). Rice starch coated iron oxide nanoparticles: A theranostic probe for photoacoustic imaging-guided photothermal cancer therapy. *Int. J. Biol. Macromol.* 183, 55–67. doi: 10.1016/j.ijbiomac.2021.04.053

Xiang, Y., Li, Y., Shu, C., Liu, Z., Wang, H., and Wang, G. (2021). Prefrontal cortex activation during verbal fluency task and tower of London task in schizophrenia and major depressive disorder. *Front. Psychiatry* 12:709875. doi: 10.3389/fpsyt.2021.709875

Yan, Z., and Rein, B. (2022). Mechanisms of synaptic transmission dysregulation in the prefrontal cortex: Pathophysiological implications. *Mol. Psychiatry* 27, 445–465. doi: 10.1038/s41380-021-01092-3

Yeung, M. K., and Chan, A. S. (2020). Functional near-infrared spectroscopy reveals decreased resting oxygenation levels and task-related oxygenation changes in mild cognitive impairment and dementia: A systematic review. *J. Psychiatr. Res.* 124, 58–76. doi: 10.1016/j.jpsychires.2020.02.017

Zeller, J. B., Herrmann, M. J., Ehlis, A. C., Polak, T., and Fallgatter, A. J. (2010). Altered parietal brain oxygenation in Alzheimer's disease as assessed with near-infrared spectroscopy. *Am. J. Geriatr. Psychiatry* 18, 433–441. doi: 10.1097/JGP.0b013e3181c65821

Zhou, S., Zhang, Y., Fu, Y., Wu, L., Li, X., Zhu, N., et al. (2022). The effect of task performance and partnership on interpersonal brain synchrony during cooperation. *Brain Sci.* 12:635. doi: 10.3390/brainsci12050635

Zhu, H., Li, J., Fan, Y., Li, X., Huang, D., and He, S. (2015). Atypical prefrontal cortical responses to joint/non-joint attention in children with autism spectrum disorder (ASD): A functional near-infrared spectroscopy study. *Biomed. Opt. Express* 6, 690–701. doi: 10.1364/BOE.6.000690

frontiers | Frontiers in Neuroscience

TYPE Original Research
PUBLISHED 15 March 2023
DOI 10.3389/fnins.2023.1116002

OPEN ACCESS

EDITED BY
Nico Sollmann,
University of California, San Francisco, United States

REVIEWED BY
Basavaraju G. Sanganahalli,
Yale University, United States
Peter Herman,
Yale University, United States

*CORRESPONDENCE
Edyta Charyasz
✉ edyta.charyasz@tuebingen.mpg.de

SPECIALTY SECTION
This article was submitted to Brain Imaging Methods, a section of the journal Frontiers in Neuroscience

RECEIVED 04 December 2022
ACCEPTED 27 February 2023
PUBLISHED 15 March 2023

CITATION
Charyasz E, Heule R, Molla F, Erb M, Kumar VJ, Grodd W, Scheffler K and Bause J (2023) Functional mapping of sensorimotor activation in the human thalamus at 9.4 Tesla. *Front. Neurosci.* 17:1116002. doi: 10.3389/fnins.2023.1116002

Functional mapping of sensorimotor activation in the human thalamus at 9.4 Tesla

Edyta Charyasz[1,2,3]*, Rahel Heule[1,2,4], Francesko Molla[2,3,5], Michael Erb[1,2], Vinod Jangir Kumar[2], Wolfgang Grodd[2], Klaus Scheffler[1,2] and Jonas Bause[2]

[1]Department of Biomedical Magnetic Resonance, University of Tübingen, Tübingen, Germany, [2]Department for High Field Magnetic Resonance, Max Planck Institute for Biological Cybernetics, Tübingen, Germany, [3]Graduate Training Centre of Neuroscience, Tübingen, Germany, [4]Center for MR Research, University Children's Hospital, Zurich, Switzerland, [5]Center for Neurology, Hertie-Institute for Clinical Brain Research, Tübingen, Germany

Although the thalamus is perceived as a passive relay station for almost all sensory signals, the function of individual thalamic nuclei remains unresolved. In the present study, we aimed to identify the sensorimotor nuclei of the thalamus in humans using task-based fMRI at a field strength of 9.4T by assessing the individual subject-specific sensorimotor BOLD response during a combined active motor (finger-tapping) and passive sensory (tactile-finger) stimulation. We demonstrate that both tasks increase BOLD signal response in the lateral nuclei group (VPL, VA, VLa, and VLp), and in the pulvinar nuclei group (PuA, PuM, and PuL). Finger-tapping stimuli evokes a stronger BOLD response compared to the tactile stimuli, and additionally engages the intralaminar nuclei group (CM and Pf). In addition, our results demonstrate reproducible thalamic nuclei activation during motor and tactile stimuli. This work provides important insight into understanding the function of individual thalamic nuclei in processing various input signals and corroborates the benefits of using ultra-high-field MR scanners for functional imaging of fine-scale deeply located brain structures.

KEYWORDS

fMRI, thalamus, ultra-high field fMRI, high-resolution imaging, thalamic nuclei, sensorimotor, tactile, motor

Abbreviations: AC, anterior commissure; AV, anteroventral; BOLD, blood-oxygen-level-dependent; CeM, central medial; CM, centromedian; DBS, deep brain stimulation; EPI, echo planar imaging; EEG, electroencephalography; FA, flip angle; fMRI, functional magnetic resonance imaging; FOV, field of view; FWHM, full width at half maximum; GLM, general linear model; HRF, hemodynamic response function; LD, lateral dorsal; LGN, lateral geniculate; LP, lateral posterior; MDl, lateral subdivision of mediodorsal thalamus; MDm, medial subdivision of mediodorsal thalamus; MEG, magnetoencephalography; MGN, medial geniculate; MPRAGE, magnetization-prepared rapid acquisition gradient echo; PET, position emission tomography; PC, posterior commissure; PCA, principal component analysis; Pf, parafascicular; PuA, anterior pulvinar; PuI, inferior pulvinar; PuL, later pulvinar; PuM, medial pulvinar; R GRAPPA, acceleration factor; SNR, signal to noise ratio; TE, echo time; TR, repetition time; VA, ventral anterior; VAmc, ventral anterior, magnocellular division; VL, ventral lateral; VLa, ventral lateral anterior; VLp, ventral lateral posterior; VM, ventral medial; VP, ventral posterior; VPL, ventral posterior lateral; VPM, ventral posterior medial.

Introduction

Sensorimotor processing engages cortical and subcortical areas. The extensive sensorimotor investigations implicate the motor cortex of the frontal lobe, the sensory cortex of the parietal lobe, and the cerebellum (Grodd et al., 2001; Hermes et al., 2012; Siero et al., 2014; Filippi et al., 2016). The sensorimotor pathway also engages the thalamus (Mo and Sherman, 2019).

The thalamus has been shown to be involved in sensorimotor processing in monkeys (Benevento et al., 1977; Darian-Smith et al., 1990), mice (Wang et al., 2021), and rats (Petersen, 2019). So far, sensorimotor functional mapping in the thalamus is under-investigated in the human brain. The thalamus encompasses small motor and sensory nuclei, and therefore requires high-resolution investigations. In this study, we aim at utilizing the power of ultra-high field fMRI to investigate the individual thalamus's functional response during sensorimotor task at the single-subject level. Such high-resolution sensorimotor mapping within the thalamus may help better strategize the potential therapeutic planning and understanding of sensorimotor dysfunctions. Assessing the individual subject-specific fMRI responses allows perceiving the overall sensorimotor experience of the participating subjects to the employed stimuli and analyzing the intersubject variability, which may arise due to anatomical or functional differences across the investigated population.

The thalamus is a paramedian symmetrical mass of gray matter within the vertebrate brain that arises during embryonic development as the main constituent of the diencephalon and attaches to the upper part of the brainstem through the telencephalon. Anatomically, the thalamus is divided in four major groups (the anterior, medial, lateral, and the posterior group), which can further be functionally distinguished into first-order and higher-order nuclei based on the origin of their driving inputs (Haber and McFarland, 2001; Sherman and Guillery, 2002; Theyel et al., 2010; Lambert et al., 2017). First-order nuclei receive driver signals from peripheral sources and project to the cerebral cortex. For example, thalamic motor nuclei such as the ventral anterior (VA) and ventral lateral (VL) receive primary afferents from the basal ganglia as well as the cerebellum and send efferents to the premotor as well as primary motor cortices (Guillery and Sherman, 2002; Bosch-Bouju et al., 2013; Gaidica et al., 2018). Higher-order nuclei, such as the pulvinar (Pu) and the mediodorsal (MD), receive their driving input from layer 5 of the cortex and participate in cortico-thalamo-cortical (or transthalamic) circuits in projecting them back to the cortex (Wurtz et al., 2005; Saalmann, 2014). While the sensorimotor involvement of the cortical areas and the cerebellum has been extensively studied for decades in humans as well as in primates (Logothetis et al., 2001; Kishore et al., 2014; Wang et al., 2018; Edwards et al., 2019) using functional magnetic resonance imaging (fMRI) (Rao et al., 1995; Lotze et al., 2000; Rosazza et al., 2014; Landelle et al., 2021), electroencephalography (EEG) (Muthukumaraswamy and Johnson, 2004; Morash et al., 2008; Zhao et al., 2019), magnetoencephalography (MEG) (Sebastiani et al., 2014), and electrophysiology (Arce-McShane et al., 2016; Ranieri et al., 2022), the human thalamus has widely remained inaccessible. Due to its central location within the brain, its small size, and the lack of sufficient contrast in various imaging modalities, the delineation of thalamic nuclei using fMRI remains challenging. Ongoing progress in the development of accelerated MR acquisition techniques, such as parallel imaging or multi-band radiofrequency (RF) pulses combined with adapted RF coil designs to maximize the achievable signal-to-noise-ratio (SNR), yields increased spatial resolution while maintaining high temporal resolution. Nevertheless, a reliable localization of thalamic nuclei and their functional activation is yet limited by insufficient SNR and consequently spatial resolution constraints at conventional clinical field strengths ($\leq$ 3 Tesla).

Consequently, in humans, the involvement of the thalamus in sensory and motor processing has only been vaguely characterized regarding the precise anatomical location and functional contribution of the various thalamic nuclei. To obtain the specific functional activation of the thalamic nuclei involved in sensorimotor and other functional processing in a robust and reproducible manner, the use of ultra-high field MR scanners may prove beneficial due to their increased SNR, enhancing spatial and temporal resolution as well as image contrast (Pohmann et al., 2011, 2016).

Thus, functional MRI at ultra-high field strength may provide an opportunity to investigate the blood oxygen level-dependent (BOLD) activations of specifically involved thalamic nuclei in sensorimotor processing. In this study, the functional involvement of thalamic nuclei during finger movement and tactile finger stimulation in humans was examined for the first time using an ultra-high field strength of 9.4 Tesla. Due to the challenges of accurately identifying and segmenting the individual fine-scale thalamic nuclei in each subject, this proof-of-principle study focused on a single-subject rather than a group analysis, which enabled to preserve spatial specificity. The results of this study may contribute to depict a more comprehensive view of the differential role of the thalamus in the context of motor and sensory processing as well as to enhance our understanding of the functional architecture of the thalamus. In addition, ultra-high field fMRI may allow a refined investigation of the role of the thalamus in neurological motor disorders like Parkinson's disease, dystonia, and essential tremor.

Materials and methods

Subjects

Ten healthy right-handed adults with normal or corrected to normal vision and a mean age of 27 years (range 21–34 years; five females) participated in the study. The study was approved by the local research ethics committee and all participants gave written informed consent prior to participation.

Experimental design and setup

All participants performed two fMRI block design tasks with the right hand: tactile-finger task and finger-tapping task during a single session. The left hand was not engaged during any experiments of this study.

For both task, the output of a trigger pulse prior to the acquisition of each volume repetition time (TR) was implemented into the MR sequence to synchronize the fMRI paradigm with the MR acquisition. The tasks were projected onto a translucent screen using a projector. The participants viewed the stimuli *via* a mirror attached to the head coil. Before the main experiment, participants performed one complete training run outside the scanner.

The tactile stimulation system used a pneumatically controlled setup to deliver precise and controlled air pressure pulses to the participant's fingertip. The custom-built electronic control circuit, connected to the air compressor and plastic tubes, was interfaced with a stimulus computer through the digital controller (mbed, LPC1768). The tubes conveyed air pressure (2.5 bar) to the pneumatic stimulus finger clips (MEG International Services Ltd., Coquitlam, Canada). The timing of the tactile stimuli was controlled using Matlab 2019b (The MathWorks, Inc., Natick, MA, USA) and the PSYCHTOOLBOX (Brainard, 1997; Pelli, 1997). The presentation and timing of the finger-tapping stimuli was controlled by Presentation® software (Version 18.0, Neurobehavioral Systems, Inc., Berkeley, CA)[1].

Tactile-finger task

The tactile stimulation was delivered concomitantly to the fingertips of the thumb (D1), index finger (D2), middle finger (D3), and ring finger (D4) in the form of air pulses through an inflatable finger clip. Each single air pulse caused deviation of the pneumatic membrane (approximately 40 mm^2) toward the skin surface by a pulse of pressed air at 2.5 bar for a duration of 250 ms. Stimulation pulses (ON-phase) were delivered every second (1 Hz) in blocks of 20 s to all four fingers, as specified above, followed by a rest period (OFF-phase) of 20 s. Data were acquired during seven runs of 12 cycles each. The stimulation was carefully timed to begin at the acquisition of the first volume of each block, following the initial trigger. To focus the subjects' attention on the stimulation and to prevent habituation, a random number of stimulation pulses (between zero and four per stimulation block) were skipped, resulting in an average of 210–240 air pulses per fingertip. The particular number of the pulses and the time at which these pulses were skipped was chosen randomly for each block. Subjects had to report to the experimenter the total number of blocks with missing pulses in the break between stimulation sessions. In addition, participants were instructed to focus on a fixation cross presented on the screen during the experiment. Two of the ten subjects (S9 and S10) could not perform the tactile task properly due to technical issues and were excluded from the subsequent analysis of those data.

Finger-tapping task

The task paradigm consisted of 12 visually cued cycles (each with a total duration of 41 s) divided into alternating finger tapping blocks (20 s) and rest blocks (20 s). Before each movement block, a 1 s interval was used to allow subjects to get ready for the task. Participants were instructed to tap their right fingers in an ordered fashion [index finger (D2), middle finger (D3), ring finger (D4), and little finger (D5), respectively] against the thumb (D1). The tapping rate was paced with a visual cue (blinking arrow). The tapping frequency was approximately 2.5 Hz. Images were collected during one run. All subjects were able to successfully complete the finger-tapping task.

MR data acquisition

MRI data were acquired on a 9.4T whole-body MRI scanner (Siemens Healthineers, Erlangen, Germany), using an in-house-built head-coil with 16 transmit and 31 receive channels (Shajan et al., 2014).

Structural imaging: A high-resolution T1-weighted scan was acquired with a magnetization-prepared rapid acquisition gradient echo (MPRAGE) sequence [inversion TR = 3.8 s; TE = 2.50 ms; FA = 6°; FOV = 192 mm; 288 sagittal slices; voxel size = 0.6 × 0.6 × 0.6 mm^3; GRAPPA acceleration factor (R) = 2 × 2; partial Fourier = 6/8] covering the whole brain for anatomical reference. In addition, whole brain structural scans for cortical and thalamic segmentation were collected on a Siemens Healthineers Prisma Fit 3T whole-body MRI scanner. For each subject, high-resolution T1-weighted MPRAGE [inversion TR = 2.4 s; TE = 2.22 s; FA = 8°; FOV = 256 mm; 208 sagittal slices; voxel size = 0.8 × 0.8 × 0.8 mm^3; GRAPPA acceleration factor (R) = 2] and T2-weighted 3D fast spin echo [TR = 3.2 s; TE = 5.63 s; FOV = 256 mm; 208 sagittal slices; voxel size = 0.8 × 0.8 × 0.8 mm^3; GRAPPA acceleration factor (R) = 2] data sets were acquired.

Task-based fMRI: Blood oxygenation level dependent (BOLD) data were collected using a 2D gradient-echo multi-band (MB) echo-planar imaging (EPI) sequence with 86 interleaved slices per volume providing full brain coverage and acquired parallel to the AC - PC line (TR = 2 s; TE = 22 ms; FA = 50°; FOV = 198; voxel size = 1.25 × 1.25 × 1.25 mm^3, R = 4, MB factor = 2, bandwidth = 1666 Hz/Px, and anteroposterior phase encoding). For the purpose of distortion correction, MB-EPI scans with reversed phase encoding direction (posterior-anterior) were performed with otherwise identical parameters as the main experiment.

Functional imaging sessions consisted of seven tactile-finger runs (255 volumes each, acquisition time of 8.5 min), one finger-tapping run (265 volumes, acquisition time of about 9 min) and one run with reversed phase encoding direction for distortion correction (10 volumes) at the end of the session.

Physiological parameters (cardiac pulsation and respiration rate) were recorded during the functional scans using MR compatible devices (Acknowledge, Biopac Systems, Inc., Goleta, CA, USA). Synchronization with the MR sequence was achieved by parallel recording of the sequence trigger signal. However, due to unstable recording by the BIOPAC system during the experiments, complete physiological data could not be collected for three subjects (S3, S4, and S6), and four subjects (S3, S6, S7, and S8) for the motor and tactile task, respectively. Therefore, the successfully recorded physiological data for the remaining individuals were not used in the subsequent analysis.

1 www.neurobs.com

MRI data analysis

Data preprocessing

The fMRI data preprocessing and analysis of both tasks was conducted by using the SPM12 software (R7771[2]) implemented in MATLAB R2017b (The MathWorks, Inc., Natick, MA, USA). Before analysis, the first five volumes of the functional data of each run were discarded to mitigate T1 saturation effects.

All functional images were first corrected for the acquisition time delay between slices, then spatially realigned to the first image to correct for rigid body motion, and subsequently corrected for thermal noise fluctuations and distortions. Image distortions were corrected by the TopUp tool (Andersson et al., 2003) of the FSL (Smith et al., 2004) library. NORDIC (Moeller et al., 2021) denoising, using PCA to correct for non-Gaussian noise distributions, was applied to the magnitude images in order to reduce thermal noise. The effect of NORDIC denoising is shown in the **Supplementary Figure 1**. The functional distortion-corrected data sets were co-registered to the anatomical data and finally spatially smoothed using a Gaussian kernel with a full width at half maximum (FWHM) of 2.5 mm.

FreeSurfer software[3] (version 6.1) (Fischl et al., 1999), incorporating a probabilistic thalamic segmentation algorithm (Iglesias et al., 2018), was used for thalamic segmentations. Our previous findings of unreliability in the application of FreeSurfer to the structural data acquired at 9.4T (0.6 mm isotropic resolution) as a result of the altered image contrast at ultra-high field prompted the use of 3T anatomical data for the purpose of segmentation despite the lower resolution (0.8 mm isotropic). Regions-of-interest (ROIs), for example, whole thalamus, or individual parcellated thalamic nuclei, were extracted as masks from the segmentation, and co-registered to each subject's anatomical images (cf. **Figure 1**). All subsequent analyses were carried out in native space. An example of the co-registration of 3T T1-weighted and T2-weighted images to 9.4T T1-weighted data is shown in the **Supplementary Figure 2**.

GLM analysis

For each subject, the general linear model (GLM) approach was used to analyze task-evoked BOLD responses, separately for the tactile and finger-tapping conditions.

For the tactile task consisting of seven runs, these runs were combined into a single GLM analysis. A separate GLM analysis was performed for the finger-tapping task, composed of one run. Task-based statistical parametric t-maps were calculated at the individual subject level using block-style boxcars convolved with a hemodynamic response function (HRF). A temporal high-pass filter with a cut-off of 128 s was applied to correct for low frequency drifts. All six motion parameters (three rotations and three translations) for each run were included as regressors of no interest to correct for residual motion-related variance.

Involvement of single thalamic nuclei was investigated based on the BOLD response to the tactile and motor tasks by using individual whole thalamus masks as explicit masks (at first level statistics).

For each of the functional tasks, an MR signal change compared to the rest condition was tested. Individual t-maps were obtained with the statistically significant activation threshold set to an uncorrected p-value < 0.001 with a minimum cluster size of five voxels, and overlaid onto the individual anatomical image. The minimum cluster size was determined through a consideration of variations in individual thalamus size. To this end, an evaluation of scaling the five voxel threshold was performed by dividing the individual mask size by the mean mask size and then multiplying by 5, resulting in values between 4.6 and 5.6 voxels. Despite this small variability, a minimum cluster size of five voxels was chosen to balance the control of false positive errors and the accurate detection of true effects in the analysis. Thalamic activated clusters were anatomically labeled by overlaying the thresholded activation maps onto the individual thalamic nuclei segmented in FreeSurfer. For the quantification of activation within each thalamic nuclei for the motor and tactile tasks, the number of activated voxels was calculated using the subject–specific thalamic nuclei masks obtained from the thalamic segmentation in FreeSurfer. To preserve the spatial specificity of the individual results and allow the assessment of intersubject functional variability, a group analysis in standard space was not conducted. Additionally, we compared the number of voxels in each thalamic nuclei mask across individual subjects to assess anatomical variability. The count of activated voxels was converted into percentages relative to the total number of voxels in each subject–specific thalamic nuclei mask to normalize for differences in individual thalamic nuclei volumes across subjects. **Figure 2** illustrates the relative deviation of individual thalamic nuclei volumes from the mean mask size (mean mask size: pooled over all subjects).

Furthermore, a supplementary whole-brain GLM analysis was performed in a similar manner without utilizing an explicit mask in the first-level statistics. The whole-brain T-statistic maps are presented for four representative subjects in **Supplementary Figure 3**, with a specific focus on highlighting activation in the cerebral cortex and cerebellum. These results are included in the **Supplementary material** due to their exploratory nature and secondary role in the study.

BOLD response time course

To assess the temporal dynamics of the BOLD signal changes in the thalamic nuclei in response to both tasks and across subjects, time course data from all the activated voxels within each individual thalamic nucleus were extracted for each run (one motor, seven tactile). The percentage change in the BOLD signal was then calculated relative to each run's rest periods, and the resulting time courses were averaged across activated voxels. Those time courses were subsequently divided into 40 s windows, corresponding to the length of one ON/OFF block, and averaged across runs and twelve blocks for each task type.

Results

In order to obtain a complete depiction of all thalamic regions activated during the motor and tactile tasks, the activations of the left and the right thalamic nuclei are presented separately. Task-related activations were identified in all subjects who entered the

2 http://www.fil.ion.ucl.ac.uk/spm

3 http://surfer.nmr.mgh.harvard.edu

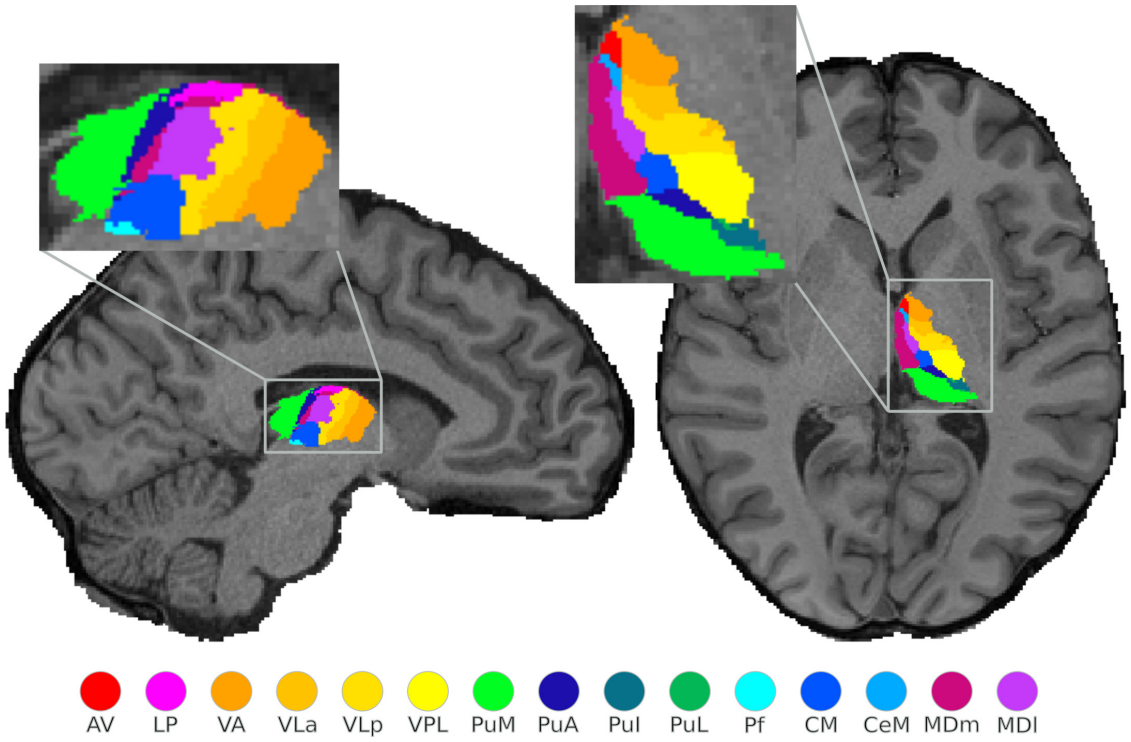

FIGURE 1
Structural segmentation of the thalamus: illustration of the probabilistically segmented left thalamic nuclei using FreeSurfer in one exemplary subject. The selected sagittal and axial view visualize only 15 nuclei, however, a complete nuclei segmentation of the thalamus was performed.

study. As will be presented below, both active and passive tasks evoked consistent activations among subjects. However, tactile-related activations tended to be reduced compared to motor-related activations.

Motor task

The percentage of activated voxels during the motor task-based fMRI experiment for the different thalamic nuclei in each subject is summarized in Figure 3 for the left and the right thalamic nuclei.

The finger-tapping task evoked a significant BOLD signal in ten and nine subjects within the left and the right thalamus, respectively, with a clear dominance of the left side. The largest and consistent fraction of activated voxels was found in the left VPL and the intralaminar nucleus CM followed by VLa and VLp of the lateral nuclei group. In addition, we found very consistent activations in the left pulvinar nuclei group (PuA, PuM, and PuL). All subjects showed activations in the left VPL and CM thalamic nuclei. Nine subjects showed activations in the left VLa, and VLp; seven subjects in the left MDm, and four subjects in the left MDl and Pf. Six subjects demonstrated contralateral activations within VLa, VPL, and PuM. Eight and seven subjects showed detectable clusters in the right CM and VLp, respectively. In one subject, S3, the bilateral anterior part of the thalamus (AV and LD nuclei) and the LP nuclei was activated.

The first-level GLM analysis results of the finger-tapping task are visualized in Figure 4 for four representative subjects (S1, S3, S5, and S6). All single-subject maps were thresholded at $p < 0.001$ (uncorrected) level and superimposed on their structural images. In summary, the fMRI maps showed dominant activation in the left VPL, CM, and VLp in all representative subjects, with strong activation in the left VLa and the bilateral VA in S3. Bilateral activation was found in MDm and MDl in subject S6.

Tactile task

Figure 5 depicts the percentage of activated voxels during the tactile task-based fMRI experiment within the left and right thalamic nuclei across all subjects, respectively. All subjects except and S7 showed bilateral activation in the thalamus. Consistent activations across all eight remaining subjects were found in the left VPL. By using a threshold of $p < 0.001$ (uncorrected), three and four subjects showed detectable clusters in the left MDm and MDl, respectively. Activation of the left VLa and left VLp nuclei was observed in five out of eight subjects. Bilateral activation was found in CM in four subjects. Like the motor-related activations, the left thalamic nuclei pulvinar region, including PuA, PuM, PuL, and PuI, were activated. No significant activity was found in the bilateral LD, LP and in the left Pf nuclei. Tactile stimulation-evoked BOLD activity in the various thalamic nuclei is shown in Figure 6 representatively for subjects S1, S3, S5, and S6. The single-subject maps (uncorrected $p < 0.0001$) showed consistent bilateral activation of VPL in S3 and ipsilateral activation in VPL, VLp, and CM in S6. Activation of the right AV was found in three subjects (S3, S5, and S8) amongst all measured subjects.

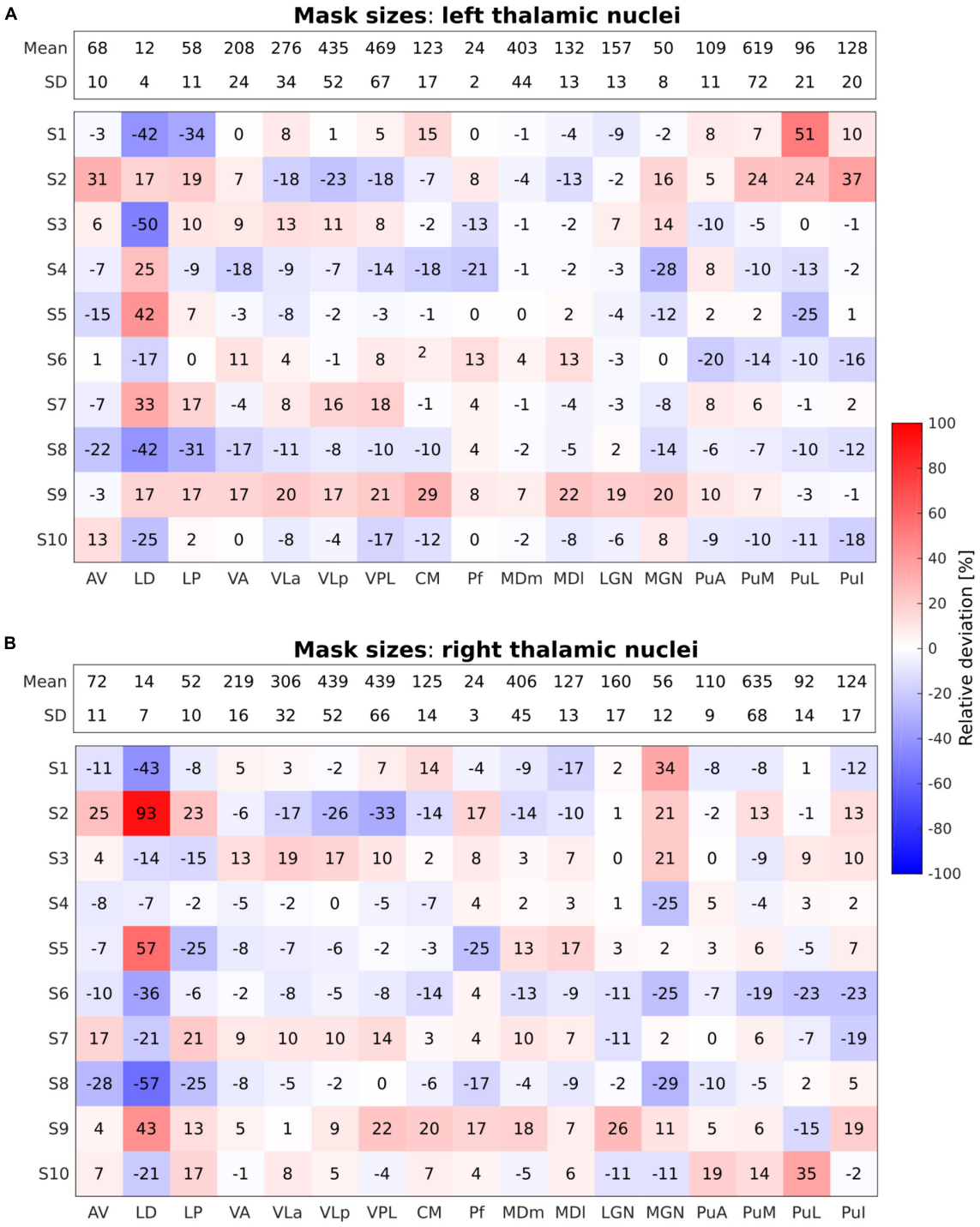

FIGURE 2
Relative deviation in percentage (%) from the mean mask sizes of the performed segmentations across all individual thalamic nuclei in all subjects for the left **(A)** and the right **(B)** thalamus. The absolute mean mask size pooled over all subjects given as number (#) of voxels along with the respective standard deviation is displayed within the bar on top across all nuclei for both left and right thalamus. Blue and red shades refer to negative and positive relative deviations, i.e., smaller and larger mask sizes as compared to the mean mask size, respectively.

To summarize, at the subject level, we found robust bilateral activation for both stimuli conditions (motor and tactile) in different thalamic nuclei. An individual GLM analysis ($p < 0.001$ uncorrected) comparing the motor task versus the tactile conditions showed that the motor task produced much stronger bilateral activation in the thalamic nuclei, for example, in the CM, VA, VLp, VLa, and PuL, even though just a single run was performed while seven runs were conducted for the tactile stimulus (cf. Supplementary Figure 4).

To further evaluate the difference in response of activated voxels to both tasks, a comparison of the average BOLD signal change time courses from the activated voxels within the thalamic

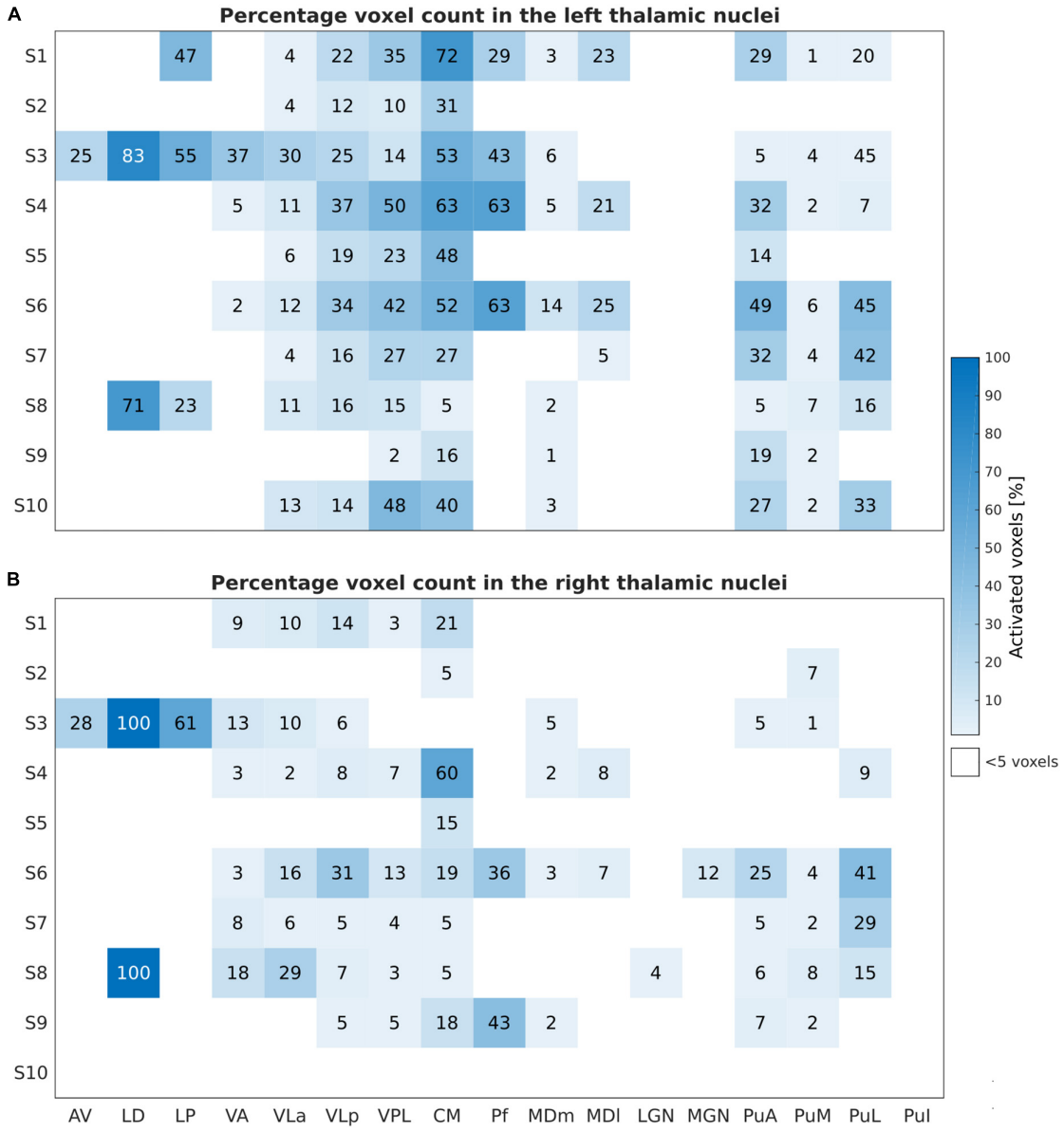

FIGURE 3
Motor task: Number of activated voxels expressed in percentage (%) relative to the subject-specific mask size during the motor task-based fMRI experiment for the left **(A)** and right **(B)** thalamic nuclei across all subjects and nuclei. These results are obtained by thresholding at an uncorrected p-value of < 0.001 and at a minimal cluster size of five voxels within the investigated ROIs.

nuclei was performed. The mean relative signal change over 12 block repetitions from the most frequently detected nuclei (left VLa, VLp, VPL, and CM) for four representative subjects are depicted in Figure 7. For the motor task, the averaged BOLD responses measured in the left thalamic nuclei yielded maximum signal changes of 1.7% to 2%. The highest increase in the BOLD signal was observed in the left VPL and CM nuclei, while the lowest increase was seen in the left VLa nucleus across all subjects. The tactile task resulted in a peak of the signal change in the same regions, with maximal values in the range of 0.5 to 0.8%. The observed maximum percent signal changes are notably lower for the tactile task as compared to the motor task, suggesting distinct patterns of neural activation in response to the two tasks. For both tasks, the shape of time courses indicates that, although the temporal patterns of the BOLD responses generally remained consistent within each individual subject across different thalamic nuclei, there is a notable inter-subject variability in the shape of these responses. These results emphasize the agreement between the time course analysis and the GLM analysis in demonstrating stronger activation in the thalamic nuclei in response to the motor task.

Discussion

In the present study, we investigated the localizability and incidence of activation in the thalamic nuclei, associated with finger-tapping movement and tactile stimulus, at an individual

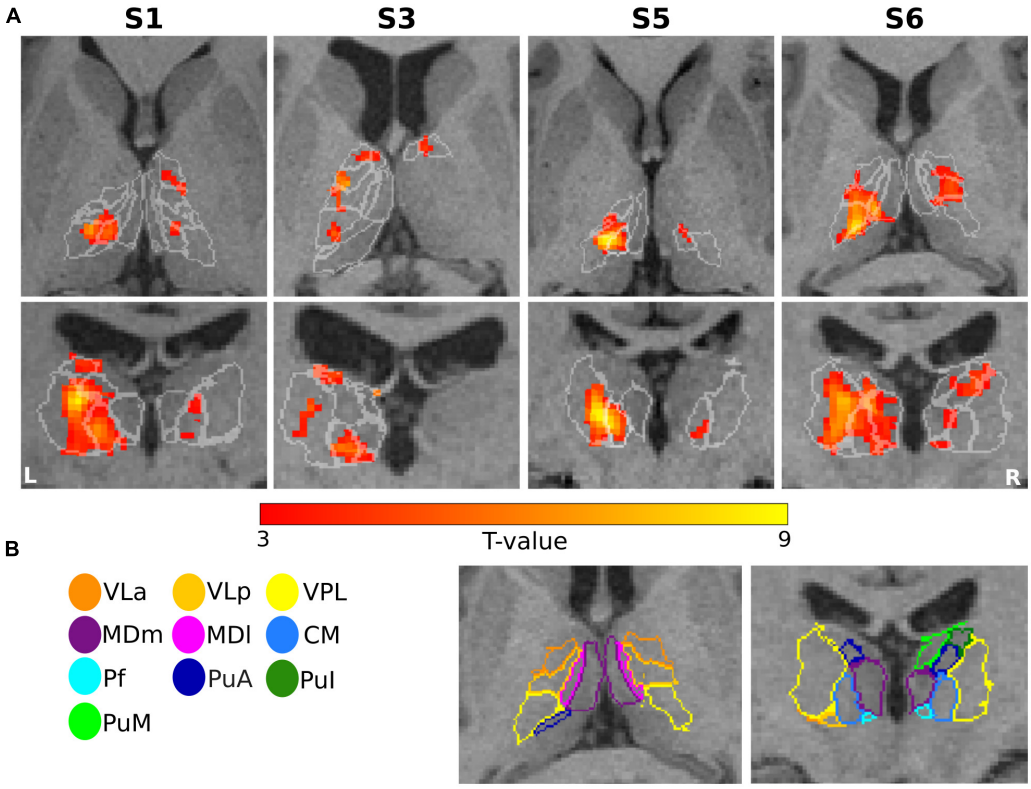

FIGURE 4
Motor task: **(A)** Results of GLM analysis in the thalamus of four representative subjects (S1, S3, S5, and S6) during the motor task-based fMRI experiment. For each subject, the *t*-contrast maps ($p < 0.001$ uncorrected, and 5-voxel minimum cluster size) are shown, with the individual T1-weighted MPRAGE image (3T) as anatomical underlay. The most representative axial (top) and coronal (bottom) slices oriented in neurological convention (the left side of the image corresponds to the left side of the brain) are depicted for each subject, emphasizing the prominent activation of the thalamic nuclei. **(B)** The contours of the segmented thalamic nuclei are shown for one subject (S6) with the same color-coding as in **Figure 1**, mapped to the anatomical MPRAGE image.

subject level using fMRI at 9.4T. The power of fMRI lies in its ability to resolve fine spatial structures and to detect changes in individual subjects with high spatial specificity, making it superior to other brain imaging modalities (e.g., MEG, EEG, and PET). The accurate delineation of the thalamic nuclei is extremely challenging due to their small sizes, necessitating imaging at ultra-high fields, which are able to provide increased SNR and resolution, in combination with sophisticated segmentation techniques, as well as favoring a single-subject analysis in native space over a group analysis in MNI space to preserve spatial specificity in individual subjects. A subject-specific assessment also avoids the issue of averaging over non-responders and responders in the individual small-sized thalamic nuclei. Therefore, to fully benefit from ultra-high field fMRI and to understand the intersubject variability as a result of potential anatomical and functional differences, we felt that a single-subject analysis is more appropriate for this first in-human study of the functional involvement of the thalamic nuclei in sensorimotor tasks. Furthermore, investigating intersubject variability in healthy volunteers may provide essential insights with respect to future studies in patients with sensory abnormalities and/or motor disabilities (e.g., sensory ataxia, Parkinson's disease).

Benefiting from the increased SNR at ultra-high field strength, we achieved a spatial resolution (1.25 mm isotropic), which is higher than the one previously reported for fMRI studies in the thalamus (Fischer and Whitney, 2012; Wang et al., 2012; Woodward et al., 2012). In accordance with prior literature pointing to the advantages of small voxel sizes for cortical specificity in BOLD fMRI (Hyde et al., 2001), we successfully detected task-specific activity in individual thalamic nuclei at the employed resolution.

During finger-tapping stimuli, the VA, VLa, VLp, VPL, and CM nuclei showed strong BOLD response. Our findings are consistent with previous findings (Ilinsky and Kultas-Ilinsky, 1987; Fang et al., 2006; Kumar et al., 2015) suggesting that the VA, VLa, and VLp nuclei are the main sources of projections to the motor cortical areas, while also additional motor-related intralaminar und medial nuclei (CM, Pf, and MD) were observed to send inputs to the primary motor areas and premotor areas. Interestingly, the motor nuclei presented in this study are also shown to be associated with the hand movement motor task (Kumar et al., 2022). Tactile stimuli evoked strong BOLD response in the VPL nucleus. Strong tactile activation was also detected in the VLp and CM nuclei. In line with a recent fMRI study in rats (Sanganahalli et al., 2022), our results indicate that the VPL nucleus plays an important role in the sensorimotor processing in humans, even during passive tactile stimulation.

In previous animal studies, the CM/PF thalamic complex was reported to be associated with attentional processing

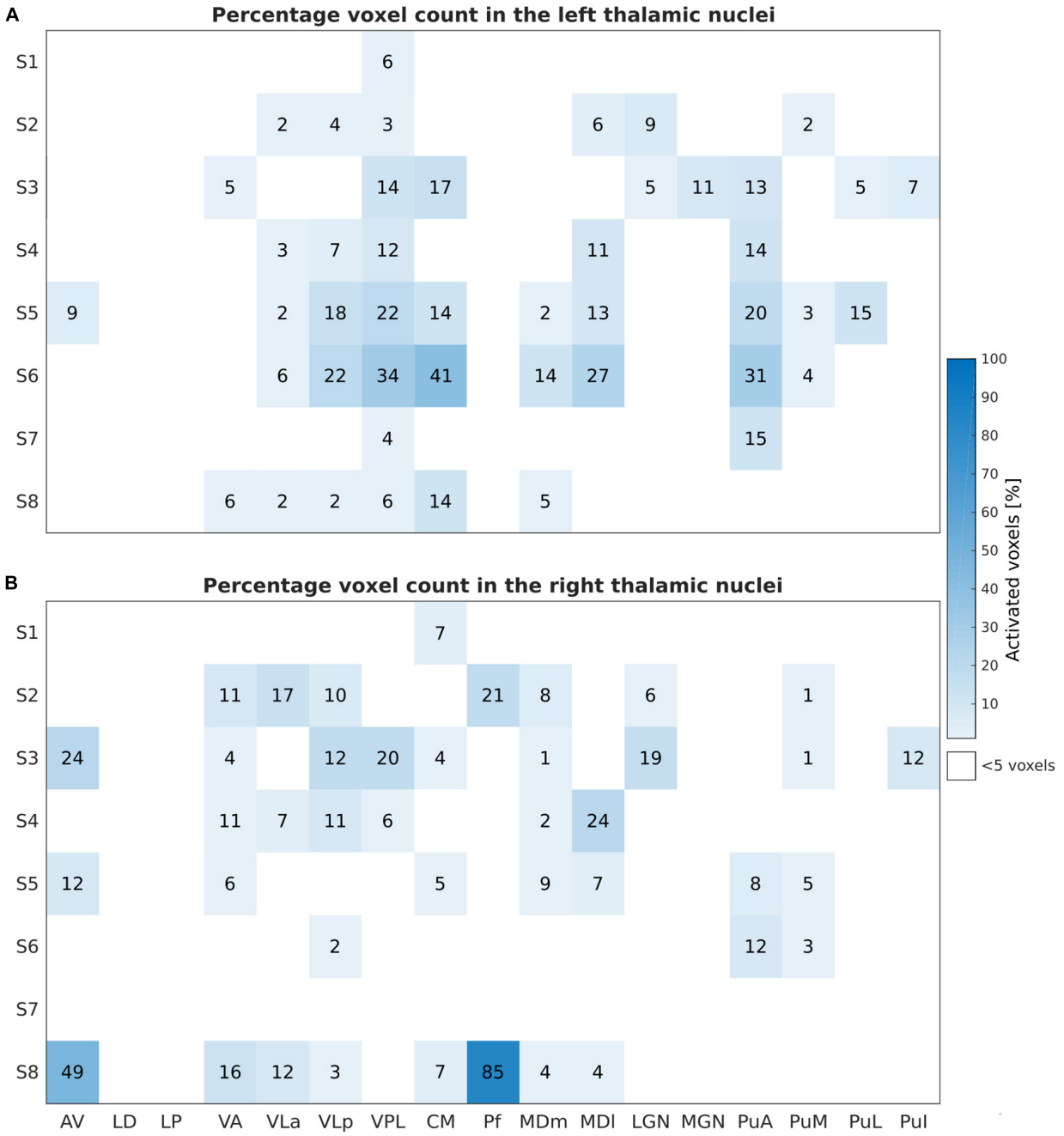

FIGURE 5
Sensory Task: Activated voxels counts (in percentage) relative to the subject-specific mask size during the tactile task-based fMRI experiment for the left **(A)** and the right **(B)** thalamic nuclei across all subjects and nuclei. Similar to **Figure 3**, the results are obtained by thresholding at $p < 0.001$, uncorrected, and at a minimal cluster size of five voxels within the investigated ROIs.

(Kinomura et al., 1996) and motor adjustment (Van der Werf et al., 2002). As a result of a neuroanatomical tracing analysis (Van der Werf et al., 2002), a distinction between Pf and CM functions was proposed, which assigned the CM nucleus with a specific involvement during sensorimotor functions and the Pf nucleus with a specific role during associative-limbic motor functions. This distinction in humans using fMRI studies is, however, not possible with our study setup. Nevertheless, our results also suggest the involvement of the CM nucleus in general attentional and sensorimotor processes.

The results of this work coincide with previous studies that have demonstrated an association between the pulvinar nuclei and attention/visual stimulus (Petersen et al., 1987; Fischer and Whitney, 2012; Zhou et al., 2016). Compared to the tactile task during which participants were asked to focus on a fixation cross, a higher pulvinar nuclei activation was found for the finger-tapping task, during which the participants viewed a blinking arrow along with the word "fingers" indicating the task. This may be further evidence of the association between the pulvinar nuclei and visual stimulus. However, in this case, the left pulvinar nuclei showed

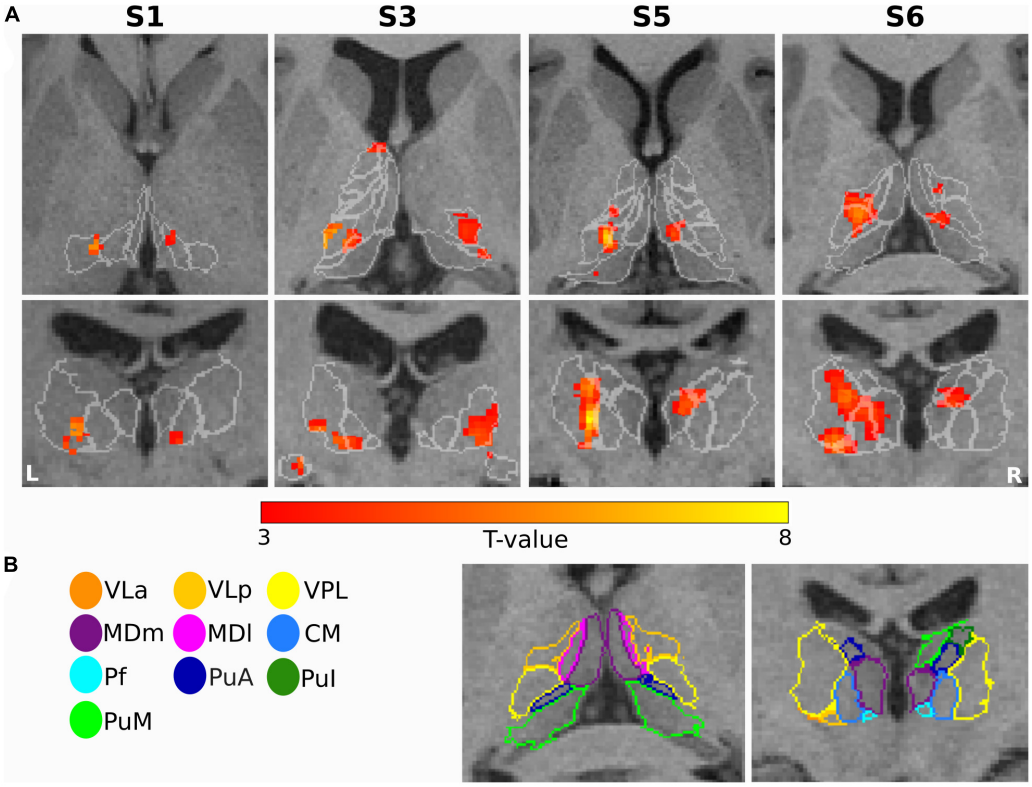

FIGURE 6
Sensory task: **(A)** Single subject thalamic t-statistic maps (uncorrected $p < 0.001$) obtained for the tactile task-based fMRI experiment. The activation maps (5-voxel minimum cluster size) for subjects S1, S3, S5, and S6 are overlaid on representative axial (top) and coronal (bottom) sections of the 3T T1-weighted MPRAGE image, accentuating the prominent activation of the thalamic nuclei. **(B)** The contours of the nuclei of the thalamus are shown for subject S6 and mapped to the anatomical MPRAGE image.

stronger activation, which may be related to a higher attention on the right hand performing the task.

Limitations and future directions

Due to the complex and laborious experimental set-up along with scan time constraints, we applied the active and passive stimuli only to the fingers of the right hand in right-handed subjects. However, we expect that active and passive fMRI tasks can evoke the same activation pattern in the contralateral side (Nakamura et al., 2020). Therefore, it appears interesting to explore in future work whether stimulating the left hand in right handed subjects would yield comparable thalamic activation features in the right hemisphere. Despite the small number of participants, our study allowed us to identify the main thalamic nuclei involved in a sensorimotor task with visual as well as focusing elements, with the findings consistent over all participants. However, because only healthy subjects participated, there is no direct clinical-radiological correlation yet. A comparison with pre-surgical data from Parkinson's disease patients eligible for deep brain stimulation (DBS) could be a potential follow-up step to establish whether functional MR image guidance may prove helpful to enable more accurate electrode placement.

Despite imaging at ultra-high field strength benefits from an enhancement of the SNR, which can be translated into an increased spatial resolution, precise anatomical segmentation based on structural ultra-high field data yet constitutes a major challenge. An increased spatial resolution may reveal more fine-grained structural details, such as small sulci and gyri, however, accurately detecting these nuances using currently available segmentation software such as FreeSurfer remains difficult. The altered contrast at ultra-high field strength, caused by differences in relaxation times as well as increased static and transmit field inhomogeneities compared to lower magnetic field strengths, results in more complex tissue contrast patterns, which cannot be handled properly by contemporary segmentation tools as those are optimized for image contrasts at lower fields. A segmentation based on structural 9.4T data would lead to inaccurate results and a cascade of errors in downstream analysis. Therefore, to segment individual thalamic nuclei, we used structural data acquired at 3T with an isotropic resolution of 0.8 mm, which was sufficiently high to resolve the anatomical structures in our 1.25 mm isotropic functional data acquired at 9.4T. The 3T segmentation results were deemed more accurate on visual inspection and successfully minimized any cascading effects.

In this study, we focused primarily on the functional localization of thalamic nuclei involved in sensorimotor processes. However, the imaging protocol was designed to cover the entire brain since in future work, we intend to investigate the functional connectivity between the individual thalamic nuclei and different cortical areas as well as basal ganglia. Furthermore, an

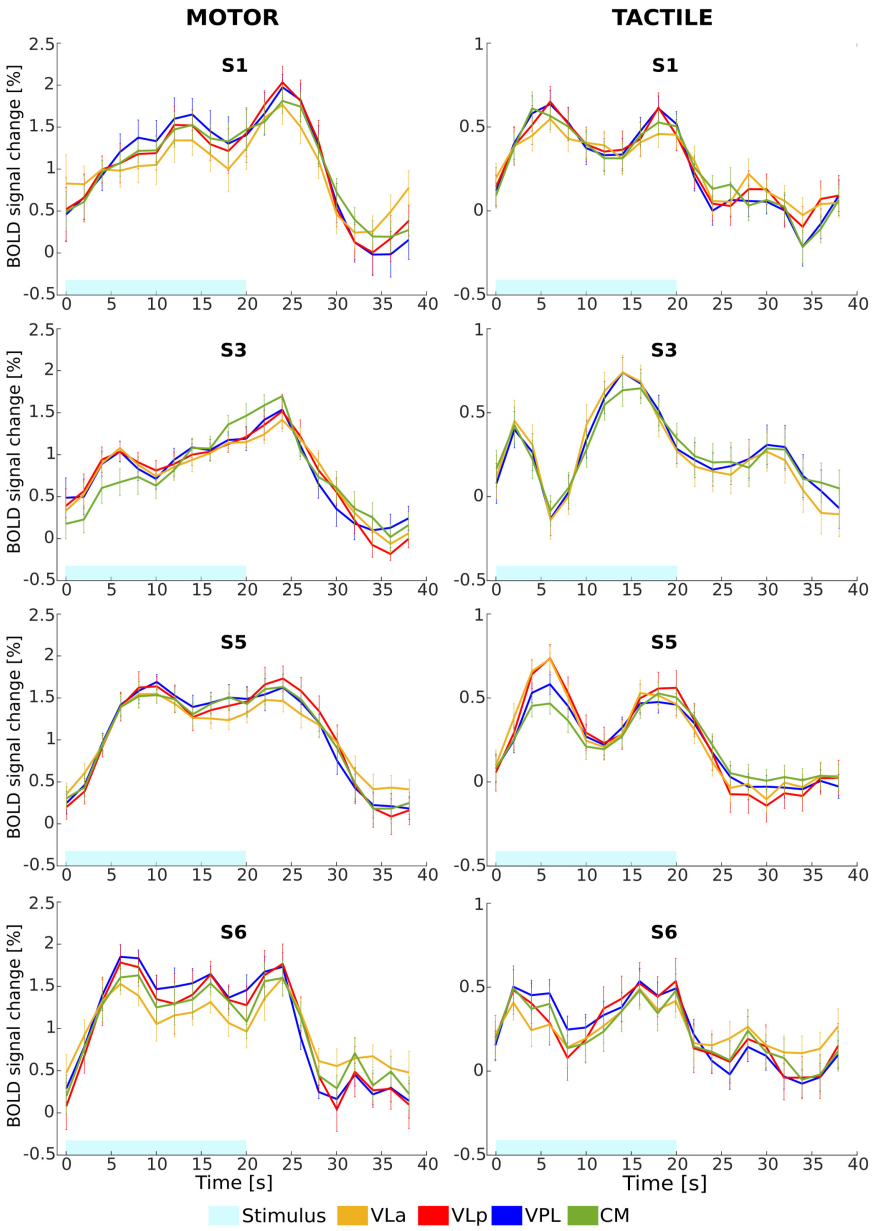

FIGURE 7
Mean relative BOLD signal change (%) time course from the activated voxels in the left VLa (yellow), VLp (rot), VPL (blue), and CM (green) nuclei in response to motor (left column) and tactile (right column) tasks for four representative subjects (S1, S3, S5, and S6). Error bars represent standard error of the mean.

improvement in future studies may involve the implementation of passive motor tasks in addition to active motor tasks as employed here. This might not only provide an interesting comparison of voluntary and non-voluntary movements, but could also avoid the strong relayed inputs from the cortex and basal ganglia. However, this requires a more complex setup to apply passive movements in an automatized manner.

To our knowledge, the present study is the first to identify the sensorimotor thalamic nuclei in humans using task-based fMRI at a field strength of 9.4T. Our data provide new insight into the functional localization of the individual thalamic nuclei, as well as further evidence for the important role of the thalamus in processing a variety of inputs. The ability to consistently reproduce such results in order to localize the individual thalamic nuclei is crucial to assess the feasibility of fMRI for pre-surgical mapping. By addressing the challenges arising from the highly variable size and shape of the thalamus across individuals and taking into account the inconsistency between common atlases, ultra-high field fMRI may have the potential to enable pre-surgical localization of thalamic nuclei in a more accurate manner tailored to each patient.

Data availability statement

The raw data supporting the conclusions of this article will be made available by the authors, without undue reservation.

Ethics statement

The studies involving human participants were reviewed and approved by Ethics Committee of University of Tübingen. The patients/participants provided their written informed consent to participate in this study.

Author contributions

EC: study design, stimulus programming, data acquisition, planning and performing the data analysis, writing–original draft, and preparing the figures. RH: assistance in data acquisition, reviewing and editing the manuscript. ME: advice for data evaluation and reviewing the manuscript. FM: assistance in data acquisition and reviewing the manuscript. VK: reviewing and editing the manuscript. WG: supervision, reviewing and editing the manuscript. KS: resources, supervision, funding acquisition, reviewing and editing the manuscript. JB: advice for MR measurements and protocol optimization, reviewing and editing the manuscript. All authors contributed to the article and approved the submitted version.

Funding

This work was supported by DFG (grant numbers: SCHE 658/12 and SCHE 658/17) and BMBF (grant number: 01GQ1805A).

Conflict of interest

The authors declare that the research was conducted in the absence of any commercial or financial relationships that could be construed as a potential conflict of interest.

Publisher's note

All claims expressed in this article are solely those of the authors and do not necessarily represent those of their affiliated organizations, or those of the publisher, the editors and the reviewers. Any product that may be evaluated in this article, or claim that may be made by its manufacturer, is not guaranteed or endorsed by the publisher.

Supplementary material

The Supplementary Material for this article can be found online at: https://www.frontiersin.org/articles/10.3389/fnins.2023.1116002/full#supplementary-material

SUPPLEMENTARY FIGURE 1
(A) Representative temporal SNR maps for GE EPI performed using an 1.25 mm isotropic resolution and a multiband factor of 2 (MB2) at 9.4T without (left) and with (right) NORDIC correction. **(B)** Thalamic activation (motor stimulus) obtained in a single subject (S5). T-maps (uncorrected $p < 0.001$) without (left) and with (right) NORDIC correction.

SUPPLEMENTARY FIGURE 2
Anatomical image quality and SPM co-registration results for one subject (S2). First, the 3T T2-weighted (T2w) image was co-registered to the 3T T1-weighted (T1w) image, which were then both co-registered to the 9.4T T1w image. A: Coronal **(top row)** and axial **(bottom row)** views of the 9.4T T1w (left), 3T T1w **(middle)**, and 3T T2w (right) whole-brain images. B: Illustration of the zoomed area marked with a blue box in A. The green and red lines indicate the image contours of the 3T T1w and 3T T2w images calculated by the CheckReg tool in SPM, respectively. Left column: contours of the co-registered 3T T1w (green) and T2w (red) images on the 9.4T T1w image. Middle column: contours of the co-registered 3T T2w image on the 3T T1w image. Right column: contours of the co-registered 3T T1w image on the 3T T2w image.

SUPPLEMENTARY FIGURE 3
Whole-brain single-subject GLM results. Panel **(A)** illustrates the task-evoked neural activity in the cerebral cortex for the motor (top row) and tactile (bottom row) task-based fMRI experiments in four representative subjects (S1, S3, S5, and S6). Similarly, panel **(B)** depicts the neural activity in the right cerebellum in response to the same tasks in the same four subjects. For each subject, the t-statistic maps ($p < 0.05$ FWE with a minimum cluster size of 20 voxels) are superimposed on the most representative axial (A) and sagittal (B) slices of a 3T T1-weighted MPRAGE image in neurological convention.

SUPPLEMENTARY FIGURE 4
Difference between motor and tactile task-based activation, calculated by subtracting the relative number of activated voxels ($p < 0.001$, uncorrected) in percentage of the tactile task (cf. **Figure 5**) from the respective value of the motor task (cf. **Figure 3**) within left **(A)** and right **(B)** thalamic nuclei. Please note that only the eight subjects, who participated in both tasks, are included here.

References

Andersson, J. L., Skare, S., and Ashburner, J. (2003). How to correct susceptibility distortions in spin-echo echo-planar images: application to diffusion tensor imaging. *Neuroimage* 20, 870–888. doi: 10.1016/S1053-8119(03)00336-7

Arce-McShane, F. I., Ross, C. F., Takahashi, K., Sessle, B. J., and Hatsopoulos, N. G. (2016). Primary motor and sensory cortical areas communicate via spatiotemporally coordinated networks at multiple frequencies. *Proc. Natl. Acad. Sci. U.S.A.* 113, 5083–5088. doi: 10.1073/pnas.1600788113

Benevento, L. A., Rezak, M., and Santos, A. (1977). An autoradiographic study of the projections of the pretectum in the rhesus monkey (*Macaca mulatta*): evidence for sensorimotor links to the thalamus and oculomotor nuclei. *Brain Res.* 127, 197–218. doi: 10.1016/0006-8993(77)90536-4

Bosch-Bouju, C., Hyland, B. I., and Parr-Brownlie, L. C. (2013). Motor thalamus integration of cortical, cerebellar and basal ganglia information: implications for normal and parkinsonian conditions. *Front. Comput. Neurosci.* 7:163. doi: 10.3389/fncom.2013.00163

Brainard, D. H. (1997). The psychophysics toolbox. *Spat. Vis.* 10, 433–436.

Darian-Smith, C., Darian-Smith, I., and Cheema, S. S. (1990). Thalamic projections to sensorimotor cortex in the macaque monkey: use of multiple retrograde fluorescent tracers. *J. Comp. Neurol.* 299, 17–46. doi: 10.1002/cne.902990103

Edwards, L. L., King, E. M., Buetefisch, C. M., and Borich, M. R. (2019). Putting the "Sensory" Into Sensorimotor Control: The Role of Sensorimotor Integration in Goal-Directed Hand Movements After Stroke. *Front. Integr. Neurosci.* 13:16. doi: 10.3389/fnint.2019.00016

Fang, P. C., Stepniewska, I., and Kaas, J. H. (2006). The thalamic connections of motor, premotor, and prefrontal areas of cortex in a prosimian primate (*Otolemur garnetti*). *Neuroscience* 143, 987–1020. doi: 10.1016/j.neuroscience.2006.08.053

Filippi, M., Messina, R., and Rocca, M. A. (2016). "fMRI of the Sensorimotor System," in *fMRI Techniques and Protocols*, ed. M. Filippi (New York, NY: Springer New York), 523–543.

Fischer, J., and Whitney, D. (2012). Attention gates visual coding in the human pulvinar. *Nat. Commun.* 3:1051. doi: 10.1038/ncomms2054

Fischl, B., Sereno, M. I., and Dale, A. M. (1999). Cortical surface-based analysis. II: Inflation, flattening, and a surface-based coordinate system. *Neuroimage* 9, 195–207. doi: 10.1006/nimg.1998.0396

Gaidica, M., Hurst, A., Cyr, C., and Leventhal, D. K. (2018). Distinct populations of motor thalamic neurons encode action initiation, action selection, and movement vigor. *J. Neurosci.* 38, 6563–6573. doi: 10.1523/JNEUROSCI.0463-18.2018

Grodd, W., Hulsmann, E., Lotze, M., Wildgruber, D., and Erb, M. (2001). Sensorimotor mapping of the human cerebellum: fMRI evidence of somatotopic organization. *Hum. Brain Mapp.* 13, 55–73. doi: 10.1002/hbm.1025

Guillery, R. W., and Sherman, S. M. (2002). The thalamus as a monitor of motor outputs. *Philos. Trans. R. Soc. Lond. B Biol. Sci.* 357, 1809–1821. doi: 10.1098/rstb.2002.1171

Haber, S., and McFarland, N. R. (2001). The place of the thalamus in frontal cortical-basal ganglia circuits. *Neuroscientist* 7, 315–324. doi: 10.1177/107385840100700408

Hermes, D., Miller, K. J., Vansteensel, M. J., Aarnoutse, E. J., Leijten, F. S., and Ramsey, N. F. (2012). Neurophysiologic correlates of fMRI in human motor cortex. *Hum. Brain Mapp.* 33, 1689–1699. doi: 10.1002/hbm.21314

Hyde, J. S., Biswal, B. B., and Jesmanowicz, A. (2001). High-resolution fMRI using multislice partial k-space GR-EPI with cubic voxels. *Magn. Reson. Med.* 46, 114–125. doi: 10.1002/mrm.1166

Iglesias, J. E., Insausti, R., Lerma-Usabiaga, G., Bocchetta, M., Van Leemput, K., Greve, D. N., et al. (2018). A probabilistic atlas of the human thalamic nuclei combining ex vivo MRI and histology. *Neuroimage* 183, 314–326. doi: 10.1016/j.neuroimage.2018.08.012

Ilinsky, I. A., and Kultas-Ilinsky, K. (1987). Sagittal cytoarchitectonic maps of the *Macaca mulatta* thalamus with a revised nomenclature of the motor-related nuclei validated by observations on their connectivity. *J. Comp. Neurol.* 262, 331–364. doi: 10.1002/cne.902620303

Kinomura, S., Larsson, J., Gulyas, B., and Roland, P. E. (1996). Activation by attention of the human reticular formation and thalamic intralaminar nuclei. *Science* 271, 512–515. doi: 10.1126/science.271.5248.512

Kishore, A., Meunier, S., and Popa, T. (2014). Cerebellar influence on motor cortex plasticity: behavioral implications for Parkinson's disease. *Front. Neurol.* 5:68. doi: 10.3389/fneur.2014.00068

Kumar, V., Mang, S., and Grodd, W. (2015). Direct diffusion-based parcellation of the human thalamus. *Brain Struct. Funct.* 220, 1619–1635. doi: 10.1007/s00429-014-0748-2

Kumar, V. J., Beckmann, C. F., Scheffler, K., and Grodd, W. (2022). Relay and higher-order thalamic nuclei show an intertwined functional association with cortical-networks. *Commun. Biol.* 5:1187. doi: 10.1038/s42003-022-04126-w

Lambert, C., Simon, H., Colman, J., and Barrick, T. R. (2017). Defining thalamic nuclei and topographic connectivity gradients in vivo. *Neuroimage* 158, 466–479. doi: 10.1016/j.neuroimage.2016.08.028

Landelle, C., Lungu, O., Vahdat, S., Kavounoudias, A., Marchand-Pauvert, V., De Leener, B., et al. (2021). Investigating the human spinal sensorimotor pathways through functional magnetic resonance imaging. *Neuroimage* 245:118684. doi: 10.1016/j.neuroimage.2021.118684

Logothetis, N. K., Pauls, J., Augath, M., Trinath, T., and Oeltermann, A. (2001). Neurophysiological investigation of the basis of the fMRI signal. *Nature* 412, 150–157. doi: 10.1038/35084005

Lotze, M., Erb, M., Flor, H., Huelsmann, E., Godde, B., and Grodd, W. (2000). fMRI evaluation of somatotopic representation in human primary motor cortex. *Neuroimage* 11(5 Pt 1), 473–481. doi: 10.1006/nimg.2000.0556

Mo, C., and Sherman, S. M. (2019). A sensorimotor pathway via higher-order thalamus. *J. Neurosci.* 39, 692–704. doi: 10.1523/JNEUROSCI.1467-18.2018

Moeller, S., Pisharady, P. K., Ramanna, S., Lenglet, C., Wu, X., Dowdle, L., et al. (2021). NOise reduction with DIstribution Corrected (NORDIC) PCA in dMRI with complex-valued parameter-free locally low-rank processing. *Neuroimage* 226:117539. doi: 10.1016/j.neuroimage.2020.117539

Morash, V., Bai, O., Furlani, S., Lin, P., and Hallett, M. (2008). Classifying EEG signals preceding right hand, left hand, tongue, and right foot movements and motor imageries. *Clin. Neurophysiol.* 119, 2570–2578. doi: 10.1016/j.clinph.2008.08.013

Muthukumaraswamy, S. D., and Johnson, B. W. (2004). Primary motor cortex activation during action observation revealed by wavelet analysis of the EEG. *Clin. Neurophysiol.* 115, 1760–1766. doi: 10.1016/j.clinph.2004.03.004

Nakamura, Y., Nakamura, Y., Pelosi, A., Djemai, B., Debacker, C., Herve, D., et al. (2020). fMRI detects bilateral brain network activation following unilateral chemogenetic activation of direct striatal projection neurons. *Neuroimage* 220:117079. doi: 10.1016/j.neuroimage.2020.117079

Pelli, D. G. (1997). The VideoToolbox software for visual psychophysics: transforming numbers into movies. *Spat. Vis.* 10, 437–442.

Petersen, C. C. H. (2019). Sensorimotor processing in the rodent barrel cortex. *Nat. Rev. Neurosci.* 20, 533–546. doi: 10.1038/s41583-019-0200-y

Petersen, S. E., Robinson, D. L., and Morris, J. D. (1987). Contributions of the pulvinar to visual spatial attention. *Neuropsychologia* 25, 97–105. doi: 10.1016/0028-3932(87)90046-7

Pohmann, R., Shajan, G., and Balla, D. Z. (2011). Contrast at high field: Relaxation times, magnetization transfer and phase in the rat brain at 16.4 T. *Magn. Reson. Med.* 66, 1572–1581. doi: 10.1002/mrm.22949

Pohmann, R., Speck, O., and Scheffler, K. (2016). Signal-to-noise ratio and MR tissue parameters in human brain imaging at 3, 7, and 9.4 tesla using current receive coil arrays. *Magn. Reson. Med.* 75, 801–809. doi: 10.1002/mrm.25677

Ranieri, F., Pellegrino, G., Ciancio, A. L., Musumeci, G., Noce, E., Insola, A., et al. (2022). Sensorimotor integration within the primary motor cortex by selective nerve fascicle stimulation. *J. Physiol.* 600, 1497–1514. doi: 10.1113/JP282259

Rao, S. M., Binder, J. R., Hammeke, T. A., Bandettini, P. A., Bobholz, J. A., Frost, J. A., et al. (1995). Somatotopic mapping of the human primary motor cortex with functional magnetic resonance imaging. *Neurology* 45, 919–924. doi: 10.1212/wnl.45.5.919

Rosazza, C., Aquino, D., D'Incerti, L., Cordella, R., Andronache, A., Zaca, D., et al. (2014). Preoperative mapping of the sensorimotor cortex: comparative assessment of task-based and resting-state FMRI. *PLoS One* 9:e98860. doi: 10.1371/journal.pone.0098860

Saalmann, Y. B. (2014). Intralaminar and medial thalamic influence on cortical synchrony, information transmission and cognition. *Front. Syst. Neurosci.* 8:83. doi: 10.3389/fnsys.2014.00083

Sanganahalli, B. G., Thompson, G. J., Parent, M., Verhagen, J. V., Blumenfeld, H., Herman, P., et al. (2022). Thalamic activations in rat brain by fMRI during tactile (forepaw, whisker) and non-tactile (visual, olfactory) sensory stimulations. *PLoS One* 17:e0267916. doi: 10.1371/journal.pone.0267916

Sebastiani, V., de Pasquale, F., Costantini, M., Mantini, D., Pizzella, V., Romani, G. L., et al. (2014). Being an agent or an observer: different spectral dynamics revealed by MEG. *Neuroimage* 102(Pt 2), 717–728. doi: 10.1016/j.neuroimage.2014.08.031

Shajan, G., Kozlov, M., Hoffmann, J., Turner, R., Scheffler, K., and Pohmann, R. (2014). A 16-channel dual-row transmit array in combination with a 31-element receive array for human brain imaging at 9.4 T. *Magn. Reson. Med.* 71, 870–879. doi: 10.1002/mrm.24726

Sherman, S. M., and Guillery, R. W. (2002). The role of the thalamus in the flow of information to the cortex. *Philos. Trans. R. Soc. Lond. B Biol. Sci.* 357, 1695–1708. doi: 10.1098/rstb.2002.1161

Siero, J. C., Hermes, D., Hoogduin, H., Luijten, P. R., Ramsey, N. F., and Petridou, N. (2014). BOLD matches neuronal activity at the mm scale: a combined 7T fMRI and ECoG study in human sensorimotor cortex. *Neuroimage* 101, 177–184. doi: 10.1016/j.neuroimage.2014.07.002

Smith, S. M., Jenkinson, M., Woolrich, M. W., Beckmann, C. F., Behrens, T. E., Johansen-Berg, H., et al. (2004). Advances in functional and structural MR image analysis and implementation as FSL. *Neuroimage* 23(Suppl. 1), S208–S219. doi: 10.1016/j.neuroimage.2004.07.051

Theyel, B. B., Llano, D. A., and Sherman, S. M. (2010). The corticothalamocortical circuit drives higher-order cortex in the mouse. *Nat. Neurosci.* 13, 84–88. doi: 10.1038/nn.2449

Van der Werf, Y. D., Witter, M. P., and Groenewegen, H. J. (2002). The intralaminar and midline nuclei of the thalamus. Anatomical and functional evidence for participation in processes of arousal and awareness. *Brain Res. Brain Res. Rev.* 39, 107–140. doi: 10.1016/s0165-0173(02)00181-9

Wang, M., He, Y., Sejnowski, T. J., and Yu, X. (2018). Brain-state dependent astrocytic Ca(2+) signals are coupled to both positive and negative BOLD-fMRI signals. *Proc. Natl. Acad. Sci. U.S.A.* 115, E1647–E1656. doi: 10.1073/pnas.1711692115

Wang, Y., Taylor, E., Zikopoulos, B., Seta, F., Huang, N., Hamilton, J. A., et al. (2021). Aging-induced microbleeds of the mouse thalamus compared to sensorimotor and memory defects. *Neurobiol. Aging* 100, 39–47. doi: 10.1016/j.neurobiolaging.2020.11.017

Wang, Z., Jia, X., Liang, P., Qi, Z., Yang, Y., Zhou, W., et al. (2012). Changes in thalamus connectivity in mild cognitive impairment: evidence from resting state fMRI. *Eur. J. Radiol.* 81, 277–285. doi: 10.1016/j.ejrad.2010.12.044

Woodward, N. D., Karbasforoushan, H., and Heckers, S. (2012). Thalamocortical dysconnectivity in schizophrenia. *Am. J. Psychiatry* 169, 1092–1099. doi: 10.1176/appi.ajp.2012.12010056

Wurtz, R. H., Sommer, M. A., and Cavanaugh, J. (2005). Drivers from the deep: the contribution of collicular input to thalamocortical processing. *Prog. Brain Res.* 149, 207–225. doi: 10.1016/S0079-6123(05)49015-9

Zhao, M., Marino, M., Samogin, J., Swinnen, S. P., and Mantini, D. (2019). Hand, foot and lip representations in primary sensorimotor cortex: a high-density electroencephalography study. *Sci. Rep.* 9:19464. doi: 10.1038/s41598-019-55369-3

Zhou, H., Schafer, R. J., and Desimone, R. (2016). Pulvinar-cortex interactions in vision and attention. *Neuron* 89, 209–220. doi: 10.1016/j.neuron.2015.11.034

frontiers | Frontiers in Neuroscience

TYPE Original Research
PUBLISHED 11 April 2023
DOI 10.3389/fnins.2023.1096232

OPEN ACCESS

EDITED BY
Nico Sollmann,
University of California,
San Francisco,
United States

REVIEWED BY
Oscar Miranda Dominguez,
University of Minnesota Twin Cities,
United States
Simon James Graham,
Sunnybrook Research Institute (SRI),
Canada

*CORRESPONDENCE
Dardo Tomasi
✉ dardo.tomasi@nih.gov

SPECIALTY SECTION
This article was submitted to
Brain Imaging Methods,
a section of the journal
Frontiers in Neuroscience

RECEIVED 11 November 2022
ACCEPTED 20 March 2023
PUBLISHED 11 April 2023

CITATION
Tomasi D and Volkow ND (2023) Brain motion networks predict head motion during rest- and task-fMRI.
Front. Neurosci. 17:1096232.
doi: 10.3389/fnins.2023.1096232

Brain motion networks predict head motion during rest- and task-fMRI

Dardo Tomasi[1]* and Nora D. Volkow[1,2]

[1]National Institute on Alcohol Abuse and Alcoholism, Bethesda, MD, United States, [2]National Institute on Drug Abuse, Bethesda, MD, United States

Introduction: The capacity to stay still during scanning, which is necessary to avoid motion confounds while imaging, varies markedly between people.

Methods: Here we investigated the effect of head motion on functional connectivity using connectome-based predictive modeling (CPM) and publicly available brain functional magnetic resonance imaging (fMRI) data from 414 individuals with low frame-to-frame motion (Δd<0.18mm). Leave-one-out was used for internal cross-validation of head motion prediction in 207 participants, and twofold cross-validation was used in an independent sample (n=207).

Results and Discussion: Parametric testing, as well as CPM-based permutations for null hypothesis testing, revealed strong linear associations between observed and predicted values of head motion. Motion prediction accuracy was higher for task- than for rest-fMRI, and for absolute head motion (d) than for Δd. Denoising attenuated the predictability of head motion, but stricter framewise displacement threshold (FD=0.2mm) for motion censoring did not alter the accuracy of the predictions obtained with lenient censoring (FD=0.5mm). For rest-fMRI, prediction accuracy was lower for individuals with low motion (mean Δd<0.02mm; n=200) than for those with moderate motion (Δd<0.04mm; n=414). The cerebellum and default-mode network (DMN) regions that forecasted individual differences in d and Δd during six different tasks- and two rest-fMRI sessions were consistently prone to the deleterious effect of head motion. However, these findings generalized to a novel group of 1,422 individuals but not to simulated datasets without neurobiological contributions, suggesting that cerebellar and DMN connectivity could partially reflect functional signals pertaining to inhibitory motor control during fMRI.

KEYWORDS

head motion, fMRI, proprioception, self-motion perception, hyperactivity, impulsivity, machine learning

Introduction

Head motion causes artifacts during magnetic resonance imaging (MRI; Friston et al., 1996; Rohde et al., 2004) and other neuroimaging modalities (Cooper et al., 1992; Nehmeh and Erdi, 2008; Catana et al., 2011), which is why patients are instructed not to move their heads during scanning. However, the capacity to lie still during scanning varies markedly between people, being dependent among other factors on brain maturation and hence much worse in children than adults (Poldrack et al., 2002). It is also impaired in some neurodevelopmental and neurodegenerative disorders such as attention deficit hyperactivity disorder (ADHD), autism, and dementias (Maknojia et al., 2019).

Head motion is particularly concerning for MRI studies of brain functional connectivity (Birn et al., 2006; Power et al., 2012; Satterthwaite et al., 2012; Van Dijk et al., 2012) because it can cause systematic group differences in connectivity (Andrews-Hanna et al., 2007; Fair et al., 2007; Damoiseaux et al., 2008; Fair et al., 2008; Greicius, 2008; Dosenbach et al., 2010) and can even mimic trait correlates of behavior (Siegel et al., 2017). While functional MRI (fMRI) studies treat motion-related signals as artifacts, removing imaging data with excessive motion (Power et al., 2012; Satterthwaite et al., 2012; Van Dijk et al., 2012; Fassbender et al., 2017; Hong et al., 2019; Maknojia et al., 2019), most studies have not investigated if group differences in head movement explain the reported connectivity differences between patients and controls (Buckner et al., 2013). Also, the time frames that drive whole-brain functional connectivity are almost never among those censored for excessive in-scanner motion (Betzel et al., 2022).

Nonetheless the previously reported association between default mode network (DMN) connectivity and in-scanner head motion during resting-state fMRI could reflect greater self-referential mental activity, which could facilitate the person's ability to stay still during scanning. Specifically, higher functional connectivity between distant default-mode network (DMN) regions was reported in subjects with low head motion compared to those with high motion (Zeng et al., 2014). However, this study did not find within-subject differences in connectivity between fMRI sessions with low and high motion (Zeng et al., 2014), suggesting that between subjects differences in head motion reflect a neurobiological trait (Pujol et al., 2014). However, no study to our knowledge has evaluated whether functional connectivity can predict an individual's head motion behavior, nor what regions or networks predominantly contribute to in-scanner head movement or might be more sensitive to motion artifacts.

Here we tested the hypothesis that individual differences in functional connectivity can be used to predict in-scanner head motion. For this purpose, we analyzed brain imaging data of 414 healthy adults who underwent six different task-fMRI and two rest-fMRI sessions from the Human Connectome Project (HCP). We investigated the reproducibility of head motion prediction in two independent HCP samples, each with 207 healthy individuals, and two novel groups from the Brain Genomics Superstruct Project (GSP), each with 711 healthy young adults.

Materials and methods

HCP datasets

The datasets used in this study were extracted from the HCP 1,200 Subjects data release.[1] HCP participants provided written informed consent as approved by the Institutional Review Board (IRB) at Washington University. To avoid phase encoding bias, the analyses were restricted to participants for whom both phase-encoding scans (left–right, LR; right–left, RL) for the two rest-fMRI sessions (R1 and R2; collected on two different days) and all six task-fMRI sessions (emotion, relational, motor, working memory, language, and gambling; Barch et al., 2013) were complete and available. Individuals were excluded from the study due to incomplete image datasets, image artifacts (identified with the aid of principal component analysis), or excessive head motion (frame-to-frame displacement, $\Delta d > 0.18$ mm). We chose this motion threshold to ensure sufficient sensitivity to head motion taking into account that the magnitude of motion-related fMRI signal changes scales with the magnitude of head motion (Satterthwaite et al., 2013b) and that micromotion > 0.2 mm can systematically bias estimates of resting-state functional connectivity (Van Dijk et al., 2012). The 414 participants were half-split into the Training sample for the optimization of prediction models, and the Test sample for the twofold cross-validation of the prediction models in an independent set of subjects. The samples were matched so there was no significant age or sex differences between the Training and Test samples (Table 1). Only one family member was kept in the study.

GSP datasets

In addition, we used imaging data from 1,422 healthy young adults (21.5 ± 2.9 years old; 800 females) from the Brain Genomics Superstruct Project[2] to cross-validate the prediction in an independent dataset. GSP individuals provided written informed consent approved by the Partners Health Care IRB and the Harvard University Committee on the Use of Human Subjects in Research and agreed to data sharing.

fMRI tasks

We aimed to test linear associations of head motion with functional connectivity strength during the resting state, and during the performance of cognitive, emotional, and motor fMRI tasks. Thus, in the HCP dataset we selected eight fMRI sessions, including those collected during the resting state (R1 and R2) and during the performance of 6 different tasks, which are described in detail elsewhere and target the following domains (Barch et al., 2013): *Emotion*, EMO (Hariri et al., 2002); *Relational processing*, REL (Smith et al., 2007); *Motor*, MOT (Buckner et al., 2011; Yeo et al., 2011); *N-back working memory*, WM (Barch et al., 2013); *Language*, LAN (Binder et al., 2011); and *Gambling*, GAM (Delgado et al., 2000).

MRI acquisition and image analyses

HCP datasets

Functional images with high spatiotemporal resolution were acquired in a 3.0 T Siemens Skyra scanner (Siemens Healthcare, Erlangen, Germany) with a 32-channel coil using a gradient echo-planar imaging (EPI) sequence (multiband factor 8, repetition time, TR = 720 ms, echo time, TE = 33.1 ms, flip angle 52°, 104 × 90 matrix size, 72 slices, and 2 mm isotropic voxels) with whole brain coverage (including the cerebellum) and automated alignment of slice positioning (e.g., "AutoAlign" mode; Smith et al., 2013; Uğurbil et al.,

1 http://www.humanconnectome.org/

2 https://www.neuroinfo.org/gsp

TABLE 1 Demographics and residual time-averaged root-mean-square (RMS) estimates of absolute (d) and relative (Δd) motion for the first 150 frames that survived scrubbing with framewise displacement threshold of 0.2mm for Training and Test HCP samples.

HCP	Training		Test		P		# Frames removed
Age [years]	29(4)		29(4)		ns		
Sex (M/F)	84/123		87/120		ns		
	d [mm] mean (SD)	**Δd [mm] mean (SD)**	**d [mm] mean (SD)**	**Δd [mm] mean (SD)**	**(d)**	**(Δd)**	**mean (SD)**
WM	0.14(0.12)	0.029(0.014)	0.12(0.08)	0.028(0.011)	0.03	ns	1.1(3.3)
LAN	0.16(0.14)	0.038(0.017)	0.14(0.15)	0.035(0.014)	ns	ns	0.9(2.4)
REL	0.23(0.16)	0.052(0.024)	0.21(0.11)	0.048(0.019)	ns	ns	1.8(2.8)
MOT	0.19(0.10)	0.043(0.018)	0.17(0.10)	0.041(0.016)	ns	ns	1.8(3.9)
GAM	0.17(0.09)	0.046(0.021)	0.16(0.08)	0.042(0.016)	ns	ns	0.7(1.8)
EMO	0.30(0.22)	0.065(0.030)	0.24(0.11)	0.060(0.024)	0.001	ns	0.7(1.8)
R1	0.04(0.02)	0.010(0.004)	0.04(0.02)	0.009(0.003)	0.05	ns	0.6(1.7)
R2	0.04(0.02)	0.010(0.005)	0.04(0.02)	0.009(0.004)	ns	ns	0.7(1.6)

EMO, emotion; LAN, language; REL, relational; GAM, gambling; MOT, motor; and WM, working memory; R1, rest1; and R2, rest2. #Frames: Average number of frames removed by scrubbing in $0 < t < 2$ min.

2013). Scans were repeated twice using left–right (LR) and right–left (RL) phase encoding directions. For the resting-state scans, the scanner room was darkened, and subjects were asked to lie with eyes open and not to fall asleep while fixating on a white cross (on a dark background) think of nothing, relax, and to remain still during scanning. The T1-weighted 3D magnetization-prepared gradient-echo image (Mugler and Brookeman, 1990; MP-RAGE; TR/TE = 2,400/2.14 ms, TI = 1 s, FA = 8°) and variable flip angle turbo spin-echo (Mugler et al., 2000; Siemens SPACE; TR/TE = 3,200/565 ms) pulse sequences were used to acquire high-resolution anatomical brain images with 0.7 mm isotropic voxels and field-of-view (FOV) = 224 mm × 224 mm. We used the "minimal preprocessing" datasets released by the HCP, which include gradient distortion correction, rigid-body realignment, field-map processing, and spatial normalization to the stereotactic space of the Montreal Neurological Institute (MNI; Glasser et al., 2013).

GSP datasets

Imaging data were collected on matched 3 T Tim Trio scanners (Siemens Healthcare, Erlangen, Germany) at Harvard University and Massachusetts General Hospital using a 12-channel phased-array head coil. Gradient-echo EPI (TR = 3 s; TE = 30 ms; flip angle = 85°, 47 slices, 3 mm isotropic resolution; 124 measurements) with whole-brain coverage, including the entire cerebellum, was used to acquire functional images with blood oxygenation level-dependent (BOLD) contrast. Participants were instructed to remain still, stay awake, and keep their eyes open during fMRI. Multi-echo T1-weighted magnetization-prepared gradient-echo (MP-RAGE; van der Kouwe et al., 2008) imaging (TR = 2.2 s; TE = 1.5/3.4/5.2/7.0 ms; flip angle = 7°; TI = 1.1 s; 144 slices, 1.2 mm isotropic resolution) was used to acquire anatomical images. The FreeSurfer (version 5.3.0) package[3] (Fischl et al., 2002) was used to automatically segment anatomical MRI scans into cortical and subcortical gray matter structures. Functional images were screened for artifacts and excessive motion. The first four image volumes were discarded for signal stabilization purposes. The University of Oxford's Center for Functional Magnetic Resonance Imaging of the Brain (FMRIB) Software Library (FSL version 5.0)[4] was used for image realignment (to correct for head motion with MCFLIRT, Motion Correction using FMRIB's Linear Image Registration Tool), and for spatial normalization to the MNI152 template using 3 mm isotropic voxels (with FLIRT, the FMRIB's Linear Image Registration Tool; Jenkinson et al., 2002; Smith et al., 2004).

In addition, displacement timeseries reflecting how much a given voxel moved as a function of time were simulated by applying the affine transformations from image realignment to the first volume (Satterthwaite et al., 2013a). These simulated time series were realigned and spatially normalized to the MNI space.

Head motion

The Euclidian norms of head displacement and frame-to-frame velocity, d_i and Δd_i, were calculated from image realignment parameters (translations along x, y, and z with respect to the first volume) for each timepoint, i:

$$d_i = \sqrt{x_i^2 + y_i^2 + z_i^2};\ \Delta d_i = \sqrt{(x_i - x_{i-1})^2 + (y_i - y_{i-1})^2 + (z_i - z_{i-1})^2} \quad (1)$$

and the average root-mean-square (RMS) values of d_i and Δd_i, across LR and RL scans and timepoints, were used as summary metrics of absolute (d; measured from t = 0) and relative (frame-to-frame; Δd) head motion, respectively, in mm.

Framewise displacements (FD) were computed for every time point from head translations and rotations:

$$FD_i = |x_i - x_{i-1}| + |y_i - y_{i-1}| + |z_i - z_{i-1}| + 50mm \times \left(|\alpha_i - \alpha_{i-1}| + |\beta_i - \beta_{i-1}| + |\gamma_i - \gamma_{i-1}|\right) \quad [2]$$

3 http://surfer.nmr.mgh.harvard.edu

4 http://www.fmrib.ox.ac.uk/fsl

where rotational angles, α, β, and γ (in radians) were converted to displacements on the surface of a sphere of radius 50 mm as in previous work (Power et al., 2012). Time points were excluded if the RMS change in BOLD signals frame-to-frame was larger than 0.5%, and exceeded the censoring threshold $FD_i > 0.5$ mm (or $FD_i > 0.2$ mm; Power et al., 2015). Global signal regression (GSR) was used in all evaluated data to remove non-neuronal sources that contribute to the global signal (Power et al., 2014). Low-pass filtering (0.10 Hz frequency cutoff) was used to attenuate physiologic noise of high-frequency components.

Effect of pipeline choices for noise suppression

To assess the effect of motion on functional connectivity we studied fMRI datasets with and without removal of motion-related signals using linear regression with the time-varying realignment parameters (Tomasi and Volkow, 2010) and independent component analysis (ICA)-based X-noiseifier, an ICA-based automatic noise detection algorithm that can minimize various types of noise sources including head motion (Salimi-Khorshidi et al., 2014).

Functional connectome

Connectivity matrices, **M**, were constructed for each fMRI dataset and subject, using the corresponding preprocessed 4D time series. To assess the functional connectivity between regions-of-interest (ROIs) we used the Interactive Data Language (IDL, L3Harris Geospatial, Broomfield, CO). Three different brain atlases were used to provide ROIs: 1) Automated Anatomical Labeling (AAL)—Tzourio-Mazoyer et al. (2002) and 2) Shen et al. (2013), both of which include the cerebellum and subcortical regions and 3) Gordon et al. (2016), which does not include the cerebellum and subcortical regions, to assess the effect of brain parcellation on the accuracy of the behavioral prediction model. In addition, we combined the cortical partitions of the Gordon atlas with the 26 subcortical (including the brainstem) and 41 cerebellar partitions of the Shen atlas in a new whole-brain atlas with 400 partitions (Gordon400). Pearson correlation coefficients between pairs of ROI time courses were calculated independently for LR and RL scans and normalized to z-scores using the Fisher transformation. This resulted in 116 × 116 (AAL), 268 × 268 (Shen), 333 × 333 (Gordon), and 400 × 400 (Gordon400) symmetric connectivity matrices for each fMRI session and participant. The LR and RL correlation matrices corresponding to the same functional session were averaged to increase signal-to-noise. To allow for comparisons between task- and rest-fMRI results that were not biased by unequal data sampling, only the first 150 frames (to correspond with the short duration of the Emotion task-fMRI; ~2 min; 176 time points) of the time series that survived scrubbing were used to compute the corresponding **M**.

Head motion prediction model

The optimization of the prediction models was carried out using connectome-based predictive modeling (CPM; Shen et al., 2017) using leave-one-out cross-validation. Specifically, at each of n iterations, one of the n individuals was excluded and the four CPM steps, *feature selection*, *feature summarization*, *model building*, and *assessment of prediction significance* were carried sequentially n times in an iterative fashion as follows. *Feature selection*: Pearson correlation was used to assess associations between head motion scores and each element of the connectivity matrices (M_{ij}) in the Training sample. Matrix elements that had significant positive or negative correlations with the observed head motion scores (RMS values of d and Δd) were identified as edges of the positive or negative adjacency matrices and included in the model. Two thresholds were tested ($p < 0.01$ or 0.05) for feature selection to ascertain that results did not depend on arbitrary threshold selection. *Feature summarization*: Edges with positive (negative) correlation with motion scores were added to compute the positive (negative) network strength, X (Y). *Model building*: a bilinear model was fitted to the data across the n-1 individuals.

$$\Psi = a + b\,X + c\,Y \tag{3}$$

Here a, b, and c are model parameters, Ψ is the observed head motion score, and X and Y are the positive and negative network strengths derived from the connectivity matrices. We also assessed linear models purely driven by positive or negative features by setting $c = 0$ or $b = 0$. *Assessment of prediction significance*: The model was then used to predict the head motion score of the remaining individual from his/her corresponding positive and negative network strengths.

In addition, we used a twofold cross-validation approach to assess how the CPM results generalize to an independent data set. Specifically, the CPM model and features derived from the Training sample were used to predict head motion in the independent Test sample. Finally, the Training and Test samples were swapped (e.g., the CPM model and features derived from the Test sample were used to predict head motion in the independent Training sample) to complete the cross-validation.

Statistical analyses

The Shapiro–Wilk normality test (Shapiro and Wilk, 1965) was used to confirm the normal distribution of the functional connectivity strength. Thus, Pearson correlation was used to assess prediction accuracy, unless otherwise specified. Since Training and Test were independent samples, we used parametric statistics to assess the statistical significance of group differences in correlation between observed and predicted motion scores. To test for differences between two dependent correlations sharing one variable we used the Williams's test (Williams, 1959), and for correlations with different variables we used the Steiger's test (Steiger, 1980). The cortical networks were labeled using the Yale network definitions (Noble and Scheinost, 2020). Statistically significant correlations for a sample size $n = 207$ were set at $p < 3.213\text{E-}03$, corresponding to $R = 0.204$, using Bonferroni corrections for 16 comparisons (8 fMRI sessions × 2 motion measures). The Bonferroni method was also used to correct for multiple comparisons the results from within- and between-network predictions with the Gordon400 parcellation atlas (14 networks). Specifically, Bonferroni corrections were carried with 14 (within-network; $R > 0.2$) or 91 (between-network; $R > 0.23$) comparisons. A permutation framework was used for null hypothesis significance testing. Specifically, 1,000 random permutations of head motion scores were used to assess the distribution of prediction accuracy under possible rearrangements of motion scores.

Results

The realignment estimates of motion (d; i.e., "absolute motion") were significantly lower for rest ($d = 0.04\,mm \pm 0.02\,mm$) than for task sessions ($d = 0.19\,mm \pm 0.14\,mm$; $p < 2E\text{-}16$; Figure 1). Similarly, the frame-to-frame motion estimates (Δd; i.e., "relative motion") were significantly lower for rest ($\Delta d = 0.010 \pm 0.004\,mm$) than for task sessions ($\Delta d = 0.044\,mm \pm 0.022\,mm$; Figure 1). There were no sex differences, but older age was associated to lower d and Δd ($p < 0.004$, $F = 11.3$, df = 3,302, ANOVA).

Prediction of head motion from fMRI data

We found a strong linear association between observed and predicted values of d using Spearman correlation ($\rho > 0.59$; $p < 2.2E\text{-}16$; Figure 2A). Prediction models based on positive and negative network strength performed similarly across fMRI sessions in the Training sample (Figure 2B), in agreement with prior studies (Finn et al., 2015), supporting the notion that the negative and positive networks contain redundant information (Rosenberg et al., 2016). The correlation between observed and predicted absolute motion scores across subjects ("R," a benchmark of prediction accuracy) did not differ between task- or rest-fMRI sessions across all parcellations ($p > 0.3$, 2-sided t-test). Across linear and bilinear models, prediction accuracy was higher for Gordon than Shen and AAL and for Shen than AAL parcellations ($p < 1E\text{-}03$, 2-sided paired t-test; Figure 2C). The linear associations between observed and predicted measures of Δd were like those of d (Figure 3). Across fMRI sessions and models, motion prediction accuracy was lower for Δd than d, independently for the Training and Test sessions ($p < 0.01$, 2-sided paired t-test, Figures 2D, 3D).

Validation in an independent sample

We confirmed the generalizability of the linear association between head motion and functional connectivity in the Test sample (e.g., using twofold cross-validation). Specifically, for each participant in the independent Test sample ($n = 207$) we predicted head motion from the positive and negative features and the model parameters derived from the Training sample (Figure 2E). In the Test sample, prediction accuracy was lower for Gordon than Shen and AAL parcellation ($p < 0.01$, 2-sided paired t-test). In the Test sample, we also found that all prediction models performed similarly across fMRI sessions. Δd-prediction accuracy was lower for the Test sample than for the Training sample ($p < 5E\text{-}07$, 2-sided paired t-test, df = 23; Figure 3F).

Sensitivity to motion

Functional connectivity studies frequently address motion concerns by minimizing BOLD signals associated with head motion.

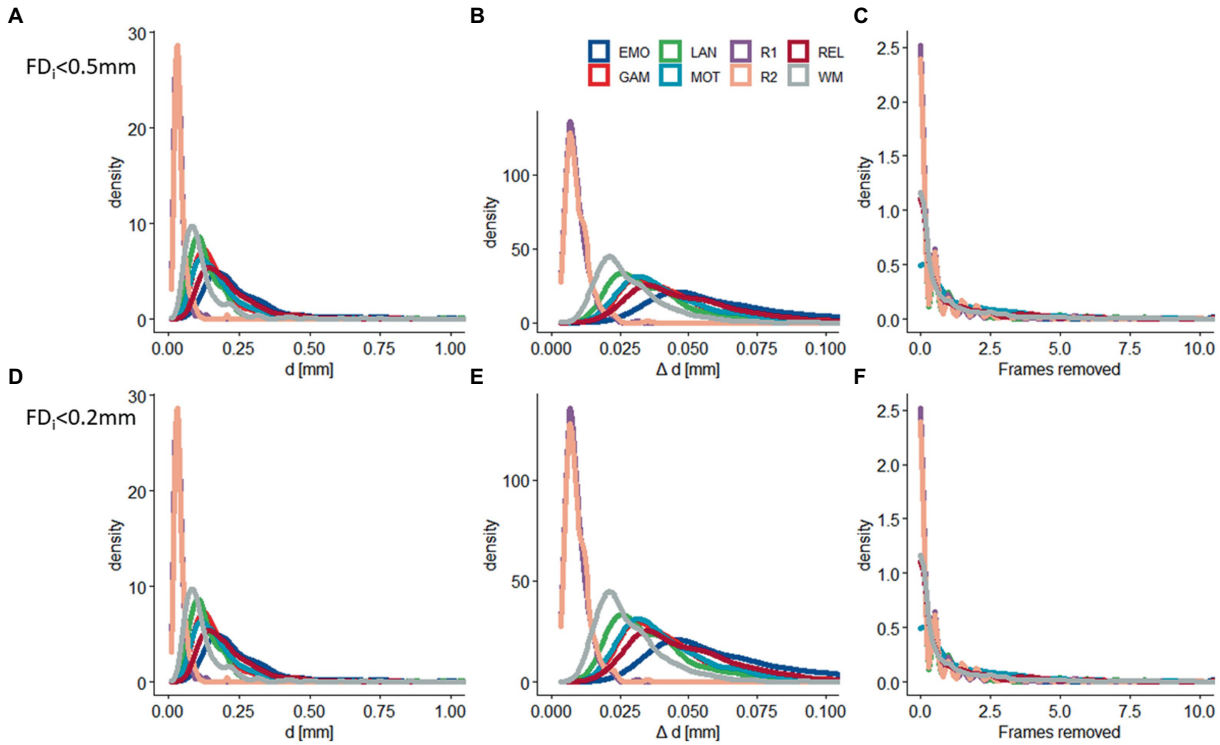

FIGURE 1
Residual head motion. Density plots showing across-subjects' distributions of residual time-averaged root-mean-square (RMS) estimates of absolute (d) and relative (Δd) motion, and the number of frames removed with framewise displacement (FD) thresholds of 0.5mm **(A–C)** and 0.2mm **(D–F)** for 6 task-fMRI sessions: (EMO: emotion; LAN: language; REL: relational; GAM: gambling; MOT: motor; and WM: working memory) and 2 rest-fMRI session (R1: rest1; and R2: rest2). Sample size: 414 healthy young adults.

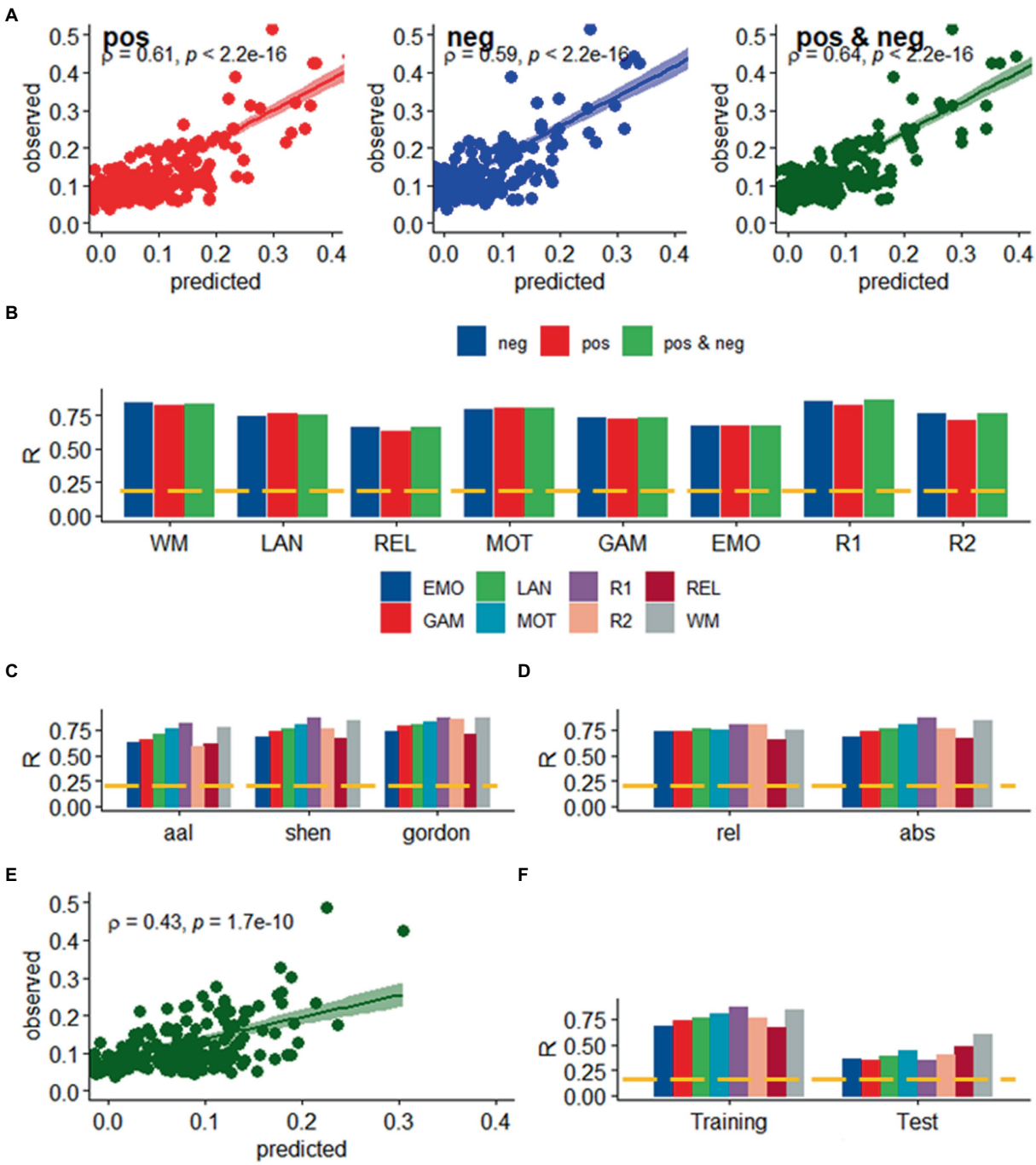

FIGURE 2
Prediction of absolute head motion. **(A)** Observed absolute head motion during fMRI sessions was predicted from positive and negative network strengths in "left out" individuals of the Training sample (n =207), using leave-one-out cross-validation for working memory (WM). **(B)** Correlation factor (R) between observed and predicted absolute motion excursions (d) did not differ across models purely based on positive, negative network strength, or both. Prediction accuracy (R) across brain parcellations **(C)** and for absolute and relative motion (Δd; **D**) in the training sample. **(E)** Functional connectivity predicted absolute head motion in an independent set of individuals ("Test sample"; n =207) using optimal models and features derived from the Training sample for the bilinear model for WM. **(F)** Prediction accuracy for absolute motion in Test and Training samples. ---p <0.05, Bonferroni corrected for 16 comparisons. Shen parcellation atlas. EMO, emotion; LAN, language; REL, relational; GAM, gambling; MOT, motor; and WM, working memory; R1, rest1; and R2, rest2. Sample size: 414 healthy young adults. Censoring threshold 0.5mm.

Popular approaches for this are based on (1) linear regression of rigid-body realignment parameters (Satterthwaite et al., 2013a) and ICA-based denoising algorithms that can minimize various types of noise sources, including head motion (Behzadi et al., 2007; Salimi-Khorshidi et al., 2014; Pruim et al., 2015); and (2) the removal of subjects with excessive micro-motion (Van Dijk et al., 2012). Here we used these approaches to assess the sensitivity of the head motion prediction model to the amount of motion in the data. The removal of 214 individuals from the original cohort of 414 individuals ("moderate motion") who had micro motion 0.18 mm > Δd > 0.08 mm in at least

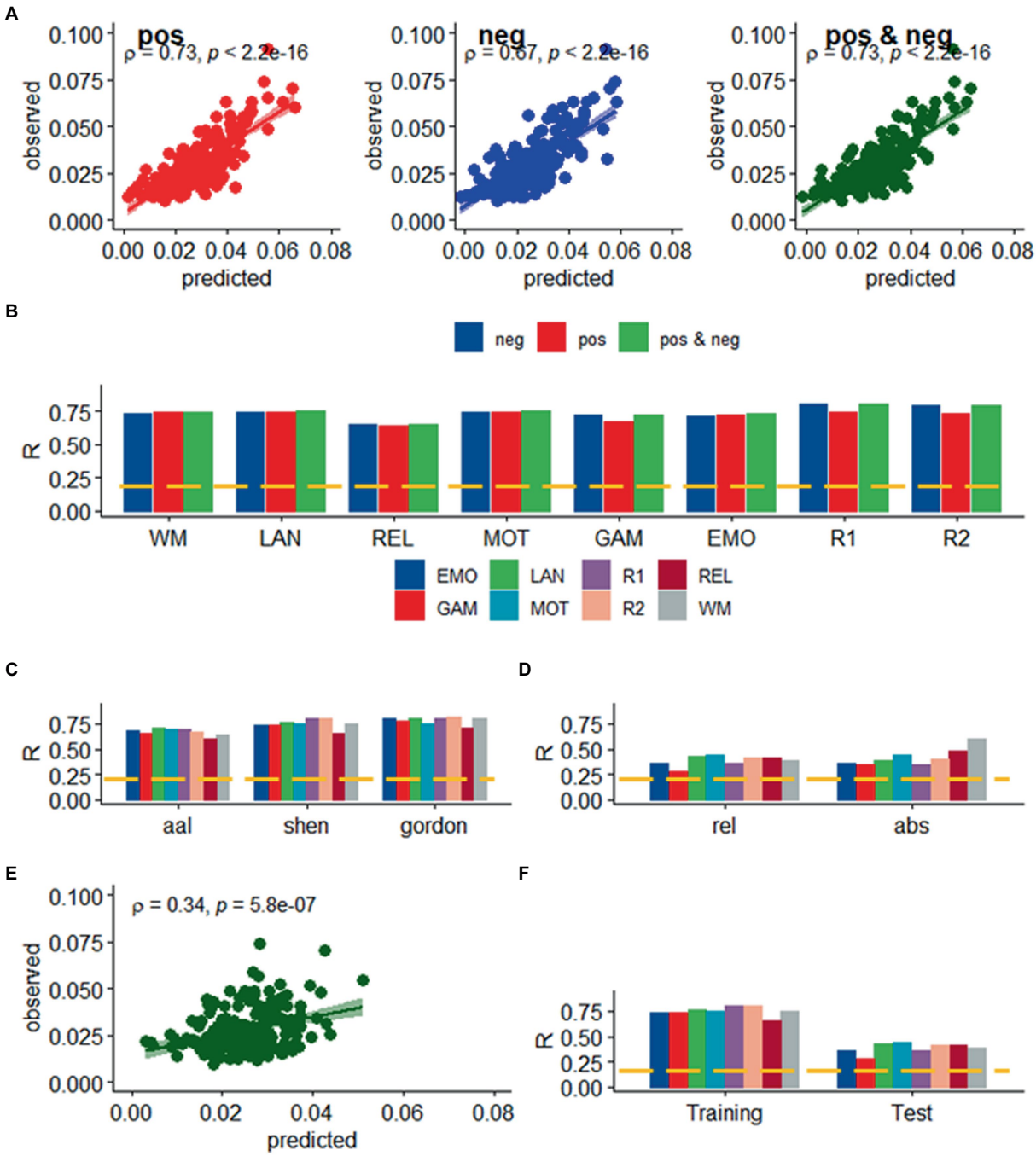

FIGURE 3
Prediction of relative head motion. **(A)** Observed relative head motion during fMRI sessions was predicted from positive and negative network strengths in "left out" individuals of the Training sample (n =207), using leave-one-out cross-validation. **(B)** Correlation factor (R) between observed and predicted relative motion excursions (Δd), as a function of fMRI session and model. Prediction accuracy (R) across brain parcellations in the training sample **(C)** and for absolute and relative motion (Δd; **D**) in the test sample. **(E)** Functional connectivity predicted relative head motion in an independent set of individuals ("Test sample"; n =207) using optimal models and features derived from the Training sample for the bilinear model for WM. **(F)** Prediction accuracy for relative motion in test and training samples. ---p <0.05, Bonferroni corrected for 16 comparisons. Shen parcellation atlas. EMO, emotion; LAN, language; REL, relational; GAM, gambling; MOT, motor; and WM, working memory; R1, rest1; and R2, rest2. Sample size, 414 healthy young adults. Censoring threshold 0.5mm.

one of the fMRI sessions resulted in a subsample of 200 individuals with "low motion" ($\Delta d < 0.08$ mm). The low-motion subsample was split into 2 groups of 100 individuals for CPM training and testing purposes.

Compared to datasets with moderate motion, datasets with ICA-based denoising (i.e., "noise suppression") demonstrated slightly attenuated head motion prediction, independently for d and Δd ($p < 0.05$, ANOVA; Figures 4A,B) and those with low motion did not

predict d or Δd in the Test sample (Figure 4C), consistent with the removal of signals correlated with rigid body motion.

We also confirmed the significance of the findings, against the null hypothesis that functional connectivity would not predict head motion, using a permutation test in which head motion (d or Δd) did not correspond to functional connectivity datasets across individuals. Under the null hypothesis, prediction accuracy had a bell-shaped distribution of $\sigma = 0.09$ (Figure 4D).

Scrubbing (censoring) is also a popular approach to control for head motion artifacts in functional connectivity (Power et al., 2012, 2014, 2015). Both for d and Δd, prediction accuracy did not differ when computed from datasets with different censoring threshold ($FD_i < 0.2$ mm, Figure 5 vs. $FD_i < 0.5$ mm, Figures 2F, 3F; $p > 0.15$, ANOVA).

Within- and between-network predictions

Next, we assessed prediction accuracy for specific network connections by restricting the features to either within-network or between-network edges. We used the 14 resting-state networks in the Gordon400 parcellation and R1 datasets with extremely low motion [$d = 0.04(0.02)$ mm; $\Delta d = 0.010(0.004)$ mm]. d- and Δd-prediction accuracies were statistically significant across within- or between-network edges and were higher for Training than Test samples ($p < 2.2e\text{-}16$; Figure 6). In the Test sample, prediction accuracy varied significantly across networks when using within-network edges (>54%; Figure 6) but less so when using between-network edges (<27%). In the Test sample, within-network prediction accuracy was significant only for the visual and ventral attention networks, subcortical regions, and the cerebellum but was significant for most between-network edges, independently for d and Δd ($p < 0.05$, corrected). Similar results emerged from task-fMRI datasets (not shown).

Predictions from simulations

To rule out potential neuronal contributions to motion prediction we assessed head motion prediction accuracy in simulated datasets in which the time-varying signals reflected only the real translations and rotations of GSP datasets, but not BOLD signal changes. Compared to the significant and reproducible d- and Δd-predictions obtained with the real GPS data, prediction accuracy in simulated data was very weak for Δd and did not reach significance for d, both for GSP1 and GSP2 (Figure 7).

Common motion-sensitive network

Hypothesizing that a unique subset of positive and negative network edges can be used to predict head motion for any of the fMRI sessions and using the moderate motion subsamples we identified edges that overlapped 25% or more across fMRI sessions, independently for positive and negative networks. Using Shen atlas partitions, the overlapping networks that predicted d had 100 positive edges and 52 negative edges, which predominantly emanated from bilateral hubs in the cerebellum Crus II (Figure 8A; Table 2) as well as medial DMN (anterior cingulum, superior medial frontal, and inferior temporal cortices) and salience network (SN; insula) regions, and the calcarine cortex (Figure 8A; Table 2). Positive edges predominantly reflected connections to

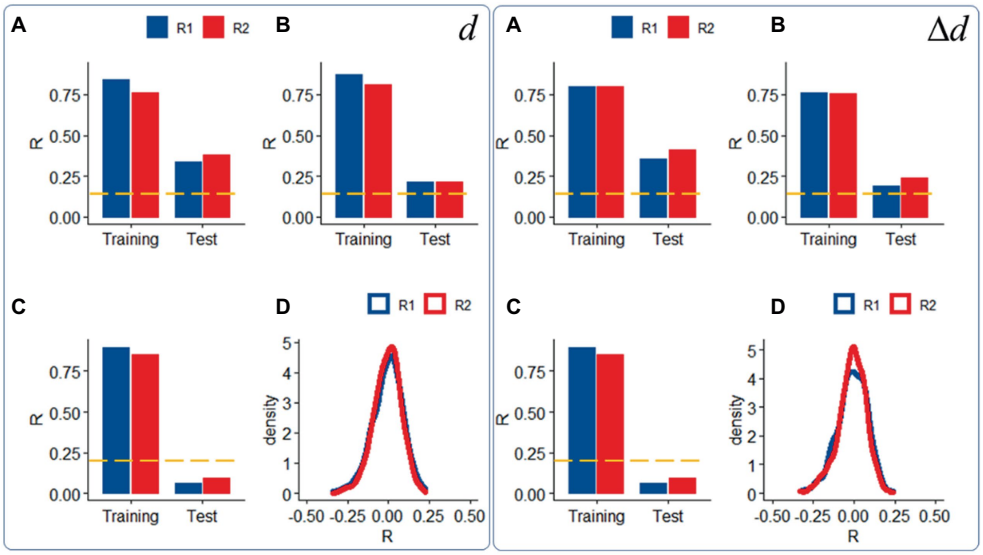

FIGURE 4
Sensitivity to motion signals: Predictability of relative (right panel) and absolute (left panel) head motion from functional connectivity datasets (R1: rest1; R2: rest2) in the Training (n =207) and Test (n =207) samples with "moderate motion" (Δd <0.04mm), without **(A)** and with **(B)** ICA-denoising (i.e., "noise suppression"), and in a "low motion" subsample of 200 (Training: 100; Test=100) individuals (Δd <0.02mm); **(C)** Density plots showing distributions of prediction accuracy obtained from 1,000 random permutations of d or Δd across individuals in the moderate motion sample for each fMRI session **(D)**. ---p <0.05, Bonferroni corrected for 2 comparisons. Shen parcellation atlas. Bilinear model. Censoring threshold 0.5mm.

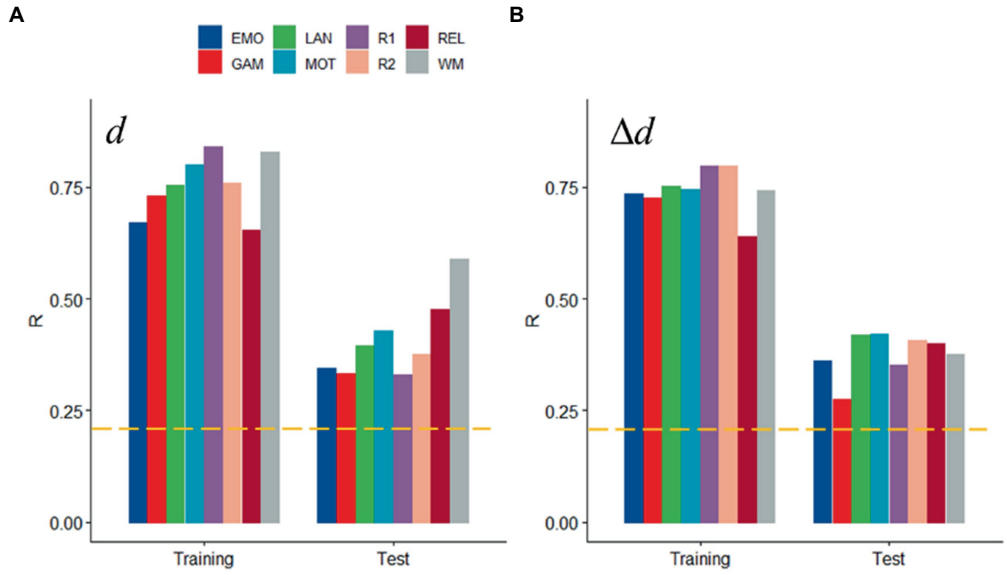

FIGURE 5
Sensitivity to head motion with censoring threshold 0.2mm: Absolute (*d*; **A**) and relative (Δ*d*; **B**) motion prediction accuracies from functional connectivity datasets. Training (*n* =207) and Test (*n* =207) samples. ---*p* <0.05, Bonferroni corrected for 16 comparisons. Shen parcellation atlas. Bilinear model.

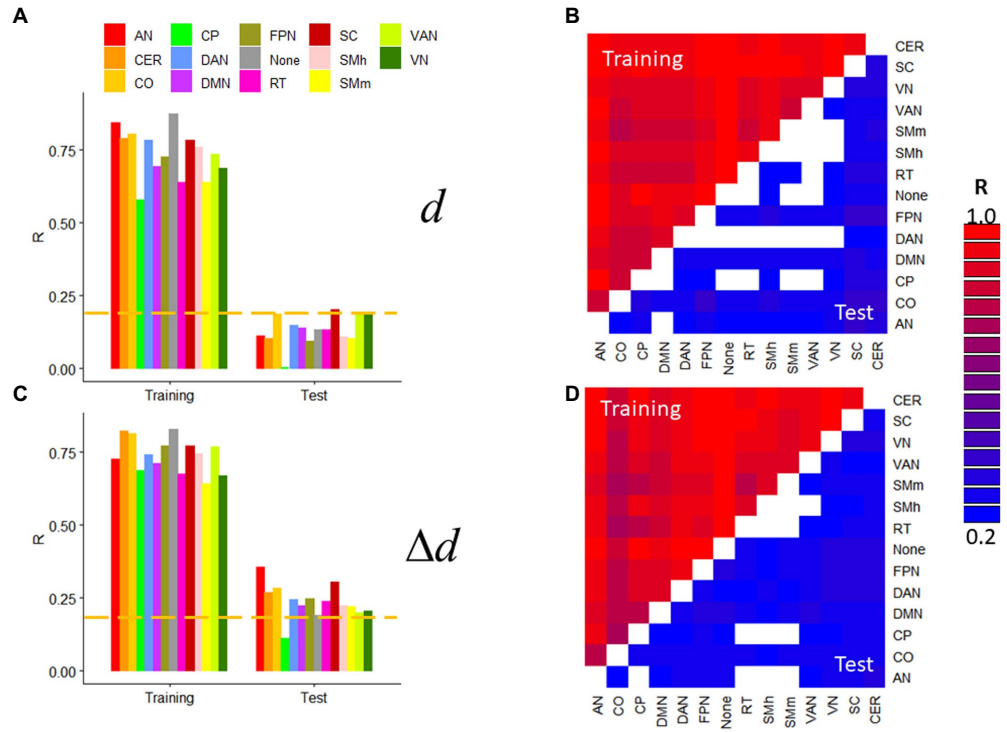

FIGURE 6
Within- and between-network predictions. Absolute (*d*; **A,B**) and relative (Δ*d*; **C,D**) motion prediction accuracies that emerged from within-network **(A,C)** and between-network (**B,D**; the threshold R>0.23 corresponds to *p* <0.05, Bonferroni corrected for 91 comparisons) edges of the functional connectivity matrix from R1. Training (*n* =207) and Test (*n* =207) samples. ---*p* <0.05, Bonferroni corrected for 14 comparisons. Gordon400 parcellation atlas. AN, auditory; CO, cingulum-operculum; CP, cingulum-parietal; DAN, dorsal-attention; DMN, default-mode; FPN, frontoparietal; RT, retrosplenial-temporal; SMh, sensorimotor-hand; SMm, sensorimotor-mouth; VAN, ventral attention; and VN, visual networks; CER, cerebellum; and SC, subcortical regions.

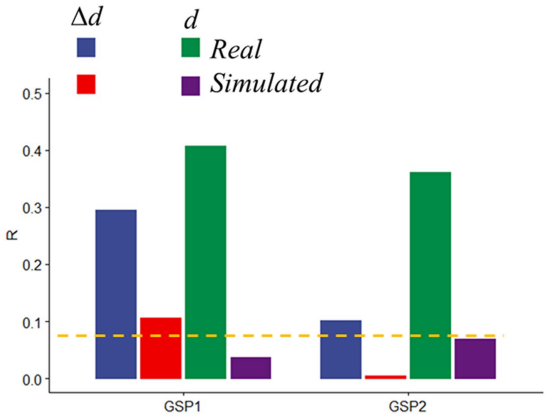

FIGURE 7
Prediction accuracy in real and simulated data. Absolute (*d*) and relative (Δ*d*) motion prediction accuracies from real and simulated functional connectivity datasets from the Brain Genomics Superstruct Project (GSP1, as the training sample, and GSP2, as the test sample; *n* =711, each). Brain parcellation: Shen; Model: bilinear. ---*p* <0.05, Bonferroni corrected.

contralateral regions (left–right cerebellum, left–right prefrontal cortex, PFC) and negative edges reflected ipsilateral and contralateral anterior-to-posterior connections (cerebellar-PFC). The overlapping networks that predicted Δ*d* were more restricted than those that predicted *d*, and had 14 positive and 44 negative edges that predominantly emanated from lateral (inferior and middle temporal gyri) and medial (superior medial frontal gyrus and precuneus) DMN, and FPN (left temporal pole) networks (Figure 8B; Table 3).

Next, we tested the prediction power of these overlapping features in the Training and Test subsamples. Specifically, we computed network strength from positive and negative edges of the overlapping networks, which we refer to as '*motion-sensitive networks*' and found that these features predicted head motion in all fMRI sessions with similar accuracy in the Training and Test subsamples, both for *d* and Δ*d* (Figure 8C, left and middle panels).

Further support for the involvement of these motion-sensitive networks in head motion prediction emerged from an independent validation study in 1,422 healthy young adults who underwent resting-state fMRI with standard spatiotemporal resolution (3 mm-isotropic; 3 s TR) under the GSP study (Holmes et al., 2015). Specifically, we found that motion-sensitive network strengths, computed using the positive and negative edges defined in the HCP absolute motion-sensitive network and the corresponding parameters of the bilinear model (Figure 8A), predicted *d* (0.13 mm ± 0.08 mm; mean ± sd) in two age- and gender-matched samples of 711 individuals: GSP1 (21.5 ± 2.9 years; 394 females) and GSP2 (21.5 ± 2.9 years; 406 females), with similar accuracy to that in the HCP subsamples (R ~ 0.3; Figure 8C). However, the predictability of Δ*d* (0.04 mm ± 0.02 mm/TR; mean ± sd) in the GSP datasets, based on the Δ*d*-motion-sensitive network and the parameters of the bilinear model (Figure 8B), was not consistent across GSP1 and GSP2 (Figure 8C). In simulated data, the parameters of the bilinear model and positive and negative edges of the *d*- and Δ*d*-motion-sensitive networks (Figures 7B, 8A) predicted Δ*d* in GSP1 and *d* in GSP2, with significantly lower accuracy than in real data (Figure 8C).

Discussion

Here we identify two motion-sensitive networks that predicted individual differences in head motion across six different task-fMRI and two rest-fMRI sessions. Reproducible predictions emerged from a Training sample of 207 individuals, using internal validation, and from an independent sample of 207 novel individuals, using twofold cross-validation. Head motion prediction was robust to changes in motion metric (*d* or Δ*d*), task-rest condition, brain parcellation, and model, demonstrating that results were stable and reproducible. We further validated our head motion prediction model in two independent datasets of 711 individuals, but similar validations failed in simulated datasets without neurobiological contributions. The predictability of head motion despite the relatively small frame-to-frame translations in this work (Δ*d* ~ 0.04 mm), compared to the stringent 0.2 mm micro motion threshold (Van Dijk et al., 2012), suggests that even extremely low amounts of head motion can influence functional connectivity.

The predictability of *d* is both surprising and interesting because "absolute motion" is a summary measure of slow motion rather than one of velocity. Here we show for the first time that the cerebellum (Crus II) reliably contributed to the prediction of *d*, whereas lateral DMN components (temporal cortex) contributed to the prediction of Δ*d*. The specificity of the cerebellum to *d*-prediction accuracy suggests that Crus II is particularly sensitive to slow head motion. The specificity of the lateral temporal DMN areas to Δ*d*-prediction accuracy suggests that this DMN subsystem is particularly sensitive to rapid head motion. However, the highly reproducible predictions of motion from within- and between-network edges (Figure 6) is consistent with the notion that all the networks are associated with head movement (Satterthwaite et al., 2013a), and not only the Crus II and temporal DMN regions.

A frequent approach to control for motion in functional connectivity studies is to exclude data with large Δ*d* (Power et al., 2012; Satterthwaite et al., 2012; Van Dijk et al., 2012) while little attention is given to *d*. However, our data shows that excluding data based on Δ*d* may not be sufficient to warrant the absence of motion effects on functional connectivity. Indeed, we show that motion prediction was higher for *d* than Δ*d*. Furthermore, functional connectivity data predicted both *d* and Δ*d* despite the use of current methods to attenuate the influence of head motion on fMRI. Prior studies showed that scrubbing with FD > 0.2 mm attenuated negative (but not positive) correlations between head motion (i.e., the average residual FD) and fMRI signals suggesting that negative relationships are likely to originate from motion artifacts (Yan et al., 2013). However, prediction accuracy from datasets with low motion (Δ*d* ~ 0.04 mm) did not differ when computed from positive or negative edges or when using stringent (FD > 0.2 mm) or lenient (FD > 0.5 mm) scrubbing thresholds.

Task-based fMRI studies, which frequently restrict head movement to minimize task-correlated motion artifacts, have demonstrated that older adults and patient populations move more during scanning than healthy controls (Seto et al., 2001; Yuan et al., 2009; Haller et al., 2014). Moreover, some have suggested that in-scanner head motion could be heritable (Engelhardt et al., 2017). Head motion is particularly problematic for resting state fMRI studies in pediatric populations, where an inverse relationship exists between head motion and age (Frew et al., 2022). Note that children have

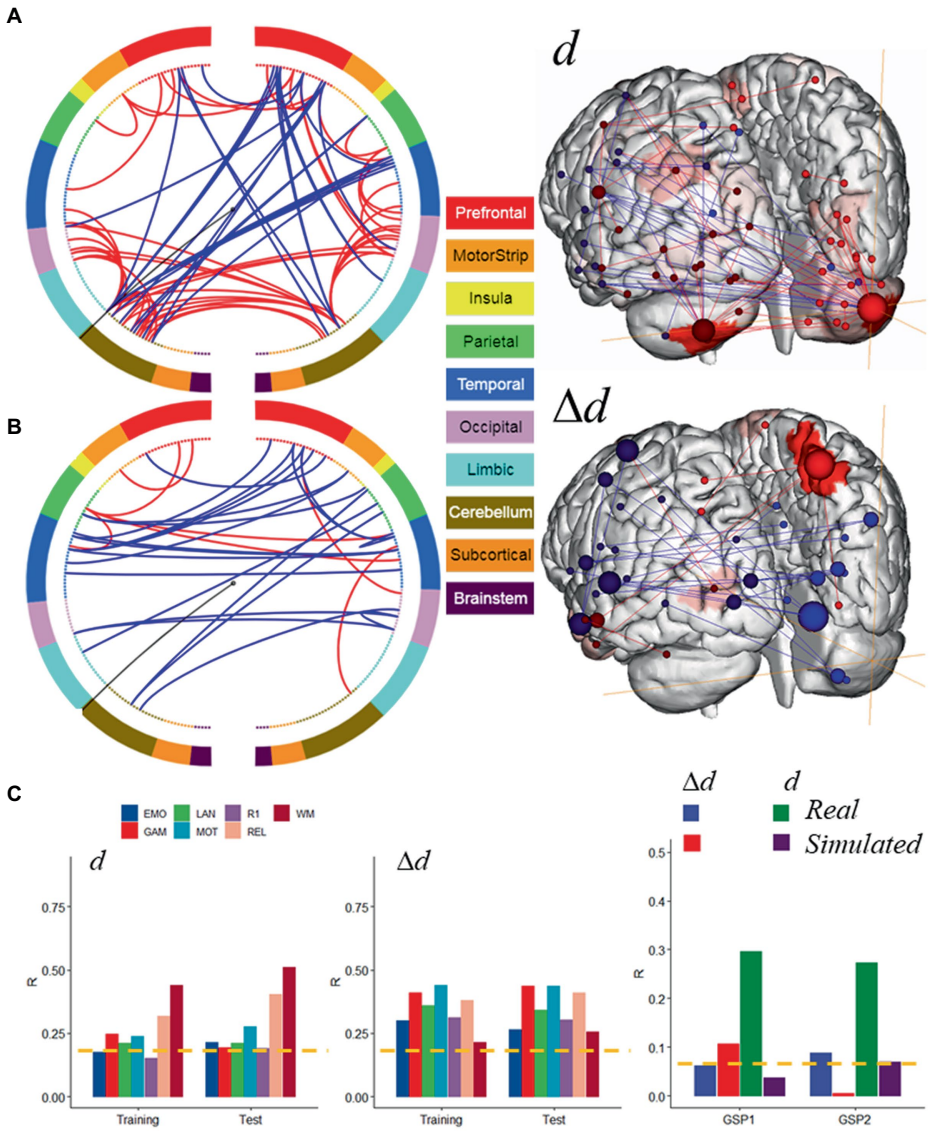

FIGURE 8
Motion-sensitive networks. Motion-network reflecting the 50% overlap of positive (—) or negative (—) networks that predicted absolute **(A)** and relative **(B)** head motion across 8 fMRI sessions and Training and Test subsamples, each of 207 individuals with moderate motion, and a glass brain plot where each node is represented as a sphere of size proportional to the number of edges of the node (right). The BioImage Suite Web (https://bioimagesuiteweb.github.io) was used to create these figures. **(C)** The motion-networks predicted absolute and relative head motion for both HCP samples and for real sessions from the Brain Genomics Superstruct Project (GSP1 and GSP2; n =711, each). Brain parcellation: Shen; Model: bilinear. ---p <0.05, Bonferroni corrected. Bilinear model parameters: a =0.016; b =0.005; c =−0.010.

greater difficulty in staying still during scanning than adults, due in part to the incomplete maturation of prefrontal cortical regions necessary for self-regulation, and also their propensity to boredom and anxiety (Morel et al., 2019). However, anxiety concerns are also relevant to adults, many of whom report some level of anxiety when undergoing MRI scans (Dziuda et al., 2019).

Pathological conditions or demographic parameters such as age can influence in-scanner head motion (Saccà et al., 2021). Thus, our findings on young healthy subjects could differ from those in older or pathological populations. Future studies are needed to investigate the extent to which this could be disentangled into contributions from the different components of the displacement (i.e., translational, rotational) and the effect of respiratory artifacts (Fair et al., 2020). It is challenging to explore all possible alterations in image preprocessing choices that might potentially interact with head motion. The use of different MRI acquisition protocols and preprocessing pipelines could reduce the reproducibility across HCP and GSP datasets. Nevertheless, the use of a different image acquisition protocol and preprocessing pipeline in the GSP and HCP datasets, allowed us to generalize our findings on motion prediction to different image acquisition protocols and preprocessing pipelines.

Since deleterious effects of head motion on fMRI data are well-documented (Power et al., 2012; Satterthwaite et al., 2012; Van Dijk et al., 2012) and considering that true brain-behavior associations have small effects (Marek et al., 2022) the predictions of head motion in this work likely reflect correlations of time-varying artifacts among

TABLE 2 Degree and coordinates of the 9 major hubs of the absolute 'motion-sensitive network' in the stereotactic space of the Montreal Neurological Institute (MNI).

Node	Region	BA/nucleus	Degree	MNI coord [mm]			Region
				x	*y*	*z*	
100	Cerebellum	Crus II	20	32	−78	−40	CB
242	Cerebellum	Crus II	15	−30	−80	−40	CB
155	Insula	47	9	−33	22	6	SN
215	Calcarine	17	5	−6	−81	12	VN
185	Inferior Temporal	21	5	−38	3	−38	DMN
148	Sup medial frontal	8	5	−11	34	51	DMN
140	Ant Cingulum	32	4	−6	48	12	DMN
141	Sup medial frontal	10	4	−12	65	4	DMN

CB, cerebellum. Networks: SN, salience; DMN, default-mode; VN, visual. Node numbers correspond to the Shen atlas.

TABLE 3 Degree and coordinates of the five major hubs of the relative "motion-sensitive network" in the stereotactic space of the Montreal Neurological Institute (MNI).

Node	Region	BA/nucleus	Degree	MNI coord [mm]			Region
				x	*y*	*z*	
57	Inferior temporal	21	4	47	4	−40	DMN
44	Precuneus	7	4	8	−57	62	DMN
191	Middle temporal	22	3	−59	−30	4	DMN
187	Temporal pole	21	3	−50	11	−31	FPN
148	Sup medial frontal	8	3	−11	34	51	DMN

Networks: DAN, dorsal attention; DMN, default-mode; VN, visual; FPN, frontoparietal. Node numbers correspond to the Shen atlas.

brain regions that are highly sensitive to motion. However, the poor prediction accuracy obtained with simulated fMRI data reflecting rigid-body motion contrasts with the successful validation of the prediction model in real data (Figure 8C), does not allow us to rule out the potential contributions of neurobiological origins in the prediction of *d*.

Together, our findings show that functional connectivity is a reproducible predictor of head motion and identify cerebellar and DMN subsystems that are highly sensitive to absolute and relative micromotion.

Data availability statement

The datasets presented in this study can be found in online repositories. The names of the repository/repositories and accession number(s) can be found at: Brain Genomics Superstruct Project (GSP) https://www.neuroinfo.org/gsp and Human Connectome Project (HCP) http://www.humanconnectome.org/.

Ethics statement

The studies involving human participants were reviewed and approved by IRB at Washington University and Partners Health Care Institutional Review Board and the Harvard University Committee. The patients/participants provided their written informed consent to participate in this study.

Author contributions

DT and NV: study conception and design, interpretation of results, and draft manuscript preparation. DT: data analyses. All authors contributed to the article and approved the submitted version.

Funding

This work was accomplished with support from the National Institutes of Alcohol Abuse and Alcoholism (ZIAAA000550).

Conflict of interest

The authors declare that the research was conducted in the absence of any commercial or financial relationships that could be construed as a potential conflict of interest.

Publisher's note

References

Andrews-Hanna, J., Snyder, A., Vincent, J., Lustig, C., Head, D., Raichle, M., et al. (2007). Disruption of large-scale brain systems in advanced aging. *Neuron* 56, 924–935. doi: 10.1016/j.neuron.2007.10.038

Barch, D., Burgess, G., Harms, M., Petersen, S., Schlaggar, B., Corbetta, M., et al. (2013). Function in the human connectome: task-fMRI and individual differences in behavior. *Neuroimage* 80, 169–189. doi: 10.1016/j.neuroimage.2013.05.033

Behzadi, Y., Restom, K., Liau, J., and Liu, T. (2007). A component based noise correction method (CompCor) for BOLD and perfusion based fMRI. *Neuroimage* 37, 90–101. doi: 10.1016/j.neuroimage.2007.04.042

Betzel, R., Cutts, S., Greenwell, S., Faskowitz, J., and Sporns, O. (2022). Individualized event structure drives individual differences in whole-brain functional connectivity. *Neuroimage* 252:118993. doi: 10.1016/j.neuroimage.2022.118993

Binder, J., Gross, W., Allendorfer, J., Bonilha, L., Chapin, J., Edwards, J., et al. (2011). Mapping anterior temporal lobe language areas with fMRI: a multicenter normative study. *Neuroimage* 54, 1465–1475. doi: 10.1016/j.neuroimage.2010.09.048

Birn, R., Diamond, J., Smith, M., and Bandettini, P. (2006). Separating respiratory-variation-related fluctuations from neuronal-activity-related fluctuations in fMRI. *Neuroimage* 31, 1536–1548. doi: 10.1016/j.neuroimage.2006.02.048

Buckner, R., Krienen, F., Castellanos, A., Diaz, J., and Yeo, B. (2011). The organization of the human cerebellum estimated by intrinsic functional connectivity. *J. Neurophysiol.* 106, 2322–2345. doi: 10.1152/jn.00339.2011

Buckner, R., Krienen, F., and Yeo, B. (2013). Opportunities and limitations of intrinsic functional connectivity MRI. *Nat. Neurosci.* 16, 832–837. doi: 10.1038/nn.3423

Catana, C., Benner, T., Van Der Kouwe, A., Byars, L., Hamm, M., Chonde, D., et al. (2011). MRI-assisted PET motion correction for neurologic studies in an integrated MR-PET scanner. *J. Nucl. Med.* 52, 154–161. doi: 10.2967/jnumed.110.079343

Cooper, J., Neumann, P., and Mccandless, B. (1992). Effect of patient motion on tomographic myocardial perfusion imaging. *J. Nucl. Med.* 33, 1566–1571.

Damoiseaux, J., Beckmann, C., Arigita, E., Barkhof, F., Scheltens, P., Stam, C., et al. (2008). Reduced resting-state brain activity in the "default network" in normal aging. *Cereb. Cortex* 18, 1856–1864. doi: 10.1093/cercor/bhm207

Delgado, M., Nystrom, L., Fissell, C., Noll, D., and Fiez, J. (2000). Tracking the hemodynamic responses to reward and punishment in the striatum. *J. Neurophysiol.* 84, 3072–3077. doi: 10.1152/jn.2000.84.6.3072

Dosenbach, N., Nardos, B., Cohen, A., Fair, D., Power, J., Church, J., et al. (2010). Prediction of individual brain maturity using fMRI. *Science* 329, 1358–1361. doi: 10.1126/science.1194144

Dziuda, Ł., Zieliński, P., Baran, P., Krej, M., and Kopka, L. (2019). A study of the relationship between the level of anxiety declared by MRI patients in the STAI questionnaire and their respiratory rate acquired by a fibre-optic sensor system. *Sci. Rep.* 9:4341. doi: 10.1038/s41598-019-40737-w

Engelhardt, L., Roe, M., Juranek, J., Demaster, D., Harden, K., Tucker-Drob, E., et al. (2017). Children's head motion during fMRI tasks is heritable and stable over time. *Dev. Cogn. Neurosci.* 25, 58–68. doi: 10.1016/j.dcn.2017.01.011

Fair, D., Cohen, A., Dosenbach, N., Church, J., Miezin, F., Barch, D., et al. (2008). The maturing architecture of the brain's default network. *Proc. Natl. Acad. Sci. U. S. A.* 105, 4028–4032. doi: 10.1073/pnas.0800376105

Fair, D., Dosenbach, N., Church, J., Cohen, A., Brahmbhatt, S., Miezin, F., et al. (2007). Development of distinct control networks through segregation and integration. *Proc. Natl. Acad. Sci. U. S. A.* 104, 13507–13512. doi: 10.1073/pnas.0705843104

Fair, D., Miranda-Dominguez, O., Snyder, A., Perrone, A., Earl, E., Van, A., et al. (2020). Correction of respiratory artifacts in MRI head motion estimates. *Neuroimage* 208:116400. doi: 10.1016/j.neuroimage.2019.116400

Fassbender, C., Mukherjee, P., and Schweitzer, J. (2017). Reprint of: minimizing noise in pediatric task-based functional MRI; adolescents with developmental disabilities and typical development. *Neuroimage* 154, 230–239. doi: 10.1016/j.neuroimage.2017.05.007

Finn, E., Shen, X., Scheinost, D., Rosenberg, M., Huang, J., Chun, M., et al. (2015). Functional connectome fingerprinting: identifying individuals using patterns of brain connectivity. *Nat. Neurosci.* 18, 1664–1671. doi: 10.1038/nn.4135

Fischl, B., Salat, D., Busa, E., Albert, M., Dieterich, M., Haselgrove, C., et al. (2002). Whole brain segmentation: automated labeling of neuroanatomical structures in the human brain. *Neuron* 33, 341–355. doi: 10.1016/S0896-6273(02)00569-X

Frew, S., Samara, A., Shearer, H., Eilbott, J., and Vanderwal, T. (2022). Getting the nod: pediatric head motion in a transdiagnostic sample during movie- and resting-state fMRI. *PLoS One* 17:e0265112. doi: 10.1371/journal.pone.0265112

Friston, K., Williams, S., Howard, R., Frackowiak, R., and Turner, R. (1996). Movement-related effects in fMRI time-series. *Magn. Reson. Med.* 35, 346–355. doi: 10.1002/mrm.1910350312

Glasser, M., Sotiropoulos, S., Wilson, J., Coalson, T., Fischl, B., Andersson, J., et al. (2013). The minimal preprocessing pipelines for the human connectome project. *Neuroimage* 80, 105–124. doi: 10.1016/j.neuroimage.2013.04.127

Gordon, E., Laumann, T., Adeyemo, B., Huckins, J., Kelley, W., and Petersen, S. (2016). Generation and evaluation of a cortical area Parcellation from resting-state correlations. *Cereb. Cortex* 26, 288–303. doi: 10.1093/cercor/bhu239

Greicius, M. (2008). Resting-state functional connectivity in neuropsychiatric disorders. *Curr. Opin. Neurol.* 21, 424–430. doi: 10.1097/WCO.0b013e328306f2c5

Haller, S., Monsch, A., Richiardi, J., Barkhof, F., Kressig, R., and Radue, E. (2014). Head motion parameters in fMRI differ between patients with mild cognitive impairment and Alzheimer disease versus elderly control subjects. *Brain Topogr.* 27, 801–807. doi: 10.1007/s10548-014-0358-6

Hariri, A., Tessitore, A., Mattay, V., Fera, F., and Weinberger, D. (2002). The amygdala response to emotional stimuli: a comparison of faces and scenes. *Neuroimage* 17, 317–323. doi: 10.1006/nimg.2002.1179

Holmes, A., Hollinshead, M., Okeefe, T., Petrov, V., Fariello, G., Wald, L., et al. (2015). Brain genomics Superstruct project initial data release with structural, functional, and behavioral measures. *Sci Data* 2:150031. doi: 10.1038/sdata.2015.31

Hong, S., Vos De Wael, R., Rai, B., Lariviere, S., Paquola, C., Valk, S., et al. (2019). Atypical functional connectome hierarchy in autism. *Nat. Commun.* 10:1022. doi: 10.1038/s41467-019-08944-1

Jenkinson, M., Bannister, P., Brady, M., and Smith, S. (2002). Improved optimization for the robust and accurate linear registration and motion correction of brain images. *Neuroimage* 17, 825–841. doi: 10.1006/nimg.2002.1132

Maknojia, S., Churchill, N., Schweizer, T., and Graham, S. (2019). Resting state fMRI: going through the motions. *Front. Neurosci.* 13:825. doi: 10.3389/fnins.2019.00825

Marek, S., Tervo-Clemmens, B., Calabro, F., Montez, D., Kay, B., Hatoum, A., et al. (2022). Reproducible brain-wide association studies require thousands of individuals. *Nature* 603, 654–660. doi: 10.1038/s41586-022-04492-9

Morel, B., Andersson, F., Samalbide, M., Binninger, G., Carpentier, E., Sirinelli, D., et al. (2019). Impact on child and parent anxiety level of a teddy bear-scale mock magnetic resonance scanner. *Pediatr. Radiol.* 50:116–120. doi: 10.1007/s00247-00019-04514-00241

Mugler, J. R., Bao, S., Mulkern, R., Guttmann, C., Robertson, R., Jolesz, F., et al. (2000). Optimized single-slab three-dimensional spin-echo MR imaging of the brain. *Radiology* 216, 891–899. doi: 10.1148/radiology.216.3.r00au46891

Mugler, J. R., and Brookeman, J. (1990). Three-dimensional magnetization-prepared rapid gradient-echo imaging (3D MP RAGE). *Magn. Reson. Med.* 15, 152–157. doi: 10.1002/mrm.1910150117

Nehmeh, S., and Erdi, Y. (2008). Respiratory motion in positron emission tomography/computed tomography: a review. *Semin. Nucl. Med.* 38, 167–176. doi: 10.1053/j.semnuclmed.2008.01.002

Noble, S., and Scheinost, D. (2020). The constrained network-based statistic: a new level of inference for neuroimaging. *Med Image Comput Comput Assist Interven* 12267, 458–468. doi: 10.1007/978-3-030-59728-3_45

Poldrack, R., Paré-Blagoev, E., and Grant, P. (2002). Pediatric functional magnetic resonance imaging: progress and challenges. *Top. Magn. Reson. Imaging* 13, 61–70. doi: 10.1097/00002142-200202000-00005

Power, J., Barnes, K., Snyder, A., Schlaggar, B., and Petersen, S. (2012). Spurious but systematic correlations in functional connectivity MRI networks arise from subject motion. *Neuroimage* 59, 2142–2154. doi: 10.1016/j.neuroimage.2011.10.018

Power, J., Mitra, A., Laumann, T., Snyder, A., Schlaggar, B., and Petersen, S. (2014). Methods to detect, characterize, and remove motion artifact in resting state fMRI. *Neuroimage* 84, 320–341. doi: 10.1016/j.neuroimage.2013.08.048

Power, J., Schlaggar, B., and Petersen, S. (2015). Recent progress and outstanding issues in motion correction in resting state fMRI. *Neuroimage* 105, 536–551. doi: 10.1016/j.neuroimage.2014.10.044

Pruim, R., Mennes, M., Van Rooij, D., Llera, A., Buitelaar, J., and Beckmann, C. (2015). ICA-AROMA: a robust ICA-based strategy for removing motion artifacts from fMRI data. *Neuroimage* 112, 267–277. doi: 10.1016/j.neuroimage.2015.02.064

Pujol, J., Macià, D., Blanco-Hinojo, L., Martínez-Vilavella, G., Sunyer, J., De La Torre, R., et al. (2014). Does motion-related brain functional connectivity reflect both artifacts and genuine neural activity? *Neuroimage* 101, 87–95. doi: 10.1016/j.neuroimage.2014.06.065

Rohde, G., Barnett, A., Basser, P., Marenco, S., and Pierpaoli, C. (2004). Comprehensive approach for correction of motion and distortion in diffusion-weighted MRI. *Magn. Reson. Med.* 51, 103–114. doi: 10.1002/mrm.10677

Rosenberg, M., Finn, E., Scheinost, D., Papademetris, X., Shen, X., Constable, R., et al. (2016). A neuromarker of sustained attention from whole-brain functional connectivity. *Nat. Neurosci.* 19, 165–171. doi: 10.1038/nn.4179

Saccà, V., Sarica, A., Quattrone, A., Rocca, F., Quattrone, A., and Novellino, F. (2021). Aging effect on head motion: a machine learning study on resting state fMRI data. *J. Neurosci. Methods* 352:109084. doi: 10.1016/j.jneumeth.2021.109084

Salimi-Khorshidi, G., Douaud, G., Beckmann, C., Glasser, M., Griffanti, L., and Smith, S. (2014). Automatic denoising of functional MRI data: combining independent

component analysis and hierarchical fusion of classifiers. *Neuroimage* 90, 449–468. doi: 10.1016/j.neuroimage.2013.11.046

Satterthwaite, T., Elliott, M., Gerraty, R., Ruparel, K., Loughead, J., Calkins, M., et al. (2013a). An improved framework for confound regression and filtering for control of motion artifact in the preprocessing of resting-state functional connectivity data. *Neuroimage* 64, 240–256. doi: 10.1016/j.neuroimage.2012.08.052

Satterthwaite, T., Wolf, D., Loughead, J., Ruparel, K., Elliott, M., Hakonarson, H., et al. (2012). Impact of in-scanner head motion on multiple measures of functional connectivity: relevance for studies of neurodevelopment in youth. *Neuroimage* 60, 623–632. doi: 10.1016/j.neuroimage.2011.12.063

Satterthwaite, T., Wolf, D., Ruparel, K., Erus, G., Elliott, M., Eickhoff, S., et al. (2013b). Heterogeneous impact of motion on fundamental patterns of developmental changes in functional connectivity during youth. *Neuroimage* 83, 45–57. doi: 10.1016/j.neuroimage.2013.06.045

Seto, E., Sela, G., Mcilroy, W., Black, S., Staines, W., Bronskill, M., et al. (2001). Quantifying head motion associated with motor tasks used in fMRI. *Neuroimage* 14, 284–297. doi: 10.1006/nimg.2001.0829

Shapiro, S., and Wilk, M. (1965). An analysis of variance test for normality (complete samples). *Biometrika* 52, 591–611. doi: 10.1093/biomet/52.3-4.591

Shen, X., Finn, E., Scheinost, D., Rosenberg, M., Chun, M., Papademetris, X., et al. (2017). Using connectome-based predictive modeling to predict individual behavior from brain connectivity. *Nat. Protoc.* 12, 506–518. doi: 10.1038/nprot.2016.178

Shen, X., Tokoglu, F., Papademetris, X., and Constable, R. (2013). Groupwise whole-brain parcellation from resting-state fMRI data for network node identification. *Neuroimage* 82:415. doi: 10.1016/j.neuroimage.2013.05.081

Siegel, J., Mitra, A., Laumann, T., Seitzman, B., Raichle, M., Corbetta, M., et al. (2017). Data quality influences observed links between functional connectivity and behavior. *Cereb. Cortex* 27, 4492–4502. doi: 10.1093/cercor/bhw253

Smith, S., Beckmann, C., Andersson, J., Auerbach, E., Bijsterbosch, J., Douaud, G., et al. (2013). Resting-state fMRI in the human connectome project. *Neuroimage* 80, 144–168. doi: 10.1016/j.neuroimage.2013.05.039

Smith, S., Jenkinson, M., Woolrich, M., Beckmann, C., Behrens, T., Johansen-Berg, H., et al. (2004). Advances in functional and structural MR image analysis and implementation as FSL. *Neuroimage* 23, S208–S219. doi: 10.1016/j.neuroimage.2004.07.051

Smith, R., Keramatian, K., and Christoff, K. (2007). Localizing the rostrolateral prefrontal cortex at the individual level. *Neuroimage* 36, 1387–1396. doi: 10.1016/j.neuroimage.2007.04.032

Steiger, J. (1980). Tests for comparing elements of a correlation matrix. *Psychol. Bull.* 87, 245–251. doi: 10.1037/0033-2909.87.2.245

Tomasi, D., and Volkow, N. (2010). Functional connectivity density mapping. *Proc. Natl. Acad. Sci. U. S. A.* 107, 9885–9890. doi: 10.1073/pnas.1001414107

Tzourio-Mazoyer, N., Landeau, B., Papathanassiou, D., Crivello, F., Etard, O. N., Mazoyer, B., et al. (2002). Automated anatomical labeling of activations in SPM using a macroscopic anatomical parcellation of the MNI MRI single-subject brain. *Neuroimage* 15, 273–289. doi: 10.1006/nimg.2001.0978

Uğurbil, K., Xu, J., Auerbach, E., Moeller, S., Vu, A., Duarte-Carvajalino, J., et al. (2013). Pushing spatial and temporal resolution for functional and diffusion MRI in the human connectome project. *Neuroimage* 80, 80–104. doi: 10.1016/j.neuroimage.2013.05.012

Van Der Kouwe, A., Benner, T., Salat, D., and Fischl, B. (2008). Brain morphometry with multiecho MPRAGE. *Neuroimage* 40, 559–569. doi: 10.1016/j.neuroimage.2007.12.025

Van Dijk, K., Sabuncu, M., and Buckner, R. (2012). The influence of head motion on intrinsic functional connectivity MRI. *Neuroimage* 59, 431–438. doi: 10.1016/j.neuroimage.2011.07.044

Williams, E. (1959). The comparison of regression variables. *J. R. Stat. Soc. Ser. B* 21, 396–399. doi: 10.1111/j.2517-6161.1959.tb00346.x

Yan, C., Cheung, B., Kelly, C., Colcombe, S., Craddock, R., Di Martino, A., et al. (2013). A comprehensive assessment of regional variation in the impact of head micromovements on functional connectomics. *Neuroimage* 76, 183–201. doi: 10.1016/j.neuroimage.2013.03.004

Yeo, B., Krienen, F., Sepulcre, J., Sabuncu, M., Lashkari, D., Hollinshead, M., et al. (2011). The organization of the human cerebral cortex estimated by intrinsic functional connectivity. *J. Neurophysiol.* 106, 1126–1165. doi: 10.1152/jn.00338.2011

Yuan, W., Altaye, M., Ret, J., Schmithorst, V., Byars, A., Plante, E., et al. (2009). Quantification of head motion in children during various fMRI language tasks. *Hum. Brain Mapp.* 30, 1481–1489. doi: 10.1002/hbm.20616

Zeng, L., Wang, D., Fox, M., Sabuncu, M., Hu, D., Ge, M., et al. (2014). Neurobiological basis of head motion in brain imaging. *Proc. Natl. Acad. Sci. U. S. A.* 111, 6058–6062. doi: 10.1073/pnas.1317424111

frontiers | Frontiers in Neuroscience

TYPE Original Research
PUBLISHED 18 May 2023
DOI 10.3389/fnins.2023.1151525

OPEN ACCESS

EDITED BY
Dahua Yu,
Inner Mongolia University of Science and Technology, China

REVIEWED BY
Wen-Ju Pan,
Emory University, United States
Cornelius Faber,
University Hospital Münster, Germany

*CORRESPONDENCE
Jennifer Rodger
✉ jennifer.rodger@uwa.edu.au

RECEIVED 26 January 2023
ACCEPTED 27 April 2023
PUBLISHED 18 May 2023

CITATION
Dai T, Seewoo BJ, Hennessy LA, Bolland SJ, Rosenow T and Rodger J (2023) Identifying reproducible resting state networks and functional connectivity alterations following chronic restraint stress in anaesthetized rats. *Front. Neurosci.* 17:1151525. doi: 10.3389/fnins.2023.1151525

Identifying reproducible resting state networks and functional connectivity alterations following chronic restraint stress in anaesthetized rats

Twain Dai[1,2], Bhedita J. Seewoo[1,3], Lauren A. Hennessy[1,2], Samuel J. Bolland[1,2], Tim Rosenow[4] and Jennifer Rodger[1,2]*

[1]School of Biological Sciences, University of Western Australia, Perth, WA, Australia, [2]Perron Institute for Neurological and Translational Science, University of Western Australia, Perth, WA, Australia, [3]Minderoo Foundation, Perth, WA, Australia, [4]Centre for Microscopy, Characterisation and Analysis, Research Infrastructure Centres, University of Western Australia, Perth, WA, Australia

Background: Resting-state functional MRI (rs-fMRI) in rodent models have the potential to bridge invasive experiments and observational human studies, increasing our understanding of functional alterations in the brains of patients with depression. A major limitation in current rodent rs-fMRI studies is that there has been no consensus on healthy baseline resting-state networks (RSNs) that are reproducible in rodents. Therefore, the present study aimed to construct reproducible RSNs in a large dataset of healthy rats and then evaluate functional connectivity changes within and between these RSNs following a chronic restraint stress (CRS) model within the same animals.

Methods: A combined MRI dataset of 109 Sprague Dawley rats at baseline and after two weeks of CRS, collected during four separate experiments conducted by our lab in 2019 and 2020, was re-analysed. The mICA and gRAICAR toolbox were first applied to detect optimal and reproducible ICA components and then a hierarchical clustering algorithm (FSLNets) was applied to construct reproducible RSNs. Ridge-regularized partial correlation (FSLNets) was used to evaluate the changes in the direct connection between and within identified networks in the same animals following CRS.

Results: Four large-scale networks in anesthetised rats were identified: the DMN-like, spatial attention-limbic, corpus striatum, and autonomic network, which are homologous across species. CRS decreased the anticorrelation between DMN-like and autonomic network. CRS decreased the correlation between amygdala and a functional complex (nucleus accumbens and ventral pallidum) in the right hemisphere within the corpus striatum network. However, a high individual variability in the functional connectivity before and after CRS within RSNs was observed.

Conclusion: The functional connectivity changes detected in rodents following CRS differ from reported functional connectivity alterations in patients with depression. A simple interpretation of this difference is that the rodent response to CRS does not reflect the complexity of depression as it is experienced by humans. Nonetheless, the high inter-subject variability of functional connectivity within networks suggests that rats demonstrate different neural phenotypes, like humans. Therefore, future efforts in classifying neural phenotypes in rodents might improve the sensitivity and translational impact of models used to address aetiology and treatment of psychiatric conditions including depression.

KEYWORDS

functional connectivity, anxiety, magnetic resonance imaging, rat brain, animal model of depression

1. Introduction

Depression is a leading cause of global disability and a highly heterogenous disorder, characterized by affective and cognitive symptoms. Accumulating studies have suggested that these core symptoms of depression are associated with disrupted affective and cognitive brain networks, revealed by magnetic resonance imaging (MRI) and computational approaches that can map the brain connectome non-invasively (Fornito et al., 2015). Resting-state functional MRI (rs-fMRI) is a non-invasive and powerful MRI modality commonly applied to investigate resting-state functional organization in the brain at the macroscale level (Xu et al., 2022) through detecting the spontaneous fluctuations of the blood oxygen level dependent (BOLD) signal (Ogawa et al., 1990). The resting-state functional organization is generally referred to as resting-state network (RSN), such as the default mode network (DMN), central executive network (CEN), and salience network (Paulus and Stein, 2010; Williams, 2017). Several consistent functional connectivity changes within and between RSNs have been observed in rs-fMRI studies of depression in humans (Mulders et al., 2015). For instance, increased connectivity is presented within the anterior DMN, as well as between the anterior DMN and salience network. In contrast, decreased connectivity is shown between the posterior DMN and CEN.

RSNs are not unique to humans, some homologous RSNs have also been observed in healthy rodents using rs-fMRI (Xu et al., 2022; Grandjean et al., 2023). For example, the core brain structures of DMN in humans, such as the cingulate, retrosplenial, and prefrontal cortex, are identified to form DMN-like functional organization in rats and mice (Lu et al., 2012; Hsu et al., 2016; Mandino et al., 2022). Animal models have traditionally been a useful tool in the study of aetiology and treatment of depression due to the ethical and practical limitations associated with controlling the natural development of a disease and dissecting the neurobiological mechanism in humans (Herzog et al., 2018; Pais-Roldan et al., 2021). The relevance of animal depression models is often controversial because no single rat model can perfectly replicate all aspects of clinical features of depression, such as depressed mood and suicidal thoughts (Harro, 2019). However, a perfect rat model of depression that exhibits all the clinical features of depression-relevant behaviors is arguably unnecessary because even patients usually do not manifest every aspect of diagnostic criteria of depression (Krishnan and Nestler, 2008). Therefore, it would still be beneficial to investigate and compare the functional connectivity between and within RSNs in health and subsequent depression models within the same animals.

To date, limited rs-fMRI studies in animal models of depression have investigated functional alterations within and between RSNs in response to interventions that induce stress and anxiety (Henckens et al., 2015; Grandjean et al., 2016; Nephew et al., 2018; Seewoo et al., 2020; Hennessy et al., 2022). Majority of these rodent studies have applied chronic restraint stress (CRS), which is a popular, simple, and validated depression model. It has been shown to induce changes in behaviors, gene expression, and protein, which are similar to those in patients with depression (Becker et al., 2021). Each of these animal studies has identified different aspects of dysfunctional RSNs that are claimed to be comparable to humans with depression. However, there is no consistent findings within these rodent rs-fMRI studies. Several reasons may explain the discrepant results, including limited sample sizes, different methodologies applied to construct and analyse RSNs, and different protocols used to induce depression-like behaviors and neurological alterations.

A major limitation in current rodent rs-fMRI studies is that there has been no consensus on healthy baseline RSNs that are reproducible in rodents (Becerra et al., 2011) regardless growing efforts has been devoted to studying RSNs in healthy animals. Identifying reproducible RSNs at baseline or in healthy condition is crucial for investigating alterations of functional connectivity following interventions used to model depression in animals. To date, limited studies have attempted to construct reproducible RSNs in rodents and they also suffer from a major pitfall of limited sample sizes (Becerra et al., 2011). Moreover, no study has examined the effects of depression models on the alterations of functional connectivity following a construction of reproducible RSNs. Therefore, the present study first aims to construct reproducible RSNs in a large dataset of 109 healthy rats and then evaluate functional connectivity changes within and between these RSNs following a depression model in the same animals.

2. Materials and methods

2.1. Ethics statement

All experimental procedures adhered to the ethics guideline of the University of Western Australia Animal Ethics Committee (RA/3/100/1640) and the National Health and Medical Research Council's Australian code for the care and use of animals for scientific purposes. All investigators had obtained the Permission to Work with Animals and were trained by the UWA Program in Animal Welfare, Ethics, and Science.

2.2. Rodent MRI data

2.2.1. Animals

The MRI data analysed in the present study was a combined dataset of rodent cohorts from previous experiments conducted by our lab in 2019 and 2020. Briefly, 109 male Sprague—Dawley rats (aged 6–7 weeks and weighing 150–250 g on arrival; $N = 12$ from Seewoo et al. (2020), $N = 56$ from Hennessy et al. (2022) and $N = 41$ unpublished) were sourced from the Animal Resources Centre (Canning Vale, WA). All rats were housed in pairs under a standard 12-h light–dark cycle with *ad libitum* food and water, in a

temperature-controlled and spacious laboratory room located at UWA's Animal Care Unit, M block building (Nedlands, WA). All animals were habituated to the new environment for one week after their arrival and prior to experiments.

96 rats underwent CRS for 2.5 h per day for 13 consecutive days. These animals' MRI scans were conducted at baseline (one or two days before the first CRS procedure) and post-CRS (two or three days after the final CRS procedure). The remaining animals ($N = 13$), served as controls: they did not undergo CRS but received MRI imaging twice at the same interval applied to the intervention group.

2.2.2. Chronic restraint stress protocols

CRS was performed on a bench situated in one corner of the laboratory room, with rats placed in a transparent plastic tube facing the wall to mitigate visual distractions. Each session started between 12:30 and 13:00 pm, lasting for 2.5 h daily to reduce the influence of circadian rhythm. Restraint tubes with adjustable tail gates used to restrict the free movement of animals were adjusted to match their body mass and size throughout 13 days of CRS (Seewoo et al., 2020). During CRS sessions, rats in the control group stayed in their home cages. Following CRS, rats in the intervention group were returned to their home cages.

2.2.3. MRI anaesthetic protocol

Animals were transferred to the National Imaging Facility located in the Harry Perkins Institute of Medical Research (Nedlands, WA) for MRI scan on the assigned day. The rat was weighed and then pre-anaesthetised in an induction box with 4% isoflurane in medical air (2 L/min). Once fully anaesthetised, the animal was transferred to a heated imaging bed and anaesthesia was initially administered through a nose cone with 4% isoflurane in medical air (1 L/min). The animal's vital status was monitored using a PC-SAM Small Animal Monitor (SA Instruments Inc., 1,030 system). Once the respiratory rate dropped to 55–60 breaths/min, isoflurane concentration was adjusted to 2% in medical air (1 L/min). After the animal was stabilized on 2% isoflurane for at least 2 min, medetomidine was delivered subcutaneously, with an initial 0.05–0.1 mg/kg bolus injection and continuous 0.15 mg/kg/h infusion. Meanwhile, the isoflurane concentration was gradually reduced to 0.5–0.75% based on the animal's respiratory rate (Seewoo et al., 2020). The combined use of isoflurane and medetomidine can induce similar functional connectivity within RSNs, compared to animals in an awaken condition (Paasonen et al., 2018). Moreover, this anaesthetic protocol can maintain strong cortical–cortical and cortical–subcortical connectivity in animals (Grandjean et al., 2014; Bukhari et al., 2017). To evaluate the potential influence of time elapsed following the induction of medetomidine on RSNs, 14 imaging sessions were randomly selected, in which the time elapsed was plotted against network metrics (see methods 2.3.5). No correlation (data not shown; $r < 0.001$) was identified and the average time elapsed was 32 min ($SD = 4$). After the imaging session, animals were administered a 0.15 mg/kg injection of atipamezole to antagonize medetomidine. Periodical monitoring for adverse events after MRI scan was performed in the following 24 h.

2.2.4. MRI acquisition

Rats were scanned using a 9.4 T Bruker Biospec 94/30 pre-clinical MRI scanner (Bruker BioSpin GmbH, Germany) with a BGA-12SHP imaging gradient system, a 72 mm or 86 mm volume resonator transmit coil (depending on hardware availability), a rat brain surface quadrature receive coil, and Avance III console. ParaVision 6.0.1 software of the Bruker controlled scanning sequences and operation for structural MRI and rs-fMRI acquisition (Seewoo et al., 2018; Han et al., 2019). High-resolution T2-weighted anatomical images with 21 coronal slices were acquired using an accelerated multi-slice 2D rapid acquisition with relaxation enhancement (RARE) sequence. A single-shot gradient-echo echo planar imaging (EPI) sequence was applied to acquire resting-state functional images with 21 coronal slices. MRI scanning parameters were summarized in Table 1. Both raw images for each scan session were compiled in one Para Vision 6.0.1 package in the format of PvDatasets. A total of 218 MRI packages were acquired at two time points (baseline and post-CRS) and included in the following data processing and analysis workflow.

TABLE 1 MRI scanning protocols for structural MRI and rs-fMRI acquisition.

Parameters	Structural MRI (RARE)	rs-fMRI (EPI)
Repetition time	2.5 s	1.5 s
Echo time	33 ms	11 ms
Scan time	2 min 55 s	7 min 30 s
Matrix size	280 × 280	94 × 70
Field of view (FOV)	28 × 28 mm^2	28.2 × 21 mm^2
Spatial resolution	0.1 mm × 0.1 mm	0.3 mm × 0.3 mm
Slice thickness	1 mm	1 mm
Slice gap	0.05 mm	0.05 mm
Slice	21	21
Repetition	1	300
Receiver bandwidth	34722 Hz	300000 Hz
Acceleration factor	8	–
Order automatic ghost correction	–	1
Fat suppression	Yes	Yes
B0 shimming	No	Yes
Read orientation	Left to right	Left to right

2.3. MRI data processing and analysis

The workflow was remotely operated on the MASSIVE's super-computing desktop (Goscinski et al., 2014) and mostly consisted of common processing steps (Moher Alsady et al., 2016; Bajic et al., 2017; Seewoo et al., 2021). Detailed scripts for executing the series of steps can be found in Supplementary material S1. Most of the processing and analysis steps were performed with the Functional MRI of the Brain (FMRIB) Software Library 6.0.3 (FSL 6.0.3; Jenkinson et al., 2012), unless otherwise specified.

2.3.1. Common image pre-processing

The pre-processing for each data package was batch processed as follows: (1). Extract DICOM (Bidgood et al., 1997) of both raw images from PVDatasets packages; (2). Convert DICOM into NifTi using

dcm2niix converter (version: 6-October-2021 for Linux system; Li et al., 2016); (3). Reorient images in the radiological view (left-anterior-superior axes); (4). Correct bias field signals for anatomical images using 3D Slicer (version: 4.8.1; Fedorov et al., 2012); (5). Strip the skull for anatomical images and create an individualized brain mask for the next step; (6). Extract the brain for functional images using the brain mask; (7). Upscale the voxel size of functional images by a factor of 10 (Bajic et al., 2017). Additionally, the quality of reorientation and brain extraction were visually inspected using FSL/slices. Only one anatomical and one functional package failed to reorient within the batch processing and were re-processed separately to correct their orientation.

2.3.2. Further functional image pre-processing

Upscaled functional brain images were further pre-processed on the FSL/MELODIC interface with registration, pre-statistic processing, and single-session ICA. To elaborate, upscaled functional brain images were first registered to their corresponding upscaled anatomical brain images and normalized to a Sprague–Dawley rat brain atlas, which was down sampled by a factor of eight from the Waxholm Space atlas (RRID:SCR_017124; Papp et al., 2014). The down-sampled atlas (voxel size: $3.125 \times 3.125 \times 3.125\,mm^3$) was used to better match the voxel size of functional data and all subsequent processing was performed in this atlas space. Following registration, pre-statistics processing was applied with motion correction (Jenkinson et al., 2002), a temporal high pass filter cut-off of 100 s. No spatial smoothing was applied at this stage (Moher Alsady et al., 2016; Bajic et al., 2017). Single-session ICA was conducted using Probabilistic ICA (Beckmann and Smith, 2004). Finally, outputs of single-session ICA in native space were further de-noised applying FMRIB's ICA-based Xnoiseifier (FIX; version: 1.068; Griffanti et al., 2014; Salimi-Khorshidi et al., 2014) with a trained network (trained-weights file) that can distinguish noise and signals, at a threshold of 20. The trained network was generated with FIX using 50 sets of hand-labelled single-session ICA components, based on each component's spatial maps, frequency, and time-course (Salimi-Khorshidi et al., 2014; Seewoo et al., 2021). Global signal regression was not used to denoise in the present study due to its potential pitfall of introducing spurious anti-correlations (Murphy et al., 2009). Finally, de-noised functional brain images were registered to the down-sampled atlas to construct de-noised and registered functional images.

2.3.3. Group-level ICA

Instead of whole brain, the multi-subject temporal concatenation group-ICA was applied on a large region of interest (ROI) comprising cerebral cortex, hippocampus, amygdala, thalamus, basil ganglia, claustrum, and hypothalamus and colliculi. Most of these structures are considered components of RSNs in humans and animals, while the colliculi and piriform cortex are typically found in rodents as additional components (Jonckers et al., 2011; Seitzman et al., 2019; Smith et al., 2019).

2.3.3.1. Atlas mask generation for the ROI

The ROI atlas mask was generated as follows: (1). Extract high-resolution masks for substructures of the ROI based on their label ID from the Waxholm Space atlas (RRID:SCR_017124; Papp et al., 2014) using ITK-SNAP/Convert3D (version: 1.0.0; Yushkevich et al., 2006); (2). Resample high-resolution masks of each substructure to the down-sampled atlas (see section 2.3.2) to create low-resolution masks and combine these low-resolution masks to form the final ROI mask (See Supplementary material 1 3.1 for detailed scripts, Supplementary material 2 for ROI and substructure masks, and Supplementary material 3 for the volume of each substructure).

2.3.3.2. Spatial smoothing effect on optimal group-ICA dimensionality

An optimal group-ICA dimensionality was estimated using the mICA toolbox, which estimates correlation values using random split-half sampling or test–retest analyses for a range of dimensionalities (Moher Alsady et al., 2016). Briefly, all de-noised and normalized functional images (see section 2.3.2) acquired at baseline ($N = 109$) and the ROI atlas mask were imported to the toolbox. The rationale for excluding rs-MRI data acquired at post-CRS is to avoid CRS-related resting-state alteration in identifying ICA template and to increase the sensitivity of further data processing in detecting group differences following CRS (Seewoo et al., 2021). Random split-half sampling with 50 repetitions were performed at 20 different levels of dimensionality ranging from 10 to 200 components with an interval of 10. For each repetition, MELODIC group-ICA was carried out on both split-half groups ($N = 54$ samples/group) and a cross-correlation matrix between components' spatial maps was calculated using Pearson's correlation. Hungarian sorting algorithm (Kuhn, 2005) was applied to match intergroup components and maximize the summed correlation of all component pairs. Mean correlation and 95% confidence interval (CI) over 50 repetitions were calculated and used to estimate the optimal dimensionality. Whether group-ICA in each dimensionality failed to converge components was also monitored. This analysis was repeated for four different Gaussian kernels of full-width half maximum (FWHM) at 6.25, 9.375, 12.5, and 15.625 mm (corresponding to twice, threefold, fourfold, fivefold the atlas voxel size; Mikl et al., 2008; Chen and Calhoun, 2018). The optimal group-ICA dimensionality under four Gaussian kernels was determined based on the global maximum of correlation outputs (Moher Alsady et al., 2016). Resultant correlation outputs of 80 combinations (20 levels of ICA dimensionality with four Gaussian kernels) were presented in a curve plot. A combination with the maximum value, corresponding to the global maximum of correlation value presented in the curve plot, was considered as an optimal dimensionality. Group-ICA outputs of all split-half sampling groups ($N = 100$) at the resultant dimensionality and Gaussian kernel were ready for the following processing.

2.3.3.3. Ranking and averaging independent component analysis by reproducibility

Ranking and averaging independent component analysis by reproducibility (RAICAR) ranks and selects components based on the reproducibility over repeated ICA realizations, in which a cross-realization correlation matrix is constructed to align components (Yang et al., 2008). Each aligned component over multiple realizations is averaged to generate the final spatial maps of that component. RAICAR is a promising tool to identify robust reproducible components to construct reproducible RSNs following an estimation of optimal decomposition dimensionality for ICA approaches. Rather than performing one run of group-ICA at the optimal dimensionality and Gaussian kernel on all baseline data, the present study applied the 100 group-ICA maps from the previous step (see section 2.3.3.2) to

gRAICAR toolbox (Yang et al., 2012) in MATLAB (version: r2019b). As running group-ICA on the same dataset several times does not produce the same spatial map and there is between-subject variability (run-to-run variability) in ICA results, conducting a RAICAR based on multiple group-ICA maps would expect to generate ICA components that are fair representatives of RSNs and being reproducible across multiple runs and subjects (Becerra et al., 2011; Pendse et al., 2011). Therefore, although gRAICAR was originally performed on individual subjects' ICA maps or functional images, this study implemented the toolbox to align and rank components over the 100 group-ICA maps. An averaged spatial map and intergroup variability (similarity and confidence of contribution) for each aligned and ranked component/node was generated. Nodes were labelled based on intergroup variability in an ascending manner, with node one having the lowest variability. The mean inter-group similarity and ratio of significant groups contributing to each node were reported with column plots. The significant of a group was set as more than 0.05 confidence of the group load [detailed explanation see Yang et al. (2012)]. Additionally, results of group load index and confidence of group load for each component were plotted and compiled in Supplementary material 4.

Spatial maps of all resultant nodes were then merged using FSL/fslmerge command and parcellated using mixture modelling approach based on the thresholded z-transformed results of each node (Woolrich et al., 2005; Moher Alsady et al., 2016). A numerical label is assigned to each voxel based on the node with the highest Z-value at that voxel. As a result, each resultant node's spatial boundary was determined. All the nodes were merged to generate a group-ICA template for a network analysis.

2.3.4. Network modelling

The group-ICA template for the ROI was mapped onto baseline data ($N = 109$; de-noised and normalized functional images, spatially smoothed at resultant Gaussian kernel in section 2.3.3.2) to derive subject-specific time series for all nodes using FSL/dual regression (Nickerson et al., 2017). Images of nodes were created using FSL/slices summary. These time series and images of nodes were then fed into FSLNets (v0.6) in MATLAB (version: r2019b) to perform network modelling. A group average network hierarchy of these nodes was generated based on full correlation using Ward's method. Clusters of highly correlated nodes were merged into large-scale functional networks. For each template network, brain structures were then identified and reported. Absolute volume of each structure with its average Z-score (representing levels of resting-state activity) were extracted using FSL/fslstats and percentage volume against its anatomical total (representing the relative size or spatial extent of resting-state activity) was then calculated (Supplementary material 3). These metrics or spatial characteristics were used to classify networks (Becerra et al., 2011). Additionally, the volumes with its average *Z*-score of brain structure covered by each node within each network were extracted and summarized in Supplementary material 5.

2.3.5. Comparison of CRS and control groups to baseline

To compare the differences in network connectivity for the CRS group between baseline and post-CRS, as well as for the control group between baseline and the second scan session, statistical analysis was conducted in parallel. Due to the difference in the sample size (13 in control, 96 in CRS group), the CRS group was not compared directly with the control group. However, by analysing control and CRS group in parallel, this longitudinal (repeated measures) approach increases the statistical power as each animal was compared to itself, meaning participant/animal variables are controlled at both time points. It also adds biological relevance because it allows investigation of individual susceptibility and response, information which is relevant to future precision medicine approaches (see discussion). In an exploratory statistical analysis, the control ($N = 13$) and CRS ($N = 96$) groups were compared to each other directly at the second time point. But the very different sample size (along with uncontrolled animal variables) resulted in low effect sizes and thus direct comparison approach was not deemed suitable (data not shown).

2.3.5.1. Identification of differences between networks

For the intervention group, the classified networks were merged using FSL/fslmerge and then mapped onto all data acquired at baseline and post-CRS ($N = 192$; de-noised and normalized functional images, spatially smoothed at resultant Gaussian kernel in section 2.3.3.2) to derive subject-specific time series for all networks using FSL/dual regression (Nickerson et al., 2017). These time series were then fed into FSLNets (v0.6) in MATLAB (version: r2019b) to determine if there were differences in the direct connection between networks following CRS. Fisher's r-to-Z transformation (Smith et al., 2011) and ridge-regularized partial correlation was applied to improve the mathematical robustness and achieve better estimation (Smith et al., 2013). The edge [direct connection; definition see Menon and Krishnamurthy (2019)] strength between each pair of networks were compared at baseline and post-CRS using paired permutation t-test with randomize (5,000 permutations, familywise error rate corrected for multiple comparisons across all edges). Raw values of significant edges ($p < 0.05$) were extracted from MATLAB and imported to RStudio (version: 2021.09.2 + 382) to estimate the effect size using 'dabestr' (Ho et al., 2019). For the control group, the same methods described above were applied to all data ($N = 26$; de-noised and normalized functional images, spatially smoothed at resultant Gaussian kernel in section 2.3.3.2). Results showing significant differences ($p < 0.05$) were reported with network images, estimation plots, mean ± SD, permutation p values, and Cohen's d with 95% CI. Raw values of significant edges between networks can be found in Supplementary material 6.

2.3.5.2. Identification of differences within each network

For the intervention and control group, the same methods described in section 2.3.5.1 were applied to each resultant network template from section 2.3.4 to detect if there were differences in the direct connection between nodes within each network at baseline and post-CRS, respectively. Results showing significant differences ($p < 0.05$) within each network were reported with node images, estimation plots, mean ± SD, permutation p values, Cohen's d with 95% CI for the intervention group, and Hedges' g with 95% CI for the control group. Raw values of significant edges within each network can be found in Supplementary material 6.

2.3.5.3. Inter-subject variability of edge strength in the intervention group

Raw values (edge value of individual animals) of abovementioned significant edges between and within networks were grouped into

three categories at baseline and post-CRS: positive (above 0.2), none (between −0.2 and 0.2), negative (below −0.2) partial correlation (Hevey, 2018). Changes in the edge strength following CRS were classified into 11 categories, including positive to more positive, positive to less positive, positive to none, positive to negative, negative to more negative, negative to less negative, negative to none, negative to positive, none to none, none to positive, none to negative. The distribution of edge changes of individual animals falling within these categories were used to indicate if there was high individual variability in terms of these edges showing significance at group level identified in sections 2.3.5.1 and 2.3.5.2. A summary of animal counts of edges showing positive, negative, and no partial correlation for each significant edge at both time points, and changes in the edge strength following CRS can be found in Supplementary material 6.

3. Results

3.1. Spatial smoothing effect on optimal group-ICA dimensionality

There was no failure of convergence in the group-ICA across all dimensionality levels under four different Gaussian kernels. As shown in Figure 1, an increase in the spatial smoothing resulted in an increase in the correlation of group-ICA spatial maps at each dimensionality ranging from 20 to 200. But there were similarly strong correlations (ranging from 0.70 to 0.77) at a dimensionality of 10 regardless of spatial smoothing. Under Gaussian kernels of FWHM 6.25 and 9.375 mm, the correlation value plummeted at first and increased gradually from the dimensionality of 50. In contrast, correlation values stabilised above 0.7, demonstrating strong or very strong associations across all dimensionality levels under Gaussian kernels of FWHM 12.5 and 15.625 mm. The correlation value (mean: 0.84, 95% CI: 0.03) at the dimensionality of 50 and Gaussian kernels of FWHM 15.625 mm was highest amongst all and considered the optimal dimensionality for further analysis.

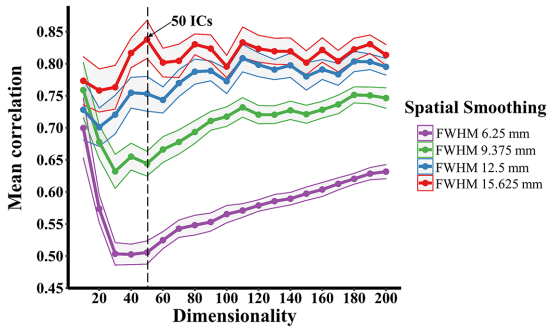

FIGURE 1
Spatial smoothing effects on determining the optimal group-ICA dimensionality. The dimensionality-reproducibility curves under four different Gaussian kernels showed that an increase in the spatial smoothing resulted in an overall increase in the correlation of group-ICA spatial maps. The number of components used in the further group-ICA decomposition was derived from the curves, where 50 independent components (ICs; arrow) was the global maximum. The Curves were plotted with mean±95% CI.

3.2. RAICAR

The resultant 50 components (optimal dimensionality) were aligned and ranked over 100 group-ICA spatial outputs with gRAICAR. Node 1 had the highest similarity and node 50 had the lowest similarity (Figure 2A). The gRAICAR also revealed that 47 nodes presented very strong inter-group consistency with a ratio of significant groups over 0.95 (Figure 2B). The last three components also had a ratio around 0.75 demonstrating strong inter-group consistency. Among these 50 reproducible components, seven were bilateral nodes, including node 4, 19, 23, 31, 37, 39, and 50 (substructures comprising these nodes see Supplementary material 5).

3.3. Networks

Network modelling based on hierarchical clustering detected four common patterns of functional connectivity in the rat brain. The data-driven approach merged the 50 nodes into four major clusters (Figure 3). Major structures covered by each network template are visualized in Figure 4 and volumes of structures with their average *Z*-score are summarized in Supplementary material 3. These networks are described below and listed in the left-to-right order of the hierarchical tree, including DMN-like network, spatial attention-limbic network, corpus striatum network, and autonomic network. Spatial symmetry was observed in some homologous brain regions within these networks.

3.3.1. Network 1 – DMN-like network (14 nodes)

The network was predominantly cortical. Most of the DMN components (cingulate, anterior retrosplenial, prelimbic, orbital, infralimbic, and frontal association cortex) demonstrated bilateral symmetry in the resting-state activity. The spatial extent of resting-state activity in the cornu ammonis/CA, parietal association and visual cortex was larger in the left hemisphere, whereas the resting-state activity of temporal association, auditory, and perirhinal cortex was completely absent in the right hemisphere. Moreover, the resting-state activity of sensorimotor structures were mostly symmetrical in the network.

3.3.2. Network 2 – spatial attention-limbic network (14 nodes)

The homologous brain regions presenting symmetrical resting-state activity were identified as follows: inferior colliculi, superior colliculi, posterior retrosplenial cortex, dorsal hippocampus, and thalamus. The spatial extent of resting-state activity of the visual, auditory, temporal association, postrhinal, and medial entorhinal cortex was larger in the right than left hemisphere, whilst parietal association, perirhinal, and primary somatosensory (trunk representation) cortex only had unilateral resting-state activity in the right hemisphere.

3.3.3. Network 3 – corpus striatum network (15 nodes)

Brain substructures demonstrating bilateral symmetry in the resting-state activity included corpus striatum (nucleus accumbens, globus pallidus, ventral pallidum, and caudate putamen), claustrum, insular, orbital, motor, secondary somatosensory cortex. The spatial extent of resting-state activity of the endopiriform nucleus, perirhinal, piriform cortex was larger in the right than left hemisphere, whereas

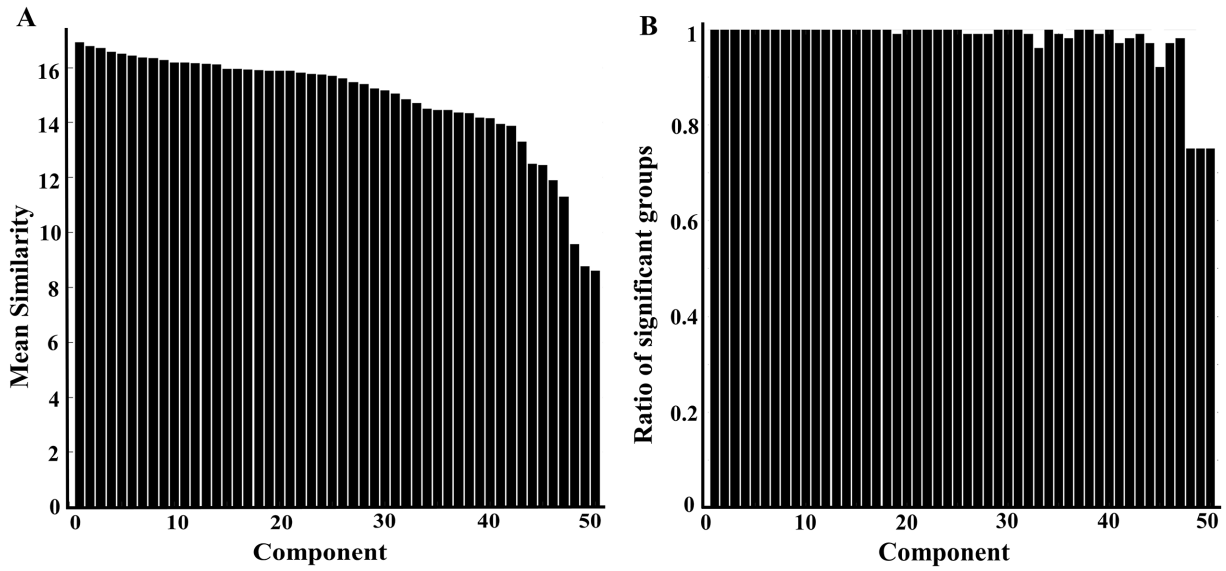

FIGURE 2
Column charts showing intergroup variability at the dimensionality of 50 following RAICAR over 100 group-ICA spatial maps. **(A)** Displaying the mean similarity of aligned 50 components. A higher value indicates the aligned component is more consistently found in different groups. **(B)** Displaying the proportion of groups contributed to the given aligned component. The first 47 components have a ratio of more than 0.95 (95/100 groups), indicating very strong intergroup consistency.

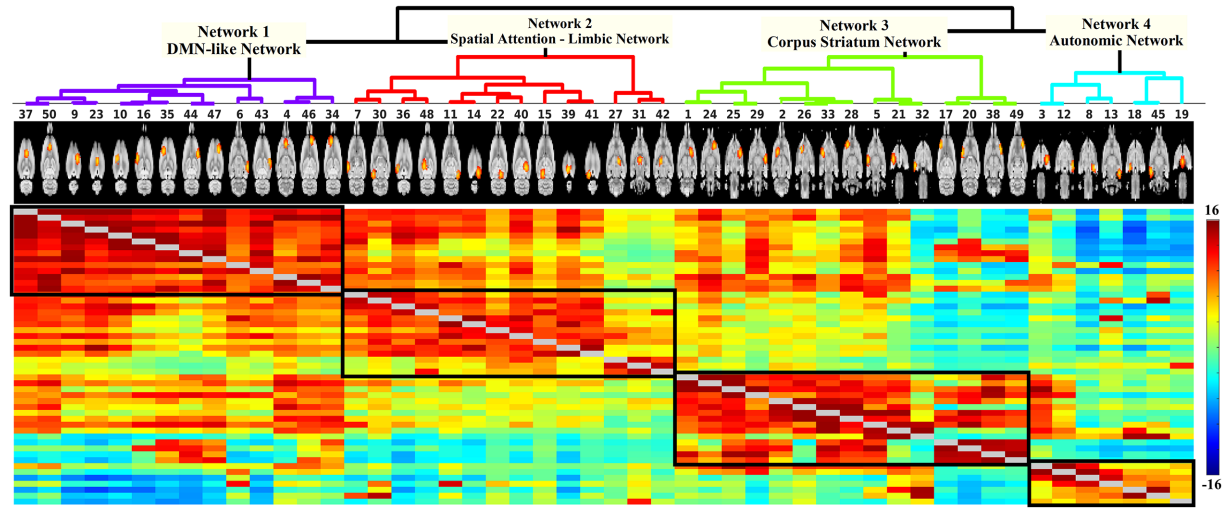

FIGURE 3
Hierarchical network of 50 components. Each node is denoted by one column. The coloured matrix demonstrates the full correlation (below and above the diagonal) of the time series between pairs of components. Darker red indicates a higher positive correlation, light green indicates no correlation, and darker blue represents higher negative correlation. The hierarchical analysis defined four major clusters (black box). Based on the spatial characteristics of each cluster, they were categorized into DMN-like network (14 nodes), spatial attention-limbic network (14 nodes), corpus striatum network (15 nodes), and autonomic network (7 nodes).

the resting-state activity of amygdala, CA, lateral entorhinal cortex was totally absent in the left hemisphere.

3.3.4. Network 4 – autonomic network (7 nodes)

The network was predominantly subcortical. Bilateral symmetry in the resting-state activity was observed in the following subcortical structures: hypothalamus, ventral hippocampus, and substantia nigra. The spatial extent of resting-state activity of amygdala and adjacent cortical regions (lateral and medial entorhinal cortex) was larger in the left than right hemisphere, but the endopiriform nucleus and piriform cortex only demonstrated unilateral resting-state activity in the left hemisphere.

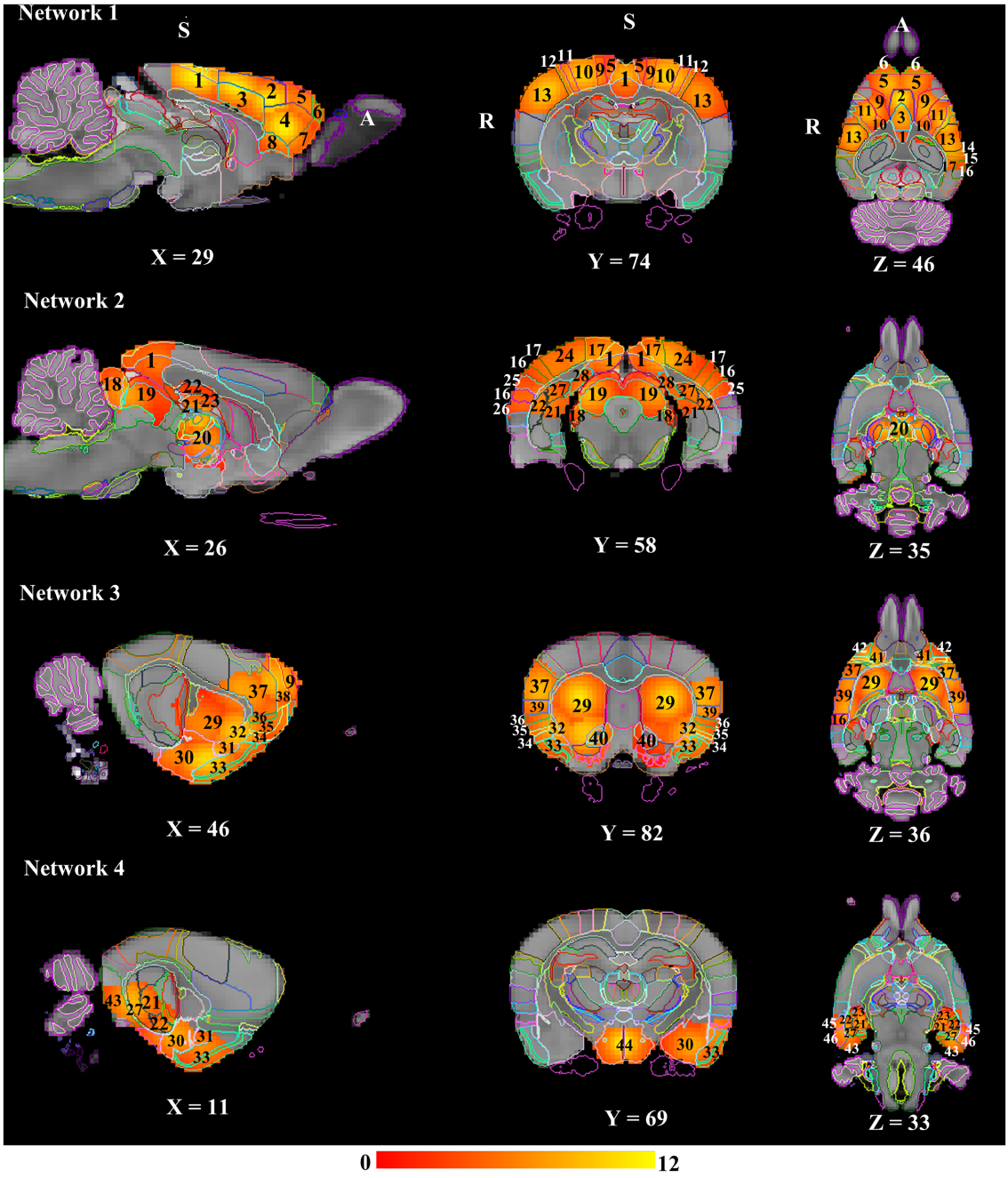

FIGURE 4
Resting state networks in anaesthetised rats. All the networks presented a marked bilateral organisation. These spatial maps were overlayed on the down-sampled atlas and labelled based on the Waxholm Space atlas (RRID: SCR_017124; Papp et al., 2014). Numbers denote: 1: Retrosplenial cortex; 2: Cg1; 3: Cg2; 4: Prelimbic cortex; 5: Secondary motor cortex; 6: Frontal association cortex; 7: Medial orbital cortex; 8: Infralimbic cortex; 9: Primary motor cortex; 10: Primary somatosensory area hindlimb representation; 11: Primary somatosensory area forelimb representation; 12: Primary somatosensory area dysgranular zone; 13: Primary somatosensory area barrel field; 14: Primary somatosensory area trunk representation; 15: Parietal association cortex; 16: Secondary auditory cortex; 17: Secondary visual cortex; 18: Inferior colliculus; 19: Superior colliculus; 20: Thalamus; 21: Dentate gyrus; 22: CA1; 23: CA3; 24: Primary visual cortex; 25: Primary auditory cortex; 26: Temporal association cortex; 27: Subiculum; 28: Presubiculum; 29: Caudate Putamen; 30: Amygdala; 31: Endopiriform nucleus; 32: Claustrum; 33: Piriform cortex; 34: Agranular insular cortex; 35: Dysgranular insular cortex; 36: Granular insular cortex; 37: Primary somatosensory area face representation; 38: Frontal association area 3; 39: Secondary somatosensory area; 40: Nucleus accumbens; 41: Lateral orbital cortex; 42: Dorsolateral orbital cortex; 43: Medial entorhinal cortex; 44: Hypothalamus; 45: Perirhinal cortex; 46: Lateral entorhinal cortex. A: Anterior; R: Right; S: Superior.

3.4. Changes in the functional connectivity between networks following CRS

As shown in Figure 5A, the edge/direct connection strength between the DMN-like network (network 1) and corpus striatum network (network 3) showed a decrease, but with weak effect size following CRS (baseline: 4.34 ± 3.02; post-CRS: 3.45 ± 2.56; p value: 0.044; Cohen's d: −0.32; 95% CI: −0.54 ~ −0.07). In contrast, the connection strength between the DMN-like network (network 1) and autonomic network (network 4) increased significantly with a medium

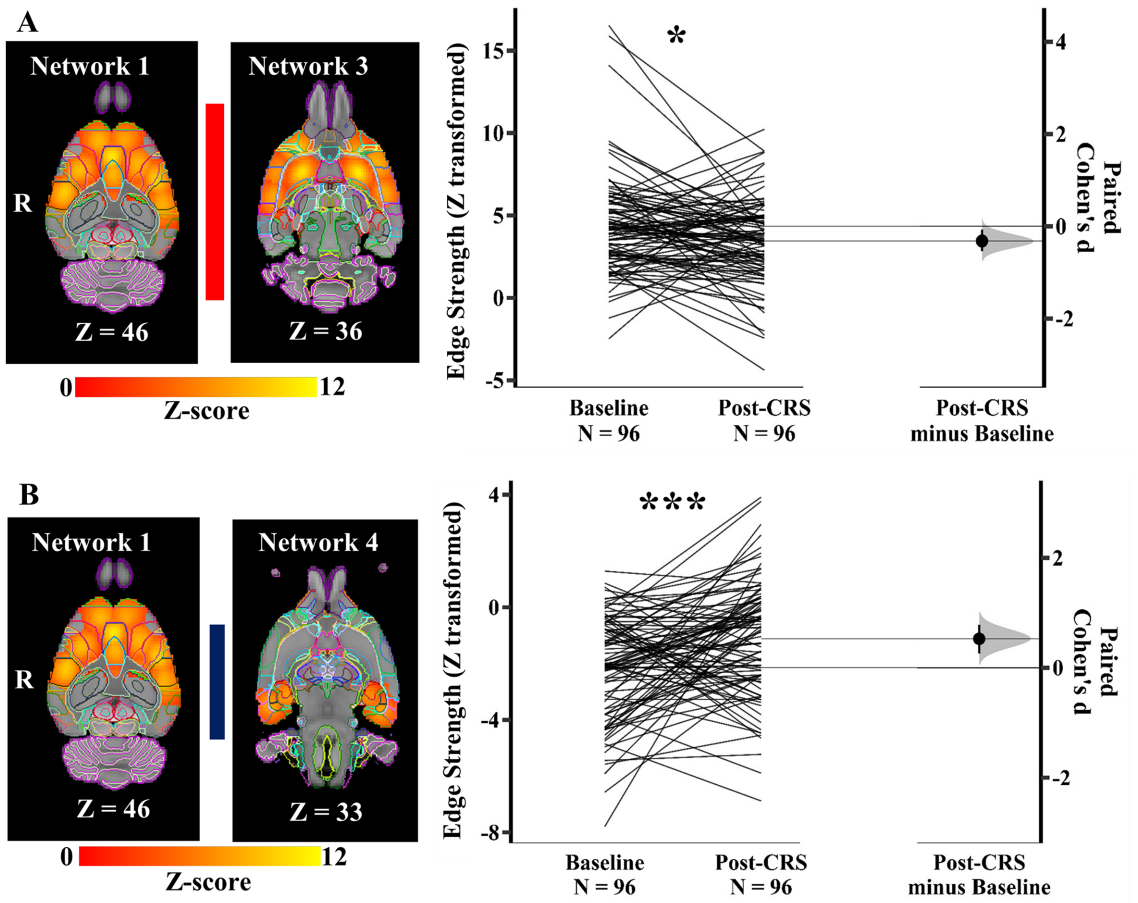

FIGURE 5
Significant edge difference following CRS between networks. **(A)** The connection strength between the DMN-like network (network 1) and corpus striatum network (network 3) displayed on the left showed a decrease following CRS. On the right, Gardner-Altman estimation plot showing a weak effect size (Cohen's d: −0.32) in the edge strength between these two networks (* denotes $p<0.05$). The raw data is plotted on the left axis as a slopegraph, with paired Cohen's d plotted as a bootstrap sampling distribution on the right axis. Each paired set of observations is connected by a line. **(B)** The anticorrelation between the DMN-like network (network 1) and autonomic network (network 4) decreased significantly following CRS. The images of networks are displayed on the left. On the right, Gardner-Altman estimation plot showing a weak effect size (Cohen's d: 0.53) in the edge strength between these two networks (*** denotes $p<0.001$). The coloured bar joining each pair of networks indicates the overall group-average connection strength. Longer suggests a stronger connection, red indicates positive, and blue means negative or anticorrelated. R: Right.

effect size following CRS (Figure 5B; baseline: −2.15 ± 1.84; post-CRS: −1.12 ± 2.06; *p* value: 0.0006; Cohen's d: 0.53; 95% CI: 0.26 ~ 0.78). In other words, the anticorrelation between DMN-like network and autonomic network decreased significantly following CRS.

3.5. Changes in the functional connectivity within each network following CRS

Within the DMN-like network (network 1), a pair of nodes (Figure 6A) showed a significant decrease in the edge/direct connection strength with medium effect size following CRS (baseline: −0.62 ± 0.91; post-CRS: −1.08 ± 0.93; *p* value: 0.040; Cohen's d: −0.49; 95% CI: −0.79 ~ −0.20). Node 37 mainly consisted of bilateral cingulate cortex (posterior part) and node 46 mainly comprised frontal association, orbital, and secondary motor cortex in the left hemisphere. Moreover, the edge strength between node 4 and 6 (Figure 6B) increased significantly with medium effect size following CRS (baseline: −0.22 ± 0.88; post-CRS: 0.25 ± 1.07; *p* value: 0.029; Cohen's d: 0.48; 95% CI: 0.21 ~ 0.76). Node 4 was a bilateral functional complex comprising infralimbic, prelimbic, and orbital cortex. Node 6 was a unilateral functional complex in the left hemisphere, mainly including auditory, temporal association, and perirhinal cortex.

Within the spatial attention-limbic network (network 2), another pair of nodes (Figure 7) demonstrated a significant decrease in edge strength with medium effect size following CRS (baseline: 0.11 ± 0.99; post-CRS: −0.52 ± 1.02; *p* value: 0.0028; Cohen's d: -0.62; 95% CI: −0.92 ~ −0.31). Node 11 was a functional complex in the left hemisphere, mainly including postrhinal, visual, auditory, temporal association, and medial entorhinal cortex. Node 42 consisted of thalamus with adjacent dentate gyrus and CA3 in the right hemisphere.

Similarly, within the corpus striatum network (network 3), another pair of nodes (Figure 8) presented a significant decrease in the direct connection strength with medium effect size following CRS (baseline: 1.11 ± 0.97; post-CRS: 0.50 ± 0.99; *p* value: 0.0028; Cohen's d: −0.62; 95% CI: −0.93 ~ −0.32). Node 21 mainly consisted of right amygdala with adjacent piriform cortex. Node 26 mostly comprised nucleus accumbens and ventral pallidum, with their adjacent piriform

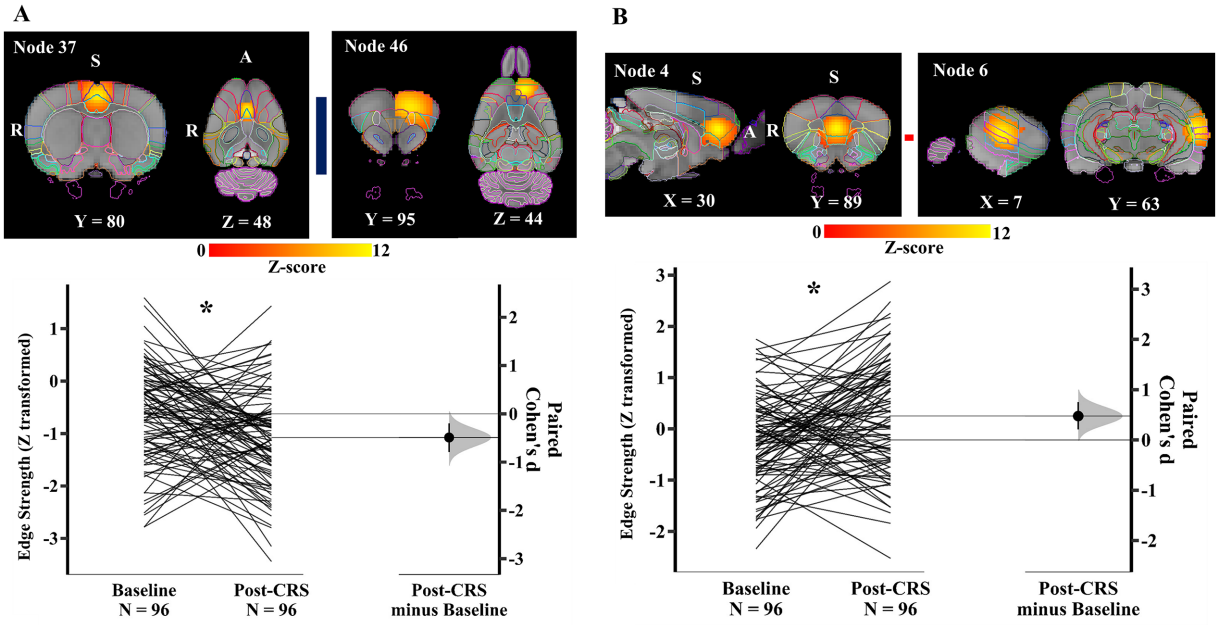

FIGURE 6
Significant edge difference following CRS within network 1 (DMN-like network). **(A)** Images of the pair of nodes are displayed on the left. Node 37 mainly consisted of bilateral cingulate cortex (posterior part) and node 46 mainly comprised frontal association, orbital, and secondary motor cortex in the left hemisphere. On the right, Gardner-Altman estimation plot showing a significant decrease with medium effect size in the edge strength between node 37 and 46 at post-CRS (* denotes $p<0.05$). The group-averaged strength was −0.62 and−1.08 at baseline and post-CRS, respectively. However, there was a high inter-subject variability in the strength changes following CRS. **(B)** Images of another pair of nodes are displayed on the left. Node 4 was a bilateral functional complex comprising infralimbic, prelimbic, and orbital cortex. Node 6 was a unilateral functional complex in the left hemisphere, mainly including auditory, temporal association, and perirhinal cortex. On the right, Gardner-Altman estimation plot showing a significant decrease with medium effect size in the edge strength between node 4 and 6 at post-CRS (* denotes $p<0.05$). The group-averaged strength was −0.22 and 0.25 at baseline and post-CRS, respectively. However, there was a high inter-subject variability in the strength changes following CRS. The coloured bar joining each pair of nodes indicates the overall group-average connection strength. Longer suggests a stronger connection, red indicates positive, and blue means negative or anti-correlated. A: Anterior; R: Right; S: Superior.

cortex in the right hemisphere. In other words, the correlation between amygdala and a functional complex (nucleus accumbens and ventral pallidum) in the right hemisphere decreased significantly following CRS.

For the control group ($N = 13$), no changes were detected between baseline and the second scan session (equivalent period to the post-CRS timepoint in the CRS group), except that a pair of nodes (node 5 and 26) presented a significant increase in the direct connection strength at the second scan session (baseline: -0.93 ± 0.78; second scan: 0.15 ± 0.61; p value: 0.0444) with strong effect size (Hedges' g: 1.5; 95% CI: 0.575 ~ 2.14; data not shown). Node 5 mainly consisted of right insular cortex with adjacent perirhinal and secondary somatosensory cortex.

3.6. High individual variability in the edge strength within networks before and after CRS

There was a high inter-subject variability in the changes of edge strength within the DMN-like network (network 1) and spatial attention-limbic network (network 2). As shown in Supplementary Material 6, for node 4 and 6, the distribution of changes in the edge strength spanned across all the 11 categories, with 26% (25/96) of the animals demonstrating a change from negative to positive correlation, followed by 11% (11/96) animals changing from negative to less negative correlation. A similar lack of clear direction for the changes in the edge strength was also observed in the pair of nodes 37 and 46, as well as nodes 11 and 42. In contrast, for nodes 21 and 26 within the corpus striatum network (network 3), the majority of changes following CRS demonstrated a decrease from positive correlation, in 64% (61/96) of animals. Additionally, a diversity of edge strength was identified in the pair of nodes 4 and 6 at baseline, with 50% (48/96) of animals presenting negative partial correlation and 32% (31/96) showing positive. A similar diversity was also observed in this pair of nodes at post-CRS, as well as other pairs of abovementioned nodes within the DMN-like and spatial attention-limbic network at both time points.

4. Discussion

The main aims of the present study were to use a large dataset to first identify reproducible RSNs in healthy Sprague Dawley rats and then evaluate CRS effects on the functional connectivity in these RSNs within the same animals. The key findings revealed four large-scale networks in the anesthetised rats, including a DMN-like network, a spatial attention-limbic network, a corpus striatum network, and an autonomic network. At a group level, CRS decreased the anticorrelation between the DMN-like network and the autonomic

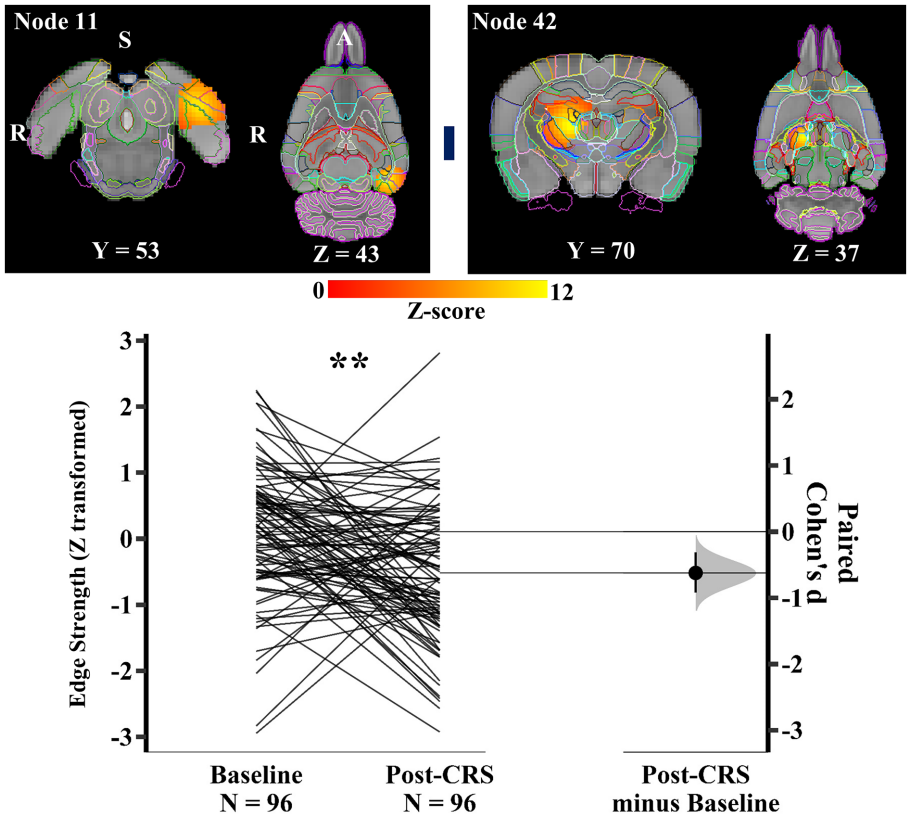

FIGURE 7
Significant edge difference following CRS within network 2 (spatial attention-limbic network). Images of a pair of nodes are displayed on the left. Node 11 was a functional complex in the left hemisphere, mainly including postrhinal, visual, auditory, temporal association, and medial entorhinal cortex. Node 42 consisted of thalamus with adjacent dentate gyrus and CA3 in the right hemisphere. On the right, Gardner-Altman estimation plot showing a significant decrease with medium effect size in the edge strength between node 11 and 42 at post-CRS (** denotes $p<0.01$). The group-averaged strength was 0.11 and−0.52 at baseline and post-CRS, respectively. However, there was a high inter-subject variability in the strength changes following CRS. The coloured bar joining each pair of networks indicates the overall group-average connection strength. Longer suggests a stronger connection, red indicates positive, and blue means negative or anti-correlated. A: Anterior; R: Right; S: Superior.

network. In addition, CRS decreased the correlation between the amygdala and a functional complex (nucleus accumbens and ventral pallidum) in the right hemisphere within the corpus striatum network. However, high individual variability in the functional connectivity before and after CRS within RSNs were observed.

4.1. Spatial smoothing and RAICAR

The overall increase in the correlation of group-ICA spatial maps along with the increase in the spatial smoothing observed in the present study, is supported by the literature (Fornito et al., 2013; Triana et al., 2020) demonstrating that increasing the magnitude of smoothness can reduce the dissimilarity between voxel time courses. The primary goal of spatial smoothing is to supress spatial noise and improve signal-to-noise ratio. Recent investigations also show that spatial smoothing enhances the functional connection strength at both individual and group level, with a stronger influence at the individual level (Alakorkko et al., 2017; Chen and Calhoun, 2018). Interestingly, the similarly strong correlation ($0.77>r>0.70$) at a dimensionality of 10 under four Gaussian kernels may indicate that the cross-correlation analysis by mICA toolbox (Moher Alsady et al., 2016) cannot differentiate the influence of spatial smoothing at a low ICA decomposition dimensionality. This can be explained by the possibility that ICA components at a lower dimensionality (e.g., 10) may be more similar between matched pairs among multiple runs of group-ICA than that components at a higher dimensionality (e.g., over 20) regardless of spatial smoothing.

The present study employs the mICA toolbox (Moher Alsady et al., 2016) to estimate an optimal ICA dimensionality as group-ICA approaches are generally unable to determine the number of components, which is usually achieved empirically. Performing group-ICA with a suboptimal dimensionality can lead to under-fitting or over-fitting of the rs-fMRI data and in turn significantly influence the interpretation of results. Therefore, determining an objective and optimal dimensionality before performing ICA is beneficial. The optimal group-ICA decomposition dimensionality (50 components under Gaussian kernels of FWHM 15.625 mm) chosen for further analysis is simply based on the global maximum recommended by Moher Alsady et al. (2016). However, it would be beneficial to conduct a systematic comparison to evaluate the differences between Gaussian kernels of FWHM 12.5 and 15.625 mm as there were strong correlations (> 0.70) of group-ICA spatial maps across different levels of dimensionality over multiple runs of ICA.

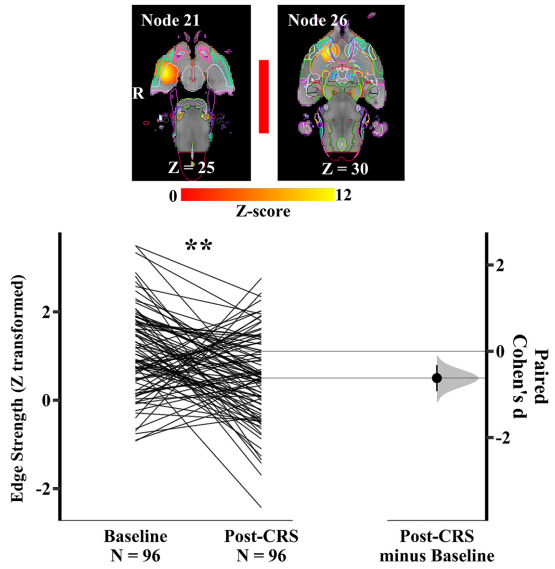

FIGURE 8
Significant edge difference following CRS within network 3 (corpus striatum network). Images of a pair of nodes are displayed on the left. Node 21 mainly consisted of right amygdala with adjacent piriform cortex. Node 26 mostly comprised nucleus accumbens and ventral pallidum, with their adjacent piriform cortex in the right hemisphere. On the right, Gardner-Altman estimation plot showing a significant decrease with medium effect size in the edge strength between node 21 and 26 at post-CRS (** denotes $p<0.01$). The coloured bar joining each pair of networks indicates the overall group-average connection strength. Longer suggests a stronger connection, red indicates positive, and blue means negative or anti-correlated. A: Anterior.

The results from the RAICAR analysis are supported by Pendse et al. (2011) stating that reliable ICA components will be present in almost all ICA runs and in turn will generate tight clusters well distinguishable from the rest. Applying multiple group-ICA runs to groups of subjects with enough diversity is expected to account for the run-to-run variability in ICA approaches both because of the non-convex objective function and inter-subject variability. However, more studies are warranted to ensure reproducible results as only one human study (Pendse et al., 2011) and another rodent study in awake rats (Becerra et al., 2011) have investigated the reproducible RSNs using multiple ICA runs on groups of randomly sampled subjects from a dataset.

4.2. Networks

The four large-scale networks classified in the present study show good similarity to the networks observed in healthy humans and rodents in the literature (Becerra et al., 2011; Smith et al., 2013; Zerbi et al., 2015; Bajic et al., 2017; Coletta et al., 2020; Xu et al., 2022).

4.2.1. Network 1 – DMN-like network

The core DMN structures (cingulate, retrosplenial, prelimbic, orbital, and infralimbic cortex) identified here based on the hierarchical analysis are consistent with previously published rodent studies using seed-based approaches or group ICA analysis with a low dimensionality from 10 to 30 (Lu et al., 2012; Stafford et al., 2014; Liska et al., 2015; Sierakowiak et al., 2015; Zerbi et al., 2015; Huang et al., 2016; Grandjean et al., 2020; Whitesell et al., 2021). Hippocampal region (CA) has been suggested as a part of the DMN in some studies (Lu et al., 2012; Zerbi et al., 2015; Huang et al., 2016), but not others (Stafford et al., 2014; Sierakowiak et al., 2015; Grandjean et al., 2020). Although somatosensory structures were shown relatively independent from the DMN in a rodent cohort based on a hierarchical analysis in Zerbi et al. (2015), but not in the present and other rodent studies (Liska et al., 2015; Huang et al., 2016; Whitesell et al., 2021). These inconsistencies may reflect the methodological differences in detecting the DMN. DMN is implicated in cognitive functions, including rumination, self-referential processing at rest, and retrieval of episodic memory in humans (Williams, 2017). DMN has shown the highest activation when individuals are at rest, and it is deactivated when performing goal-directed tasks.

4.2.2. Network 2 – spatial attention-limbic network

The components of this network are similar to what has been observed in awake rodents from other studies (Zhang et al., 2010; Becerra et al., 2011). The colliculi have been well-known to be involved in spatial attention and retrosplenial cortex is considered playing a key function in several cognitive functions, including spatial memory. The asymmetrical resting-state activity of the visual, auditory, and medial entorhinal cortex is consistent with the right-hemispheric lateralization for spatial attention in humans (Agcaoglu et al., 2015; O'Regan and Serrien, 2018).

4.2.3. Network 3 – corpus striatum network

The network is one of the basal ganglia networks observed in previous rodent and human studies (Becerra et al., 2011; Smith et al., 2013; Zerbi et al., 2015). The striatum, insula, orbital cortex, and amygdala forming the cortico–amygdala–striatal circuit mediate emotion processing through collectively processing information in terms of salient stimuli and attentional states in both rodents and primates (Cho et al., 2013; Heilbronner et al., 2016). The asymmetrical resting-state activity of amygdala, CA, and lateral entorhinal cortex in the network agrees with the literature demonstrating a rightwards lateralization of affective processing in humans and primates (Decety and Moriguchi, 2007).

4.2.4. Network 4 – autonomic network

The networks are commonly observed in awake and anesthetized rodents as an ICA component (Hutchison et al., 2010; Liang et al., 2011). The key component of autonomic network – the hypothalamus plays an important role in numerous homeostatic behaviors. The involvement of the hippocampus in the network is considered to be associated with defensive/stress behaviors (Becerra et al., 2011).

4.3. Functional connectivity alterations following CRS

The decreased anticorrelation between the whole DMN-like network and subcortical autonomic network in the present study has not previously been reported. Although the mechanism underlying the anticorrelation between the DMN-like and autonomic network is unknown, a meta-analysis study has suggested that these two networks are both associated with autonomic regulation in humans (Beissner

et al., 2013). Moreover, studies have reported that the activation of some core structures of the DMN has a downstream inhibitory effect on the activity of hypothalamus and amygdala regarding stress response and negative emotions of anxiety (Etkin et al., 2011; Herman et al., 2016). Disinhibition in the top-down cortical–subcortical circuits may result in excessive stress responses and over-processing of negative emotions, which are associated with anxiety-related disorders (Fridman et al., 2021). The decreased anticorrelation following CRS in the present study can be explained by the top-down disinhibition theory, meaning chronic stress may induce disinhibition from DMN to subcortical autonomic network that regulates stress and anxiety.

This is also the first time that a decreased correlation between the amygdala and a functional complex (nucleus accumbens and ventral pallidum) in the right hemisphere within the corpus striatum network is reported in an animal model. These structures are parts of the reward system, the nucleus accumbens receives glutamatergic inputs from the basolateral amygdala and project GABAergic signals to the ventral pallidum (Hirter et al., 2021). The nucleus accumbens is considered to play a role in one of the core symptoms of depression – anhedonia (Heshmati and Russo, 2015; Liu et al., 2021). For example, the nucleus accumbens has a lower resting-state functional connectivity with some cortical regions in patients with depression. However, the neuroimaging study (Liu et al., 2021) did not analyse the connectivity between amygdala, nucleus accumbens and ventral pallidum. Future studies in investigating the correspondence of functional connectivity between these three subcortical structures in rodent models and patients with depression are necessary.

In contrast with the present results, some human neuroimaging studies have reported that depression is commonly associated with hyperconnectivity within the DMN, as well as aberrant cross-network interaction among DMN, central executive and salience networks (Hamilton et al., 2013; Brakowski et al., 2017). A simple interpretation of the divergent functional connectivity between rodents and humans is that the rodent response to CRS does not reflect the complexity of depression as it is experienced by humans. The limitations of animal models of depression and anxiety-like behavior are beyond the scope of the present article and have been extensively discussed elsewhere (Becker et al., 2021). However, even in humans, findings regarding the direction of functional connectivity alteration within and between human brain networks are still inconclusive because depression is highly heterogenous with various neurobiological substrates (Drysdale et al., 2017). The present study also reveals that there is high inter-subject variability of functional connectivity at baseline and post-CRS in rats as well, suggesting that it may be possible to classify rodent neural phenotypes to refine the connectivity analysis. Future studies should investigate rodent phenotypes using not only brain connectivity but also behavioural measures, potentially providing opportunity to model tailored approaches to prevention and treatment of neuropsychiatric conditions including depression.

4.4. Limitations and future direction

Additional limitations are worth mentioning. First, only male late adolescent/young adult Sprague–Dawley rats were used in the analysis due to data availability. This means that the brains of these animals were still developing during the CRS intervention and may have confounded interpretation of the network changes (Hennessy et al., 2022). However, this age range is relevant to studying mood disorders in young people. It is expected that the present approach of using large datasets will lead to a better understanding of how the developing brain is impacted by environmental stressors, and how this may lead to long-term changes in mood regulation. Future studies including female rats, aged rats, other inbred and outbred strains will be necessary to assess the generalizability of present results.

Moreover, the level of anaesthesia is a key consideration in MRI studies and the present study applied combined use of isoflurane and medetomidine at doses, which have been found to provide stable anaesthesia with the least impact on brain activity (Grandjean et al., 2014; Bukhari et al., 2017; Paasonen et al., 2018; Grandjean et al., 2023). At the time the experiments in this study were carried out, a standard time for the change of anaesthesia before rs-fMRI scanning was not established. Rather, individual animals' breathing rate was employed as an indicator because individual animals have been found to vary in their response to isoflurane and medetomidine (Seewoo et al., 2020). Recently, a standard 45-min period in mice has been recommended after switching from isoflurane alone to the combined regimen of isoflurane and medetomidine (ISO/MED; Pradier et al., 2021). However, considering the experimental design, it is not clear whether differences in brain activity between isoflurane alone (at 1%) and three combined regimes (ISO-0.6%/MED-25 min, ISO-0.2%/MED-45 min, ISO-0.2%/MED-100 min) resulted from the reduction in the isoflurane concentration or waiting period following the induction of medetomidine. While additional study on time-dependency of anaesthetic on brain activity is needed, the consistent timing (32 min ± 4) of the combined anaesthetic protocol employed in the present study allows confident interpretation of results.

In terms of analysis, the parcellation approach to define the spatial boundary of functional nodes may be too simple and can be improved with more sophisticated approaches (e.g., advanced clustering methods) to address the uncertainty resulting from regions where multiple nodes overlap and *Z*-scores are low. Finally, only hierarchical clustering analysis was applied to classify the networks. Future efforts in systematically comparing the differences on the RSN classification with other algorithms, such as the fuzzy-c-means clustering algorithm (Lee et al., 2012) and deep learning algorithms like Siamese ICA (Chou et al., 2022), are necessary.

5. Conclusion

The present study is the first to construct reproducible RSNs in anaesthetized rats through identifying optimal and reproducible functional components, and in turn evaluate functional connectivity changes in the RSNs following a CRS model within the same animals. The key findings revealed four large-scale networks that are homologous across species, decreased anticorrelation between DMN-like and autonomic network, decreased correlation between amygdala and a functional complex (nucleus accumbens and ventral pallidum) in the right hemisphere within the corpus striatum network. Moreover, high inter-subject variability of functional connectivity is observed within networks, indicating rats may demonstrate different neural phenotypes as humans. Therefore, future efforts in classifying neural phenotypes in rodents might improve the sensitivity and translational impact of models used to address aetiology and treatment of psychiatric conditions including depression.

Data availability statement

The original contributions presented in the study are included in the article/Supplementary material, further inquiries can be directed to the corresponding author.

Ethics statement

The animal study was reviewed and approved by University of Western Australia Animal Ethics Committee (RA/3/100/1640).

Author contributions

TD and JR conceived and designed the study. LH and SB collected a subset of data that is not previously published. TD carried out the analysis with guidance from BS and TR, and wrote the first draft of the manuscript. All authors contributed to the article and approved the submitted version.

Funding

JR is supported by a Senior Fellowship from MSWA and the Perron Institute for Neurological and Translational Science. TD is supported by the Australian Government International Research Training Program scholarship, and Byron Kakulas Prestige scholarship.

Acknowledgments

The authors acknowledge the facilities and scientific and technical assistance of the National Imaging Facility, a National Collaborative Research Infrastructure Strategy (NCRIS) capability, at the Centre for Microscopy, Characterisation and Analysis, The University of Western Australia.

Conflict of interest

The authors declare that the research was conducted in the absence of any commercial or financial relationships that could be construed as a potential conflict of interest.

Publisher's note

Supplementary material

The Supplementary material for this article can be found online at: https://www.frontiersin.org/articles/10.3389/fnins.2023.1151525/full#supplementary-material

References

Agcaoglu, O., Miller, R., Mayer, A. R., Hugdahl, K., and Calhoun, V. D. (2015). Lateralization of resting state networks and relationship to age and gender. *Neuroimage* 104, 310–325. doi: 10.1016/j.neuroimage.2014.09.001

Alakorkko, T., Saarimaki, H., Glerean, E., Saramaki, J., and Korhonen, O. (2017). Effects of spatial smoothing on functional brain networks. *Eur. J. Neurosci.* 46, 2471–2480. doi: 10.1111/ejn.13717

Bajic, D., Craig, M. M., Mongerson, C. R. L., Borsook, D., and Becerra, L. (2017). Identifying rodent resting-state brain networks with independent component analysis. *Front. Neurosci.* 11:685. doi: 10.3389/fnins.2017.00685

Becerra, L., Pendse, G., Chang, P. C., Bishop, J., and Borsook, D. (2011). Robust reproducible resting state networks in the awake rodent brain. *PLoS One* 6:e25701. doi: 10.1371/journal.pone.0025701

Becker, M., Pinhasov, A., and Ornoy, A. (2021). Animal models of depression: what can they teach us about the human disease? *Diagnostics* 11:123. doi: 10.3390/diagnostics11010123

Beckmann, C. F., and Smith, S. M. (2004). Probabilistic independent component analysis for functional magnetic resonance imaging. *IEEE Trans. Med. Imaging* 23, 137–152. doi: 10.1109/TMI.2003.822821

Beissner, F., Meissner, K., Bär, K.-J., and Napadow, V. (2013). The autonomic brain: an activation likelihood estimation meta-analysis for central processing of autonomic function. *J. Neurosci.* 33, 10503–10511. doi: 10.1523/JNEUROSCI.1103-13.2013

Bidgood, W. D. Jr., Horii, S. C., Prior, F. W., and Van Syckle, D. E. (1997). Understanding and using DICOM, the data interchange standard for biomedical imaging. *J. Am. Med. Inform. Assoc.* 4, 199–212. doi: 10.1136/jamia.1997.0040199

Brakowski, J., Spinelli, S., Dorig, N., Bosch, O. G., Manoliu, A., Holtforth, M. G., et al. (2017). Resting state brain network function in major depression - depression symptomatology, antidepressant treatment effects, future research. *J. Psychiatr. Res.* 92, 147–159. doi: 10.1016/j.jpsychires.2017.04.007

Bukhari, Q., Schroeter, A., Cole, D. M., and Rudin, M. (2017). Resting state fMRI in mice reveals anesthesia specific signatures of brain functional networks and their interactions. *Front. Neural Circuits* 11:5. doi: 10.3389/fncir.2017.00005

Chen, Z., and Calhoun, V. (2018). Effect of spatial smoothing on task fMRI ICA and functional connectivity. *Front. Neurosci.* 12:15. doi: 10.3389/fnins.2018.00015

Cho, Y. T., Ernst, M., and Fudge, J. L. (2013). Cortico–amygdala–striatal circuits are organized as hierarchical subsystems through the primate amygdala. *J. Neurosci.* 33, 14017–14030. doi: 10.1523/JNEUROSCI.0170-13.2013

Chou, Y., Chang, C., Remedios, S. W., Butman, J. A., Chan, L., and Pham, D. L. (2022). Automated classification of resting-state fMRI ICA components using a deep Siamese network. *Front. Neurosci.* 16:768634. doi: 10.3389/fnins.2022.768634

Coletta, L., Pagani, M., Whitesell, J. D., Harris, J. A., Bernhardt, B., and Gozzi, A. (2020). Network structure of the mouse brain connectome with voxel resolution. *Sci. Adv.* 6:eabb7187. doi: 10.1126/sciadv.abb7187

Decety, J., and Moriguchi, Y. (2007). The empathic brain and its dysfunction in psychiatric populations: implications for intervention across different clinical conditions. *Biopsychosoc. Med.* 1:22. doi: 10.1186/1751-0759-1-22

Drysdale, A. T., Grosenick, L., Downar, J., Dunlop, K., Mansouri, F., Meng, Y., et al. (2017). Resting-state connectivity biomarkers define neurophysiological subtypes of depression. *Nat. Med.* 23, 28–38. doi: 10.1038/nm.4246

Etkin, A., Egner, T., and Kalisch, R. (2011). Emotional processing in anterior cingulate and medial prefrontal cortex. *Trends Cogn. Sci.* 15, 85–93. doi: 10.1016/j.tics.2010.11.004

Fedorov, A., Beichel, R., Kalpathy-Cramer, J., Finet, J., Fillion-Robin, J. C., Pujol, S., et al. (2012). 3D slicer as an image computing platform for the quantitative imaging network. *Magn. Reson. Imaging* 30, 1323–1341. doi: 10.1016/j.mri.2012.05.001

Fornito, A., Zalesky, A., and Breakspear, M. (2013). Graph analysis of the human connectome: promise, progress, and pitfalls: mapping the connectome. *Neuroimage* 80, 426–444. doi: 10.1016/j.neuroimage.2013.04.087

Fornito, A., Zalesky, A., and Breakspear, M. (2015). The connectomics of brain disorders. *Nat. Rev. Neurosci.* 16, 159–172. doi: 10.1038/nrn3901

Fridman, A. J., Yang, X., Vilgis, V., Keenan, K. E., Hipwell, A. E., Guyer, A. E., et al. (2021). Brain structure and parasympathetic function during rest and stress in young adult women. *Brain Struct. Funct.* 226, 1195–1207. doi: 10.1007/s00429-021-02234-7

Goscinski, W. J., Mcintosh, P., Felzmann, U., Maksimenko, A., Hall, C. J., Gureyev, T., et al. (2014). The multi-modal Australian ScienceS imaging and visualization environment (MASSIVE) high performance computing infrastructure: applications in neuroscience and neuroinformatics research. *Front. Neuroinform.* 8:30. doi: 10.3389/fninf.2014.00030

Grandjean, J., Azzinnari, D., Seuwen, A., Sigrist, H., Seifritz, E., Pryce, C. R., et al. (2016). Chronic psychosocial stress in mice leads to changes in brain functional connectivity and metabolite levels comparable to human depression. *Neuroimage* 142, 544–552. doi: 10.1016/j.neuroimage.2016.08.013

Grandjean, J., Canella, C., Anckaerts, C., Ayranci, G., Bougacha, S., Bienert, T., et al. (2020). Common functional networks in the mouse brain revealed by multi-Centre resting-state fMRI analysis. *Neuroimage* 205:116278. doi: 10.1016/j.neuroimage.2019.116278

Grandjean, J., Desrosiers-Gregoire, G., Anckaerts, C., Angeles-Valdez, D., Ayad, F., Barrière, D. A., et al. (2023). A consensus protocol for functional connectivity analysis in the rat brain. *Nat. Neurosci.* 26, 673–681. doi: 10.1038/s41593-023-01286-8

Grandjean, J., Schroeter, A., Batata, I., and Rudin, M. (2014). Optimization of anesthesia protocol for resting-state fMRI in mice based on differential effects of anesthetics on functional connectivity patterns. *Neuroimage* 102, 838–847. doi: 10.1016/j.neuroimage.2014.08.043

Griffanti, L., Salimi-Khorshidi, G., Beckmann, C. F., Auerbach, E. J., Douaud, G., Sexton, C. E., et al. (2014). ICA-based artefact removal and accelerated fMRI acquisition for improved resting state network imaging. *Neuroimage* 95, 232–247. doi: 10.1016/j.neuroimage.2014.03.034

Hamilton, J. P., Chen, M. C., and Gotlib, I. H. (2013). Neural systems approaches to understanding major depressive disorder: an intrinsic functional organization perspective. *Neurobiol. Dis.* 52, 4–11. doi: 10.1016/j.nbd.2012.01.015

Han, S., Son, J. P., Cho, H., Park, J. Y., and Kim, S. G. (2019). Gradient-echo and spin-echo blood oxygenation level–dependent functional MRI at ultrahigh fields of 9.4 and 15.2 tesla. *Magn. Reson. Med.* 81, 1237–1246. doi: 10.1002/mrm.27457

Harro, J. (2019). Animal models of depression: pros and cons. *Cell Tissue Res.* 377, 5–20. doi: 10.1007/s00441-018-2973-0

Heilbronner, S. R., Rodriguez-Romaguera, J., Quirk, G. J., Groenewegen, H. J., and Haber, S. N. (2016). Circuit-based corticostriatal homologies between rat and primate. *Biol. Psychiatry* 80, 509–521. doi: 10.1016/j.biopsych.2016.05.012

Henckens, M. J., van der Marel, K., van der Toorn, A., Pillai, A. G., Fernández, G., Dijkhuizen, R. M., et al. (2015). Stress-induced alterations in large-scale functional networks of the rodent brain. *Neuroimage* 105, 312–322. doi: 10.1016/j.neuroimage.2014.10.037

Hennessy, L. A., Seewoo, B. J., Jaeschke, L. A., Mackie, L. A., Figliomeni, A., Arena-Foster, Y., et al. (2022). Accelerated low-intensity rTMS does not rescue anxiety behaviour or abnormal connectivity in young adult rats following chronic restraint stress. *Neuroimage* 2:100104. doi: 10.1016/j.ynirp.2022.100104

Herman, J. P., Mcklveen, J. M., Ghosal, S., Kopp, B., Wulsin, A., Makinson, R., et al. (2016). Regulation of the hypothalamic-pituitary-adrenocortical stress response. *Compr. Physiol.* 6:603. doi: 10.1002/cphy.c150015

Herzog, D. P., Beckmann, H., Lieb, K., Ryu, S., and Müller, M. B. (2018). Understanding and predicting antidepressant response: using animal models to move toward precision psychiatry. *Front. Psych.* 9:512. doi: 10.3389/fpsyt.2018.00512

Heshmati, M., and Russo, S. J. (2015). Anhedonia and the brain reward circuitry in depression. *Curr. Behav. Neurosci. Rep.* 2, 146–153. doi: 10.1007/s40473-015-0044-3

Hevey, D. (2018). Network analysis: a brief overview and tutorial. *Health Psychol. Behav. Med.* 6, 301–328. doi: 10.1080/21642850.2018.1521283

Hirter, K. N., Miller, E. N., Stimpson, C. D., Phillips, K. A., Hopkins, W. D., Hof, P. R., et al. (2021). The nucleus accumbens and ventral pallidum exhibit greater dopaminergic innervation in humans compared to other primates. *Brain Struct. Funct.* 226, 1909–1923. doi: 10.1007/s00429-021-02300-0

Ho, J., Tumkaya, T., Aryal, S., Choi, H., and Claridge-Chang, A. (2019). Moving beyond P values: data analysis with estimation graphics. *Nature methods* 16, 565–566. doi: 10.1038/s41592-019-0470-3

Hsu, L.-M., Liang, X., Gu, H., Brynildsen, J. K., Stark, J. A., Ash, J. A., et al. (2016). Constituents and functional implications of the rat default mode network. *Proc. Natl. Acad. Sci.* 113, E4541–E4547. doi: 10.1073/pnas.1601485113

Huang, S.-M., Wu, Y.-L., Peng, S.-L., Peng, H.-H., Huang, T.-Y., Ho, K.-C., et al. (2016). Inter-strain differences in default mode network: a resting state fMRI study on spontaneously hypertensive rat and Wistar Kyoto rat. *Sci. Rep.* 6:21697. doi: 10.1038/srep21697

Hutchison, R. M., Mirsattari, S. M., Jones, C. K., Gati, J. S., and Leung, L. S. (2010). Functional networks in the anesthetized rat brain revealed by independent component analysis of resting-state FMRI. *J. Neurophysiol.* 103, 3398–3406. doi: 10.1152/jn.00141.2010

Jenkinson, M., Bannister, P., Brady, M., and Smith, S. (2002). Improved optimization for the robust and accurate linear registration and motion correction of brain images. *Neuroimage* 17, 825–841. doi: 10.1006/nimg.2002.1132

Jenkinson, M., Beckmann, C. F., Behrens, T. E., Woolrich, M. W., and Smith, S. M. (2012). FSL. *Neuroimage* 62, 782–790. doi: 10.1016/j.neuroimage.2011.09.015

Jonckers, E., Van Audekerke, J., De Visscher, G., Van Der Linden, A., and Verhoye, M. (2011). Functional connectivity fMRI of the rodent brain: comparison of functional connectivity networks in rat and mouse. *PLoS One* 6:e18876. doi: 10.1371/journal.pone.0018876

Krishnan, V., and Nestler, E. J. (2008). The molecular neurobiology of depression. *Nature* 455, 894–902. doi: 10.1038/nature07455

Kuhn, H. W. (2005). The Hungarian method for the assignment problem. *Nav. Res. Logist.* 52, 7–21. doi: 10.1002/nav.20053

Lee, M. H., Hacker, C. D., Snyder, A. Z., Corbetta, M., Zhang, D., Leuthardt, E. C., et al. (2012). Clustering of resting state networks. *PLoS One* 7:e40370. doi: 10.1371/journal.pone.0040370

Li, X., Morgan, P. S., Ashburner, J., Smith, J., and Rorden, C. (2016). The first step for neuroimaging data analysis: DICOM to NIfTI conversion. *J. Neurosci. Methods* 264, 47–56. doi: 10.1016/j.jneumeth.2016.03.001

Liang, Z., King, J., and Zhang, N. (2011). Uncovering intrinsic connectional architecture of functional networks in awake rat brain. *J. Neurosci.* 31, 3776–3783. doi: 10.1523/jneurosci.4557-10.2011

Liska, A., Galbusera, A., Schwarz, A. J., and Gozzi, A. (2015). Functional connectivity hubs of the mouse brain. *Neuroimage* 115, 281–291. doi: 10.1016/j.neuroimage.2015.04.033

Liu, R., Wang, Y., Chen, X., Zhang, Z., Xiao, L., and Zhou, Y. (2021). Anhedonia correlates with functional connectivity of the nucleus accumbens subregions in patients with major depressive disorder. *Neuroimage* 30:102599. doi: 10.1016/j.nicl.2021.102599

Lu, H., Zou, Q., Gu, H., Raichle, M. E., Stein, E. A., and Yang, Y. (2012). Rat brains also have a default mode network. *Proc. Natl. Acad. Sci.* 109, 3979–3984. doi: 10.1073/pnas.1200506109

Mandino, F., Vrooman, R. M., Foo, H. E., Yeow, L. Y., TAW, B., Salvan, P., et al. (2022). A triple-network organization for the mouse brain. *Mol. Psychiatry* 27, 865–872. doi: 10.1038/s41380-021-01298-5

Menon, S. S., and Krishnamurthy, K. (2019). A comparison of static and dynamic functional connectivities for identifying subjects and biological sex using intrinsic individual brain connectivity. *Sci. Rep.* 9:5729. doi: 10.1038/s41598-019-42090-4

Mikl, M., Marecek, R., Hlustik, P., Pavlicova, M., Drastich, A., Chlebus, P., et al. (2008). Effects of spatial smoothing on fMRI group inferences. *Magn. Reson. Imaging* 26, 490–503. doi: 10.1016/j.mri.2007.08.006

Moher Alsady, T., Blessing, E. M., and Beissner, F. (2016). MICA-A toolbox for masked independent component analysis of fMRI data. *Hum. Brain Mapp.* 37, 3544–3556. doi: 10.1002/hbm.23258

Mulders, P. C., Van Eijndhoven, P. F., Schene, A. H., Beckmann, C. F., and Tendolkar, I. (2015). Resting-state functional connectivity in major depressive disorder: a review. *Neurosci. Biobehav. Rev.* 56, 330–344. doi: 10.1016/j.neubiorev.2015.07.014

Murphy, K., Birn, R. M., Handwerker, D. A., Jones, T. B., and Bandettini, P. A. (2009). The impact of global signal regression on resting state correlations: are anti-correlated networks introduced? *Neuroimage* 44, 893–905. doi: 10.1016/j.neuroimage.2008.09.036

Nephew, B. C., Febo, M., Huang, W., Colon-Perez, L. M., Payne, L., Poirier, G. L., et al. (2018). Early life social stress and resting state functional connectivity in postpartum rat anterior cingulate circuits. *J. Affect. Disord.* 229, 213–223. doi: 10.1016/j.jad.2017.12.089

Nickerson, L. D., Smith, S. M., Ongur, D., and Beckmann, C. F. (2017). Using dual regression to investigate network shape and amplitude in functional connectivity analyses. *Front. Neurosci.* 11:115. doi: 10.3389/fnins.2017.00115

O'regan, L., and Serrien, D. J. (2018). Individual differences and hemispheric asymmetries for language and spatial attention. *Front. Hum. Neurosci.* 12:380. doi: 10.3389/fnhum.2018.00380

Ogawa, S., Lee, T. M., Nayak, A. S., and Glynn, P. (1990). Oxygenation-sensitive contrast in magnetic-resonance image of rodent brain at high magnetic-fields. *Magn. Reson. Med.* 14, 68–78. doi: 10.1002/mrm.1910140108

Paasonen, J., Stenroos, P., Salo, R. A., Kiviniemi, V., and Grohn, O. (2018). Functional connectivity under six anesthesia protocols and the awake condition in rat brain. *Neuroimage* 172, 9–20. doi: 10.1016/j.neuroimage.2018.01.014

Pais-Roldan, P., Mateo, C., Pan, W. J., Acland, B., Kleinfeld, D., Snyder, L. H., et al. (2021). Contribution of animal models toward understanding resting state functional connectivity. *Neuroimage* 245:118630. doi: 10.1016/j.neuroimage.2021.118630

Papp, E. A., Leergaard, T. B., Calabrese, E., Johnson, G. A., and Bjaalie, J. G. (2014). Waxholm space atlas of the Sprague Dawley rat brain. *Neuroimage* 97, 374–386. doi: 10.1016/j.neuroimage.2014.04.001

Paulus, M. P., and Stein, M. B. (2010). Interoception in anxiety and depression. *Brain Struct. Funct.* 214, 451–463. doi: 10.1007/s00429-010-0258-9

Pendse, G. V., Borsook, D., and Becerra, L. (2011). A simple and objective method for reproducible resting state network (RSN) detection in fMRI. *PLoS One* 6:e27594. doi: 10.1371/journal.pone.0027594

Pradier, B., Wachsmuth, L., Nagelmann, N., Segelcke, D., Kreitz, S., Hess, A., et al. (2021). Combined resting state-fMRI and calcium recordings show stable brain states for task-induced fMRI in mice under combined ISO/MED anesthesia. *Neuroimage* 245:118626. doi: 10.1016/j.neuroimage.2021.118626

Salimi-Khorshidi, G., Douaud, G., Beckmann, C. F., Glasser, M. F., Griffanti, L., and Smith, S. M. (2014). Automatic denoising of functional MRI data: combining independent component analysis and hierarchical fusion of classifiers. *Neuroimage* 90, 449–468. doi: 10.1016/j.neuroimage.2013.11.046

Seewoo, B. J., Feindel, K. W., Etherington, S. J., and Rodger, J. (2018). Resting-state fMRI study of brain activation using low-intensity repetitive transcranial magnetic stimulation in rats. *Sci. Rep.* 8:6706. doi: 10.1038/s41598-018-24951-6

Seewoo, B. J., Hennessy, L. A., Feindel, K. W., Etherington, S. J., Croarkin, P. E., and Rodger, J. (2020). Validation of chronic restraint stress model in young adult rats for the study of depression using longitudinal multimodal MR imaging. *eNeuro* 7, 1–22. doi: 10.1523/eneuro.0113-20.2020

Seewoo, B. J., Joos, A. C., and Feindel, K. W. (2021). An analytical workflow for seed-based correlation and independent component analysis in interventional resting-state fMRI studies. *Neurosci. Res.* 165, 26–37. doi: 10.1016/j.neures.2020.05.006

Seitzman, B. A., Snyder, A. Z., Leuthardt, E. C., and Shimony, J. S. (2019). The state of resting state networks. *Top. Magn. Reson. Imaging* 28, 189–196. doi: 10.1097/RMR.0000000000000214

Sierakowiak, A., Monnot, C., Aski, S. N., Uppman, M., Li, T.-Q., Damberg, P., et al. (2015). Default mode network, motor network, dorsal and ventral basal ganglia networks in the rat brain: comparison to human networks using resting state-fMRI. *PLoS One* 10:e0120345. doi: 10.1371/journal.pone.0120345

Smith, S. M., Miller, K. L., Salimi-Khorshidi, G., Webster, M., Beckmann, C. F., Nichols, T. E., et al. (2011). Network modelling methods for FMRI. *Neuroimage* 54, 875–891. doi: 10.1016/j.neuroimage.2010.08.063

Smith, S. M., Vidaurre, D., Beckmann, C. F., Glasser, M. F., Jenkinson, M., Miller, K. L., et al. (2013). Functional connectomics from resting-state fMRI. *Trends Cogn. Sci.* 17, 666–682. doi: 10.1016/j.tics.2013.09.016

Smith, J. B., Watson, G. D. R., Liang, Z., Liu, Y., Zhang, N., and Alloway, K. D. (2019). A role for the claustrum in salience processing? *Front. Neuroanat.* 13:64. doi: 10.3389/fnana.2019.00064

Stafford, J. M., Jarrett, B. R., Miranda-Dominguez, O., Mills, B. D., Cain, N., Mihalas, S., et al. (2014). Large-scale topology and the default mode network in the mouse connectome. *Proc. Natl. Acad. Sci.* 111, 18745–18750. doi: 10.1073/pnas.1404346111

Triana, A. M., Glerean, E., Saramaki, J., and Korhonen, O. (2020). Effects of spatial smoothing on group-level differences in functional brain networks. *Netw Neurosci* 4, 556–574. doi: 10.1162/netn_a_00132

Whitesell, J. D., Liska, A., Coletta, L., Hirokawa, K. E., Bohn, P., Williford, A., et al. (2021). Regional, layer, and cell-type-specific connectivity of the mouse default mode network. *Neuron* 109, 545–559.e8. doi: 10.1016/j.neuron.2020.11.011

Williams, L. M. (2017). Defining biotypes for depression and anxiety based on large-scale circuit dysfunction: a theoretical review of the evidence and future directions for clinical translation. *Depress. Anxiety* 34, 9–24. doi: 10.1002/da.22556

Woolrich, M. W., Behrens, T. E., Beckmann, C. F., and Smith, S. M. (2005). Mixture models with adaptive spatial regularization for segmentation with an application to FMRI data. *IEEE Trans. Med. Imaging* 24, 1–11. doi: 10.1109/TMI.2004.836545

Xu, N., Lagrow, T. J., Anumba, N., Lee, A., Zhang, X., Yousefi, B., et al. (2022). Functional connectivity of the brain across rodents and humans. *Front. Neurosci.* 16:816331. doi: 10.3389/fnins.2022.816331

Yang, Z., Laconte, S., Weng, X., and Hu, X. (2008). Ranking and averaging independent component analysis by reproducibility (RAICAR). *Hum. Brain Mapp.* 29, 711–725. doi: 10.1002/hbm.20432

Yang, Z., Zuo, X. N., Wang, P., Li, Z., Laconte, S. M., Bandettini, P. A., et al. (2012). Generalized RAICAR: discover homogeneous subject (sub)groups by reproducibility of their intrinsic connectivity networks. *Neuroimage* 63, 403–414. doi: 10.1016/j.neuroimage.2012.06.060

Yushkevich, P. A., Piven, J., Hazlett, H. C., Smith, R. G., Ho, S., Gee, J. C., et al. (2006). User-guided 3D active contour segmentation of anatomical structures: significantly improved efficiency and reliability. *Neuroimage* 31, 1116–1128. doi: 10.1016/j.neuroimage.2006.01.015

Zerbi, V., Grandjean, J., Rudin, M., and Wenderoth, N. (2015). Mapping the mouse brain with rs-fMRI: an optimized pipeline for functional network identification. *Neuroimage* 123, 11–21. doi: 10.1016/j.neuroimage.2015.07.090

Zhang, N., Rane, P., Huang, W., Liang, Z., Kennedy, D., Frazier, J. A., et al. (2010). Mapping resting-state brain networks in conscious animals. *J. Neurosci. Methods* 189, 186–196. doi: 10.1016/j.jneumeth.2010.04.001

frontiers | Frontiers in Neuroscience

TYPE Brief Research Report
PUBLISHED 15 June 2023
DOI 10.3389/fnins.2023.1186558

OPEN ACCESS

EDITED BY
Nico Sollmann,
University of California, San Francisco,
United States

REVIEWED BY
Itamar Ronen,
Brighton and Sussex Medical School,
United Kingdom
François-Xavier Lejeune,
Institut National de la Santéet de la Recherche Médicale (INSERM), France

*CORRESPONDENCE
Daniel Paech
✉ d.paech@dkfz.de

†These authors have contributed equally to this work and share last authorship

RECEIVED 14 March 2023
ACCEPTED 26 May 2023
PUBLISHED 15 June 2023

CITATION
Ebersberger L, Kratzer FJ, Potreck A, Niesporek SC, Keymling M, Nagel AM, Bendszus M, Wick W, Ladd ME, Schlemmer H-P, Hoffmann A, Platt T and Paech D (2023) First application of dynamic oxygen-17 magnetic resonance imaging at 7 Tesla in a patient with early subacute stroke. *Front. Neurosci.* 17:1186558. doi: 10.3389/fnins.2023.1186558

First application of dynamic oxygen-17 magnetic resonance imaging at 7 Tesla in a patient with early subacute stroke

Louise Ebersberger[1,2,3], Fabian J. Kratzer[4], Arne Potreck[5], Sebastian C. Niesporek[4], Myriam Keymling[1], Armin M. Nagel[4,6], Martin Bendszus[5], Wolfgang Wick[7], Mark E. Ladd[2,4,8], Heinz-Peter Schlemmer[1], Angelika Hoffmann[5,9], Tanja Platt[4†] and Daniel Paech[1,10*†]

[1]Division of Radiology, German Cancer Research Center (DKFZ), Heidelberg, Germany, [2]Faculty of Medicine, University of Heidelberg, Heidelberg, Germany, [3]Department of Pediatrics, Bern University Hospital, Bern, Switzerland, [4]Division of Medical Physics in Radiology, German Cancer Research Center (DKFZ), Heidelberg, Germany, [5]Department of Neuroradiology, Heidelberg University Hospital, Heidelberg, Germany, [6]Institute of Radiology, Friedrich-Alexander University Erlangen-Nürnberg (FAU), Erlangen University Hospital, Erlangen, Germany, [7]Department of Neurology, Heidelberg University Hospital, Heidelberg, Germany, [8]Faculty of Physics and Astronomy, University of Heidelberg, Heidelberg, Germany, [9]Department of Neuroradiology, Bern University Hospital, Bern, Switzerland, [10]Department of Neuroradiology, Bonn University Hospital, Bonn, Germany

Dynamic oxygen-17 (^{17}O) magnetic resonance imaging (MRI) is an imaging method that enables a direct and non-invasive assessment of cerebral oxygen metabolism and thus potentially the distinction between viable and non-viable tissue employing a three-phase inhalation experiment. The purpose of this investigation was the first application of dynamic ^{17}O MRI at 7 Tesla (T) in a patient with stroke. In this proof-of-concept experiment, dynamic ^{17}O MRI was applied during ^{17}O inhalation in a patient with early subacute stroke. The analysis of the relative ^{17}O water ($H_2{}^{17}O$) signal for the affected stroke region compared to the healthy contralateral side revealed no significant difference. However, the technical feasibility of ^{17}O MRI has been demonstrated paving the way for future investigations in neurovascular diseases.

KEYWORDS

oxygen-17 MRI, stroke, metabolic imaging, ultra-high field, 7 Tesla, oxygen metabolism

1. Introduction

According to the World Health Organization, stroke is a common cause of disability and currently the second leading cause of death world-wide (The top 10 causes of death, 2020). This disease is not only deadly, but is a common cause of disability as it often entails permanent neurological deficits with enormous impact on the patient's quality of life (Hong, 2011). Despite the improvement of patient outcome with mechanical recanalization, patients still benefit from the therapy to a variable degree. Neuroimaging before, but also after recanalization may support outcome prediction by, e.g., distinguishing viable tissue from unviable tissue.

Oxygen extraction fraction magnetic resonance imaging (MRI) is a promising technique for identification of at-risk tissue in stroke (Fan et al., 2020). However, this imaging technique only provides indirect information on tissue oxygenation, unlike

oxygen-15 (^{15}O) positron emission tomography (PET). Even though ^{15}O PET is considered the gold standard for oxygen imaging, having detected ischemic penumbra *in vivo* for the first time (Zaro-Weber et al., 2019), clinical routine imaging with this method is challenging due to its complexity and long measurement duration as well as the use of the radioactive ^{15}O isotope with very short half-life (~ 123 s) (Fox and Raichle, 1986; Delapaz and Gupte, 2011).

Oxygen-17 (^{17}O) imaging makes use of the MR properties of the non-radioactive oxygen isotope ^{17}O, which can be applied during the MR experiment either by administration of ^{17}O-labeled water or by inhalation of ^{17}O gas ($^{17}O_2$). The first *in vivo* ^{17}O experiments were performed three decades ago with indirect (Hopkins and Barr, 1987) and direct (Arai et al., 1990, 1991; Pekar et al., 1991) detection of physiological properties. The indirect ^{17}O MR approaches are based on the detection of changes in T2- or T1ρ-weighted proton NMR signals caused by ^{17}O-^{1}H scalar coupling and chemical exchange (Zhu et al., 2005), while the direct ^{17}O MR approach measures ^{17}O water ($H_2{}^{17}O$) itself. In preclinical studies, ^{17}O MRI has been used to study various species including mouse, rat, cat and swine at field strengths between 3 Tesla (T) and 16.4 T (Zhu and Chen, 2017). A ^{17}O MRI approach for studying the cerebral oxygen metabolism was developed for rats about two decades ago (Zhu et al., 2002). Since then, several pathologies have been studied in mice using ^{17}O MRI, such as amyloidosis (Baligand et al., 2021) and Huntington's disease (Lou et al., 2016). The safe and feasible application of indirect (Harada et al., 2022) and direct ^{17}O MRI (Fiat et al., 1993, 2004), and ^{17}O MR spectroscopy (Zhu et al., 2005) to humans has been demonstrated. The metabolic model presented by Atkinson and Thulborn (2010) paved the way for the three-phase $^{17}O_2$ inhalation experiments used in dynamic ^{17}O MRI. This methodical setup measures the metabolized $H_2{}^{17}O$ that accumulates during cellular respiration, while the $^{17}O_2$ gas does not contribute to the measured signal.

Hence, dynamic ^{17}O MRI enables the direct and non-invasive assessment of cerebral oxygen metabolism (Atkinson and Thulborn, 2010), and could thus directly measure oxygen consumption of hypoperfused ischemic tissue. In clinical research, dynamic ^{17}O MRI has primarily been used for brain tumor imaging, confirming the Warburg theorem of lower oxygen metabolism in cancer (Hoffmann et al., 2014; Paech et al., 2020). Dynamic ^{17}O MRI is a tool that can reflect the aerobic oxygen metabolism, hence the potential for clinical stroke imaging has been hypothesized on several occasions. As early as 2011, the application of dynamic ^{17}O MRI to cerebral ischemia in humans has been proposed by Delapaz and Gupte (2011). Two years later a preclinical study by Zhu et al. (2013) demonstrated the successful application of ^{17}O MRI for stroke imaging in a mouse model and suggested the possibility of extending the method to stroke patients. In 2020, Rapalino highlighted the prospect of this modality for investigating cerebral ischemia (Rapalino, 2020). Although ^{17}O MRI has been postulated to be a promising research tool for stroke imaging, cerebral ischemia has not yet been studied in humans with this method.

The scope of this study was to evaluate the feasibility of dynamic ^{17}O MRI for application in stroke. In this proof-of-concept study, we included one patient with early subacute stroke caused by vasculitis, employing dynamic ^{17}O MRI at 7 T.

2. Patient and methods

2.1. Patient

One patient (male, age 55) was included for this proof-of-concept study. The patient had a known history of vasculitis and had been diagnosed with acute stroke in the left middle cerebral artery territory, affecting the basal ganglia and a small region of the parietal-occipital cortex, see Figure 1. Computer tomography and standard clinical MR images at 3 T for anatomical and diffusion imaging had been performed immediately upon admission to the University Hospital Heidelberg, Germany. The dynamic ^{17}O MRI at 7 T was performed in the early subacute state, 5 days later. At the time of the oxygen imaging the patient was not experiencing any severe neurological deficits (National Institutes of Health Stroke Scale (NIHSS): 1). Prior to the examination, written informed consent was obtained in accordance with the institutional guidelines and the study was approved by the ethics committee of the Medical Faculty Heidelberg, Germany (S-154/2014).

2.2. Materials and methods

2.2.1. MRI protocol and dynamic ^{17}O experiment

The clinical magnetic resonance (MR) data were acquired at 3 T employing a whole-body system (Prisma; Siemens Healthcare, Erlangen, Germany) and included the standard protocol for stroke imaging at the local department for neuroradiology, including T2-weighted fluid-attenuated inversion recovery (T2-FLAIR), T2 turbo spin echo (TSE), susceptibility-weighted imaging (SWI), time-of-flight (TOF), diffusion-weighted imaging (DWI), and T1-weighted magnetization prepared rapid gradient echo (MPRAGE) pre and post contrast administration.

The oxygen data were obtained on a 7 T whole-body MR system (Magnetom 7 T; Siemens Healthcare, Erlangen, Germany) using a home-built ^{17}O birdcage head coil with an additional proton (^{1}H) channel (Hoffmann et al., 2014; Niesporek et al., 2018). At 7 T, the total duration of the patient measurement amounted to approximately 40 min, including 30 min (shortened patient protocol) (Paech et al., 2020) of dynamic ^{17}O imaging (TE/TR = 0.56 ms/20 ms, flip angle: 60°, t_{pulse} = 1 ms, readout duration = 5.5 ms, nominal resolution: (7.5 mm)^3, number of projections: 90000) applying a density-adapted radial pulse sequence (Nagel et al., 2009) and 10 min acquisition of a gradient echo (GRE) image (TE/TR = 3.25 ms/7.5 ms, flip angle: 10°, matrix size: 256x256x176, nominal resolution: (1 mm)^3) for registration. To estimate the effective resolution of the oxygen images, the point spread function (PSF) was simulated considering the readout trajectory, T_1 and T_2* relaxation [T_1 = 5 ms, WM: T_2* = 2.8 ms, GM: T_2* = 2.5 ms, CSF: T_2* = 5 ms (Niesporek et al., 2018)] and the reconstruction filter (Hamming). T_2* bias for the different tissues was estimated by calculating the signal at the echo time TE = 0.56 ms: $e^{-\frac{TE}{T_2^*}}$.

The ^{17}O imaging for the healthy volunteers was 40 min (number of projections: 120000, see Supplementary material). A sliding window reconstruction was applied to the ^{17}O data sets (per image: 3000 projections, acquisitions time: 1 min; patient: 30 images, volunteers: 40 images).

The ^{17}O measurement is a dynamic experiment with three inhalation phases: during the first phase, the patient breathes regular

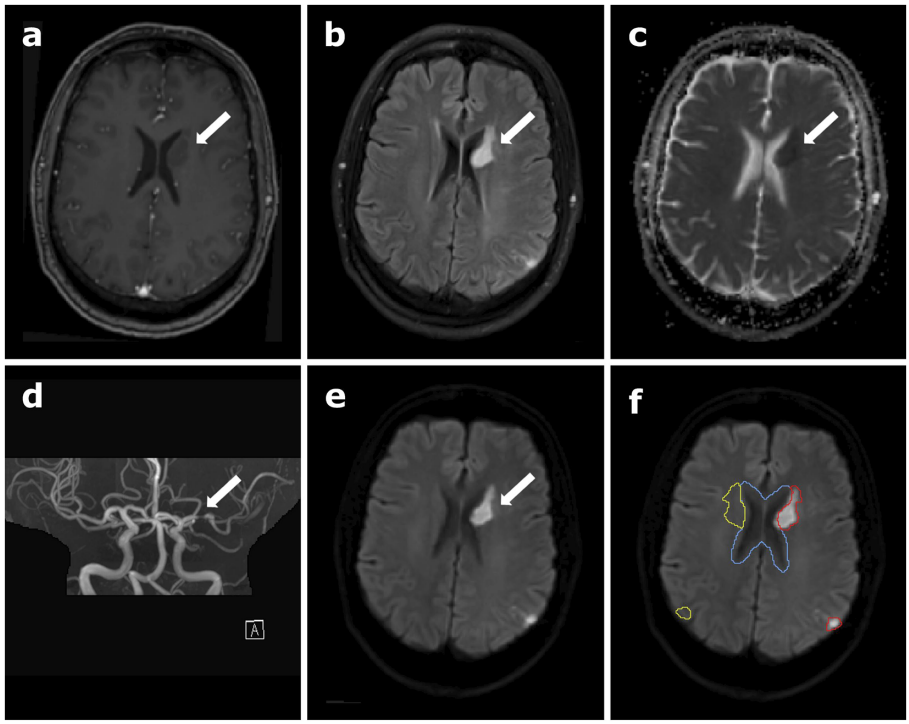

FIGURE 1
Clinical data of the patient depicting the stroke region, **(A)** contrast-enhanced T1-weighted magnetization prepared rapid gradient echo (MPRAGE) data, **(B)** T2-weighted fluid-attenuated inversion recovery (T2 FLAIR), **(C)** apparent diffusion coefficient (ADC) map calculated from diffusion-weighted imaging (DWI), **(D)** time-of-flight angiography (TOF), **(E)** B1000 DWI, and **(F)** B1000 DWI overlaid with the different regions of interest (ROI) used for data analysis in oxygen-17 (^{17}O) MR data: the red contour outlines the stroke region, and cerebral spinal fluid (CSF) is delineated in blue. The yellow contour shows the mirrored stroke ROI, comprising healthy brain tissue. The white arrows indicate the location of the stroke.

room air through an MR-compatible breathing mask (baseline phase, 5 min). Subsequently, the inhalation system is switched to a reservoir containing approximately 4 L of 70% $^{17}O_2$-enriched oxygen gas, starting the second phase (inhalation phase, approximately 6 min). Then, a second switch back to room air initiates the last phase, which lasts until 30 min of continuous MR data are acquired. The details concerning the experimental set up have been described in previous studies (Niesporek et al., 2018; Paech et al., 2020).

2.2.2. Image registration and segmentation

For the 7 T data, the GRE images were registered to the ^{17}O images automatically using the FLIRT algorithm of FSL (FMRIB Software Library) (Jenkinson and Smith, 2001; Jenkinson et al., 2002). The co-registration of the clinical 3 T images to the 7 T GRE images was conducted by manual pre-registration followed by an automatic registration, again using the FLIRT algorithm. Masks for cerebral gray matter (GM), cerebral white matter (WM) and cerebral spinal fluid (CSF) were obtained by applying the FAST segmentation tool for an automatic segmentation to the MPRAGE data set (Zhang et al., 2001). Further regions-of-interest (ROIs) included the stroke area (striatal and cortical stroke together), the mirrored control area and the ventricles, which were segmented manually in the Medical Imaging Interaction Toolkit (MITK) (Wolf et al., 2005; Nolden et al., 2013) according to the B1000 diffusion images, see Figure 1F. These segmentations were performed by two readers in consensus, reader 1 (L.E.) with 2 years and reader 2 (D.P.) with 10 years of experience in neuroimaging and were applied for further investigations. To check for inter-reading variability, a second reading has been performed by reader 1, blinded to the original segmentation (see Supplementary material).

2.2.3. Data analysis

A binary mask based partial volume correction (PVC) was performed on the oxygen data set, as proposed by Niesporek et al. (2015, 2018), which applies the geometric transfer matrix (GTM) PVC method. This algorithm takes into account anatomical information using the tissue masks for GM, WM, and CSF and for the stroke area as well as the simulated tissue-specific PSF. This approach provides a region-specific PV-corrected signal value within each mask and for each time point.

Additionally, the relative $H_2{}^{17}O$ signal evolution was investigated without PVC within different ROIs: ventricles, stroke area, mirrored control and the remaining healthy brain tissue (whole brain minus ROIs of stroke area, mirrored control and ventricles). Since the stroke area lies in proximity to the ventricles, the influence of partial volume effects on the stroke area was minimized for this analysis without PVC by dilating the ventricle ROI twice using the segmentation utilities tool in MITK and subtracting the overlap from the stroke and mirrored control ROIs, resulting in a smaller stroke ROI.

To obtain the relative curves, all data points were normalized to the mean of the baseline (5 min). The relative $H_2{}^{17}O$ signal evolutions of the patient were compared to those of three healthy volunteers (all male, ages 28, 37 and 65), each measured twice with ^{17}O MRI at 7 T in the past (Niesporek et al., 2018). The data analysis and the testing

procedure for the healthy volunteers can be found in the Supplementary material. For all measurements, five data points around the second switch from $^{17}O_2$ inhalation back to room air, thus the point of longest $^{17}O_2$ inhalation, were averaged and compared. Additionally, the standard deviation was calculated for the first five data points of the baseline.

Furthermore, the relative ^{17}O signal increase is obtained by subtracting a baseline image during breathing of room air from a ^{17}O image at the end of $^{17}O_2$ inhalation (maximum signal); then dividing the result by the baseline image (Paech et al., 2020). Data of the two images were acquired in 3 min each. For smoothing of these relative ^{17}O images and for obtaining a refined image resolution, a Hamming filter was applied, as well as eightfold zero-filling.

3. Results

3.1. Effective resolution of oxygen images and T_2* influences

The simulated full width half maximum (FWHM) of the PSF is approximately 2.3 voxels, which results in an effective resolution of the oxygen images of *circa* ((17–17.5)mm)^3 for WM and GM. For CSF, the FWHM is approximately 2.2 voxels and the effective resolution (16 mm)^3. Due to the T_2* decay the signal at TE for the different tissues was estimated to be: CSF: 100%, WM: 92%, GM: 89%.

3.2. Data analysis

The relative PV-corrected time evolution in the stroke ROI is depicted in Supplementary Figure S2 in the Supplementary material in comparison to the time evaluation without PVC. The PV-corrected data shows a high noise level. Relative $H_2{}^{17}O$ signal evolutions without PVC for healthy brain tissue, CSF, stroke ROI and mirrored control are depicted in Figure 2. The evaluation of the relative $H_2{}^{17}O$ signal evolution revealed no significant difference between the stroke area and the mirrored control area.

The relative signal after the inhalation phase was analyzed by averaging five data points (5 min) around the time of the second switch. Here, the healthy brain tissue, encompassing the complete brain tissue minus the ventricles, stroke and mirrored control ROI, showed a relative mean signal (5 data points around the second switching time, evenly spaced 60 s apart, corresponding to 5 min in total) of 1.181 (Figure 2A). The evaluation for CSF resulted in a relative mean $H_2{}^{17}O$ signal of 1.135 (Figure 2B). Due to the smaller ROI size, the stroke and the mirrored control region, Figures 2C,D show larger signal fluctuations compared to the relative curves of healthy brain tissue and CSF (Figures 2A,B). The evaluation of the relative $H_2{}^{17}O$ signal in the stroke ROI yielded a relative mean signal (5 data points around the second switching time) of 1.158, while the mirrored control exhibited a relative mean $H_2{}^{17}O$ signal of 1.168.

For better comparability, the relative oxygen signal evolution for stroke (Figure 2D), and its mirrored control (Figure 2C), were overlaid in Figure 2E. Averaging five data points around the time of the second switch, the signal increase in the stroke area is about 0.9% less than in the mirrored control. The analysis of six data sets obtained from three healthy volunteers showed differences between −1.9 and + 0.3% between the left ROI (equivalent to stroke) and right ROI (equivalent to mirrored control). Furthermore, the standard deviation in the baseline (relative to the mean) in the healthy subjects is 2.2% (left) and 2.3% (right), respectively. The detailed analysis is shown in Supplementary Tables S1, S2 and Supplementary Figure S3 in the Supplementary material.

In the relative ^{17}O images, the lateral ventricles containing CSF show a low ^{17}O signal increase, indicating a region with low metabolic activity. The stroke area exhibits a similarly low ^{17}O signal increase, indicated by a white arrow in Figure 3. However, also the mirrored control area shows a low ^{17}O signal increase. The outer cortex regions show a rather homogenous relative signal distribution. The cerebellum exhibits a high ^{17}O signal increase, indicating high metabolic activity.

4. Discussion

4.1. Data interpretation

In this proof-of-concept study, dynamic ^{17}O MRI was applied for the first time during ^{17}O inhalation in a patient with early subacute stroke.

Firstly, the PV-corrected relative $H_2{}^{17}O$ signal evolution of the stroke area, corresponding to a very small ROI, showed high signal fluctuations. The noise level impeded the reliable interpretation of changes in the oxygen signal evolution, as they cannot be confidently attributed to regionally altered metabolic activity. Further investigations with PVC might be possible in patients with larger stroke areas. However, the patient's condition will likely be worse and might not allow for dynamic ^{17}O MRI.

Secondly, the evaluation of the relative $H_2{}^{17}O$ signal evolution in the patient revealed no significant difference between the stroke area and the mirrored control area. The deviation between stroke and mirrored control in the patient was in the same order of magnitude as in the healthy volunteers, and in the same order of magnitude as the calculated standard deviation in the volunteer data sets during the baseline (breathing room air).

The relative ^{17}O images showed visual differences between the cortex regions, the cerebellum and the CSF, as shown in the literature. The CSF exhibited a low ^{17}O signal, since it does not contain cells, but instead drains the metabolized $H_2{}^{17}O$ water from the surrounding brain tissue (Paech et al., 2020). The relative images showed lower signal increase in the stroke area but also in the mirrored control areas, suggesting a lower metabolic activity within this region, yet this might be due to spillover effects from the adjacent ventricles. This spill over is a result of the FWHM of the PSF of *circa* 2.2–2.3 voxels. Additionally, if signal contributions from CSF and brain tissues are measured in the same voxel, the quantification can be slightly biased towards the CSF value due to its longer T_2* of 5 ms (GM/WM: 89/92% of CSF signal).

The influence of the segmentation variability of the stroke area on these results has been considered. However, the high dice coefficient of 86.3% for the two readings performed for the stroke ROI, together with the relatively low resolution of the oxygen images of [(17–17.5) mm]^3, lead to the conclusion that slight changes of the segmentations on the high-resolution proton images do not markedly affect the evaluation of the ^{17}O data.

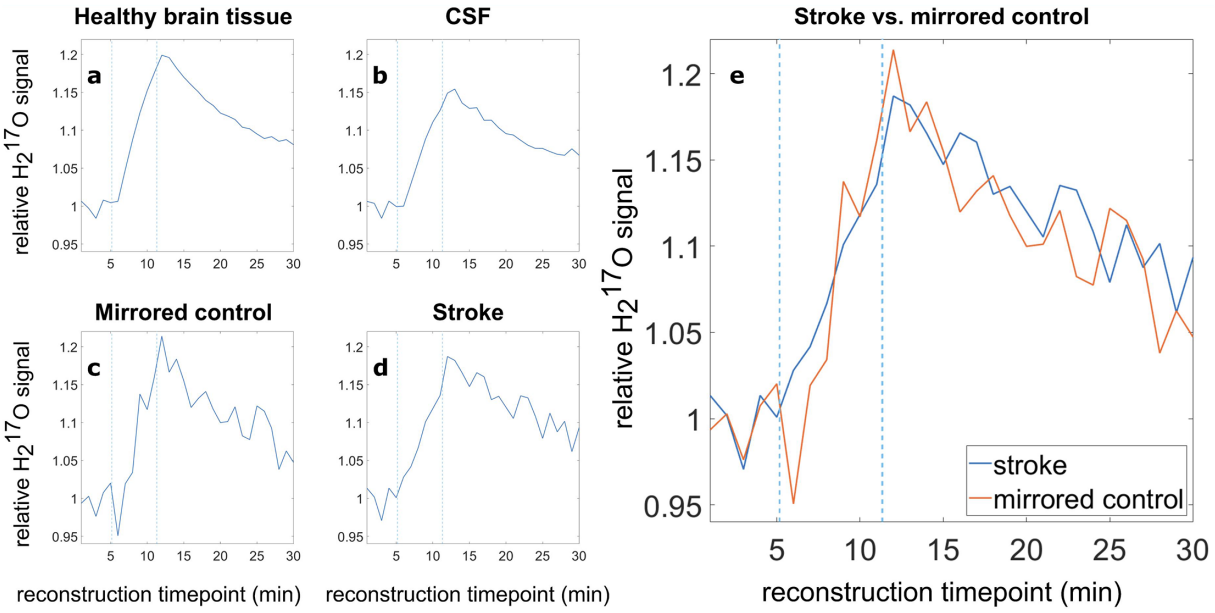

FIGURE 2
Relative ^{17}O water ($H_2{}^{17}O$) signal evolution in various tissue types, **(A)** healthy brain tissue, **(B)** CSF, **(C)** the mirrored control, **(D)** the stroke region, and **(E)** direct comparison of the relative $H_2{}^{17}O$ signal in the stroke ROI (blue) and the mirrored contralateral healthy ROI (orange). Blue dashed lines indicate the switching times from room air to ^{17}O-enriched gas and back to room air.

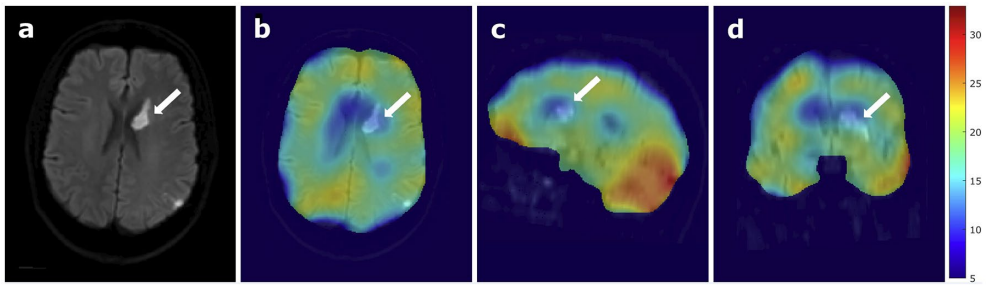

FIGURE 3
^{17}O MRI at 7 Tesla in a patient with stroke, **(A)** B1000 DWI of the patient only and **(B)** overlaid with relative ^{17}O images, showing the stroke region in an axial view, **(C)** sagittal view, and **(D)** coronal view. The white arrows indicate the location of the stroke.

These findings demonstrated the general feasibility of employing dynamic ^{17}O MRI in a patient with stroke, but did not show a significant quantitative difference between the stroke region and the mirrored control in this particular patient.

This motivates future investigations in patients with larger strokes that are not located in vicinity to the ventricles. A ^{15}O PET study in patients with acute stroke showed that the investigation of a stroke in the basal ganglia near the CSF afforded less prominent results in comparison to larger strokes located in the cortex (Zaro-Weber et al., 2019). Thus, dynamic ^{17}O MRI remains a promising imaging technique for detection of changes in oxygen metabolism that are possibly associated with neuronal impairment or death.

The direct comparison to other metabolic imaging techniques, first and foremost ^{15}O PET, would be especially interesting as well as the investigation of acute stroke with dynamic ^{17}O MRI. In clinical routine MRI is more feasible than PET and less complex for stroke imaging (Zaro-Weber et al., 2019). However, the overestimation of both penumbra and ischemic core poses a problem when using mismatch imaging (Delapaz and Gupte, 2011), so that further development of novel imaging methods remains crucial for the improvement of stroke diagnostics.

In this study, we were able to conduct the first 7 T dynamic ^{17}O experiment in a study participant with early subacute stroke. The results of this study did not show a significant difference between the stroke region and the mirrored healthy contralateral side, motivating the investigation of patients with a larger stroke area, preferably with location in the cortex. Technical advances including even higher magnetic field strengths and improvement of hardware equipment could boost the resolution of dynamic ^{17}O MRI and might pave the way for clinical application in stroke in the future (Platt et al., 2021).

4.2. Limitations

This study demonstrated the feasibility of employing ^{17}O MRI in a patient with early subacute stroke. For better assessment, further examinations in patients with stroke would be beneficial. The investigated cerebral ischemia in the basal ganglia was relatively small and in proximity to the lateral ventricles. Since the CSF itself does not exhibit metabolic activity, this is an area of low metabolic turnover. Due to partial volume effects, the adjacent CSF might bias the metabolic signal within the stroke ROI. However, prior extraction of the CSF region with a security margin and the use of a mirrored control region on the contralateral side reduced this bias. The measurement of a larger cerebral infarction would probably yield more distinct results, but these patients would be rather instable for this complex examination. Furthermore, the measurement at 7 T was conducted in the early subacute stroke time frame. The investigation of (hyper-)acute stroke within less than 48 h after symptom onset might provide more information concerning the viability of the hypo- or hyperperfused tissue, but would be even more challenging in the clinical setting. However, continuous monitoring of the patient in the stroke unit is recommended for the first 48 h, which impedes research studies in this time frame.

As for the comparison of the clinical data to the three data sets of healthy participants, the demographics are quite similar which allows for fair comparability between the data sets. All investigated subjects are male and the patient's age (55 years) lies between the age of volunteer 1 (age 65) and 2 (age 37).

Data availability statement

The raw data supporting the conclusions of this article are available only upon scientific request because patient data are included. The corresponding author (DP) may be contacted to request the data.

Ethics statement

The studies involving human participants were reviewed and approved by IRB committee, University of Heidelberg, Germany. The patients/participants provided their written informed consent to participate in this study.

Author contributions

LE, AP, AH, TP, and DP: study conceptualization. LE, FK, SN, AN, TP, and DP: technical methodology. LE, AP, MK, AH, and TP: patient examinations. LE, FK, AN, TP, and DP: data processing. LE, AN, TP, and DP: statistical analysis. LE: writing first draft. LE, FK, AP, SN, MK, AN, MB, WW, ML, H-PS, AH, TP, and DP: reviewing and editing first draft. AN, MB, WW, ML, H-PS, AH, TP, and DP: scientific supervision. All authors contributed to the article and approved the submitted version.

Acknowledgments

The authors thank Nukem Isotopes Imaging (Alzenau, Germany) for their supply with $^{17}O_2$ gas at a reduced cost.

Conflict of interest

The authors declare that the research was conducted in the absence of any commercial or financial relationships that could be construed as a potential conflict of interest.

Publisher's note

Supplementary material

The Supplementary material for this article can be found online at: https://www.frontiersin.org/articles/10.3389/fnins.2023.1186558/full#supplementary-material

References

Arai, T., Mori, K., Nakao, S. I., Watanabe, K., Kito, K., Aoki, M., et al. (1991). In vivo oxygen-17 nuclear magnetic resonance for the estimation of cerebral blood flow and oxygen consumption. *Biochem. Biophys. Res. Commun.* 179, 954–961. doi: 10.1016/0006-291X(91)91911-U

Arai, T., Nakao, S. I., Mori, K., Ishimori, K., Morishima, I., Miyazawa, T., et al. (1990). Cerebral oxygen utilization analyzed by the use of oxygen-17 and its nuclear magnetic resonance. *Biochem. Biophys. Res. Commun.* 169, 153–158. doi: 10.1016/0006-291X(90)91447-Z

Atkinson, I. C., and Thulborn, K. R. (2010). Feasibility of mapping the tissue mass corrected bioscale of cerebral metabolic rate of oxygen consumption using 17-oxygen and 23-sodium MR imaging in a human brain at 9.4 T. *NeuroImage* 51, 723–733. doi: 10.1016/j.neuroimage.2010.02.056

Baligand, C., Barret, O., Tourais, A., Pérot, J. B., Thenadey, D., Petit, F., et al. (2021). Zero Echo time (17)O-MRI reveals decreased cerebral metabolic rate of oxygen consumption in a murine model of amyloidosis. *Meta* 11:263. doi: 10.3390/metabo11050263

Delapaz, R., and Gupte, P. (2011). Potential application of (1)(7)O MRI to human ischemic stroke. *Adv. Exp. Med. Biol.* 701, 215–222. doi: 10.1007/978-1-4419-7756-4_29

Fan, A. P., Khalil, A. A., Fiebach, J. B., Zaharchuk, G., Villringer, A., Villringer, K., et al. (2020). Elevated brain oxygen extraction fraction measured by MRI susceptibility relates to perfusion status in acute ischemic stroke. *J. Cereb. Blood Flow Metab.* 40, 539–551. doi: 10.1177/0271678X19827944

Fiat, D., Dolinsek, J., Hankiewicz, J., Dujovny, M., and Ausman, J. (1993). Determination of regional cerebral oxygen consumption in the human: 17O natural abundance cerebral magnetic resonance imaging and spectroscopy in a whole body system. *Neurol. Res.* 15, 237–248. doi: 10.1080/01616412.1993.11740143

Fiat, D., Hankiewicz, J., Liu, S., Trbovic, S., and Brint, S. (2004). 17O magnetic resonance imaging of the human brain. *Neurol. Res.* 26, 803–808. doi: 10.1179/016164104X5156

Fox, P. T., and Raichle, M. E. (1986). Focal physiological uncoupling of cerebral blood flow and oxidative metabolism during somatosensory stimulation in human subjects. *Proc. Natl. Acad. Sci. U. S. A.* 83, 1140–1144. doi: 10.1073/pnas.83.4.1140

Harada, T., Kudo, K., Kameda, H., Sato, R., Shirai, T., Bito, Y., et al. (2022). Phase I randomized trial of (17) O-labeled water: safety and feasibility study of indirect proton MRI for the evaluation of cerebral water dynamics. *J. Magn. Reson. Imaging* 56, 1874–1882. doi: 10.1002/jmri.28210

Hoffmann, S. H., Radbruch, A., Bock, M., Semmler, W., and Nagel, A. M. (2014). Direct (17)O MRI with partial volume correction: first experiences in a glioblastoma patient. *MAGMA* 27, 579–587. doi: 10.1007/s10334-014-0441-8

Hong, K. S. (2011). Disability-adjusted life years analysis: implications for stroke research. *J. Clin. Neurol.* 7, 109–114. doi: 10.3988/jcn.2011.7.3.109

Hopkins, A. L., and Barr, R. G. (1987). Oxygen-17 compounds as potential NMR T2 contrast agents: enrichment effects of H2(17)O on protein solutions and living tissues. *Magn. Reson. Med.* 4, 399–403. doi: 10.1002/mrm.1910040413

Jenkinson, M., Bannister, P., Brady, M., and Smith, S. (2002). Improved optimization for the robust and accurate linear registration and motion correction of brain images. *NeuroImage* 17, 825–841. doi: 10.1006/nimg.2002.1132

Jenkinson, M., and Smith, S. (2001). A global optimisation method for robust affine registration of brain images. *Med. Image Anal.* 5, 143–156. doi: 10.1016/S1361-8415(01)00036-6

Lou, S., Lepak, V. C., Eberly, L. E., Roth, B., Cui, W., Zhu, X. H., et al. (2016). Oxygen consumption deficit in Huntington disease mouse brain under metabolic stress. *Hum. Mol. Genet.* 25, 2813–2826. doi: 10.1093/hmg/ddw138

Nagel, A. M., Laun, F. B., Weber, M. A., Matthies, C., Semmler, W., and Schad, L. R. (2009). Sodium MRI using a density-adapted 3D radial acquisition technique. *Magn. Reson. Med.* 62, 1565–1573. doi: 10.1002/mrm.22157

Niesporek, S. C., Hoffmann, S. H., Berger, M. C., Benkhedah, N., Kujawa, A., Bachert, P., et al. (2015). Partial volume correction for in vivo (23)Na-MRI data of the human brain. *NeuroImage* 112, 353–363. doi: 10.1016/j.neuroimage.2015.03.025

Niesporek, S. C., Umathum, R., Lommen, J. M., Behl, N. G. R., Paech, D., Bachert, P., et al. (2018). Reproducibility of CMRO2 determination using dynamic (17) O MRI. *Magn. Reson. Med.* 79, 2923–2934. doi: 10.1002/mrm.26952

Nolden, M., Zelzer, S., Seitel, A., Wald, D., Müller, M., Franz, A. M., et al. (2013). The medical imaging interaction toolkit: challenges and advances: 10 years of open-source development. *Int. J. Comput. Assist. Radiol. Surg.* 8, 607–620. doi: 10.1007/s11548-013-0840-8

Paech, D., Nagel, A. M., Schultheiss, M. N., Umathum, R., Regnery, S., Scherer, M., et al. (2020). Quantitative dynamic oxygen 17 MRI at 7.0 T for the cerebral oxygen metabolism in glioma. *Radiology* 295, 181–189. doi: 10.1148/radiol.2020191711

Pekar, J., Ligeti, L., Ruttner, Z., Lyon, R. C., Sinnwell, T. M., van Gerderen, P., et al. (1991). In vivo measurement of cerebral oxygen consumption and blood flow using 17O magnetic resonance imaging. *Magn. Reson. Med.* 21, 313–319. doi: 10.1002/mrm.1910210217

Platt, T., Ladd, ME., and Paech D. (2021). 7 Tesla and Beyond: Advanced Methods and Clinical Applications in Magnetic Resonance Imaging. *Invest Radiol*. 56, 705–725.

Rapalino, O. (2020). A direct window into brain Cancer metabolism by using MRI. *Radiology* 295, 190–191. doi: 10.1148/radiol.2020192820

The top 10 causes of death. (2020). Available at: https://www.who.int/news-room/fact-sheets/detail/the-top-10-causes-of-death (accessed June 27, 2022).

Wolf, I., Vetter, M., Wegner, I., Böttger, T., Nolden, M., Schöbinger, M., et al. (2005). The medical imaging interaction toolkit. *Med. Image Anal.* 9, 594–604. doi: 10.1016/j.media.2005.04.005

Zaro-Weber, O., Fleischer, H., Reiblich, L., Schuster, A., Moeller-Hartmann, W., and Heiss, W. D. (2019). Penumbra detection in acute stroke with perfusion magnetic resonance imaging: validation with (15) O-positron emission tomography. *Ann. Neurol.* 85, 875–886. doi: 10.1002/ana.25479

Zhang, Y., Brady, M., and Smith, S. (2001). Segmentation of brain MR images through a hidden Markov random field model and the expectation-maximization algorithm. *IEEE Trans. Med. Imaging* 20, 45–57. doi: 10.1109/42.906424

Zhu, X. H., and Chen, W. (2017). In vivo(17)O MRS imaging – quantitative assessment of regional oxygen consumption and perfusion rates in living brain. *Anal. Biochem.* 529, 171–178. doi: 10.1016/j.ab.2016.08.026

Zhu, X. H., Chen, J. M., Tu, T. W., Chen, W., and Song, S. K. (2013). Simultaneous and noninvasive imaging of cerebral oxygen metabolic rate, blood flow and oxygen extraction fraction in stroke mice. *NeuroImage* 64, 437–447. doi: 10.1016/j.neuroimage.2012.09.028

Zhu, X. H., Zhang, Y., Tian, R. X., Lei, H., Zhang, N., Zhang, X., et al. (2002). Development of (17)O NMR approach for fast imaging of cerebral metabolic rate of oxygen in rat brain at high field. *Proc. Natl. Acad. Sci. U. S. A.* 99, 13194–13199. doi: 10.1073/pnas.202471399

Zhu, X. H., Zhang, N., Zhang, Y., Zhang, X., Ugurbil, K., and Chen, W. (2005). In vivo 17O NMR approaches for brain study at high field. *NMR Biomed.* 18, 83–103. doi: 10.1002/nbm.930

Frontiers in Neuroscience

Provides a holistic understanding of brain function from genes to behavior

Part of the most cited neuroscience journal series which explores the brain - from the new eras of causation and anatomical neurosciences to neuroeconomics and neuroenergetics.

Discover the latest Research Topics

See more →

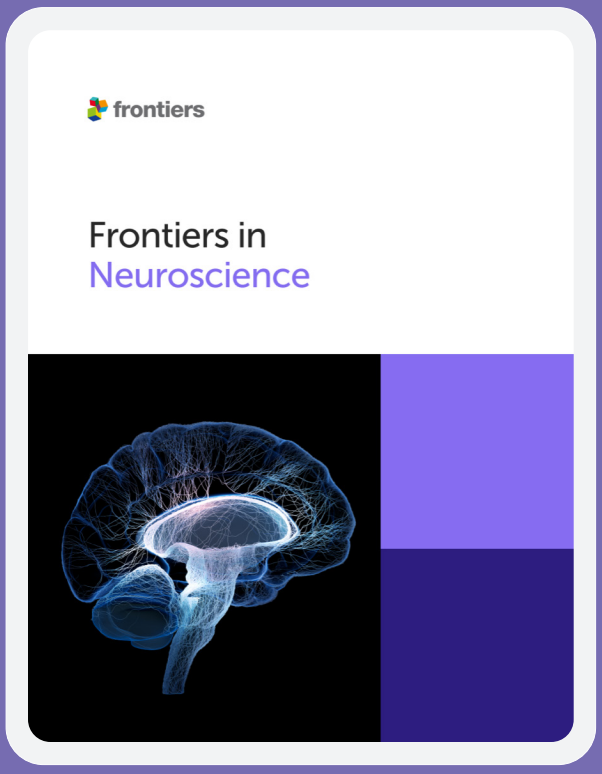

Frontiers

Avenue du Tribunal-Fédéral 34
1005 Lausanne, Switzerland
frontiersin.org

Contact us

+41 (0)21 510 17 00
frontiersin.org/about/contact